



UNIVERSITAT DE  
BARCELONA

## Formulation and screening of drug nanocarriers using microfluidic technology

Adrianna Glinkowska Mares

**ADVERTIMENT.** La consulta d'aquesta tesi queda condicionada a l'acceptació de les següents condicions d'ús: La difusió d'aquesta tesi per mitjà del servei TDX ([www.tdx.cat](http://www.tdx.cat)) i a través del Dipòsit Digital de la UB ([diposit.ub.edu](http://diposit.ub.edu)) ha estat autoritzada pels titulars dels drets de propietat intel·lectual únicament per a usos privats emmarcats en activitats d'investigació i docència. No s'autoritza la seva reproducció amb finalitats de lucre ni la seva difusió i posada a disposició des d'un lloc aliè al servei TDX ni al Dipòsit Digital de la UB. No s'autoritza la presentació del seu contingut en una finestra o marc aliè a TDX o al Dipòsit Digital de la UB (framing). Aquesta reserva de drets afecta tant al resum de presentació de la tesi com als seus continguts. En la utilització o cita de parts de la tesi és obligat indicar el nom de la persona autora.

**ADVERTENCIA.** La consulta de esta tesis queda condicionada a la aceptación de las siguientes condiciones de uso: La difusión de esta tesis por medio del servicio TDR ([www.tdx.cat](http://www.tdx.cat)) y a través del Repositorio Digital de la UB ([diposit.ub.edu](http://diposit.ub.edu)) ha sido autorizada por los titulares de los derechos de propiedad intelectual únicamente para usos privados enmarcados en actividades de investigación y docencia. No se autoriza su reproducción con finalidades de lucro ni su difusión y puesta a disposición desde un sitio ajeno al servicio TDR o al Repositorio Digital de la UB. No se autoriza la presentación de su contenido en una ventana o marco ajeno a TDR o al Repositorio Digital de la UB (framing). Esta reserva de derechos afecta tanto al resumen de presentación de la tesis como a sus contenidos. En la utilización o cita de partes de la tesis es obligado indicar el nombre de la persona autora.

**WARNING.** On having consulted this thesis you're accepting the following use conditions: Spreading this thesis by the TDX ([www.tdx.cat](http://www.tdx.cat)) service and by the UB Digital Repository ([diposit.ub.edu](http://diposit.ub.edu)) has been authorized by the titular of the intellectual property rights only for private uses placed in investigation and teaching activities. Reproduction with lucrative aims is not authorized nor its spreading and availability from a site foreign to the TDX service or to the UB Digital Repository. Introducing its content in a window or frame foreign to the TDX service or to the UB Digital Repository is not authorized (framing). Those rights affect to the presentation summary of the thesis as well as to its contents. In the using or citation of parts of the thesis it's obliged to indicate the name of the author.

Doctoral Thesis

# Formulation and screening of drug nanocarriers using microfluidic technology

Adrianna Glinkowska Mares

Thesis co-supervisors:

Dr. Lorenzo Albertazzi & Dr. Sílvia Pujals Riatós



UNIVERSITAT DE  
BARCELONA

# Formulation and screening of drug nanocarriers using microfluidic technology

Memòria presentada per optar al grau de doctor per la Universitat de Barcelona

Programa de doctorat en Nanociències

**Autora:** Adrianna Glinkowska Mares



**Directors:** Dr. Lorenzo Albertazzi & Dra. Sílvia Pujals Riatós

**Tutor:** Dr. Josep Samitier Martí

Barcelona, 2021



UNIVERSITAT DE  
BARCELONA



*At the end it is always a little bit of experience and a little bit of planets and moon alignment.*

*The most effective way to do it, is to do it.*

# Table of contents

Chapter 1   Introduction: Nanocarriers in anticancer therapy .....	6
1.1 Types of nanoparticles for cancer treatment .....	8
Lipid-based .....	8
Drug Conjugates .....	9
Viral Nanoparticles .....	10
Inorganic Nanoparticles .....	10
Polymeric Nanocarriers .....	12
1.2 Strategies for drug delivery .....	14
Passive delivery .....	14
Active targeting .....	15
1.3 Characterization of NPs .....	17
1.4 Formulation of polymeric Nanoparticles .....	19
Self-assembly.....	19
Emulsification.....	19
Nanoprecipitation .....	20
1.5 Microfluidic-assisted Nanoprecipitation .....	22
Hydrodynamic Flow Focusing.....	23
Fluid micromixers for combinatorial formulation.....	24
1.6 Microfabrication of microfluidic devices.....	26
Photolithography and PDMS.....	26
Other materials .....	27
1.7 Preclinical models for screening Drug Delivery Systems .....	29
In vitro cell culture .....	29
In vivo animal studies.....	30
Culture shock: The missing link .....	30
1.8 Aim and content of the thesis.....	37
1.9 References .....	39
Chapter 2   Formulation of tunable size PLGA-PEG drug nanocarriers using microfluidic technology .....	53
2.1 Introduction.....	54
2.2 Microfluidic hydrodynamic flow focusing and manual bulk formulation .....	56
2.3 Particle diameter tunability using microfluidic chip .....	57
2.4 Encapsulation of fluorescent compounds.....	60
2.5 NPs incubation with MCF-7 cells .....	62
2.6 Conclusions.....	63

2.7	Experimental section .....	65
2.8	References .....	70
Chapter 3	Microfluidic mixer for combinatorial formulation of drug nanocarriers .....	76
3.1	Introduction .....	77
3.2	Fabrication and characterization of prototype passive micromixer .....	82
3.3	Fluorescence test of micromixer performance .....	83
3.4	Combinatorial microfluidic formulation of color-coded nanocarriers .....	86
3.5	Beyond PDMS: Micromixer in glass .....	90
3.6	Conclusions .....	93
3.7	Experimental section .....	94
3.8	References .....	95
Chapter 4	Real-time imaging of micelle stability in a microfluidic cancer-on-a-chip .....	98
4.1	Introduction .....	99
4.2	The system: amphiphilic PEG-dendron micelles and cancer-on-a-chip .....	101
4.3	Characterization of reconstructed barriers in microfluidic cancer-on-a-chip model .....	104
4.4	Increased extravasation of micelles is induced in tumor blood vessel chip .....	107
4.5	Time- and space-resolved micelle stability revealed in 3D tumor microenvironment model .....	111
4.6	Stability of hybrids dictates their infiltration/extravasation .....	115
4.7	Conclusions .....	118
4.8	Experimental section .....	119
4.9	References .....	123
Chapter 5	Discussion .....	128
	Conclusions .....	135
	Outlook .....	137
	Glossary .....	138
	Acknowledgements .....	140
	Funding Acknowledgments .....	142
	Thesis Summary .....	143
	Resumen en castellano .....	145





## Statement of Originality

The author of this thesis, Adrianna Glinkowska Mares, considers it to be original and that it complies with the ethical codes and good practices without containing plagiarism.

Then, I declare the following elements of this thesis to be considered a contribution to knowledge:

- **Glinkowska Mares, A.**, Feiner-Gracia, N., Buzhor, M., Rodriguez-Trujillo, R., Samitier Marti, J., Pujals, S., Albertazzi, L., Real-Time Ratiometric Imaging of Micelles Assembly State in a Microfluidic Cancer-on-a-Chip, *ACS Appl. Bio Mater.* 2021, 4, 1, 669-681
- **Glinkowska Mares, A.**, Paccassoni, G., Samitier Marti, J., Pujals, S., Albertazzi, L., Formulation of tunable size PLGA-PEG nanoparticles for drug delivery using microfluidic technology, *PLOS One*, 2021,
- **Glinkowska Mares, A.**, Feiner-Gracia, Delgado L., Albertazzi, L., Pujals, S., Towards cellular ultrastructural characterization in organ-on-a-chip by Transmission Electron Microscopy, *Appl. Nano*, 2021,

Signed:



10/04/2021, Barcelona

## Chapter 1| Introduction: Nanocarriers in anticancer therapy

*This chapter presents a brief introduction to the topic of nanocarriers used to treat cancer disease. It lists different types of nanomaterials with their clinically approved examples. Furthermore, it focuses on polymer-based nanocarriers and their formulation with microfluidic devices. Finally, it describes preclinical models for screening of drug delivery systems, with the focus on 3D cell culture in microfluidic chips.*

Drug delivery systems (DDS) are approaches, formulations, devices and technologies used for transporting therapeutics inside the body, with the focus on improving their safety and efficacy. DDS in anticancer therapy are designed to address issues related to the administration of the small molecule drugs, such as low bioavailability, short circulation time and lack of selectivity.<sup>1</sup> These systems aim to enhance the general therapeutic effect, with purpose to withstand physiological conditions, arrive to a target site and release the carried molecules in the area of disease. Preferably the payload release should be controlled and sustained, meanwhile the system itself should be biodegradable, and neutral to the organism. The DDS in cancer treatment are largely implemented for parenteral route of administration, which holds a top place for treatment of hospitalized and bed-ridden patients.<sup>2</sup>

In the last years we could see an exponentially growing numbers of patents and publications in the field of nanoparticles (NPs) for drug delivery. Many of the proposed solutions are intended for common in anticancer therapy intravenous route of administration.<sup>3,4</sup> The engineered NPs face challenges upon entering the systemic circulation, such as shear stress and presence of plasma proteins. Their design needs to permit them to endure, and to complete their mission in extravasation from the blood vessel to the tissue matrix, where finally they can reach the cancer cells and release the therapeutic agent as schematically shown in Figure 1.1.<sup>5</sup>

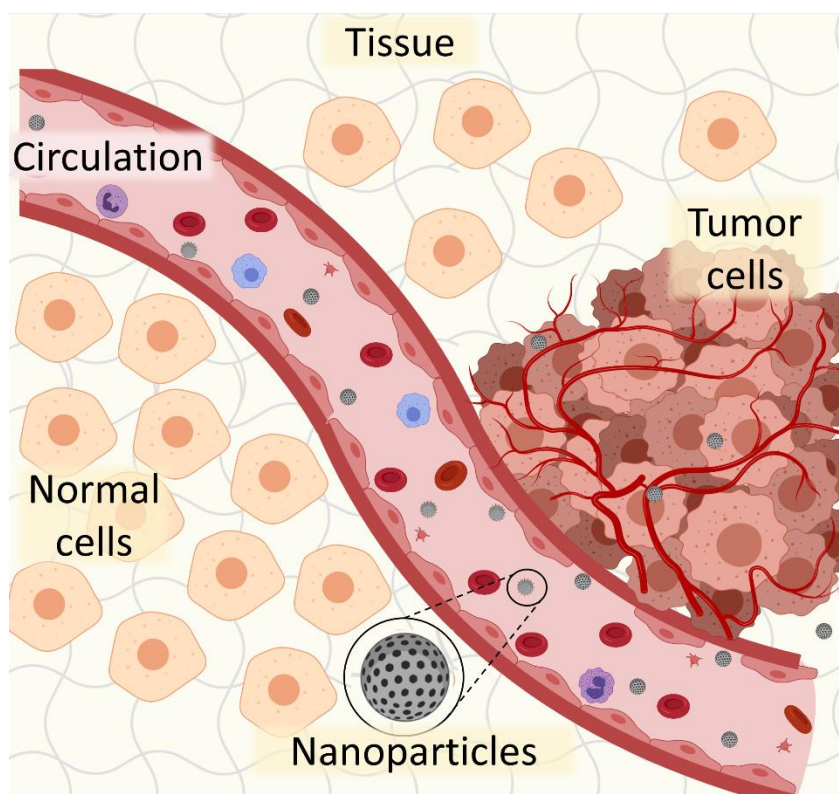


Figure 1.1 Scheme of nanoparticle journey in a blood vessel toward the disease site (tumor cells).

## 1.1 Types of nanoparticles for cancer treatment

Current therapies are mostly based on radiation or on chemotherapeutics that attack most common feature of cancer cells: rapid division. The non-selective mechanism of their action is harmful to other quickly dividing healthy cells, such as bone marrow cells, digestive tract cells or macrophages.<sup>6,7</sup> Patients with administered chemotherapeutic agents suffer multiple side effects related to the systemic toxicity caused by the treatment. The interest in the nanocarriers for drug delivery is based on the potential improvements that they could contribute to, in terms of protection of the human body from undesired cytotoxicity and the protection of potent therapeutics from preliminary deactivation or elimination.

Nanoparticle-based therapeutics aim to solve current issues caused by conventional treatments, such as: systemic toxicity, lack of selectivity toward cancer cells, poor stability in physiological conditions, low circulation half-life and poor water solubility.<sup>5,8</sup> Their multifunctional nature combines targeting, drug delivery, stability and diagnostic properties. Five main categories of nanosized structures can be distinguished in clinical cancer care (Figure 1.2), however many of the DDS present hybrid nature, intertwining materials from more than one group.

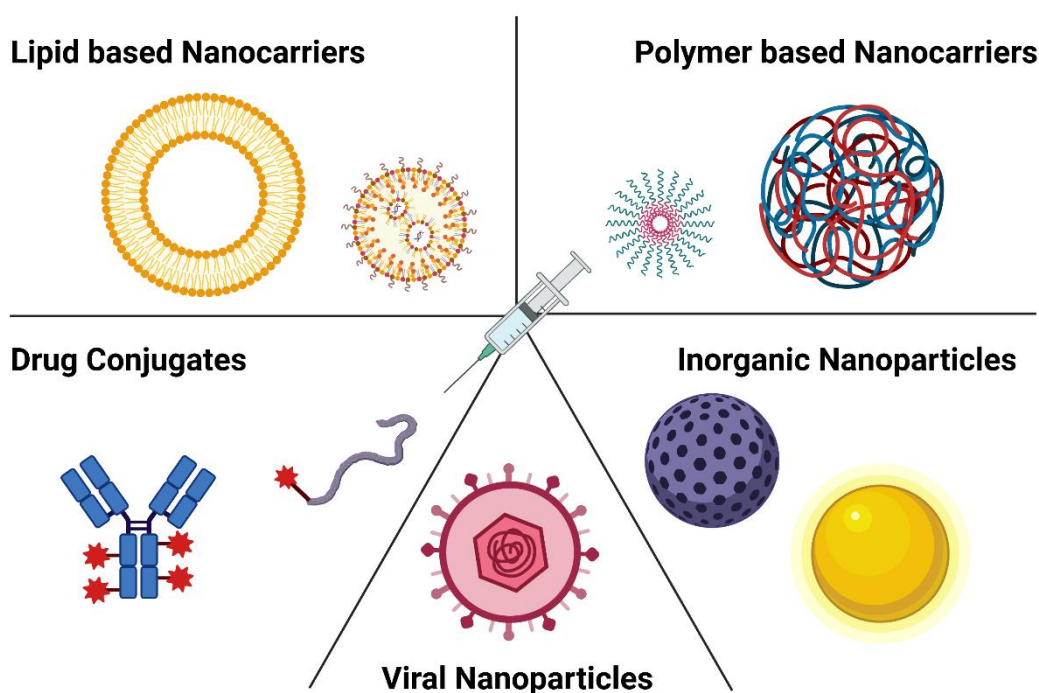


Figure 1.2 Five groups of drug nanocarriers applied into anticancer therapy.<sup>3</sup>

### Lipid-based

Lipid-based formulations of nanoparticles are one of the systems, which turned out so far most successful in terms of agency approval. First liposome-describing publication appeared in 1964<sup>9</sup>

and this discovery was translated into a market-available treatment almost 30 years later (Doxil, 1995). Doxil is a PEGylated, liposomal formulation of Doxorubicin (Figure 1.3), a drug routinely employed for breast and ovary cancer treatment. The new formulation exhibited prolonged circulation and significantly reduced the acute cardiac toxicity (among decrease of multiple other side effects) compared to patients under the traditional Doxorubicin treatment.<sup>10</sup> However, it does not demonstrate improvement in survival of treated patients.<sup>11</sup>

Liposomes are made of lipids, which spontaneously can organize themselves in aqueous medium into a bilayer micro- and nanoparticles, thanks to their amphiphilic nature. Their size and morphology can be controlled with the formulation parameters, yielding particles as small as few nm and with one or more bilayers. Furthermore, their nature allows to entrap hydrophilic and hydrophobic molecules in the lipid membrane and aqueous core, respectively. The structure of liposomes resembles the cell membrane, and their biocompatibility and biodegradability make them a versatile candidate for drug delivery.<sup>12,13</sup>

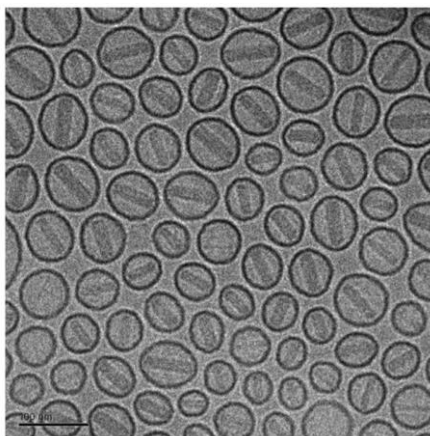


Figure 1.3 Cryo-TEM image of Doxil (EU: Caelyx) revealing the morphology of Doxorubicin loaded liposomes, scale bar 100 nm.<sup>14</sup>

### Drug Conjugates

Drug conjugates are a broad family of drugs or therapeutic proteins chemically linked to a polymer, antibody, lipid, peptide or another carrier. They are considered as drug nanocarriers, because of their nanoscale size and therapeutic effect. Among them the antibody-drug conjugates (ADCs) are interesting candidates for anticancer therapies, as the monoclonal antibodies can selectively target cancer cells expressing certain antigens.<sup>15</sup> One of the earliest FDA approved ADCs is Mylotarg, Pfizer/Wytech, (approved: 2001, withdrawn: 2010 and reapproved: 2017), which consists of Gemtuzumab ozogamicin, an antibody specific for CD33 antigen, linked with an acidic environment sensitive peptide to a cytotoxic drug calicheamicin, causing DNA breakage. This efficient mechanism directs the nanocarrier to the cancer cell, where the peptide link undergoes a cleavage once in the lysosome, and releases extremely toxic drug.<sup>3,16</sup> Next to the ADCs are polymer-drug conjugates (PDCs), as for example a 130 nm particle of serum albumin bound with paclitaxel (Abraxane, approved in 2003). This formulation allows to use very poorly

water-soluble pharmaceutical ingredient to treat breast cancer with improved drug bioavailability and lowered undesired toxicity.<sup>17</sup> Following the success of albumin, also synthetic polymer drug conjugates are under development, with many of them being currently under clinical trials.<sup>18</sup>

### Viral Nanoparticles

Viral nanoparticles demonstrated to be efficient vectors in gene transfers to tissues in various disease treatments.<sup>19</sup> This naturally existing forms invade a living host and hijack its genetic instructions to replicate. Virus protein-based capsids, measuring roughly 20-500 nm (Figure 1.4), can be engineered into nature-inspired vectors for genetic information. In the anticancer therapy the virus vector strategies are based on delivering genetic material to induce death-leading destruction of signaling pathways in cancer cells, attack their vasculature to cut off supplies or activate immune system response.<sup>3,20</sup> The mentioned approaches are currently commercialized or under clinical trials. The first approved oncolytic virus (Imlygic, 2015), consists of T-VEC, derived from human herpes simplex virus 1, engineered to causes infection of rapidly dividing cells, and equipped with macrophage-colony stimulating factor for provoking antitumor immune response<sup>21</sup>. The virus vectors require significant amount of bioengineering and rise safety concerns related to toxicity and immunogenicity, however they take important position in development of cancer treatments.

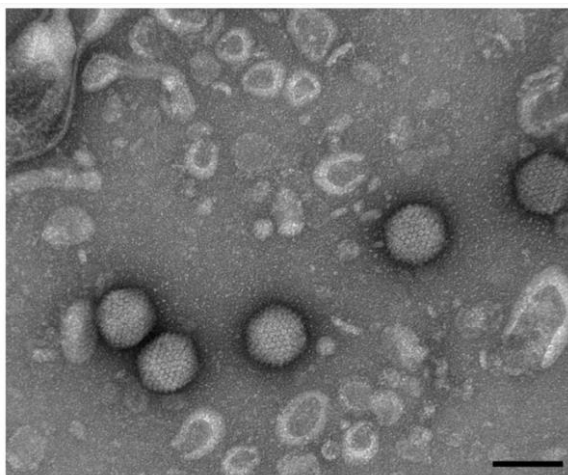


Figure 1.4 TEM image of adenovirus with visible triangular facets structures on the surface. Scale bar 100 nm.<sup>22</sup>

### Inorganic Nanoparticles

Inorganic nanoparticles are very diverse category, currently in the exploration phase for anticancer therapy application with the focus on diagnostic or theranostic purposes. Dominating are metal/metal oxide, silica-based and carbon-based NPs, with their very special optical, magnetic and electrical properties usually very dependent on particle size. They are flexible for surface chemistry modifications; however it is important to mention that they are not

biodegradable and often require coating with an organic compound, either for better stabilization or bioavailability.

In 1974 iron hydroxide dextran complex nanoparticles (CosmoFer) were the first inorganic nanomedicine in the history to be FDA approved (to treat iron deficiency).<sup>23</sup> Further, iron-based NPs were applied in cancer diagnostics as contrast agent in magnetic resonance imaging (MRI), owing to their superparamagnetic properties. 10 years ago, EMA approved NanoTherm, superparamagnetic IONPs, to treat recurring glioblastoma multiforme (Figure 1.5). The therapy uses the strong response of the NPs to an alternating magnetic field, that generates heat with local temperature rise to 40-45°C, causing tumor cell death.<sup>24,25</sup>

Early diagnostics are fundamental in further treatment and prognosis. Interesting candidate are Quantum Dots (QDs), semiconductor nanocrystals, an excellent contrast for imaging however, very cytotoxic.<sup>23</sup> Another type of NPs with unique optical properties are gold NPs (AuNPs), which additionally possess interesting catalytical and thermal characteristics, functional flexibility and demonstrate low toxicity. Despite that, they are still under development for an anticancer treatment application, and have shown promising results in photothermal and radiofrequency-based therapies, with generation of similar heat effect as IONPs.<sup>24,26</sup>

Similarly, Carbon-based NPs with good optical properties are currently in the clinical trials for imaging and diagnosis of leaky tumor lymphatic system, which could improve the precision of surgical procedures.<sup>23</sup>

Lastly, tunable and biocompatible silica-based NPs are currently in clinical trials in form of 30 nm NPs with near-infrared fluorophore (Cornell Dots)<sup>27</sup> and as a silica-gold nanoshells for solid tumor treatment with infrared radiation (AuroLase).<sup>28</sup>

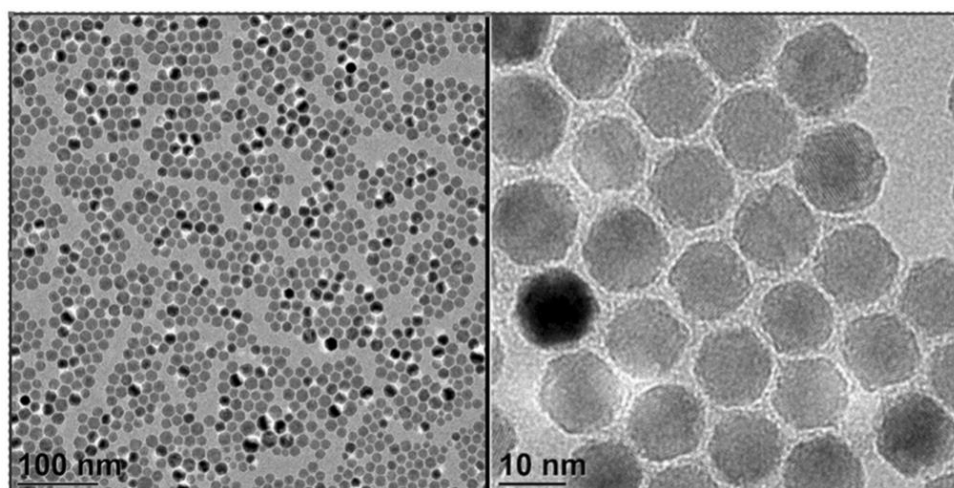


Figure 1.5 TEM image of iron oxide NPs covered with oleic acid and coated with DMSA.<sup>29</sup>

## Polymeric Nanocarriers

Polymer-based nanoparticles are a family of organic nanocarriers made of naturally occurring (e.g. albumin, collagen, chitosan) or synthetic (e.g. poly(lactide), polyesters, poly(caprolactone)) polymers. The use of polymeric compounds to deliver small molecule drugs provides several advantages, such as prolonged circulation time and improved bioavailability already demonstrated for albumin-paclitaxel polymer drug conjugate (Abraxane). Furthermore, the polyethylene glycol coating (PEGylation) is one of the most common strategies in providing stealth to the formulated NPs (as for example in Doxil).<sup>30</sup> Moreover, the polymeric nanocarriers are biocompatible and some are biodegradable, what makes them safe for drug delivery. The therapeutic agents can be covalently bound to polymer chains or physically entrapped in the polymer matrix, what makes the polymeric NP DDS versatile in terms of a drug selection and drug release method.<sup>31,32</sup> Other advantage is the design flexibility, based on synthesis method, functionalization strategies and rather economical formulation, that does not require toxic or high-energy procedures.<sup>33</sup> The precursor materials used for generation of polymer drug nanocarriers can vary between monomers, single chain polymers, di-block copolymers etc. that yield different forms such as: polymer drug conjugates, unimolecular hyperbranched dendrimers, polymersomes, polymeric micelles and nanospheres as schematically demonstrated in Figure 1.6.<sup>8,33</sup>

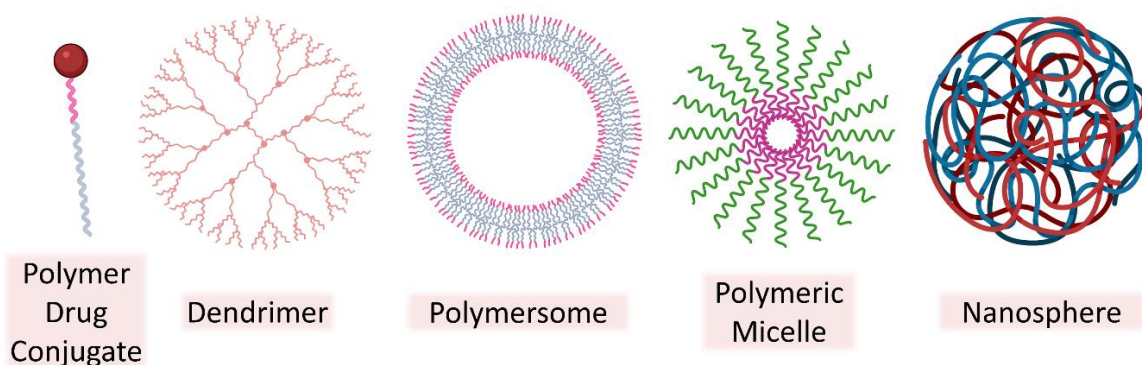


Figure 1.6 Types of polymer-based drug nanocarriers.

Well advanced in the clinical trials are polymeric micelles with amphiphilic core/shell structure. They are formed from block copolymers in self-assembly process, induced by change of the environment surrounding polymer chains. In aqueous media the hydrophobic parts concentrate in the core of a NP and hydrophilic blocks are exposed in the surface, stabilizing the NP. Hydrophobic molecules can be spontaneously entrapped in the NP core during the formulation and released upon an exposure to a stimulus or during matrix degradation or swelling.<sup>34</sup> An example of a drug nanocarrier, currently under clinical trials, is Genexol-PM, a paclitaxel encapsulated into polyethylene glycol-poly(d,l-lactide) matrix, developed and approved in South Korea.<sup>35</sup> Other example in phase II of clinical trials is polyethylene glycol - poly(glycolic acid) cisplatin nanocarrier (NC-6004, Nanoplatin) designed to treat head and neck



cancer.<sup>36</sup> Among the polymeric nanocarriers there is also the first targeted polymer NP formulation in advanced clinical trials (BIND-014). This poly(lactic-co-glycolic acid) – polyethylene glycol-based carrier of docetaxel is surface-functionalized with prostate-specific membrane antigen (PSMA) targeting ligands.<sup>37</sup> The above-mentioned examples well advanced in clinics concentrate around core-corona polymeric NPs demonstrating their versatility and applicability in anticancer therapy.

Other polymer-based nanoparticles, such as dendrimers - hyperbranched molecules, reach their final nanometric size depending on the level of branching, that is achieved upon the synthesis process. They can potentially serve as DDS of covalently bound drug molecules, which furthermore can be co-functionalized with other molecules (for imaging or targeting).<sup>8,38</sup> Furthermore, polymersomes – vesicles with properties similar to liposomes, can encapsulate lipophilic and hydrophilic drugs, thanks to their nature. They have potential to improve therapeutic outcomes comparing to the currently approved therapies, however low formulation feasibility hinders their translation into clinical trials.<sup>39</sup>

Despite the extensive research carried out in the field of polymer drug nanocarriers the path through clinical approval is lengthy and difficult. So far there are no treatments that proved to be advantageous when compared to currently available formulations, what results in no EMA/FDA approval. However, considering the contribution of polymeric NPs into nanomedicine and number of prototypes being tested in humans, the prognosis of improved treatment outcomes seems just a matter of time.

## 1.2 Strategies for drug delivery

The design of nanocarriers for drug delivery is largely propelled by the phenomena reported as enhanced permeability and retention (EPR) effect observed in the patients diagnosed with solid tumors. Briefly, it was found that the tumor vasculature can be impaired and appear as “leaky” as demonstrated in Figure 1.7, either due to the presence of cancer cells, that release harmful molecules or abnormally rapid angiogenesis leading to defective vasculature.<sup>8,40,41</sup> Following the EPR characteristics, nanoparticles intended for intravenous administration should be between 20 nm and 200 nm in diameter to be able to escape systemic circulation through the gaps in impaired blood vessels and avoid renal excretion or Reticuloendothelial System.<sup>24</sup>

### Passive delivery

Nanoparticles designed for passive delivery entirely rely on the EPR phenomenon, the nanocarrier should along with the minimization of drug toxic effects, allow the therapeutic molecule to circulate in the system, increasing its chances for escape through the compromised tumor blood vessels. Previously mentioned products, such as Doxil: Doxorubicin encapsulated in PEGylated liposomes, Abraxane: Paclitaxel conjugated to albumin or Oncaspar: PEG-protein conjugate<sup>42</sup> are examples of this approach. The incorporation of PEG, albumin or other polymers giving “stealth” properties, allows the NPs to avoid opsonization and finally sequestration by the mononuclear phagocyte system (MPS) elongating their systemic circulation time.<sup>43,44</sup> Here it is important to mention that recent studies demonstrate certain immune response toward PEG molecules, as well as its influence on accelerated blood clearance, however up to now it is still clinically accepted polymer, and novel solutions to avoid its drawbacks are under development.<sup>45</sup>

The passive delivery strategy in nanocarriers design has helped to lower the side effects of the conventional therapies, however the low NPs accumulation in solid tumors still remains a challenge. Despite the leaky vasculature allowing for the carrier extravasation, administered NPs do not penetrate the diseased site at satisfactory level. Often tumorous blood vessels have irregular or obstructed blood flow, what further complicates drug delivery along with the presence of extracellular matrix and intratumoral pressure.<sup>46</sup> This obstacles and significant heterogeneity of the EPR effect among the cancer patients, encourage investigation of more efficient method to deliver the drugs.<sup>47</sup>

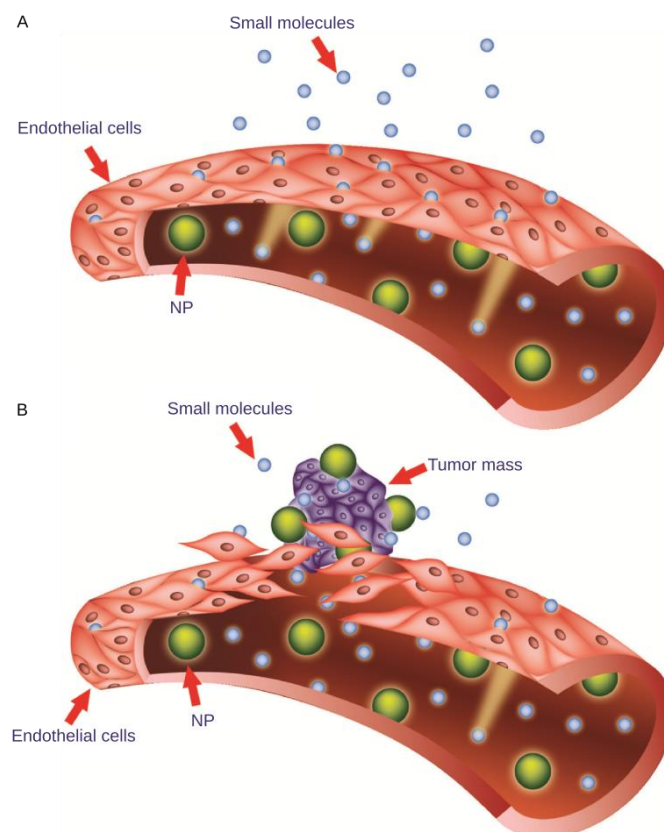


Figure 1.7 Scheme representing leakiness in tumor blood vessels, that facilitates passive delivery of drugs nanocarriers. A. Healthy endothelial wall permits passage of small molecules, B. Impaired tumor blood vessel leaks small molecules and NPs.<sup>48</sup>

### Active targeting

Active targeting drug nanocarriers are the hope for more efficient anticancer therapy. The poor accumulation in solid tumor could be boosted with the incorporation of targeting ligands on the nanocarrier surface, to enhance and promote the particle selective uptake in a receptor-expressing cancer cell. Targeting moieties can vary between antibodies (or their fragments), proteins, aptamers or receptor ligands (e.g. mannose or folic acid). They can be covalently bound directly to the surface of a NP with active groups or to a surface-coating polymer.<sup>49,50</sup> One of the polymers commonly applied for this purpose is PEG, to which targeting ligands can be directly conjugated, as it was done for BIND-014 nanocarrier functionalized with PSMA.<sup>37</sup>

Other targeting strategies involve viral nanoparticles with demonstrated efficient targeting of rapidly dividing cells<sup>21</sup> or nanocarriers in form of antibody-drug conjugates.<sup>15</sup> Targeting ligand NPs are also promising tool in the field of early cancer diagnostics, as for example trastuzumab conjugated to SPIONs, which demonstrated positive results in MRI-based detection of HER2-positive breast cancers.<sup>51</sup>

Targeting strategies envision a solution for the deficiencies of passive delivery; however, they are still in their infancy. There is a need for identification of a disease specific or significantly overexpressed biomarker, which is not so trivial, as the receptor expression among cancer patients is found to be heterogenous.<sup>52</sup> Another obstacle is the conjugation of targeting ligands, which

ideally should be homogenously distributed across all the nanocarriers and exposed in the optimal orientation for the receptor binding.<sup>53,54</sup> The pivotal role in achieving these goals plays patient diagnostic and stratification for clinical trials and development of advanced nanocarrier characterization techniques.<sup>55,56</sup>

### 1.3 Characterization of NPs

Clinical application of NPs requires their thorough characterization and analysis. Physicochemical properties of NPs are measured to predict their biological interactions and study the product shelf stability. Crucial features such as particle size, dispersity, surface charge, drug loading, stability in solution and biological media, degradation, drug release profile, targeting properties, etc. are typically examined.

The nanoscale **size analysis** requires advanced techniques and the results originating from one method may not be equal to another. Commonly particle diameter is analyzed with Dynamic Light Scattering (DLS), Laser Diffraction (LD), Transmission Electron Microscopy (TEM), Atomic Force Microscopy (AFM), electrophoresis, size exclusion chromatography (SEC), etc., depending on NPs material. This property is important from the perspective of particle biodistribution and cellular uptake and should be always provided with size distribution data.<sup>57,58</sup> Right next to the size analysis, the **Zeta Potential** of new materials is investigated to acquire complementary information related to NPs potential biodistribution. Zeta Potential measurement describes surface charge of NPs, which is an indicator of their stability in suspension. It also implies the biological interactions between nanocarrier and blood components, as well as the type of cellular response upon the exposure to the introduced NPs.<sup>59,60</sup>

Nanocarrier **drug loading and release** are crucial to determine dosing and to achieve the therapeutic effect. Usually these analyses rely on Liquid Chromatography (LC) or mass spectrometry (MS) techniques, which provide a quantitative information about the payload. The obtained data is used to predict the bioavailability of the drug at the disease site. These studies approximate of the *in vivo* release in human, as an important role is played by the pharmacokinetics and biodistribution in the first place, that cannot be reproduced *in vitro*. The cargo release can be triggered by a stimulus (temperature, pH, radiation, etc.) or occur gradually, upon swelling or degradation of the nanocarrier, however it should be well understood and controlled to avoid undesired cytotoxicity.<sup>61,62</sup>

In the case of **active targeting** NPs, the targeting moiety is quantified and its affinity with targeted receptor assessed. However, the targeting efficiency is difficult to predict, due to the complexity of human organism versus *in vitro* tests. And even *in vivo* experiments fail to provide solid evidence of active targeting benefits over passive delivery nanocarriers. This implies there is not enough understanding in the NPs design, further supported by the little difference of accumulated NPs found in the disease site.<sup>63,64</sup>

Nanotechnology, and nanomedicine in particular, are very broad and relatively new disciplines in the field of life sciences. For this reason, the standardization of procedures and methods is not in place yet, what complicates the development of NPs, comparison between different research labs and ultimately the clinical translation. However there are efforts

undertaken to unify the reporting practices to improve our understanding of materials, their performance and to rise the value of published literature.<sup>65,66</sup>

Furthermore, majority of the characterization methods provide an information on the bulk material. Due to that, only average values are obtainable, and the heterogeneities among the NPs are not well investigated. Their statistical relevance in particle size, surface charge, drug loading or orientation of targeting ligands, may be vital for the understanding of drug nanocarriers. Specifically, the formulation optimization relies on characterization-based feedback, therefore the selected methods should be well established to allow controlled tuning of particular parameters.<sup>53</sup>

## 1.4 Formulation of polymeric Nanoparticles

The process of obtaining NPs depends on the material they are made of. Typically, metal and semiconductor nanoparticles are formulated via chemical synthesis, yielding colloidal nanosuspensions, that can be further processed into dry NPs. Usually these processes are well controlled, relatively inexpensive and scalable, however often toxic compounds are involved in some of the steps, which is a concern for biomedical application.<sup>67</sup> Other method, exploited especially for silica NPs and metal alkoxides, is sol-gel process, in which polycondensation plays the important role. Importantly for medical applications, sol-gel process is performed at room temperature and yields pure materials, with high control of the outcome NPs.<sup>67</sup>

Polymer nanoparticles formulation can proceed from previously synthesized raw polymers, or during polymerization process. They both have in common the step of polymer precipitation, in which self-assembly plays role in NPs formation.<sup>68</sup>

### Self-assembly

Self-assembly is a process of spontaneous reorganization in which more thermodynamically favored forms are created. This bottom-up phenomenon occurs in nature, where building blocks arrange themselves into constructs, such as it takes place in the formation of double-stranded DNA helix. Self-assembly has a pivotal role in nanotechnology, where it is exploited for fabrication of variety of materials used in solar cells, electronics, biotechnology and medicine, just to name few. In chemistry the self-assembly is often associated to supramolecular structures, whose arrangement is driven by molecular recognition, rather than covalent bonding.<sup>69</sup>

The prerequisite for self-assembly is the availability of units with similar characteristics, such as size, charge or hydrophobicity that will drive the process and result in stronger or weaker interactions. External stimuli, such as temperature, light, pressure, etc. can induce the reorganization of these units into more energetically stable forms under the current conditions.<sup>67</sup>

Polymer NPs can be formulated during monomer polymerization process; however it yields or involves toxic compounds, that disqualifies them from biomedical applications. Therefore, formulation from the preformed polymer raw material is the method of choice. Following procedures are most commonly used in fabrication of polymeric drug nanocarriers.

### Emulsification

Emulsification process, which employs minimum two non-miscible phases. Emulsions are formed when water phase is dispersed into oil phase (or other way round) with the help of surfactants, which stabilize micro- or nanodroplets. More complex systems of water-oil-water or oil-water-oil are also used in the double-emulsion formulation, required for co-encapsulation of compounds in more elaborated systems. In the emulsification process, one of the phases contains

dissolved polymer (and a drug) and it is added to the remaining phase. As the emulsification is not spontaneous, an external force is used to disperse the polymer-bearing phase into the other: continuous phase (Figure 1.8). Some of the techniques involve stirring, sonication, mechanical pushing through a mesh or similar high-energy processes, to generate a shear force that “breaks” the dispersed phase into droplets. Each droplet becomes a micro- or nanoenvironment where particle self-assembles, therefore the droplet formation and stabilization is of crucial importance. Lastly the polymer solvent is extracted from the emulsion, leaving precipitated NPs, stabilized by a surfactant, in the remaining phase. This method allows to formulate nano- and submicron particles, with size dispersity dependent on the uniformity of the generated droplets.<sup>70,71</sup>

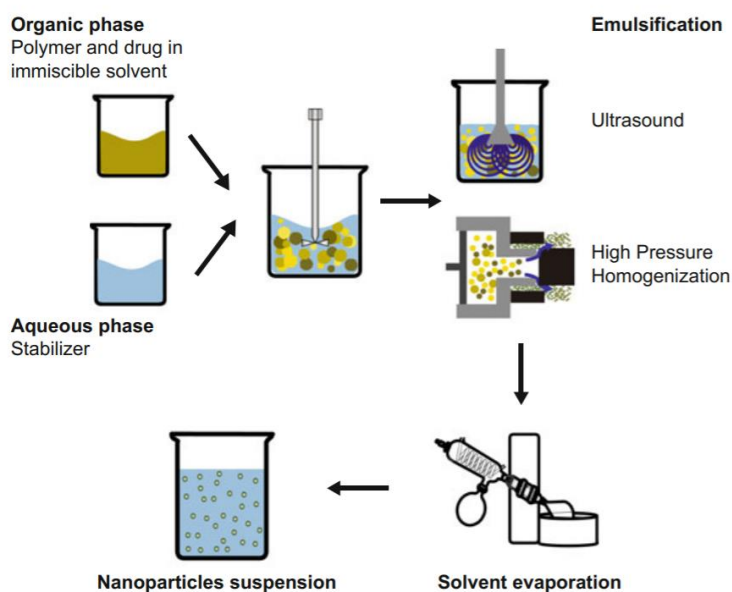


Figure 1.8 Scheme of emulsification process used to obtain nanoparticles.<sup>71</sup>

An alternative way of emulsification without high-energy sources involves initially miscible phases, like acetone and aqueous fraction, that are separated by addition of salting-out ionic compound (e.g.  $MgCl_2$ ). Their miscibility increases upon addition of water, that has reverse-salting out effect and leads to the polymer precipitation within the process progress. Similar method, based on Ouzo effect, uses two miscible phases (one containing polymer and oil) that are initially saturated, and addition of water causes the solubility to decrease, resulting in polymer precipitation.<sup>72</sup>

### Nanoprecipitation

Nanoprecipitation is another method for polymer NPs formulation, similar to the emulsification modifications described above. It allows to formulate monodisperse NPs below 100 nm in diameter in one-step. In this process two miscible phases are used: organic solvent (with dissolved polymer and a drug) and antisolvent (an aqueous phase, also called a nonsolvent). Upon the mixing of solvent and antisolvent, local solubility of the polymer is suddenly decreased as the



solvent is displaced, what promotes polymer self-assembly into nanoparticles. The formed nanosuspension can be stabilized with surfactants, however their use is not necessary for the formulation step and amphiphilic-polymer particles demonstrate good stability in aqueous media. Last step consists of solvent extraction, what makes the solvent selection shifted toward the volatile ones. Since the last thirty years this simple, scalable and reproducible method became widely used to formulate drug nanocarriers, exploring different type of polymers, such as PLA, PLGA, poly( $\epsilon$ -caprolactone), PMMA.<sup>71,73</sup>

The NPs formulated with nanoprecipitation are in general smaller and more monodisperse comparing to the emulsification approach. For both methods the process parameters, such as temperature, concentration of compounds and the composition of both phases impact the physiochemical characteristics of resulting NPs. In the nanoprecipitation process the formation of the NPs is divided into three phases: nucleation, growth, and aggregation as presented in the Figure 1.9 (left panel). The pivotal role in the output of nanoprecipitation plays the mixing of solvent and antisolvent phase, that contributes to homogenous supersaturation responsible for polymer nucleation. Namely, poorer mixing results in low nucleation rate and a growth of larger particles because the polymer aggregation occurs in the presence of higher fractions of organic solvent ( $\tau_{mix} > \tau_{agg}$ ). On the other hand, if mixing occurs faster than the time scale for aggregation ( $\tau_{mix} < \tau_{agg}$ ), the aggregation phase takes place when mixing is almost complete (Figure 1.9, right panel). In this situation, the organic solvent fraction is lower, more nuclei are formed and there are less free polymer chains that could insert into formed nanoparticles, causing their growth.<sup>74</sup> Importantly, the mixing of the two phases depends also on other factors such as: temperature, inherent diffusivity of the solvent and polymer concentration.

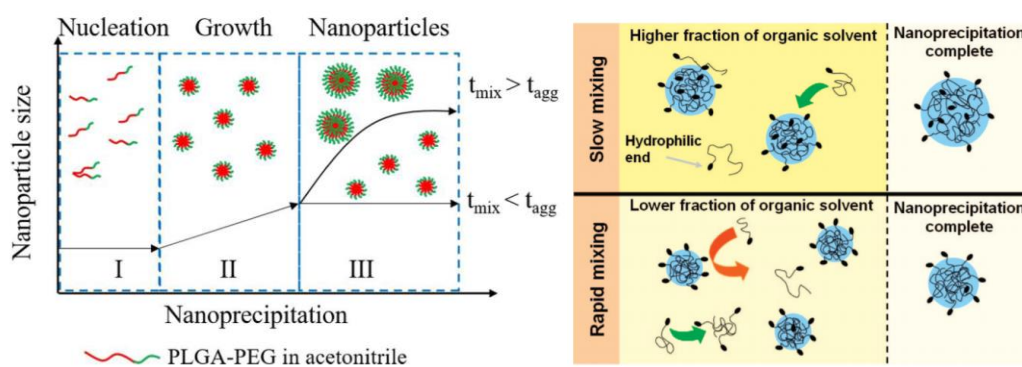


Figure 1.9 Scheme of three phases of particle formation in nanoprecipitation process (left panel) and the impact of phase mixing on the particle growth (right panel).<sup>74</sup>

## 1.5 Microfluidic-assisted Nanoprecipitation

To control the nanoprecipitation mixing parameter it is to be one step closer toward tailor-made formulation. In traditional formulation via nanoprecipitation by manual bulk mixing, the modification of particle size is mostly achieved by changes in polymer chains molecular weight. It complicates the subsequent analysis and studies due to the variability in polymers batches: an integral feature originating from polymerization process.<sup>75</sup> To face this challenge a solution with volume-restricted microchannels was proposed: microfluidic technology.

**Microfluidic technology** emerged with rapidly developing micro- and nanofabrication methods, used in production of electronic devices. Microfluidic chips can have different patterns and designs, but they share the feature of microchannels with width and height between tens to hundreds of micrometers and length in millimetric scale. Microfluidic devices diffused into life sciences, including pharmaceutical and biochemical fields, adapting different names, such as Organ-on-Chip (OoC), Lab-on-Chip (LoC), bio-microelectromechanical systems (BioMEMS) or miniaturized total analysis systems ( $\mu$ TAS).<sup>76</sup>

Microvolumes are manipulated in the microchannels with use of syringe or pressure pumps to enable controlled addition of fluids. The microscale allows for more economical use of compounds, but importantly it opens exploration of new system where the forces acting on liquids in typical lab-scale reactors and their volume-to-surface ratio become negligible. Here, fluids are handled at low Reynolds numbers (typically  $Re < 1$  in microfluidic devices), which correspond to laminar regime, where inertia of the fluid is negligible in comparison to the significance of viscosity force (Figure 1.10).<sup>76,77</sup>

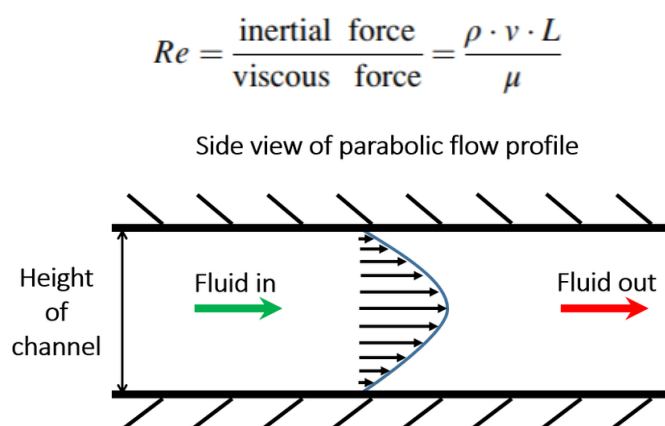


Figure 1.10 Scheme of laminar flow profile in a microfluidic channel present at low Reynold's numbers.<sup>76</sup>

Laminar flow in microchannels intensifies the importance of diffusion, a process in which molecules are transported from higher to lower concentration. Meanwhile the diffusion-based transport leads to the equilibrium of concentration gradients, the fluids are also transported by convection. The comparison of diffusion and convection time is described with Peclet number

Pe, and for large Pe gradients will exist, meanwhile for low Pe they will be equalized (Figure 1.11).<sup>78</sup>

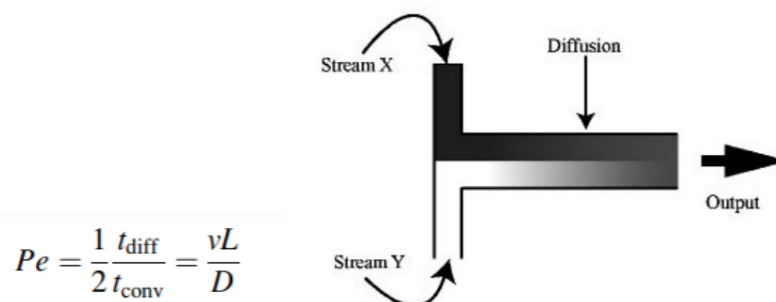


Figure 1.11 The Peclet number equation describing concentration gradient of two streams, dependent on diffusion and convection time.<sup>78</sup>

### Hydrodynamic Flow Focusing

Nanoprecipitation in microfluidic chip offers homogenous microenvironment of reaction, where diffusion can be controlled by fluid properties and modification of flow rates. It is particularly important in the formulation of polymeric drug nanocarriers, where the reproducibility in typical batch methods fluctuates. Microfluidic chip nanoprecipitation is a convenient tool for a spatial separation of the three phases of nanoparticle self-assembly, described above and illustrated in Figure 1.12, where particle nucleation, growth and (optional) agglomeration are showed. Different chip geometries and designs were explored so far, however the use of cross-shaped (or 3 inlets microfluidic chip) for hydrodynamic flow focusing (HFF) is a compromise between the feasibility of chip fabrication and the flexibility in nanoparticle formulation.<sup>79–81</sup>

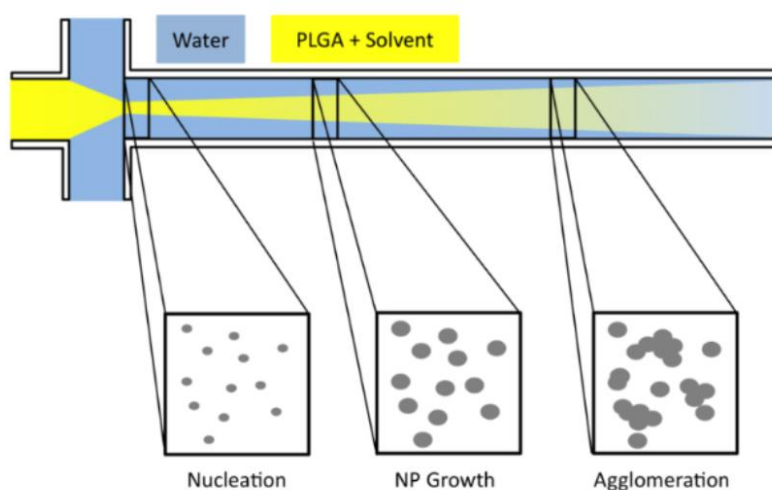


Figure 1.12 Schematic illustration of the three phases of NPs formation: nucleation, growth and (optional) agglomeration in a microfluidic chip. Solvent phase is demonstrated as diffusing stream toward the chip outlet.<sup>82</sup>

Thus far microfluidic chips have proved themselves useful in controlled formulation of tunable-properties nanoparticles for drug delivery over the traditional bulk/batch methods.<sup>83</sup> Especially size tunability was investigated in the recent years and positively correlated to the mixing of the

injected phases.<sup>82</sup> The lead position belongs to polymer-based NPs and the nanoprecipitation process; however microfluidic devices are also used in self-assembly of liposomes, supramolecular structures and creation of various shapes and meta-stable structures as demonstrated in Figure 1.13.<sup>12,84–89</sup>

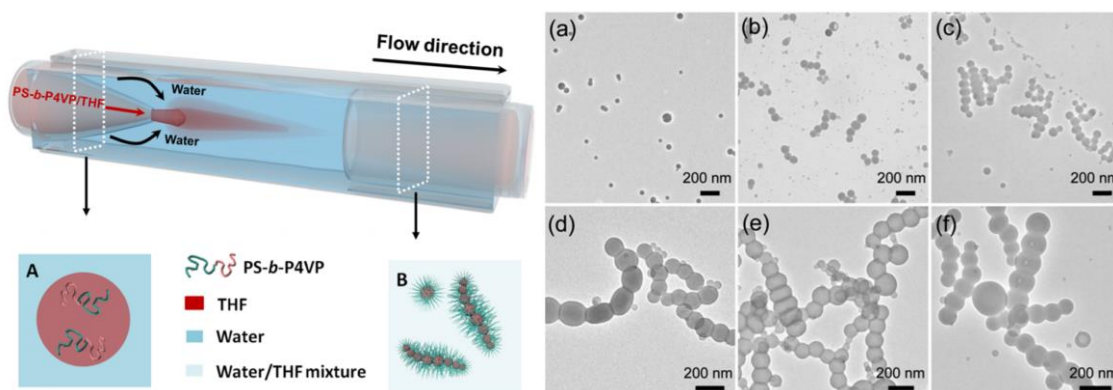


Figure 1.13 Microfluidic device assisted self-assembly of micelles with different shapes in response to the change of fluidic parameters. Left panel represents the scheme of the device and right panel TEM images, scale bar 200 nm.<sup>90</sup>

Similar systems for microfluidic nanoprecipitation have been patented or commercialized,<sup>91</sup> however it is important to say that they are not in pharmaceutical industry use yet. They provide very fine platforms for small scale research and formulation, however their scale up, in a traditional its meaning, would compromise the microfluidic properties. One of the options for increasing the production scale is parallelization of microfluidic devices, to ensure the microscale channels and identical reaction environment are maintained.<sup>92,93</sup>

#### Fluid micromixers for combinatorial formulation

Diffusion controlled mixing is one of the advantages of use of microfluidic chips, however some processes require thorough mixing, where the diffusion-based process is not sufficient. This applies especially when more than one solvent phase is introduced and needs to be blended with other streams, prior to the NPs precipitation<sup>78</sup>. The introduction of multiple streams can give an advantage in a rapid microfluidic formulation of combined precursors NPs as represented in the Figure 1.14.<sup>94</sup> Specifically, it is interesting to premix NPs precursors such as different polymer chain lengths, conjugates, as well as various drug molecules, that will yield nanocarriers from the same process with subtle and controlled modifications of their characteristics. Well mixed final stream is essential here for formulation of homogenous NPs in the HFF microdevice. The advantage of this approach is the formulation and testing of small quantities of materials. Furthermore, it opens door to formulation of personalized nanocarrier prototypes, in a single device, which can be useful in approaching the cancer patient heterogeneity.<sup>52,95</sup> The personalization strategies propose also high throughput screening of barcoded formulations, meaning that the NPs are first labelled with a “code” and can be later identified *in vitro* or *in vivo*, revealing most promising candidates.<sup>96,97</sup> From this perspective, the fluid micromixers appear as

an interesting platform to accelerate the process of NPs precursor mixing at low microfluidic flow rates, that can be later combined with the NPs formulation device.

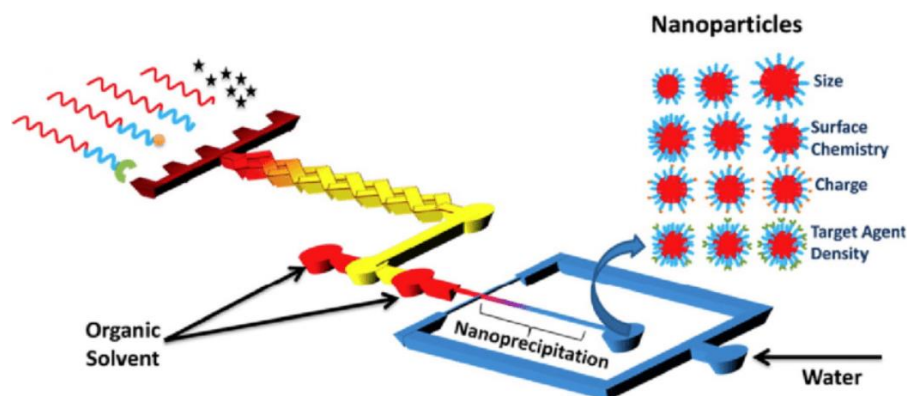


Figure 1.14 Setup consisting of mixing and nanoprecipitation chips for combinatorial formulation of nanoparticles.<sup>94</sup>

The selection of a microfluidic mixer can be done among passive and active mixing devices. In principle the passive micromixers promote chaotic advection and improved diffusion, thanks to the features incorporated in their design. On the other hand, the active micromixers require external energy to actuate the mixing process, this may include magnetic field, pressure or electrostatic forces.<sup>98,99</sup> Due to their nature, usually they are more complicated to fabricate and introduce into the microfluidic setups, comparing to the passive systems, however they offer control over the mixing intensity.

## 1.6 Microfabrication of microfluidic devices

Fabrication technique and material for a microfluidic device depends on its application, whether biocompatibility, durability, optical transparency, or other features are in the scope. Nevertheless, the fabrication often is performed in a cleanroom or similar space with controlled environment, as the cleanliness and contamination-free process are at stake. Furthermore, the fabrication involves toxic compounds, UV exposure or machinery that can be only operated by trained professionals.

### Photolithography and PDMS

Polydimethylsiloxane (PDMS) is the gold standard for fabrication of microfluidic chips with a tens of nanometers of resolution. It is biocompatible, permeable to gasses, optically transparent, flexible, and relatively easy and cost-efficient in fabrication. PDMS allows rapid prototyping, incorporation of other elements such as built-in electrodes, adjustable thickness, and its surface can be modified from hydrophobic to hydrophilic.<sup>100</sup> The fabrication of PDMS chip is schematically illustrated in the Figure 1.15, it usually relies on photolithography, where a replica master mold is created on a glass or silicon wafer with a photopolymerization of a SU-8 photoresist. In the next step (soft lithography) the unpolymerized PDMS is poured over the microstructures, cured and extracted with the molded pattern, which later is enclosed into a channel with glass or PDMS layer.<sup>101</sup> Despite the process being user-friendly and cost efficient, it is important to remember that PDMS has one major drawback, that can affect some studies. The polymer matrix absorbs and desorbs small hydrophobic molecules (drugs, dyes, etc.), thus affecting their concentration interacting with the elements present in the microfluidic channel (encapsulation into nanocarriers, sensors, cells, extracellular matrix). It is important from the quantitative point of view in case of drug nanocarriers formulation, but also in qualitative analysis of stimuli-response studies in microfluidic Organ-on-Chip (OoC) .<sup>102-104</sup>

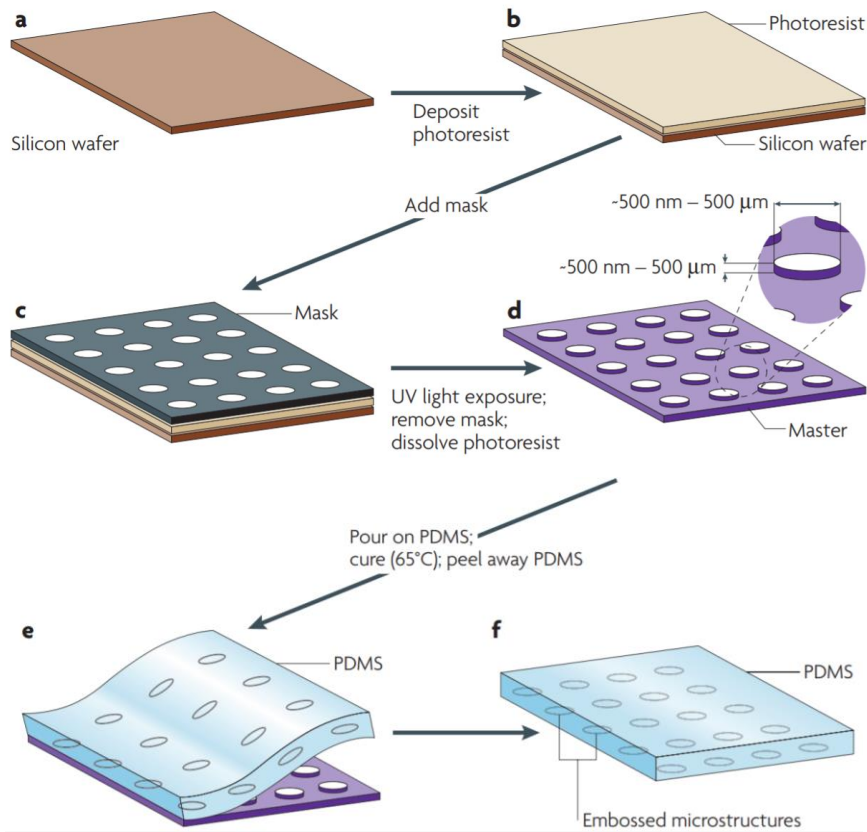


Figure 1.15 Schematic illustration of photolithography based microfabrication of PDMS replica.<sup>105</sup>

### Other materials

Borosilicate glass is another common material for fabrication of microfluidic chips. Similarly, to PDMS it is characterized by optical transparency, however in contrary it is not flexible and represents excellent chemical resistance to many compounds. Few-micrometer structures are achievable in glass, with the use of techniques such as wet chemical and dry etching or laser ablation. These processes require specialistic precision equipment and further glass to glass bonding protocols in order to enclose the channels. There are number of rapid and cost-efficient methods, however usually they do not provide the desired resolution, as the high-end methods do.<sup>76,106,107</sup>

Especially in the Organ-on-a-Chip technology, other than PDMS or PDMS-glass constructs, popular are cyclo-olefin copolymer (COC) and cyclo-olefin polymer (COP) chips, which have excellent optical characteristics, very low permeability to water vapor or gases and low absorption of molecules. Fabrication of COC, COP or polystyrene (PS, inexpensive polymer, commonly used in traditional cell culture) chips requires thermoforming with injection molding or hot embossing processes, which are usually unattainable in a small-scale research.<sup>108</sup> They are attractive from the industrial point of view and indeed there are COC/COP or PS based chips available in a commercial scale. In many cases they include parts, proprietary polymers or

bonding technologies not disclosed by the companies, nevertheless they are adapted for a small- and industrial-scale research.<sup>109-111</sup>

Thermoplastic polymers can be also processed using 3D printing, an additive manufacturing method where a heated polymer is extruded through the printer nozzle. However, 3D printing is not limited to the extrusion process only, as the stereolithography is explored in the field of microfabrication with even better resolution than the heat-operating option. In stereolithography apparatus the polymer is photopolymerized layer by layer with a UV exposure. Although these methods are a good option for rapid and cost-efficient prototyping (especially for demanding geometries) they provide lower resolution than photolithography.<sup>112,113</sup> An alternative direct fabrication method engages micromilling process. It is a subtractive technique, based on cutting to remove material from the bulk to create microstructures. It provides similar resolution to hot embossing and 3D printing, with commonly PMMA, PS, PC and COC used as the substrates.<sup>114</sup>

In summary, there is a broad spectrum of fabrication methods, however the choice is usually a compromise between prototyping flexibility, cost, durability, and the final resolution of the fabricated microstructures. These parameters may differ, depending on the application of a microfluidic chip, especially when comparing the devices used for the formulation of drug nanocarriers and chips used for their screening *in vitro*, such as organ-on-a-chip platforms.



## 1.7 Preclinical models for screening Drug Delivery Systems

The previous parts described anticancer drug nanocarriers and their formulation strategies with microfluidic devices, and this part focuses on the screening of potential therapeutics. The process of conceptualization of a drug or a delivery system until it becomes available to the patient is a lengthy path with many endeavors. These efforts are exponentially longer in case of nano-scaled formulations intended for parenteral route of administration in oncology patients. The whole way takes on average 20 years and costs at least hundreds of millions of € per one new product in this category as illustrated in Figure 1.16. The regulatory bodies (EMA, FDA) dictate guidelines in testing and approving new treatments throughout all the production steps and clinical trials, which are there to ensure patients safety and the product efficacy. Eventually, one out of 1000-2000 candidates makes it to the market.<sup>115-117</sup>

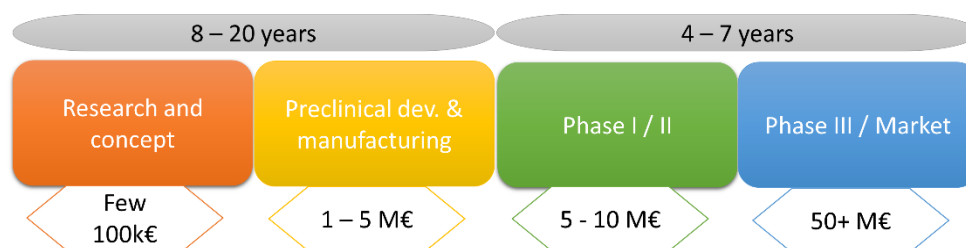


Figure 1.16 Schematic representation of a process starting from small scale formulation of a DDS to its commercialization.<sup>115,117</sup>

The preclinical trial phase refines the selection of most promising candidates, improves understanding of their action mechanism, efficacy, toxicity, stability, biocompatibility and other important characteristic.<sup>118</sup> It is also the phase preceding the first in-human tests, in which formulations are granted a pass or rejected from entering the next stage. Given that, it is an essential phase for a drug development and often for the future of the organization working on it.

The preclinical tests use *in vitro* and *in vivo* models, namely cell culture and animal subjects to bioevaluate the prototype formulation.

### In vitro cell culture

The *in vitro* tests use cell lines or human/animal derived cells, depending on the application.<sup>119,120</sup> This approach is relatively easy, cost efficient, does not require a lot of testing material and the assays are widely established.<sup>121,122</sup> Thanks to the *in vitro* studies the nanocarrier can be examined in different conditions with quick access to data at any timepoint of the test. The information can be extracted by various techniques: for example, the NP-cell interaction can be studied using fluorescence or electron microscopy, which allow to localize particles within the cell or material toxicity can be evaluated using fluorometric assays.<sup>123,124</sup>

These crucial information should help to understand the DDS properties, give a feedback on its design and be possible to correlate with *in vivo* tests.<sup>125-127</sup> However, traditional cell culture models are not flawless, they lack many aspects in terms of similarity to human body or laboratory animals. Some of them being static culture conditions, so different to the environment in tissues or organs, as well as vulnerability to sedimentation of the NPs onto the cells or to the administration method.<sup>128-131</sup> Furthermore, cells geometry simplified to a 2D layers, grown on a stiff support, often does not represent physiological conditions, which enforce a 3D arrangement, promoting different biological activities in the area of cell metabolism, morphology, proliferation, signaling, etc.<sup>132,133</sup> Additionally, many tests are performed in a cell matrix-deprived monoculture, which neglects interactions with associated cells and matrices.<sup>134,135</sup> Due to the above-mentioned reasons, the predictability of *in vivo* studies outcomes on the base of 2D static cell monoculture is limited and *in vitro/in vivo* correlation often poor.<sup>136,137</sup>

### In vivo animal studies

An inseparable part of the preclinical development are tests on animal models. They provide dynamic environment to screen drug candidates in terms of dosing (toxicity), drug release, pharmacokinetics, biodegradability, etc.<sup>138</sup> In contrary to the cell culture, they are much more complex and adequate, however the sampling for data retrieval is not as trivial as for cell culture, as it requires predetermined blood withdrawals or *ex vivo* tissue imaging.<sup>138-141</sup> It is important to mention that the animal trials are significantly more costly, study designs happen to be inadequate, and the use of animals rises ethical questions. Furthermore, animals are different species than human, meaning metabolic activity, blood viscosity or organ architecture, just to name few, are not well reproduced in animal models.<sup>142-144</sup> In fact, about 4 in 5 animal tested DDS candidates are not safe to use in humans, and can cause life-threatening conditions,<sup>145</sup> and eventually more than 95% animal-tested prototypes inevitably fails the clinical trials preceding introduction to the market.<sup>146-148</sup>

### Culture shock: The missing link

The challenge in the development of new medicines is raised by limited availability of human models in preclinical research on disease target identification, drug efficacy and toxicity. Late and expensive failures in clinical trials are the result of existing gap between *in vitro* and *in vivo* models. There is a need for an alternative method in preclinical testing, and it is believed that the 3D cell culture models (Figure 1.17) could result in a paradigm shift for biomedical research, leading to efficient identification of effective drugs and to the improvement of medical care quality.

In the last 20 years we have witnessed the expansion of 3D cell culture models recapitulating some of the physiologically essential features.<sup>149</sup> Despite being relatively young, the 3D cell culture became relevant in the understanding and recreating disease development and, importantly, unveiling the cell-DDS interaction. Currently it is adapted not only by researchers, but already by pharmaceutical companies to strengthen the preclinical development in obtaining meaningful data.<sup>150–153</sup> The words: “In 10 years, anyone trying to use 2-D analyses to get relevant and novel biological information will find it difficult to get funded” (Mihael H. Polymeropoulos, cofounder and CEO of Vanda Pharmaceuticals, 2003) currently have become very adequate, seeing how the 3D dynamic cell culture is revolutionizing *in vitro* studies.<sup>154,155</sup>

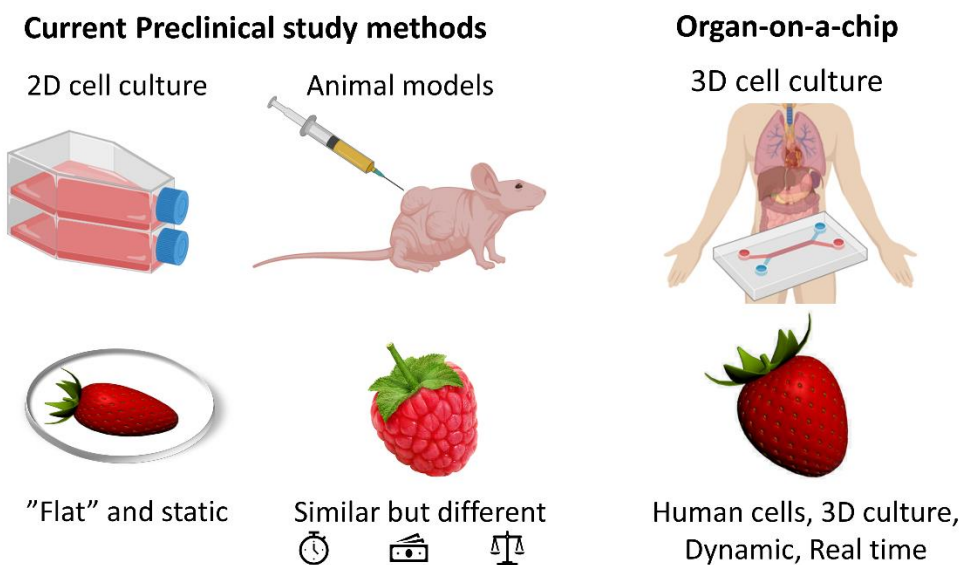


Figure 1.17 Schematic illustration of current methods in preclinical studies and emerging organ-on-a-chip technology as a bridging approach in preclinical trials.

### *Organ-on-a-Chip: the promise and state of art*

Organ-on-a-chip (OoC) is a device with one or more biocompatible microfluidic chambers, allowing growth and maintenance of 3D cell culture under sterile and controlled conditions. The microfluidic channels can be perfused with media to exert shear stress or to supply nutrients, drugs, nanoparticles, immune cells, bacteria or viruses to the cell culture. The chip design permits other manipulations, like mechanical or electrical stimulation as well as modifications of cell microenvironment to mimic physiological conditions or to induce disease pathology at the tissue level.<sup>149</sup> It is important to mention that the ultimate goal of OoC is not to build complete living organs or a “human-on-a-chip”, but to recapitulate human functionalities at the organ level. The OoC are prognosed to have a societal impact by reduction of healthcare costs, as the drug development could become better, safer, faster and cheaper. Drug repurposing is considered an area most likely to benefit from the 3D models, what can be already seen with the OoC addressing the urgent need for a rapid solution during the viral pandemics.<sup>156</sup>

### *The biology of OoC: Cells*

Currently OoCs are being developed for cancer, cardiovascular disease, neurological and brain diseases, autoimmune diseases, skin and a variety of others.<sup>157</sup> Model cell lines, primary cells derived from patients or human induced pluripotent stem (iPS) cells are cultured in chips to recapitulate these tissues.<sup>158</sup> Most often the immortalized cell lines are used, because they are readily available, reproducible, relatively easy in handling and they can be directly compared to the broadly existing 2D studies. There are more than 600 lines (from different species) available to address scientific questions focused on recapitulating different tissues in OoC devices. The alternative to them are patient derived primary cells, which offer advantageous personalization of a study, important not only in receiving a precise response in the screening of a drug, but also in the modeling of particular disease development.<sup>159</sup> This is especially interesting in cancer research, where the cancer heterogeneity among the patients is very high.<sup>160</sup> However, in contrary to the established cell lines, their availability may not be continuous and overall it is more laborious to extract primary cells.<sup>161</sup> They also require more experience in handling and can rapidly undergo phenotypic changes upon culturing out of the native environment. Ultimately it is important to be aware that meanwhile the cell lines may exhibit same to primary cells signaling pathways, cell response to applied treatment can be to some extent different among them. This discrepancies between cell lines and primary cells were already demonstrated in the literature and linked to varying levels of molecular expression, morphological characteristics or cell activity.<sup>159,162,163</sup> The newest alternative to the cell lines and primary cells are human iPS cells. They can be derived from different cells of the body (skin, blood, urine) from healthy individuals and from patients with disease of interest, allowing for personalized analysis of drug response. The iPS cells can be differentiated into cells specific for different tissues, such as: neural, liver, gastrointestinal, cardiac, lung, skin or kidney. Overall, they are recognized as reproducible, robust, and relevant for many diseases. The drawback is that they require optimized differentiation protocols and standardization, yet the reprogrammed cells become more similar to immature cells, rather than adult form.<sup>164,165</sup>

### *The biology of OoC: Matrices*

The mechanical properties of tissues are mostly given by the presence of extracellular matrix (ECM). Physiologically, cells can have direct contact or indirectly communicate between each other through the surrounding ECM, which supports their signaling and regulates cell arrangement and activity.<sup>166,167</sup> Microfluidic chip channels are suitable for recreating the native cell 3D environment, which promotes natural geometries and connections. In the OoC devices the ECM is modeled with synthetic or natural hydrogels. Most commonly used are Matrigel and collagen, however there are other hydrogels available, such as gelatin and its methacrylate, fibrin, alginate, agarose, PLGA-based hydrogels and many more.<sup>157</sup>

Matrigel is a tradename of commercially available product invented in the 1980s, based on basement proteins derived from mouse tumor cells. It contains structural and functional proteins (e.g. collagen type IV, laminin), growth factors and enzymes that make it suitable for studying tumor spheroids development.<sup>149,168</sup> However Matrigel has proved itself to be robust in 3D cancer cell culture studies, the ideal model would use more appropriate matrix, derived from the cells relevant to the studied tissue. Its inventors admitted already close to 20 years ago that it is surprising the Matrigel was not superseded yet by more suitable gel.<sup>154</sup>

Collagen, a fibrous protein most abundant in the human body, provides mechanical support to connective tissues (different collagen types are known). It is often used as a 3D cell culture matrix because of its similarity across the species and controllability in terms of stiffness and concentration. This hydrogel is frequently found in 3D models of gut, skin and endothelial barrier, however its degradation allows relatively short culture times and similarly to Matrigel, it has rather poor control over singular properties.<sup>169</sup>

It is demonstrated that the physical, chemical and mechanical properties of the matrix impact cell growth, adhesion, communication and overall activity.<sup>170</sup> Hydrogels commonly used on the OoC devices are a simpler model than human derived ECM, however they are a compromise between, complexity, accuracy and availability.

### *The design of OoCs*

In general, the microfluidic chip design can be divided into compartmentalized or sandwich conformation (Figure 1.18). Both of them allow real-time molecular and functional monitoring; however the conducted studies and analysis methods partially differ between them. The flagship of sandwich designs is the Wyss Institute's lung-on-a-chip, for the first time reconstituting function of alveolar-capillary interface of human lung. This model is especially suitable for studying interfaces between two biological regions. The novelty of this chip design is a horizontal, porous flexible membrane mimicking lung air sac arrangement. Furthermore, the lateral vacuum channels facilitate breathing-resembling stretching and relaxing of membrane and adhered cells. The authors in their study described complex response of perfused immune cells to the presence of bacteria, as well as cell response to cytokines and nanoparticles exposure, with the last one being compared to a full lung of mice inhaling nanoparticles.<sup>171</sup> This breakthrough successfully correlated *in vitro* results with responses observed in human body. Its versatility was demonstrated in later publications based on the same or similar model, but investigating lung cancer treatment, cancer migration to other organs, recreating human gut or screening drugs during viral pandemics.<sup>156,172-176</sup>

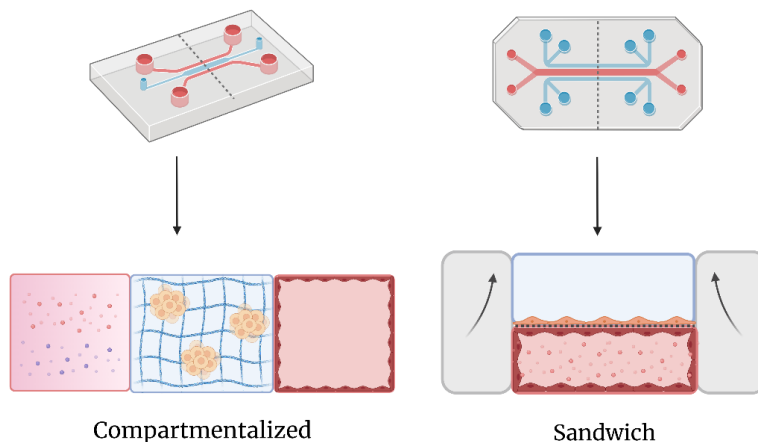


Figure 1.18 Scheme of OoC compartmentalized (left) and sandwich (conformation) conformation, with a top view and a cross section of microchannels area (indicated by dashed line).

Since the first prototypes of compartmentalized chip design were developed a decade ago at MIT in Kamm's lab, they truly dominated and revolutionized the 3D cell culture world. Characteristic for this chip are parallel microchannels separated by micropatterns, which allow to introduce and retain gel matrices (collagen, Matrigel, fibrin, etc.) by surface tension force. This solution permits to precisely confine the scaffold without scarifying the barrier(wall)-free contact between the adherent channels. As a result molecules, nanoparticles and cells can freely diffuse and migrate across the channels without constrains.<sup>177,178</sup> For these reasons the microscopy-friendly compartmental model quickly became popular device in research focused on cancer and endothelial barrier (Figure 1.19). There are many studies in the field of cancer cells migration,<sup>179-182</sup> vascularization and angiogenesis,<sup>183-186</sup> endothelial barrier permeability,<sup>187-189</sup> impact of 3D cell architecture on the biological functions<sup>190-192</sup> and penetration into tumor.<sup>191,193-195</sup> In the last years various modifications were applied to the chip design to assess the differences in nanoparticles passage through the endothelial barrier affected by the presence of cancer cells.<sup>187,188,196,197</sup> The micropatterned compartmental model proved itself very versatile and useful, hence it became commercialized and similar prototypes quickly appeared on the market to facilitate also high-throughput analysis in 3D cell culture.<sup>109,110</sup>

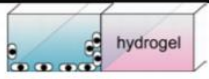











	cell seeding	morphogenesis	Purpose of Experiment
individual cells			migration of various cell types
epithelial monolayer			angiogenesis (surface coating regulates 3D capillary morphogenesis)
tissue-like 3D structure			metastasis of cancer cells, EMT, hepatocytic tissue, neurons
embedded cells in hydrogel (spheroid / individual cells)			EMT, metastasis of cancer cells, differentiation of stem cells
floating cells			transendothelial migration (neutrophils, CTCs)
co-culture			co-culture with endothelial monolayer (cancer angiogenesis)

Figure 1.19 Table illustrating versatility of compartmentalized microfluidic chip in cancer-related research.<sup>198</sup>

### Monitoring and analysis in OoCs

Majority of OoC used to recapitulate disease development or to screen drug delivery candidates are reliant upon fluorescence microscopy as a method for information retrieval.<sup>199</sup> For examples the lung-on-a-chip and its recorded trans-membrane migration of fluorescent immune cells<sup>171</sup> or fluorescently labeled cancer cell intravasation monitored in a chip reconstructing tumor-endothelial barrier interface.<sup>178</sup> Despite being accessible method, fluorescence microscopy requires addition of labelling molecules and cannot reveal all the interesting information. Moreover, continuous monitoring with laser light can cause cell phototoxicity and some of the features can be labelled and imaged only after experiment termination, missing the intermediate points.

There is a number of alternative methods to support in-line monitoring of the OoC environment complimentary to the microscopy. Often they require an integration of new elements into the chip design, such as electrodes. For example, well established in 2D cell culture Trans-epithelial Electrical Resistance (TEER), was used to measure integrity of epithelial barrier in a gut- and lung-on-a-chip models, revealing viability of the systems, as well as barrier disruptions<sup>200</sup>. Another example of electrode-incorporated model is a cancer-on-a-chip, where the authors compare various breast cancer cell lines, and report prominent impedance changes for more metastatic cells.<sup>201</sup> Different chip with integrated electrodes and similar principle of measurement was also proposed for real-time screening of cell apoptosis and death when

exposed to drug molecules.<sup>202</sup> In other study, the authors embedded an electrofluidic system with pressure sensor into the chip body to control the flow induced shear stress on endothelial cells.<sup>203</sup>

Microsensors measuring pH and oxygen levels in the cell area together with glucose and lactate sensors at the outlet were integrated to monitor brain cancer cells metabolism and to follow alterations and cell recoveries upon the exposure to various substances.<sup>204</sup> Another example of glucose and lactate online measurement was incorporated into liver-on-a-chip, where the mitochondrial respiration was followed with phosphorescence microprobes, allowing to detect early signs of mitochondrial stress.<sup>205</sup>

Different methods are being developed for the real-time monitoring of events crucial for reliable assessment of OoC functionality. Up to now their main weakness is the comparability of the results, heavily dependent on the chip design and fabrication, as the distance or localization of the sensing parts impacts the readout.<sup>206</sup>

In the future this heterogeneities should be unified for robust feedback on physiological phenomena.



## 1.8 Aim and content of the thesis

This first introductory chapter demonstrates that drug nanocarriers hold a great promise of success in treating cancer disease. This belief is strongly supported by the number of publications and clinical trial filings resulting from research efforts on engineering an effective nano-based drug delivery system. The described and unique properties of NPs are also the reason why it is difficult to master them in formulation procedures. Yet the tumor heterogeneity among patients calls for more personalized approach, tailor-made for single or small group of patients, what at the moment is difficult to achieve: first because tiny-size batch productions are industrially not viable and secondly, because the patient-specific response to the treatment cannot be easily reproduced *in vitro* or in animal models. Development of a drug nanocarrier is a lengthy path, sometimes going in loops. The key success factors rely on controlled formulation, characterization-based feedback regarding particle features and properties, as well as on their performance *in vitro* and in animal models, which at the moment poorly resemble the disease development.

Microfluidic platforms applied to the field of nanomedicine have an increasing importance, as they enable a range of micro-scale processes which cannot be reproduced in typical reactors. They offer controlled environment with a minimal use of compounds. Moreover, the microchannels represent a scale relevant for biological activities. Although microfluidic chips are not widely implemented as standard procedures, the scientific community came to the realization that they have powerful bridging capabilities. Their use calls for multidisciplinary efforts, on the edge of different scientific fields, such as engineering, biology, physics and chemistry. Chip fabrication needs special training or alternatively researchers can reach out for commercial solutions that emerged in the last 10 years. Nevertheless, the chip integration into typical laboratory activities needs some expertise and adaptation in order to be used to its fullest.

The main aim of this work is to demonstrate how **microfluidic technology** could accelerate the development of drug delivery systems from their design and formulation to *in vitro* screening. Within this framework the first goal was to apply microfluidics for a controlled formulation of polymeric nanoparticles. Thus, the second chapter describes PLGA-PEG diblock co-polymer self-assembly into drug/dye nanocarriers and explores process in a microfluidic chip. The **hydrodynamic flow focusing** device provides narrow and controlled environment for **nanoprecipitation** process, adapted here to fabricate the NPs. The use of microfluidic technology allowed to tune the particle size by modification of process parameters, what could not be achieved with traditional manual bulk method. The formulated NPs were characterized with typical bulk methods as well as techniques allowing for **analysis of a single particle**, such as Transmission Electron Microscopy (TEM) and Total Internal Reflection Fluorescence (TIRF) microscopy.

The third chapter tackles the topic of high throughput combinatorial formulation of NPs toward personalized nanomedicine. It proposes a microfluidic chip that can promote *rapid mixing* of different NPs precursors. A prototype of *passive microfluidic mixer* is fabricated in PDMS, characterized, and evaluated. It provides efficient mixing of five independent streams that can be controlled in supplying desired quantities of the precursor solutions. Further the chip is fabricated in glass to eliminate one of the PDMS drawbacks related to the absorption of small organic molecules, such as the dyes used in the evaluation. Finally, a setup of the micromixer and nanoprecipitation chip (presented in the previous chapter) is assembled and used for proof-of-concept formulation of NPs. The process yields monodisperse dye nanocarriers, self-assembled from the blend of precursors mixed in the presented chip. The purpose of such microfluidic device is to support the concept of NPs barcoding for screening of best drug delivery candidate - an emerging topic in the field of nanomedicine.

Finally, the last, fourth chapter delves into *in vitro* screening of drug nanocarriers. Here a microfluidic *cancer-on-a-chip* platform is proposed for real time stability monitoring of polymeric micelles. It uses microfluidic technology to recreate *3D perfusable tumor blood vessel* model, reconstructing physiologically relevant barriers that NPs encounter upon administration, such as: flow in the blood vessel, endothelial barrier, extracellular matrix and cancer cell spheroid. The platform's compatibility with confocal microscopy and the spectral properties of tested NPs allow to resolve their stability at the mentioned barriers. The obtained results are compared to previously reported 2D *in vitro* studies based on the same cell line and micelles, revealing discrepancies between the static 2D monoculture and the 3D cancer-on-a-chip model.

Altogether the application of microfluidic technology in the field of drug delivery development is explored throughout these Chapters. The obtained results rose from the multidisciplinary approach, that combined knowledge from different areas of science, which is essential in adaptation of new methods and technologies to accelerate delivery of new therapies to the patients.

## 1.9 References

- (1) Dragojevic, S.; Ryu, J. S.; Raucher, D. Polymer-Based Prodrugs: Improving Tumor Targeting and the Solubility of Small Molecule Drugs in Cancer Therapy. *Molecules* **2015**, *20* (12), 21750–21769. <https://doi.org/10.3390/molecules201219804>.
- (2) Allen, T. M.; Cullis, P. R. Drug Delivery Systems: Entering the Mainstream. *DRUG Discov.* **2004**, *303*, 6.
- (3) Wicki, A.; Witzigmann, D.; Balasubramanian, V.; Huwyler, J. Nanomedicine in Cancer Therapy: Challenges, Opportunities, and Clinical Applications. *J. Controlled Release* **2015**, *200*, 138–157. <https://doi.org/10.1016/j.jconrel.2014.12.030>.
- (4) Gulati, N.; Gupta, H. Parenteral Drug Delivery: A Review. *Recent Pat. Drug Deliv. Formul.* **2011**, *5* (2), 133–145. <https://doi.org/10.2174/18722111795471391>.
- (5) Blanco, E.; Shen, H.; Ferrari, M. Principles of Nanoparticle Design for Overcoming Biological Barriers to Drug Delivery. *Nat. Biotechnol.* **2015**, *33* (9), 941–951. <https://doi.org/10.1038/nbt.3330>.
- (6) Mitchell, E. P. Gastrointestinal Toxicity of Chemotherapeutic Agents. *Semin. Oncol.* **2006**, *33* (1), 106–120. <https://doi.org/10.1053/j.seminoncol.2005.12.001>.
- (7) Hu, W.; Sung, T.; Jessen, B. A.; Thibault, S.; Finkelstein, M. B.; Khan, N. K.; Sacca, A. I. Mechanistic Investigation of Bone Marrow Suppression Associated with Palbociclib and Its Differentiation from Cytotoxic Chemotherapies. *Clin. Cancer Res.* **2016**, *22* (8), 2000–2008. <https://doi.org/10.1158/1078-0432.CCR-15-1421>.
- (8) Cho, K.; Wang, X.; Nie, S.; Chen, Z. (Georgia); Shin, D. M. Therapeutic Nanoparticles for Drug Delivery in Cancer. *Clin. Cancer Res.* **2008**, *14* (5), 1310–1316. <https://doi.org/10.1158/1078-0432.CCR-07-1441>.
- (9) Bangham, A. D.; Horne, R. W. Negative Staining of Phospholipids and Their Structural Modification by Surface-Active Agents as Observed in the Electron Microscope. *J. Mol. Biol.* **1964**, *8* (5), 660–IN10. [https://doi.org/10.1016/S0022-2836\(64\)80115-7](https://doi.org/10.1016/S0022-2836(64)80115-7).
- (10) Markman, M. Pegylated Liposomal Doxorubicin in the Treatment of Cancers of the Breast and Ovary. *Expert Opin. Pharmacother.* **2006**, *7* (11), 1469–1474. <https://doi.org/10.1517/14656566.7.11.1469>.
- (11) Petersen, G. H.; Alzghari, S. K.; Chee, W.; Sankari, S. S.; La-Beck, N. M. Meta-Analysis of Clinical and Preclinical Studies Comparing the Anticancer Efficacy of Liposomal versus Conventional Non-Liposomal Doxorubicin. *J. Controlled Release* **2016**, *232*, 255–264. <https://doi.org/10.1016/j.jconrel.2016.04.028>.
- (12) Bozzuto, G.; Molinari, A. Liposomes as Nanomedical Devices. *Int. J. Nanomedicine* **2015**, *10*, 975–999. <https://doi.org/10.2147/IJN.S68861>.
- (13) Allen, T. M.; Cullis, P. R. Liposomal Drug Delivery Systems: From Concept to Clinical Applications. *Adv. Drug Deliv. Rev.* **2013**, *65* (1), 36–48. <https://doi.org/10.1016/j.addr.2012.09.037>.
- (14) Tinkle, S.; McNeil, S. E.; Mühlebach, S.; Bawa, R.; Borchard, G.; Barenholz, Y. (Chezy); Tamarkin, L.; Desai, N. Nanomedicines: Addressing the Scientific and Regulatory Gap. *Ann. N. Y. Acad. Sci.* **2014**, *1313* (1), 35–56. <https://doi.org/10.1111/nyas.12403>.
- (15) Chari, R. V. J.; Miller, M. L.; Widdison, W. C. Antibody–Drug Conjugates: An Emerging Concept in Cancer Therapy. *Angew. Chem. Int. Ed.* **2014**, *53* (15), 3796–3827. <https://doi.org/10.1002/anie.201307628>.
- (16) Selby, C.; Yacko, L. R.; Glode, A. E. Gemtuzumab Ozogamicin: Back Again. *J. Adv. Pract. Oncol.* **2019**, *10* (1), 68–82.

- (17) Miele, E.; Spinelli, G. P.; Miele, E.; Tomao, F.; Tomao, S. Albumin-Bound Formulation of Paclitaxel (Abraxane® ABI-007) in the Treatment of Breast Cancer. *Int. J. Nanomedicine* **2009**, *4*, 99–105.
- (18) Thakor, P.; Bhavana, V.; Sharma, R.; Srivastava, S.; Singh, S. B.; Mehra, N. K. Polymer–Drug Conjugates: Recent Advances and Future Perspectives. *Drug Discov. Today* **2020**, *25* (9), 1718–1726. <https://doi.org/10.1016/j.drudis.2020.06.028>.
- (19) Yildiz, I.; Shukla, S.; Steinmetz, N. F. Applications of Viral Nanoparticles in Medicine. *Curr. Opin. Biotechnol.* **2011**, *22* (6), 901–908. <https://doi.org/10.1016/j.copbio.2011.04.020>.
- (20) Kay, M. A.; Glorioso, J. C.; Naldini, L. Viral Vectors for Gene Therapy: The Art of Turning Infectious Agents into Vehicles of Therapeutics. *Nat. Med.* **2001**, *7* (1), 33–40. <https://doi.org/10.1038/83324>.
- (21) Pol, J.; Kroemer, G.; Galluzzi, L. First Oncolytic Virus Approved for Melanoma Immunotherapy. *Oncol Immunology* **2016**, *5* (1), e1115641. <https://doi.org/10.1080/2162402X.2015.1115641>.
- (22) Goldsmith, C. S.; Miller, S. E. Modern Uses of Electron Microscopy for Detection of Viruses. *Clin. Microbiol. Rev.* **2009**, *22* (4), 552–563. <https://doi.org/10.1128/CMR.00027-09>.
- (23) Huang, H.; Feng, W.; Chen, Y.; Shi, J. Inorganic Nanoparticles in Clinical Trials and Translations. *Nano Today* **2020**, *35*, 100972. <https://doi.org/10.1016/j.nantod.2020.100972>.
- (24) Bobo, D.; Robinson, K. J.; Islam, J.; Thurecht, K. J.; Corrie, S. R. Nanoparticle-Based Medicines: A Review of FDA-Approved Materials and Clinical Trials to Date. *Pharm. Res.* **2016**, *33* (10), 2373–2387. <https://doi.org/10.1007/s11095-016-1958-5>.
- (25) Maier-Hauff, K.; Ulrich, F.; Nestler, D.; Niehoff, H.; Wust, P.; Thiesen, B.; Orawa, H.; Budach, V.; Jordan, A. Efficacy and Safety of Intratumoral Thermotherapy Using Magnetic Iron-Oxide Nanoparticles Combined with External Beam Radiotherapy on Patients with Recurrent Glioblastoma Multiforme. *J. Neurooncol.* **2011**, *103* (2), 317–324. <https://doi.org/10.1007/s11060-010-0389-0>.
- (26) Sztandera, K.; Gorzkiewicz, M.; Klajnert-Maculewicz, B. Gold Nanoparticles in Cancer Treatment. *Mol. Pharm.* **2019**, *16* (1), 1–23. <https://doi.org/10.1021/acs.molpharmaceut.8b00810>.
- (27) Gad, S. C.; Sharp, K. L.; Montgomery, C.; Payne, J. D.; Goodrich, G. P. Evaluation of the Toxicity of Intravenous Delivery of Auroshell Particles (Gold–Silica Nanoshells). *Int. J. Toxicol.* **2012**, *31* (6), 584–594. <https://doi.org/10.1177/1091581812465969>.
- (28) Rastinehad, A. R.; Anastos, H.; Wajswol, E.; Winoker, J. S.; Sfakianos, J. P.; Doppalapudi, S. K.; Carrick, M. R.; Knauer, C. J.; Taouli, B.; Lewis, S. C.; Tewari, A. K.; Schwartz, J. A.; Canfield, S. E.; George, A. K.; West, J. L.; Halas, N. J. Gold Nanoshell-Localized Photothermal Ablation of Prostate Tumors in a Clinical Pilot Device Study. *Proc. Natl. Acad. Sci.* **2019**, *116* (37), 18590–18596. <https://doi.org/10.1073/pnas.1906929116>.
- (29) Wierzbinski, K. R.; Szymanski, T.; Rozwadowska, N.; Rybka, J. D.; Zimna, A.; Zalewski, T.; Nowicka-Bauer, K.; Malcher, A.; Nowaczyk, M.; Krupinski, M.; Fiedorowicz, M.; Bogorodzki, P.; Grieb, P.; Giersig, M.; Kurpisz, M. K. Potential Use of Superparamagnetic Iron Oxide Nanoparticles for in Vitro and in Vivo Bioimaging of Human Myoblasts. *Sci. Rep.* **2018**, *8* (1), 3682. <https://doi.org/10.1038/s41598-018-22018-0>.
- (30) Suk, J. S.; Xu, Q.; Kim, N.; Hanes, J.; Ensign, L. M. PEGylation as a Strategy for Improving Nanoparticle-Based Drug and Gene Delivery. *Adv. Drug Deliv. Rev.* **2016**, *99*, 28–51. <https://doi.org/10.1016/j.addr.2015.09.012>.
- (31) Delplace, V.; Couvreur, P.; Nicolas, J. Recent Trends in the Design of Anticancer Polymer Prodrug Nanocarriers. *Polym Chem* **2014**, *5* (5), 1529–1544. <https://doi.org/10.1039/C3PY01384G>.
- (32) Musumeci, T.; Ventura, C. A.; Giannone, I.; Ruozi, B.; Montenegro, L.; Pignatello, R.; Puglisi, G. PLA/PLGA Nanoparticles for Sustained Release of Docetaxel. *Int. J. Pharm.* **2006**, *325* (1), 172–179. <https://doi.org/10.1016/j.ijpharm.2006.06.023>.

- (33) Banik, B. L.; Fattahi, P.; Brown, J. L. Polymeric Nanoparticles: The Future of Nanomedicine. *WIREs Nanomedicine Nanobiotechnology* **2016**, *8* (2), 271–299. <https://doi.org/10.1002/wnan.1364>.
- (34) Ghosh, B.; Biswas, S. Polymeric Micelles in Cancer Therapy: State of the Art. *J. Controlled Release* **2021**, *332*, 127–147. <https://doi.org/10.1016/j.jconrel.2021.02.016>.
- (35) van Eerden, R. A. G.; Mathijssen, R. H. J.; Koolen, S. L. W. Recent Clinical Developments of Nanomediated Drug Delivery Systems of Taxanes for the Treatment of Cancer. *Int. J. Nanomedicine* **2020**, *15*, 8151–8166. <https://doi.org/10.2147/IJN.S272529>.
- (36) NanoCarrier Co., Ltd. *Phase IIa/IIb Clinical Trial of NC-6004 in Combination With Pembrolizumab in Subjects With Recurrent or Metastatic Squamous Cell Carcinoma of the Head and Neck Who Have Failed Platinum or a Platinum-Containing Regimen*; Clinical trial registration NCT03771820; [clinicaltrials.gov](https://clinicaltrials.gov), 2020.
- (37) Autio, K. A.; Dreicer, R.; Anderson, J.; Garcia, J. A.; Alva, A.; Hart, L. L.; Milowsky, M. I.; Posadas, E. M.; Ryan, C. J.; Graf, R. P.; Dittamore, R.; Schreiber, N. A.; Summa, J. M.; Youssoufian, H.; Morris, M. J.; Scher, H. I. Safety and Efficacy of BIND-014, a Docetaxel Nanoparticle Targeting Prostate-Specific Membrane Antigen for Patients With Metastatic Castration-Resistant Prostate Cancer: A Phase 2 Clinical Trial. *JAMA Oncol.* **2018**, *4* (10), 1344–1351. <https://doi.org/10.1001/jamaoncol.2018.2168>.
- (38) Kannan, R. M.; Nance, E.; Kannan, S.; Tomalia, D. A. Emerging Concepts in Dendrimer-Based Nanomedicine: From Design Principles to Clinical Applications. *J. Intern. Med.* **2014**, *276* (6), 579–617. <https://doi.org/10.1111/joim.12280>.
- (39) Sharma, A. K.; Prasher, P.; Aljabali, A. A.; Mishra, V.; Gandhi, H.; Kumar, S.; Mutalik, S.; Chellappan, D. K.; Tambuwala, M. M.; Dua, K.; Kapoor, D. N. Emerging Era of “Somes”: Polymersomes as Versatile Drug Delivery Carrier for Cancer Diagnostics and Therapy. *Drug Deliv. Transl. Res.* **2020**, *10* (5), 1171–1190. <https://doi.org/10.1007/s13346-020-00789-2>.
- (40) Golombek, S. K.; May, J.-N.; Theek, B.; Appold, L.; Drude, N.; Kiessling, F.; Lammers, T. Tumor Targeting via EPR: Strategies to Enhance Patient Responses. *Adv. Drug Deliv. Rev.* **2018**, *130*, 17–38. <https://doi.org/10.1016/j.addr.2018.07.007>.
- (41) Fang, J.; Nakamura, H.; Maeda, H. The EPR Effect: Unique Features of Tumor Blood Vessels for Drug Delivery, Factors Involved, and Limitations and Augmentation of the Effect. *Adv. Drug Deliv. Rev.* **2011**, *63* (3), 136–151. <https://doi.org/10.1016/j.addr.2010.04.009>.
- (42) Dinndorf, P. A.; Gootenberg, J.; Cohen, M. H.; Keegan, P.; Pazdur, R. FDA Drug Approval Summary: Pegaspargase (Oncaspar®) for the First-Line Treatment of Children with Acute Lymphoblastic Leukemia (ALL). *The Oncologist* **2007**, *12* (8), 991–998. <https://doi.org/10.1634/theoncologist.12-8-991>.
- (43) Owens, D. E.; Peppas, N. A. Opsonization, Biodistribution, and Pharmacokinetics of Polymeric Nanoparticles. *Int. J. Pharm.* **2006**, *307* (1), 93–102. <https://doi.org/10.1016/j.ijpharm.2005.10.010>.
- (44) Monopoli, M. P.; Åberg, C.; Salvati, A.; Dawson, K. A. Biomolecular Coronas Provide the Biological Identity of Nanosized Materials. *Nat. Nanotechnol.* **2012**, *7* (12), 779–786. <https://doi.org/10.1038/nnano.2012.207>.
- (45) Fang, Y.; Xue, J.; Gao, S.; Lu, A.; Yang, D.; Jiang, H.; He, Y.; Shi, K. Cleavable PEGylation: A Strategy for Overcoming the “PEG Dilemma” in Efficient Drug Delivery. *Drug Deliv.* **2017**, *24* (2), 22–32. <https://doi.org/10.1080/10717544.2017.1388451>.
- (46) Kobayashi, H.; Watanabe, R.; Choyke, P. L. Improving Conventional Enhanced Permeability and Retention (EPR) Effects; What Is the Appropriate Target? *Theranostics* **2013**, *4* (1), 81–89. <https://doi.org/10.7150/thno.7193>.

- (47) Nichols, J. W.; Bae, Y. H. EPR: Evidence and Fallacy. *J. Controlled Release* **2014**, *190*, 451–464. <https://doi.org/10.1016/j.jconrel.2014.03.057>.
- (48) Pearce, A. K.; O'Reilly, R. K. Insights into Active Targeting of Nanoparticles in Drug Delivery: Advances in Clinical Studies and Design Considerations for Cancer Nanomedicine. *Bioconjug. Chem.* **2019**, *30* (9), 2300–2311. <https://doi.org/10.1021/acs.bioconjchem.9b00456>.
- (49) Upponi, J. R.; Torchilin, V. P. Passive vs. Active Targeting: An Update of the EPR Role in Drug Delivery to Tumors. In *Nano-Oncologicals: New Targeting and Delivery Approaches*; Alonso, M. J., Garcia-Fuentes, M., Eds.; Advances in Delivery Science and Technology; Springer International Publishing: Cham, 2014; pp 3–45. [https://doi.org/10.1007/978-3-319-08084-0\\_1](https://doi.org/10.1007/978-3-319-08084-0_1).
- (50) Attia, M. F.; Anton, N.; Wallyn, J.; Omran, Z.; Vandamme, T. F. An Overview of Active and Passive Targeting Strategies to Improve the Nanocarriers Efficiency to Tumour Sites. *J. Pharm. Pharmacol.* **2019**, *71* (8), 1185–1198. <https://doi.org/10.1111/jphp.13098>.
- (51) Hathaway, H. J.; Butler, K. S.; Adolphi, N. L.; Lovato, D. M.; Belfon, R.; Fegan, D.; Monson, T. C.; Trujillo, J. E.; Tessier, T. E.; Bryant, H. C.; Huber, D. L.; Larson, R. S.; Flynn, E. R. Detection of Breast Cancer Cells Using Targeted Magnetic Nanoparticles and Ultra-Sensitive Magnetic Field Sensors. *Breast Cancer Res.* **2011**, *13* (5), R108. <https://doi.org/10.1186/bcr3050>.
- (52) Guo, M.; Peng, Y.; Gao, A.; Du, C.; Herman, J. G. Epigenetic Heterogeneity in Cancer. *Biomark. Res.* **2019**, *7* (1), 1–19. <https://doi.org/10.1186/s40364-019-0174-y>.
- (53) Rabanel, J.-M.; Adibnia, V.; Tehrani, S. F.; Sanche, S.; Hildgen, P.; Banquy, X.; Ramassamy, C. Nanoparticle Heterogeneity: An Emerging Structural Parameter Influencing Particle Fate in Biological Media? *Nanoscale* **2019**, *11* (2), 383–406. <https://doi.org/10.1039/C8NR04916E>.
- (54) Muro, S. Challenges in Design and Characterization of Ligand-Targeted Drug Delivery Systems. *J. Controlled Release* **2012**, *164* (2), 125–137. <https://doi.org/10.1016/j.jconrel.2012.05.052>.
- (55) Lammers, T.; Kiessling, F.; Ashford, M.; Hennink, W.; Crommelin, D.; Strom, G. Cancer Nanomedicine: Is Targeting Our Target? *Nat. Rev. Mater.* **2016**, *1* (9), 16069. <https://doi.org/10.1038/natrevmats.2016.69>.
- (56) Shi, J.; Kantoff, P. W.; Wooster, R.; Farokhzad, O. C. Cancer Nanomedicine: Progress, Challenges and Opportunities. *Nat. Rev. Cancer* **2017**, *17* (1), 20–37. <https://doi.org/10.1038/nrc.2016.108>.
- (57) L. Moore, T.; Rodriguez-Lorenzo, L.; Hirsch, V.; Balog, S.; Urban, D.; Jud, C.; Rothen-Rutishauser, B.; Lattuada, M.; Petri-Fink, A. Nanoparticle Colloidal Stability in Cell Culture Media and Impact on Cellular Interactions. *Chem. Soc. Rev.* **2015**, *44* (17), 6287–6305. <https://doi.org/10.1039/C4CS00487F>.
- (58) Sperling, R. A.; Liedl, T.; Duhr, S.; Kudera, S.; Zanella, M.; Lin, C.-A. J.; Chang, W. H.; Braun, D.; Parak, W. J. Size Determination of (Bio)Conjugated Water-Soluble Colloidal Nanoparticles: A Comparison of Different Techniques. *J. Phys. Chem. C* **2007**, *111* (31), 11552–11559. <https://doi.org/10.1021/jp070999d>.
- (59) Glass, J. J.; Chen, L.; Alcantara, S.; Crampin, E. J.; Thurecht, K. J.; De Rose, R.; Kent, S. J. Charge Has a Marked Influence on Hyperbranched Polymer Nanoparticle Association in Whole Human Blood. *ACS Macro Lett.* **2017**, *6* (6), 586–592. <https://doi.org/10.1021/acsmacrolett.7b00229>.
- (60) Albanese, A.; Tang, P. S.; Chan, W. C. W. The Effect of Nanoparticle Size, Shape, and Surface Chemistry on Biological Systems. *Annu. Rev. Biomed. Eng.* **2012**, *14* (1), 1–16. <https://doi.org/10.1146/annurev-bioeng-071811-150124>.
- (61) Drummond, D. C.; Noble, C. O.; Hayes, M. E.; Park, J. W.; Kirpotin, D. B. Pharmacokinetics and in Vivo Drug Release Rates in Liposomal Nanocarrier Development. *J. Pharm. Sci.* **2008**, *97* (11), 4696–4740. <https://doi.org/10.1002/jps.21358>.
- (62) Ding, C.; Li, Z. A Review of Drug Release Mechanisms from Nanocarrier Systems. *Mater. Sci. Eng. C* **2017**, *76*, 1440–1453. <https://doi.org/10.1016/j.msec.2017.03.130>.

- (63) Torrice, M. Does Nanomedicine Have a Delivery Problem? *ACS Cent. Sci.* **2016**, *2* (7), 434–437. <https://doi.org/10.1021/acscentsci.6b00190>.
- (64) Colombo, M.; Fiandra, L.; Alessio, G.; Mazzucchelli, S.; Nebuloni, M.; De Palma, C.; Kantner, K.; Pelaz, B.; Rotem, R.; Corsi, F.; Parak, W. J.; Prospero, D. Tumour Homing and Therapeutic Effect of Colloidal Nanoparticles Depend on the Number of Attached Antibodies. *Nat. Commun.* **2016**, *7* (1), 13818. <https://doi.org/10.1038/ncomms13818>.
- (65) Faria, M.; Björnalm, M.; Thurecht, K. J.; Kent, S. J.; Parton, R. G.; Kavallaris, M.; Johnston, A. P. R.; Gooding, J. J.; Corrie, S. R.; Boyd, B. J.; Thordarson, P.; Whittaker, A. K.; Stevens, M. M.; Prestidge, C. A.; Porter, C. J. H.; Parak, W. J.; Davis, T. P.; Crampin, E. J.; Caruso, F. Minimum Information Reporting in Bio–Nano Experimental Literature. *Nat. Nanotechnol.* **2018**, *13* (9), 777–785. <https://doi.org/10.1038/s41565-018-0246-4>.
- (66) Mulvaney, P.; Parak, W. J.; Caruso, F.; Weiss, P. S. Standardizing Nanomaterials. *ACS Nano* **2016**, *10* (11), 9763–9764. <https://doi.org/10.1021/acsnano.6b07629>.
- (67) Kulkarni, S. K. *Nanotechnology: Principles and Practices*; Springer International Publishing: Cham, 2015. <https://doi.org/10.1007/978-3-319-09171-6>.
- (68) Crucho, C. I. C.; Barros, M. T. Polymeric Nanoparticles: A Study on the Preparation Variables and Characterization Methods. *Mater. Sci. Eng. C* **2017**, *80*, 771–784. <https://doi.org/10.1016/j.msec.2017.06.004>.
- (69) Davis, A. V.; Yeh, R. M.; Raymond, K. N. Supramolecular Assembly Dynamics. *Proc. Natl. Acad. Sci.* **2002**, *99* (8), 4793–4796. <https://doi.org/10.1073/pnas.052018299>.
- (70) Vauthier, C.; Bouchemal, K. Methods for the Preparation and Manufacture of Polymeric Nanoparticles. *Pharm. Res.* **2009**, *26* (5), 1025–1058. <https://doi.org/10.1007/s11095-008-9800-3>.
- (71) *Polymer Nanoparticles for Nanomedicines: A Guide for Their Design, Preparation and Development*, 1st ed. 2016.; Ponchel, G., Vauthier, C., Eds.; Springer International Publishing : Imprint: Springer: Cham, 2016. <https://doi.org/10.1007/978-3-319-41421-8>.
- (72) Ganachaud, F.; Katz, J. L. Nanoparticles and Nanocapsules Created Using the Ouzo Effect: Spontaneous Emulsification as an Alternative to Ultrasonic and High-Shear Devices. *ChemPhysChem* **2005**, *6* (2), 209–216. <https://doi.org/10.1002/cphc.200400527>.
- (73) Fessi, H.; Puisieux, F.; Devissaguet, J. Ph.; Ammoury, N.; Benita, S. Nanocapsule Formation by Interfacial Polymer Deposition Following Solvent Displacement. *Int. J. Pharm.* **1989**, *55* (1), R1–R4. [https://doi.org/10.1016/0378-5173\(89\)90281-0](https://doi.org/10.1016/0378-5173(89)90281-0).
- (74) Karnik, R.; Gu, F.; Basto, P.; Cannizzaro, C.; Dean, L.; Kyei-Manu, W.; Langer, R.; Farokhzad, O. C. Microfluidic Platform for Controlled Synthesis of Polymeric Nanoparticles. *Nano Lett.* **2008**, *8* (9), 2906–2912. <https://doi.org/10.1021/nl801736q>.
- (75) Luxenhofer, R. Polymers and Nanomedicine: Considerations on Variability and Reproducibility When Combining Complex Systems. *Nanomed.* **2015**, *10* (20), 3109–3119. <https://doi.org/10.2217/nnm.15.139>.
- (76) *Microsystems for Pharmatechnology*; Dietzel, A., Ed.; Springer International Publishing: Cham, 2016. <https://doi.org/10.1007/978-3-319-26920-7>.
- (77) Elvira, K. S.; i Solvas, X. C.; Wootton, R. C. R.; deMello, A. J. The Past, Present and Potential for Microfluidic Reactor Technology in Chemical Synthesis. *Nat. Chem.* **2013**, *5* (11), 905–915. <https://doi.org/10.1038/nchem.1753>.
- (78) Beebe, D. J.; Mensing, G. A.; Walker, G. M. Physics and Applications of Microfluidics in Biology. *Annu. Rev. Biomed. Eng.* **2002**, *4* (1), 261–286. <https://doi.org/10.1146/annurev.bioeng.4.112601.125916>.
- (79) Anton, N.; Bally, F.; Serra, C. A.; Ali, A.; Arntz, Y.; Mely, Y.; Zhao, M.; Marchioni, E.; Jakhmola, A.; Vandamme, T. F. A New Microfluidic Setup for Precise Control of the Polymer Nanoprecipitation

- Process and Lipophilic Drug Encapsulation. *Soft Matter* **2012**, *8* (41), 10628–10635. <https://doi.org/10.1039/C2SM25357G>.
- (80) Kang, X.; Luo, C.; Wei, Q.; Xiong, C.; Chen, Q.; Chen, Y.; Ouyang, Q. Mass Production of Highly Monodisperse Polymeric Nanoparticles by Parallel Flow Focusing System. *Microfluid. Nanofluidics* **2013**, *15* (3), 337–345. <https://doi.org/10.1007/s10404-013-1152-6>.
- (81) Abdelkarim, M.; Abd Allah, N. H.; Elsabahy, M.; Abdelgawad, M.; Abouelmagd, S. A. Microchannel Geometry vs Flow Parameters for Controlling Nanoprecipitation of Polymeric Nanoparticles. *Colloids Surf. Physicochem. Eng. Asp.* **2021**, *611*, 125774. <https://doi.org/10.1016/j.colsurfa.2020.125774>.
- (82) Lababidi, N.; Sigal, V.; Koenneke, A.; Schwarzkopf, K.; Manz, A.; Schneider, M. Microfluidics as Tool to Prepare Size-Tunable PLGA Nanoparticles with High Curcumin Encapsulation for Efficient Mucus Penetration. *Beilstein J. Nanotechnol.* **2019**, *10* (1), 2280–2293. <https://doi.org/10.3762/bjnano.10.220>.
- (83) Donno, R.; Gennari, A.; Lallana, E.; De La Rosa, J. M. R.; d’Arcy, R.; Treacher, K.; Hill, K.; Ashford, M.; Tirelli, N. Nanomanufacturing through Microfluidic-Assisted Nanoprecipitation: Advanced Analytics and Structure-Activity Relationships. *Int. J. Pharm.* **2017**, *534* (1), 97–107. <https://doi.org/10.1016/j.ijpharm.2017.10.006>.
- (84) Kolishetti, N.; Dhar, S.; Valencia, P. M.; Lin, L. Q.; Karnik, R.; Lippard, S. J.; Langer, R.; Farokhzad, O. C. Engineering of Self-Assembled Nanoparticle Platform for Precisely Controlled Combination Drug Therapy. *Proc. Natl. Acad. Sci.* **2010**, *107* (42), 17939–17944. <https://doi.org/10.1073/pnas.1011368107>.
- (85) Tresset, G.; Marculescu, C.; Salonen, A.; Ni, M.; Iliescu, C. Fine Control Over the Size of Surfactant–Polyelectrolyte Nanoparticles by Hydrodynamic Flow Focusing <http://pubs.acs.org/doi/full/10.1021/ac4006155> (accessed Mar 12, 2021). <https://doi.org/10.1021/ac4006155>.
- (86) Heshmatnezhad, F.; Nazar, A. R. S. Synthesis of Polycaprolactone Nanoparticles through Flow-Focusing Microfluidic-Assisted Nanoprecipitation. *Chem. Eng. Technol.* **2020**, *43* (10), 2073–2082. <https://doi.org/10.1002/ceat.202000222>.
- (87) Wagner, J.; Köhler, J. M. Continuous Synthesis of Gold Nanoparticles in a Microreactor. *Nano Lett.* **2005**, *5* (4), 685–691. <https://doi.org/10.1021/nl050097t>.
- (88) Shestopalov, I.; Tice, J. D.; Ismagilov, R. F. Multi-Step Synthesis of Nanoparticles Performed on Millisecond Time Scale in a Microfluidic Droplet-Based System. *Lab. Chip* **2004**, *4* (4), 316. <https://doi.org/10.1039/b403378g>.
- (89) Numata, M.; Sato, A.; Nogami, R. Energy-Dissipative Self-Assembly Driven in Microflow: A Time-Programmed Self-Organization and Decomposition of Metastable Nanofibers. *Chem. Lett.* **2015**, *44* (7), 995–997. <https://doi.org/10.1246/cl.150292>.
- (90) Tan, Z.; Lan, W.; Liu, Q.; Wang, K.; Hussain, M.; Ren, M.; Geng, Z.; Zhang, L.; Luo, X.; Zhang, L.; Zhu, J. Kinetically Controlled Self-Assembly of Block Copolymers into Segmented Wormlike Micelles in Microfluidic Chips. *Langmuir* **2019**, *35* (1), 141–149. <https://doi.org/10.1021/acs.langmuir.8b03028>.
- (91) Nsamela, A. Microfluidics for PLGA Nanoparticle Synthesis: A Review. *Elveflow* **2020**.
- (92) Han, T.; Zhang, L.; Xu, H.; Xuan, J. Factory-on-Chip: Modularised Microfluidic Reactors for Continuous Mass Production of Functional Materials. *Chem. Eng. J.* **2017**, *326*, 765–773. <https://doi.org/10.1016/j.cej.2017.06.028>.
- (93) Jeong, H.-H.; Issadore, D.; Lee, D. Recent Developments in Scale-up of Microfluidic Emulsion Generation via Parallelization. *Korean J. Chem. Eng.* **2016**, *33* (6), 1757–1766. <https://doi.org/10.1007/s11814-016-0041-6>.



- (94) Valencia, P. M.; Pridgen, E. M.; Rhee, M.; Langer, R.; Farokhzad, O. C.; Karnik, R. Microfluidic Platform for Combinatorial Synthesis and Optimization of Targeted Nanoparticles for Cancer Therapy. *ACS Nano* **2013**, *7* (12), 10671–10680. <https://doi.org/10.1021/nn403370e>.
- (95) Yaari, Z.; da Silva, D.; Zinger, A.; Goldman, E.; Kagal, A.; Tshuva, R.; Barak, E.; Dahan, N.; Hershkovitz, D.; Goldfeder, M.; Roitman, J. S.; Schroeder, A. Theranostic Barcoded Nanoparticles for Personalized Cancer Medicine. *Nat. Commun.* **2016**, *7* (1), 13325. <https://doi.org/10.1038/ncomms13325>.
- (96) Andreiuk, B.; Reisch, A.; Lindecker, M.; Follain, G.; Peyri ras, N.; Goetz, J. G.; Klymchenko, A. S. Fluorescent Polymer Nanoparticles for Cell Barcoding In Vitro and In Vivo. *Small* **2017**, *13* (38), 1701582. <https://doi.org/10.1002/sml.201701582>.
- (97) Medina, D. X.; Householder, K. T.; Ceton, R.; Kovalik, T.; Heffernan, J. M.; Shankar, R. V.; Bowser, R. P.; Wechsler-Reya, R. J.; Sirianni, R. W. Optical Barcoding of PLGA for Multispectral Analysis of Nanoparticle Fate in Vivo. *J. Controlled Release* **2017**, *253*, 172–182. <https://doi.org/10.1016/j.jconrel.2017.02.033>.
- (98) Nguyen, N.-T.; Wu, Z. Micromixers—a Review. *J. Micromechanics Microengineering* **2004**, *15* (2), R1–R16. <https://doi.org/10.1088/0960-1317/15/2/R01>.
- (99) Cai, G.; Xue, L.; Zhang, H.; Lin, J. A Review on Micromixers. *Micromachines* **2017**, *8* (9), 274. <https://doi.org/10.3390/mi8090274>.
- (100) Maoz, B. M.; Herland, A.; Henry, O. Y. F.; Leineweber, W. D.; Yadid, M.; Doyle, J.; Mannix, R.; Kujala, V. J.; FitzGerald, E. A.; Parker, K. K.; Ingber, D. E. Organs-on-Chips with Combined Multi-Electrode Array and Transepithelial Electrical Resistance Measurement Capabilities. *Lab. Chip* **2017**, *17* (13), 2294–2302. <https://doi.org/10.1039/C7LC00412E>.
- (101) Huh, D.; Kim, H. J.; Fraser, J. P.; Shea, D. E.; Khan, M.; Bahinski, A.; Hamilton, G. A.; Ingber, D. E. Microfabrication of Human Organs-on-Chips. *Nat. Protoc.* **2013**, *8* (11), 2135–2157. <https://doi.org/10.1038/nprot.2013.137>.
- (102) van Meer, B. J.; de Vries, H.; Firth, K. S. A.; van Weerd, J.; Tertoolen, L. G. J.; Karperien, H. B. J.; Jonkheijm, P.; Denning, C.; IJzerman, A. P.; Mummery, C. L. Small Molecule Absorption by PDMS in the Context of Drug Response Bioassays. *Biochem. Biophys. Res. Commun.* **2017**, *482* (2), 323–328. <https://doi.org/10.1016/j.bbrc.2016.11.062>.
- (103) Li, N.; Schwartz, M.; Ionescu-Zanetti, C. PDMS Compound Adsorption in Context. *J. Biomol. Screen.* **2009**, *14* (2), 194–202. <https://doi.org/10.1177/1087057108327326>.
- (104) When PDMS Isn't the Best. *Anal. Chem.* **2007**, *79* (9), 3248–3253. <https://doi.org/10.1021/ac071903e>.
- (105) Weibel, D. B.; DiLuzio, W. R.; Whitesides, G. M. Microfabrication Meets Microbiology. *Nat. Rev. Microbiol.* **2007**, *5* (3), 209–218. <https://doi.org/10.1038/nrmicro1616>.
- (106) Silverio, V.; Cardoso de Freitas, S. Microfabrication Techniques for Microfluidic Devices. In *Complex Fluid-Flows in Microfluidics*; Galindo-Rosales, F. J., Ed.; Springer International Publishing: Cham, 2018; pp 25–51. [https://doi.org/10.1007/978-3-319-59593-1\\_2](https://doi.org/10.1007/978-3-319-59593-1_2).
- (107) Wlodarczyk, K. L.; Hand, D. P.; Maroto-Valer, M. M. Maskless, Rapid Manufacturing of Glass Microfluidic Devices Using a Picosecond Pulsed Laser. *Sci. Rep.* **2019**, *9* (1), 20215. <https://doi.org/10.1038/s41598-019-56711-5>.
- (108) Jena, R. K.; Yue, C. Y.; Lam, Y. C. Micro Fabrication of Cyclic Olefin Copolymer (COC) Based Microfluidic Devices. *Microsyst. Technol.* **2012**, *18* (2), 159–166. <https://doi.org/10.1007/s00542-011-1366-z>.
- (109) 3D cell culture chips <http://www.aimbiotech.com/store/p1/dax-1.html> (accessed Jun 3, 2020).
- (110) MIMETAS Organ-on-a-Chip <https://mimetas.com/> (accessed Feb 22, 2021).
- (111) Assay Chips. *microfluidic ChipShop*.

- (112) Bhushan, B.; Caspers, M. An Overview of Additive Manufacturing (3D Printing) for Microfabrication. *Microsyst. Technol.* **2017**, *23* (4), 1117–1124. <https://doi.org/10.1007/s00542-017-3342-8>.
- (113) Balakrishnan, H. K.; Badar, F.; Doeven, E. H.; Novak, J. I.; Merenda, A.; Dumée, L. F.; Loy, J.; Guijt, R. M. 3D Printing: An Alternative Microfabrication Approach with Unprecedented Opportunities in Design. *Anal. Chem.* **2021**, *93* (1), 350–366. <https://doi.org/10.1021/acs.analchem.0c04672>.
- (114) Guckenberger, D. J.; de Groot, T. E.; Wan, A. M. D.; Beebe, D. J.; Young, E. W. K. Micromilling: A Method for Ultra-Rapid Prototyping of Plastic Microfluidic Devices. *Lab. Chip* **2015**, *15* (11), 2364–2378. <https://doi.org/10.1039/C5LC00234F>.
- (115) Eaton, M. A. W.; Levy, L.; Fontaine, O. M. A. Delivering Nanomedicines to Patients: A Practical Guide. *Nanomedicine Nanotechnol. Biol. Med.* **2015**, *11* (4), 983–992. <https://doi.org/10.1016/j.nano.2015.02.004>.
- (116) Chang, E. H.; Harford, J. B.; Eaton, M. A. W.; Boisseau, P. M.; Dube, A.; Hayeshi, R.; Swai, H.; Lee, D. S. Nanomedicine: Past, Present and Future – A Global Perspective. *Biochem. Biophys. Res. Commun.* **2015**, *468* (3), 511–517. <https://doi.org/10.1016/j.bbrc.2015.10.136>.
- (117) Jang, H. L.; Zhang, Y. S.; Khademhosseini, A. Boosting Clinical Translation of Nanomedicine. *Nanomed.* **2016**, *11* (12), 1495–1497. <https://doi.org/10.2217/nnm-2016-0133>.
- (118) Dobrovolskaia, M. A.; Aggarwal, P.; Hall, J. B.; McNeil, S. E. Preclinical Studies To Understand Nanoparticle Interaction with the Immune System and Its Potential Effects on Nanoparticle Biodistribution. *Mol. Pharm.* **2008**, *5* (4), 487–495. <https://doi.org/10.1021/mp800032f>.
- (119) Gimble, J. M.; Guilak, F.; Bunnell, B. A. Clinical and Preclinical Translation of Cell-Based Therapies Using Adipose Tissue-Derived Cells. *Stem Cell Res. Ther.* **2010**, *1* (2), 1–8. <https://doi.org/10.1186/scrt19>.
- (120) Gillet, J.-P.; Varma, S.; Gottesman, M. M. The Clinical Relevance of Cancer Cell Lines. *JNCI J. Natl. Cancer Inst.* **2013**, *105* (7), 452–458. <https://doi.org/10.1093/jnci/djt007>.
- (121) Karabasz, A.; Szczepanowicz, K.; Cierniak, A.; Bereta, J.; Bzowska, M. In Vitro Toxicity Studies of Biodegradable, Polyelectrolyte Nanocapsules. *Int. J. Nanomedicine* **2018**, *13*, 5159–5172. <https://doi.org/10.2147/IJN.S169120>.
- (122) Jain, A. K.; Singh, D.; Dubey, K.; Maurya, R.; Mittal, S.; Pandey, A. K. Chapter 3 - Models and Methods for In Vitro Toxicity. In *In Vitro Toxicology*; Dhawan, A., Kwon, S., Eds.; Academic Press, 2018; pp 45–65. <https://doi.org/10.1016/B978-0-12-804667-8.00003-1>.
- (123) Del Prado-Audelo, M. L.; Magaña, J. J.; Mejía-Contreras, B. A.; Borbolla-Jiménez, F. V.; Giraldo-Gomez, D. M.; Piña-Barba, M. C.; Quintanar-Guerrero, D.; Leyva-Gómez, G. In Vitro Cell Uptake Evaluation of Curcumin-Loaded PCL/F68 Nanoparticles for Potential Application in Neuronal Diseases. *J. Drug Deliv. Sci. Technol.* **2019**, *52*, 905–914. <https://doi.org/10.1016/j.jddst.2019.05.042>.
- (124) Albanese, A.; Chan, W. C. W. Effect of Gold Nanoparticle Aggregation on Cell Uptake and Toxicity. *ACS Nano* **2011**, *5* (7), 5478–5489. <https://doi.org/10.1021/nn2007496>.
- (125) Lu Senlin; Duffin Rodger; Poland Craig; Daly Paul; Murphy Fiona; Drost Ellen; MacNee William; Stone Vicki; Donaldson Ken. Efficacy of Simple Short-Term in Vitro Assays for Predicting the Potential of Metal Oxide Nanoparticles to Cause Pulmonary Inflammation. *Environ. Health Perspect.* **2009**, *117* (2), 241–247. <https://doi.org/10.1289/ehp.11811>.
- (126) Li, Y.; Liu, J.; Zhong, Y.; Zhang, J.; Wang, Z.; Wang, L.; An, Y.; Lin, M.; Gao, Z.; Zhang, D. Biocompatibility of Fe<sub>3</sub>O<sub>4</sub>@Au Composite Magnetic Nanoparticles in Vitro and in Vivo. *Int. J. Nanomedicine* **2011**, *6*, 2805–2819. <https://doi.org/10.2147/IJN.S24596>.
- (127) Zhang, D.; Luo, G.; Ding, X.; Lu, C. Preclinical Experimental Models of Drug Metabolism and Disposition in Drug Discovery and Development. *Acta Pharm. Sin. B* **2012**, *2* (6), 549–561. <https://doi.org/10.1016/j.apsb.2012.10.004>.

- (128) Moore, T. L.; Urban, D. A.; Rodriguez-Lorenzo, L.; Milosevic, A.; Crippa, F.; Spuch-Calvar, M.; Balog, S.; Rothen-Rutishauser, B.; Lattuada, M.; Petri-Fink, A. Nanoparticle Administration Method in Cell Culture Alters Particle-Cell Interaction. *Sci. Rep.* **2019**, *9* (1), 900. <https://doi.org/10.1038/s41598-018-36954-4>.
- (129) Yazdimamaghani, M.; Barber, Z. B.; Hadipour Moghaddam, S. P.; Ghandehari, H. Influence of Silica Nanoparticle Density and Flow Conditions on Sedimentation, Cell Uptake, and Cytotoxicity. *Mol. Pharm.* **2018**, *15* (6), 2372–2383. <https://doi.org/10.1021/acs.molpharmaceut.8b00213>.
- (130) Fede, C.; Fortunati, I.; Weber, V.; Rossetto, N.; Bertasi, F.; Petrelli, L.; Guidolin, D.; Signorini, R.; De Caro, R.; Albertin, G.; Ferrante, C. Evaluation of Gold Nanoparticles Toxicity towards Human Endothelial Cells under Static and Flow Conditions. *Microvasc. Res.* **2015**, *97*, 147–155. <https://doi.org/10.1016/j.mvr.2014.10.010>.
- (131) Rinkeauer, A. C.; Press, A. T.; Raasch, M.; Pietsch, C.; Schweizer, S.; Schwörer, S.; Rudolph, K. L.; Mosig, A.; Bauer, M.; Traeger, A.; Schubert, U. S. Comparison of the Uptake of Methacrylate-Based Nanoparticles in Static and Dynamic in Vitro Systems as Well as in Vivo. *J. Controlled Release* **2015**, *216*, 158–168. <https://doi.org/10.1016/j.jconrel.2015.08.008>.
- (132) Kapałczyńska, M.; Kolenda, T.; Przybyła, W.; Zajączkowska, M.; Teresiak, A.; Filas, V.; Ibbs, M.; Bliźniak, R.; Łuczewski, Ł.; Lamperska, K. 2D and 3D Cell Cultures – a Comparison of Different Types of Cancer Cell Cultures. *Arch. Med. Sci. AMS* **2018**, *14* (4), 910–919. <https://doi.org/10.5114/aoms.2016.63743>.
- (133) Smalley, K. S. M.; Lioni, M.; Herlyn, M. Life Isn't Flat: Taking Cancer Biology to the next Dimension. *Vitro Cell. Dev. Biol. - Anim.* **2006**, *42* (8), 242–247. <https://doi.org/10.1290/0604027.1>.
- (134) Snyder-Talkington, B. N.; Qian, Y.; Castranova, V.; Guo, N. L. New Perspectives for in Vitro Risk Assessment of Multiwalled Carbon Nanotubes: Application of Coculture and Bioinformatics. *J. Toxicol. Environ. Health Part B* **2012**, *15* (7), 468–492. <https://doi.org/10.1080/10937404.2012.736856>.
- (135) Kämpfer, A. A. M.; Urbán, P.; Gioria, S.; Kanase, N.; Stone, V.; Kinsner-Ovaskainen, A. Development of an in Vitro Co-Culture Model to Mimic the Human Intestine in Healthy and Diseased State. *Toxicol. In Vitro* **2017**, *45*, 31–43. <https://doi.org/10.1016/j.tiv.2017.08.011>.
- (136) Merkel, O. M.; Urbanics, R.; Bedőcs, P.; Rozsnyay, Z.; Rosivall, L.; Toth, M.; Kissel, T.; Szabenyi, J. In Vitro and in Vivo Complement Activation and Related Anaphylactic Effects Associated with Polyethylenimine and Polyethylenimine-Graft-Poly(Ethylene Glycol) Block Copolymers. *Biomaterials* **2011**, *32* (21), 4936–4942. <https://doi.org/10.1016/j.biomaterials.2011.03.035>.
- (137) Dobrovolskaia, M. A.; McNeil, S. E. Understanding the Correlation between in Vitro and in Vivo Immunotoxicity Tests for Nanomedicines. *J. Controlled Release* **2013**, *172* (2), 456–466. <https://doi.org/10.1016/j.jconrel.2013.05.025>.
- (138) Fan, J.; de Lannoy, I. A. M. Pharmacokinetics. *Biochem. Pharmacol.* **2014**, *87* (1), 93–120. <https://doi.org/10.1016/j.bcp.2013.09.007>.
- (139) Varna, M.; Ratajczak, P.; Ferreira, I.; Leboeuf, C.; Bousquet, G.; Janin, A. In Vivo Distribution of Inorganic Nanoparticles in Preclinical Models. **2012**, *2012*. <https://doi.org/10.4236/jbnb.2012.322033>.
- (140) Hrkach, J.; Hoff, D. V.; Ali, M. M.; Andrianova, E.; Auer, J.; Campbell, T.; Witt, D. D.; Figa, M.; Figueiredo, M.; Horhota, A.; Low, S.; McDonnell, K.; Peeke, E.; Retnarajan, B.; Sabnis, A.; Schnipper, E.; Song, J. J.; Song, Y. H.; Summa, J.; Tompsett, D.; Troiano, G.; Hoven, T. V. G.; Wright, J.; LoRusso, P.; Kantoff, P. W.; Bander, N. H.; Sweeney, C.; Farokhzad, O. C.; Langer, R.; Zale, S. Preclinical Development and Clinical Translation of a PSMA-Targeted Docetaxel

- Nanoparticle with a Differentiated Pharmacological Profile. *Sci. Transl. Med.* **2012**, *4* (128), 128ra39-128ra39. <https://doi.org/10.1126/scitranslmed.3003651>.
- (141) Simon-Yarza, T.; Mielcarek, A.; Couvreur, P.; Serre, C. Nanoparticles of Metal-Organic Frameworks: On the Road to In Vivo Efficacy in Biomedicine. *Adv. Mater.* **2018**, *30* (37), 1707365. <https://doi.org/10.1002/adma.201707365>.
- (142) Worp, H. B. van der; Howells, D. W.; Sena, E. S.; Porritt, M. J.; Rewell, S.; O'Collins, V.; Macleod, M. R. Can Animal Models of Disease Reliably Inform Human Studies? *PLOS Med.* **2010**, *7* (3), e1000245. <https://doi.org/10.1371/journal.pmed.1000245>.
- (143) Mak, I. W.; Evaniew, N.; Ghert, M. Lost in Translation: Animal Models and Clinical Trials in Cancer Treatment. *Am. J. Transl. Res.* **2014**, *6* (2), 114–118.
- (144) Denayer, T.; Stöhr, T.; Van Roy, M. Animal Models in Translational Medicine: Validation and Prediction. *New Horiz. Transl. Med.* **2014**, *2* (1), 5–11. <https://doi.org/10.1016/j.nhtm.2014.08.001>.
- (145) Hünig, T. The Storm Has Cleared: Lessons from the CD28 Superagonist TGN1412 Trial. *Nat. Rev. Immunol.* **2012**, *12* (5), 317–318. <https://doi.org/10.1038/nri3192>.
- (146) Hartung, T. Food for Thought Look Back in Anger – What Clinical Studies Tell Us About Preclinical Work. *ALTEX* **2013**, *30* (3), 275–291.
- (147) Perrin, S. Preclinical Research: Make Mouse Studies Work. *Nat. News* **2014**, *507* (7493), 423. <https://doi.org/10.1038/507423a>.
- (148) McGonigle, P.; Ruggeri, B. Animal Models of Human Disease: Challenges in Enabling Translation. *Biochem. Pharmacol.* **2014**, *87* (1), 162–171. <https://doi.org/10.1016/j.bcp.2013.08.006>.
- (149) Breslin, S.; O'Driscoll, L. Three-Dimensional Cell Culture: The Missing Link in Drug Discovery. *Drug Discov. Today* **2013**, *18* (5), 240–249. <https://doi.org/10.1016/j.drudis.2012.10.003>.
- (150) TissUse establishes a liver-endocrine tissues multi-organ model for risk assessment with Bayer <https://www.biospace.com/article/tissuse-establishes-a-liver-endocrine-tissues-multi-organ-model-for-risk-assessment-with-bayer/> (accessed Feb 18, 2021).
- (151) admin. TissUse Smart Hair Transplants in Japan. *Hair Loss Cure* **2020**, 2020.
- (152) Vahav, I.; Broek, L. J. van den; Thon, M.; Monsuur, H. N.; Spiekstra, S. W.; Atac, B.; Scheper, R. J.; Lauster, R.; Lindner, G.; Marx, U.; Gibbs, S. Reconstructed Human Skin Shows Epidermal Invagination towards Integrated Neopapillae Indicating Early Hair Follicle Formation in Vitro. *J. Tissue Eng. Regen. Med.* **2020**, *14* (6), 761–773. <https://doi.org/10.1002/term.3039>.
- (153) Petreus, T.; Cadogan, E.; Hughes, G.; Smith, A.; Reddy, V.; Lau, A.; O'Connor, M.; Critchlow, S.; Ashford, M.; O'Connor, L. O. A Novel Tumour-on-Chip Microfluidic Platform Advances Assessment of Drug Pharmacokinetics and Treatment Response; preprint; In Review, 2021. <https://doi.org/10.21203/rs.3.rs-121081/v1>.
- (154) Abbott, A. Biology's New Dimension. *Nature* **2003**, *424* (6951), 870–872. <https://doi.org/10.1038/424870a>.
- (155) Leong, D. T.; Ng, K. W. Probing the Relevance of 3D Cancer Models in Nanomedicine Research. *Adv. Drug Deliv. Rev.* **2014**, *79–80*, 95–106. <https://doi.org/10.1016/j.addr.2014.06.007>.
- (156) Si, L.; Bai, H.; Rodas, M.; Cao, W.; Oh, C. Y.; Jiang, A.; Moller, R.; Hoagland, D.; Oishi, K.; Horiuchi, S.; Uhl, S.; Blanco-Melo, D.; Albrecht, R. A.; Liu, W.-C.; Jordan, T.; Nilsson-Payant, B. E.; Logue, J.; Haupt, R.; McGrath, M.; Weston, S.; Nurani, A.; Kim, S. M.; Zhu, D. Y.; Benam, K. H.; Goyal, G.; Gilpin, S. E.; Prantil-Baun, R.; Powers, R. K.; Carlson, K.; Frieman, M.; tenOever, B. R.; Ingber, D. E. Human Organ Chip-Enabled Pipeline to Rapidly Repurpose Therapeutics during Viral Pandemics; preprint; Microbiology, 2020. <https://doi.org/10.1101/2020.04.13.039917>.
- (157) Caddeo, S.; Boffito, M.; Sartori, S. Tissue Engineering Approaches in the Design of Healthy and Pathological In Vitro Tissue Models. *Front. Bioeng. Biotechnol.* **2017**, *5*. <https://doi.org/10.3389/fbioe.2017.00040>.

- (158) Kishi, S.; Matsumoto, T.; Ichimura, T.; Brooks, C. R. Human Reconstructed Kidney Models. *Vitro Cell. Dev. Biol. - Anim.* **2021**. <https://doi.org/10.1007/s11626-021-00548-8>.
- (159) Astashkina, A. I.; Mann, B. K.; Prestwich, G. D.; Grainger, D. W. Comparing Predictive Drug Nephrotoxicity Biomarkers in Kidney 3-D Primary Organoid Culture and Immortalized Cell Lines. *Biomaterials* **2012**, *33* (18), 4712–4721. <https://doi.org/10.1016/j.biomaterials.2012.03.001>.
- (160) Borrell, B. How Accurate Are Cancer Cell Lines? *Nature* **2010**, *463* (7283), 858–858. <https://doi.org/10.1038/463858a>.
- (161) Pamies, D.; Bal-Price, A.; Chesné, C.; Coecke, S.; Dinnyes, A.; Eskes, C.; Grillari, R.; Gstraunthaler, G.; Hartung, T.; Jennings, P.; Leist, M.; Martin, U.; Passier, R.; Schwamborn, J. C.; Stacey, G. N.; Ellinger-Ziegelbauer, H.; Daneshian, M. Advanced Good Cell Culture Practice for Human Primary, Stem Cell-Derived and Organoid Models as Well as Microphysiological Systems. *ALTEX - Altern. Anim. Exp.* **2018**, *35* (3), 353–378. <https://doi.org/10.14573/altex.1710081>.
- (162) Pan, C.; Kumar, C.; Bohl, S.; Klingmueller, U.; Mann, M. Comparative Proteomic Phenotyping of Cell Lines and Primary Cells to Assess Preservation of Cell Type-Specific Functions. *Mol. Cell. Proteomics* **2009**, *8* (3), 443–450. <https://doi.org/10.1074/mcp.M800258-MCP200>.
- (163) Kaur, G.; Dufour, J. M. Cell Lines. *Spermatogenesis* **2012**, *2* (1), 1–5. <https://doi.org/10.4161/spmg.19885>.
- (164) Rowe, R. G.; Daley, G. Q. Induced Pluripotent Stem Cells in Disease Modelling and Drug Discovery. *Nat. Rev. Genet.* **2019**, *20* (7), 377–388. <https://doi.org/10.1038/s41576-019-0100-z>.
- (165) Bezenah, J. R.; Kong, Y. P.; Putnam, A. J. Evaluating the Potential of Endothelial Cells Derived from Human Induced Pluripotent Stem Cells to Form Microvascular Networks in 3D Cultures. *Sci. Rep.* **2018**, *8* (1), 2671. <https://doi.org/10.1038/s41598-018-20966-1>.
- (166) Moysidou, C.-M.; Barberio, C.; Owens, R. M. Advances in Engineering Human Tissue Models. *Front. Bioeng. Biotechnol.* **2020**, *8*, 620962. <https://doi.org/10.3389/fbioe.2020.620962>.
- (167) Baker, B. M.; Chen, C. S. Deconstructing the Third Dimension: How 3D Culture Microenvironments Alter Cellular Cues. *J. Cell Sci.* **2012**, *125* (Pt 13), 3015–3024. <https://doi.org/10.1242/jcs.079509>.
- (168) Kleinman, H. K.; Martin, G. R. Matrigel: Basement Membrane Matrix with Biological Activity. *Semin. Cancer Biol.* **2005**, *15* (5), 378–386. <https://doi.org/10.1016/j.semcancer.2005.05.004>.
- (169) Lee, S. H.; Shim, K. Y.; Kim, B.; Sung, J. H. Hydrogel-Based Three-Dimensional Cell Culture for Organ-on-a-Chip Applications. *Biotechnol. Prog.* **2017**, *33* (3), 580–589. <https://doi.org/10.1002/btpr.2457>.
- (170) Huang, G.; Li, F.; Zhao, X.; Ma, Y.; Li, Y.; Lin, M.; Jin, G.; Lu, T. J.; Genin, G. M.; Xu, F. Functional and Biomimetic Materials for Engineering of the Three-Dimensional Cell Microenvironment. *Chem. Rev.* **2017**, *117* (20), 12764–12850. <https://doi.org/10.1021/acs.chemrev.7b00094>.
- (171) Huh, D.; Matthews, B. D.; Mammoto, A.; Montoya-Zavala, M.; Hsin, H. Y.; Ingber, D. E. Reconstituting Organ-Level Lung Functions on a Chip. *Science* **2010**, *328* (5986), 1662–1668. <https://doi.org/10.1126/science.1188302>.
- (172) Hassell, B. A.; Goyal, G.; Lee, E.; Sontheimer-Phelps, A.; Levy, O.; Chen, C. S.; Ingber, D. E. Human Organ Chip Models Recapitulate Orthotopic Lung Cancer Growth, Therapeutic Responses, and Tumor Dormancy In Vitro. *Cell Rep.* **2017**, *21* (2), 508–516. <https://doi.org/10.1016/j.celrep.2017.09.043>.
- (173) Xu, Z.; Li, E.; Guo, Z.; Yu, R.; Hao, H.; Xu, Y.; Sun, Z.; Li, X.; Lyu, J.; Wang, Q. Design and Construction of a Multi-Organ Microfluidic Chip Mimicking the in Vivo Microenvironment of Lung Cancer Metastasis. *ACS Appl. Mater. Interfaces* **2016**, *8* (39), 25840–25847. <https://doi.org/10.1021/acsami.6b08746>.
- (174) Jalili-Firoozinezhad, S.; Gazzaniga, F. S.; Calamari, E. L.; Camacho, D. M.; Fadel, C. W.; Bein, A.; Swenor, B.; Nestor, B.; Cronce, M. J.; Tovaglieri, A.; Levy, O.; Gregory, K. E.; Breault, D. T.; Cabral,

- J. M. S.; Kasper, D. L.; Novak, R.; Ingber, D. E. A Complex Human Gut Microbiome Cultured in an Anaerobic Intestine-on-a-Chip. *Nat. Biomed. Eng.* **2019**, *3* (7), 520–531. <https://doi.org/10.1038/s41551-019-0397-0>.
- (175) Ashammakhi, N.; Nasiri, R.; Barros, N. R. de; Tebon, P.; Thakor, J.; Goudie, M.; Shamloo, A.; Martin, M. G.; Khademhosseini, A. Gut-on-a-Chip: Current Progress and Future Opportunities. *Biomaterials* **2020**, *255*, 120196. <https://doi.org/10.1016/j.biomaterials.2020.120196>.
- (176) Kim, H. J.; Huh, D.; Hamilton, G.; Ingber, D. E. Human Gut-on-a-Chip Inhabited by Microbial Flora That Experiences Intestinal Peristalsis-like Motions and Flow. *Lab. Chip* **2012**, *12* (12), 2165–2174. <https://doi.org/10.1039/C2LC40074J>.
- (177) Vickerman, V.; Blundo, J.; Chung, S.; Kamm, R. Design, Fabrication and Implementation of a Novel Multi-Parameter Control Microfluidic Platform for Three-Dimensional Cell Culture and Real-Time Imaging. *Lab. Chip* **2008**, *8* (9), 1468–1477. <https://doi.org/10.1039/b802395f>.
- (178) Zervantonakis, I. K.; Hughes-Alford, S. K.; Charest, J. L.; Condeelis, J. S.; Gertler, F. B.; Kamm, R. D. Three-Dimensional Microfluidic Model for Tumor Cell Intravasation and Endothelial Barrier Function. *Proc. Natl. Acad. Sci.* **2012**, *109* (34), 13515–13520. <https://doi.org/10.1073/pnas.1210182109>.
- (179) Jeon, J. S.; Zervantonakis, I. K.; Chung, S.; Kamm, R. D.; Charest, J. L. In Vitro Model of Tumor Cell Extravasation. *PLOS ONE* **2013**, *8* (2), e56910. <https://doi.org/10.1371/journal.pone.0056910>.
- (180) Truong, D.; Puleo, J.; Llave, A.; Mouneimne, G.; Kamm, R. D.; Nikkhah, M. Breast Cancer Cell Invasion into a Three Dimensional Tumor-Stroma Microenvironment. *Sci. Rep.* **2016**, *6*, 34094. <https://doi.org/10.1038/srep34094>.
- (181) Kim, M.-C.; Whisler, J.; Silberberg, Y. R.; Kamm, R. D.; Asada, H. H. Cell Invasion Dynamics into a Three Dimensional Extracellular Matrix Fibre Network. *PLOS Comput. Biol.* **2015**, *11* (10), e1004535. <https://doi.org/10.1371/journal.pcbi.1004535>.
- (182) Kalchman, J.; Fujioka, S.; Chung, S.; Kikkawa, Y.; Mitaka, T.; Kamm, R. D.; Tanishita, K.; Sudo, R. A Three-Dimensional Microfluidic Tumor Cell Migration Assay to Screen the Effect of Anti-Migratory Drugs and Interstitial Flow. *Microfluid. Nanofluidics* **2013**, *14* (6), 969–981. <https://doi.org/10.1007/s10404-012-1104-6>.
- (183) Jeong, G. S.; Han, S.; Shin, Y.; Kwon, G. H.; Kamm, R. D.; Lee, S.-H.; Chung, S. Sprouting Angiogenesis under a Chemical Gradient Regulated by Interactions with an Endothelial Monolayer in a Microfluidic Platform. *Anal. Chem.* **2011**, *83* (22), 8454–8459. <https://doi.org/10.1021/ac202170e>.
- (184) Farahat, W. A.; Wood, L. B.; Zervantonakis, I. K.; Schor, A.; Ong, S.; Neal, D.; Kamm, R. D.; Asada, H. H. Ensemble Analysis of Angiogenic Growth in Three-Dimensional Microfluidic Cell Cultures. *PLOS ONE* **2012**, *7* (5), e37333. <https://doi.org/10.1371/journal.pone.0037333>.
- (185) Ko, J.; Ahn, J.; Kim, S.; Lee, Y.; Lee, J.; Park, D.; Jeon, N. L. Tumor Spheroid-on-a-Chip: A Standardized Microfluidic Culture Platform for Investigating Tumor Angiogenesis. *Lab. Chip* **2019**, *19* (17), 2822–2833. <https://doi.org/10.1039/C9LC00140A>.
- (186) Nashimoto, Y.; Okada, R.; Hanada, S.; Arima, Y.; Nishiyama, K.; Miura, T.; Yokokawa, R. Vascularized Cancer on a Chip: The Effect of Perfusion on Growth and Drug Delivery of Tumor Spheroid. *Biomaterials* **2020**, *229*, 119547. <https://doi.org/10.1016/j.biomaterials.2019.119547>.
- (187) Ho, Y. T.; Adriani, G.; Beyer, S.; Nhan, P.-T.; Kamm, R. D.; Kah, J. C. Y. A Facile Method to Probe the Vascular Permeability of Nanoparticles in Nanomedicine Applications. *Sci. Rep.* **2017**, *7* (1), 707. <https://doi.org/10.1038/s41598-017-00750-3>.
- (188) Tang, Y.; Soroush, F.; Sheffield, J. B.; Wang, B.; Prabhakarandian, B.; Kiani, M. F. A Biomimetic Microfluidic Tumor Microenvironment Platform Mimicking the EPR Effect for Rapid Screening of Drug Delivery Systems. *Sci. Rep.* **2017**, *7* (1), 9359. <https://doi.org/10.1038/s41598-017-09815-9>.

- (189) Young, E. W. K.; Watson, M. W. L.; Srigunapalan, S.; Wheeler, A. R.; Simmons, C. A. Technique for Real-Time Measurements of Endothelial Permeability in a Microfluidic Membrane Chip Using Laser-Induced Fluorescence Detection. *Anal. Chem.* **2010**, *82* (3), 808–816. <https://doi.org/10.1021/ac901560w>.
- (190) Griffith, L. G.; Swartz, M. A. Capturing Complex 3D Tissue Physiology in Vitro. *Nat. Rev. Mol. Cell Biol.* **2006**, *7* (3), 211–224. <https://doi.org/10.1038/nrm1858>.
- (191) Xu, X.; Farach-Carson, M. C.; Jia, X. Three-Dimensional in Vitro Tumor Models for Cancer Research and Drug Evaluation. *Biotechnol. Adv.* **2014**, *32* (7), 1256–1268. <https://doi.org/10.1016/j.biotechadv.2014.07.009>.
- (192) Ng, C. P.; Pun, S. H. A Perfusable 3D Cell–Matrix Tissue Culture Chamber for in Situ Evaluation of Nanoparticle Vehicle Penetration and Transport. *Biotechnol. Bioeng.* **2008**, *99* (6), 1490–1501. <https://doi.org/10.1002/bit.21698>.
- (193) Albanese, A.; Lam, A. K.; Sykes, E. A.; Rocheleau, J. V.; Chan, W. C. W. Tumour-on-a-Chip Provides an Optical Window into Nanoparticle Tissue Transport. *Nat. Commun.* **2013**, *4*, 2718. <https://doi.org/10.1038/ncomms3718>.
- (194) Lazzari, G.; Couvreur, P.; Mura, S. Multicellular Tumor Spheroids: A Relevant 3D Model for the in Vitro Preclinical Investigation of Polymer Nanomedicines. *Polym. Chem.* **2017**, *8* (34), 4947–4969. <https://doi.org/10.1039/C7PY00559H>.
- (195) Sindhvani, S.; Syed, A. M.; Ngai, J.; Kingston, B. R.; Maiorino, L.; Rothschild, J.; MacMillan, P.; Zhang, Y.; Rajesh, N. U.; Hoang, T.; Wu, J. L. Y.; Wilhelm, S.; Zilman, A.; Gadde, S.; Sulaiman, A.; Ouyang, B.; Lin, Z.; Wang, L.; Egeblad, M.; Chan, W. C. W. The Entry of Nanoparticles into Solid Tumours. *Nat. Mater.* **2020**. <https://doi.org/10.1038/s41563-019-0566-2>.
- (196) Wang, H.-F.; Ran, R.; Liu, Y.; Hui, Y.; Zeng, B.; Chen, D.; Weitz, D. A.; Zhao, C.-X. Tumor-Vasculature-on-a-Chip for Investigating Nanoparticle Extravasation and Tumor Accumulation. *ACS Nano* **2018**, *12* (11), 11600–11609. <https://doi.org/10.1021/acsnano.8b06846>.
- (197) Chen, Y.; Gao, D.; Wang, Y.; Lin, S.; Jiang, Y. A Novel 3D Breast-Cancer-on-Chip Platform for Therapeutic Evaluation of Drug Delivery Systems. *Anal. Chim. Acta* **2018**, *1036*, 97–106. <https://doi.org/10.1016/j.aca.2018.06.038>.
- (198) Shin, Y.; Han, S.; Jeon, J. S.; Yamamoto, K.; Zervantonakis, I. K.; Sudo, R.; Kamm, R. D.; Chung, S. Microfluidic Assay for Simultaneous Culture of Multiple Cell Types on Surfaces or within Hydrogels. *Nat. Protoc.* **2012**, *7* (7), 1247–1259. <https://doi.org/10.1038/nprot.2012.051>.
- (199) Zhang, B.; Korolj, A.; Lai, B. F. L.; Radisic, M. Advances in Organ-on-a-Chip Engineering. *Nat. Rev. Mater.* **2018**, *3* (8), 257–278. <https://doi.org/10.1038/s41578-018-0034-7>.
- (200) Henry, O. Y. F.; Villenave, R.; Crouce, M. J.; Leineweber, W. D.; Benz, M. A.; Ingber, D. E. Organs-on-Chips with Integrated Electrodes for Trans-Epithelial Electrical Resistance (TEER) Measurements of Human Epithelial Barrier Function. *Lab. Chip* **2017**, *17* (13), 2264–2271. <https://doi.org/10.1039/C7LC00155J>.
- (201) Nguyen, T. A.; Yin, T.-I.; Reyes, D.; Urban, G. A. Microfluidic Chip with Integrated Electrical Cell-Impedance Sensing for Monitoring Single Cancer Cell Migration in Three-Dimensional Matrixes. *Anal. Chem.* **2013**, *85* (22), 11068–11076. <https://doi.org/10.1021/ac402761s>.
- (202) Velasco, V.; Joshi, K.; Chen, J.; Esfandyarpour, R. Personalized Drug Efficacy Monitoring Chip. *Anal. Chem.* **2019**, *91* (23), 14927–14935. <https://doi.org/10.1021/acs.analchem.9b03291>.
- (203) Liu, M.-C.; Shih, H.-C.; Wu, J.-G.; Weng, T.-W.; Wu, C.-Y.; Lu, J.-C.; Tung, Y.-C. Electrofluidic Pressure Sensor Embedded Microfluidic Device: A Study of Endothelial Cells under Hydrostatic Pressure and Shear Stress Combinations. *Lab. Chip* **2013**, *13* (9), 1743–1753. <https://doi.org/10.1039/C3LC41414K>.

- (204) Weltin, A.; Slotwinski, K.; Kieninger, J.; Moser, I.; Jobst, G.; Wego, M.; Ehret, R.; A. Urban, G. Cell Culture Monitoring for Drug Screening and Cancer Research: A Transparent, Microfluidic, Multi-Sensor Microsystem. *Lab. Chip* **2014**, *14* (1), 138–146. <https://doi.org/10.1039/C3LC50759A>.
- (205) Bavli, D.; Prill, S.; Ezra, E.; Levy, G.; Cohen, M.; Vinken, M.; Vanfleteren, J.; Jaeger, M.; Nahmias, Y. Real-Time Monitoring of Metabolic Function in Liver-on-Chip Microdevices Tracks the Dynamics of Mitochondrial Dysfunction. *Proc. Natl. Acad. Sci.* **2016**, *113* (16), E2231–E2240. <https://doi.org/10.1073/pnas.1522556113>.
- (206) Bhatia, S. N.; Ingber, D. E. Microfluidic Organs-on-Chips. *Nat. Biotechnol.* **2014**, *32* (8), 760–772. <https://doi.org/10.1038/nbt.2989>.



## Chapter 2 | Formulation of tunable size PLGA-PEG drug nanocarriers using microfluidic technology

*This chapter reproduces almost literally the article: **Formulation of tunable size PLGA-PEG nanoparticles for drug delivery using microfluidic technology**, submitted to PLOS One, 2021, status: submitted, by Adrianna Glinkowska Mares, Gaia Pacassoni, Josep Samitier Marti, Silvia Pujals, Lorenzo Albertazzi. My contribution to this manuscript was the execution of experimental part, design of experiments and writing the manuscript. G. Pacassoni contributed to the experimental part and data analysis. S. Pujals and L. Albertazzi supervised the work and contributed to experimental planning. J. Samitier, S. Pujals and L. Albertazzi provided periodic feedback on the results and reviewed the manuscript.*

*This chapter presents a study on self-assembly of amphiphilic di-block copolymers (PLGA-PEG) performed in a microfluidic hydrodynamic flow focusing chip. Here, the main focus was placed on particle size tunability upon formulation in the microfluidic chip. The study comparing traditional manual bulk mixing and microfluidic process was executed, yielding monodisperse nanoparticles in both cases. The particles were further characterized using bulk methods and single particle advanced microscopy techniques. Drug/dye encapsulation into the nanocarriers was evaluated with three different molecules for both formulation procedures. Additionally, the NPs were tested in vitro to assess their biological performance.*

## 2.1 Introduction

Since more than three decades polymeric nanoparticles (NPs) are investigated as drug delivery systems (DDSs) for treatment of several diseases with a focus on cancer.<sup>1-6</sup> They carry a promise of improved therapeutic effect thanks to their unique properties, such as size, shape, porosity, charge or modifiable surface.<sup>7-10</sup> One of the key features of a nanocarrier is the nanoscale size that promotes escape through small gateways, such as the gaps in tumorous vasculature, that are the fundament of passive drug delivery design.<sup>11,12</sup> Furthermore, the NP surface can be modified to limit the adsorption of proteins, to eventually minimize the uptake by immune cells and provide longer circulation.<sup>13,14</sup> Importantly, polymeric nanocarriers can encapsulate various therapeutic molecules, sensitive to the physiological conditions, where they would be prematurely deactivated or could cause undesired cytotoxicity.<sup>15,16</sup> Another advantage of drug encapsulation is the improved bioavailability of poorly water-soluble compounds, which are the majority of active pharmaceutical ingredients.<sup>17,18</sup> Encapsulated payload can be released in a controlled way upon the degradation of the nanocarrier's polymeric matrix, offering sustainable delivery of the drug, what is important for a positive therapeutic effect.<sup>19,20</sup> Additionally, the NPs can actively target specific sites thanks to the surface functionalization with targeting ligands, which was confirmed *in vitro* and *in vivo*.<sup>21-23</sup> This approach leads to more efficient biodistribution and potentially lower toxicity or side effects. The combination of these features creates a promising drug delivery system with improved pharmacokinetics and better therapeutic outcome comparing to the currently available solutions.<sup>24</sup>

One of the most studied polymers in drug delivery is Poly(lactic-co-glycolic) acid (PLGA), which has already been FDA- and EMA-approved for various applications.<sup>25,26</sup> PLGA breaks down to the lactic and glycolic acids, ensuring the biocompatibility and biodegradability required for safe use in humans.<sup>27,28</sup> The tunability of the lactic to glycolic acid ratio and the polymer chain length, allow to adjust the polymer matrix degradation providing controlled drug release, ranging from days to years.<sup>27,29</sup> The summary of PLGA properties makes it the most versatile polymer in parenterally administered drug delivery systems, currently used in the form of emulsions, microparticles and implants.<sup>30-32</sup>

In the course of PLGA-based achievements in the field of drug delivery, it naturally became engaged in the development of a nanoparticle based systems. Block copolymers, such as PLGA with polyethylene glycol (PEG) are widely used to formulate NPs. The conjugated PEG allows to minimize the use of formulation stabilizers and importantly, it decreases the formation of protein corona after administration and results in extended systemic circulation of the NPs.<sup>33-36</sup> Furthermore, the PEG chain terminated with targeting ligands, demonstrated positive results in *in vitro* studies.<sup>22,37</sup>

The PLGA-PEG amphiphilic di-block copolymer can be folded into NPs via self-assembly, by addition of the polymer solution into a miscible antisolvent (AS). In this process the PLGA-PEG solubility suddenly

decreases and it starts to precipitate, forming kinetically frozen NPs.<sup>38-40</sup> Therefore in the nanoprecipitation method, the uniform mixing of both liquids is crucial to obtain homogenous NPs.<sup>41-43</sup> Ideally, the process should be robust and reproducible to control the NP properties, which later dictate their fate in human body and determine success of the DDS.

In the last two decades microfluidic technology appeared as an interesting alternative in the formulation of NPs. In contrary to the manual bulk mixing method, it offers precise and homogenous mixing of the polymer solution with the antisolvent phase.<sup>44-48</sup> This approach uses microfluidic chips similar to these known for microparticle formation.<sup>49-52</sup> It is based on the laminar flow of the liquids confined in the microchannels and results in hydrodynamic flow focusing (HFF) of the solvent (S) phase. The restricted volume allows to limit the diffusion distance of solvent and antisolvent, therefore it regulates the mixing of the two liquids that can be further controlled by modification of stream flow rates or chip design.<sup>53-56</sup> The fine control over this process results in tunability of the NP properties, such as its size, surface characteristics or crystallinity.<sup>57-59</sup> It reduces batch-to-batch variability and enables the investigation on how the NPs properties can be tailored upon formulation parameters, what was not possible within the bulk mixing method.<sup>45,60,61</sup> Another advantage in the use of microfluidic chips is the possibility of simulations of fluid dynamics by computational methods. The diffusion can be visualized to better understand process parameters and to improve the experimental planning.<sup>62,63</sup>

Taking into account the successfulness of PLGA in DDS, the rapidly developing microfluidic technology was quickly introduced into the formulation of PLGA micor- and nanoparticles. Different chip geometries, formulation compounds and PLGA conjugates were explored, demonstrating improved control over the particle properties and resulting in various sophisticated PLGA-based nanocarrier systems.<sup>64-66</sup>

In our work we investigated the impact of the microfluidic chip assisted HFF nanoprecipitation on the particle size tunability and cargo loading in comparison to the manual bulk mixing method. We performed surfactant-/stabilizer-free formulation of PLGA-PEG NPs in a microfluidic chip at different S and AS flow rates, and by a manual dropwise addition of the S to the AS phase at parallel volumes. We studied encapsulation efficiency of fluorescent molecules with different hydrophobicity. Obtained NPs were characterized using bulk and single-particle methods for general and more detailed information. Our data confirmed that the particle diameter can be tailored and controlled with the use of microfluidic chip in the formulation process. The advanced microscopy techniques used to characterize single NPs allowed us to reveal heterogeneities present in the batches and indicated more homogenous dye loading in the HFF-formulated NPs. Furthermore, the bioevaluation of NPs obtained via microfluidic formulation demonstrated cell internalization and biocompatibility.

## 2.2 Microfluidic hydrodynamic flow focusing and manual bulk formulation

Particles were formulated via nanoprecipitation method, using manual dropwise addition in bulk mixing and a microfluidic setup facilitating hydrodynamic flow focusing (Figure 2.1a and 2.1b, respectively). The polymer was dissolved in acetonitrile (ACN), an organic solvent miscible with water, which was the antisolvent for PLGA-PEG.<sup>67</sup> The diffusion of ACN into water reduces solubility of the polymer and, as a response to this change of environment, the amphiphilic blocks rapidly self-assemble into NPs. In this process the PLGA blocks concentrate in the core of the NP and most of the PEG chains are exposed on the surface, forming the corona,<sup>40</sup> as schematically The PLGA blocks concentrate in the core of the NP and most of the PEG chains are exposed on the surface, forming the corona,<sup>40</sup> as schematically illustrated in the

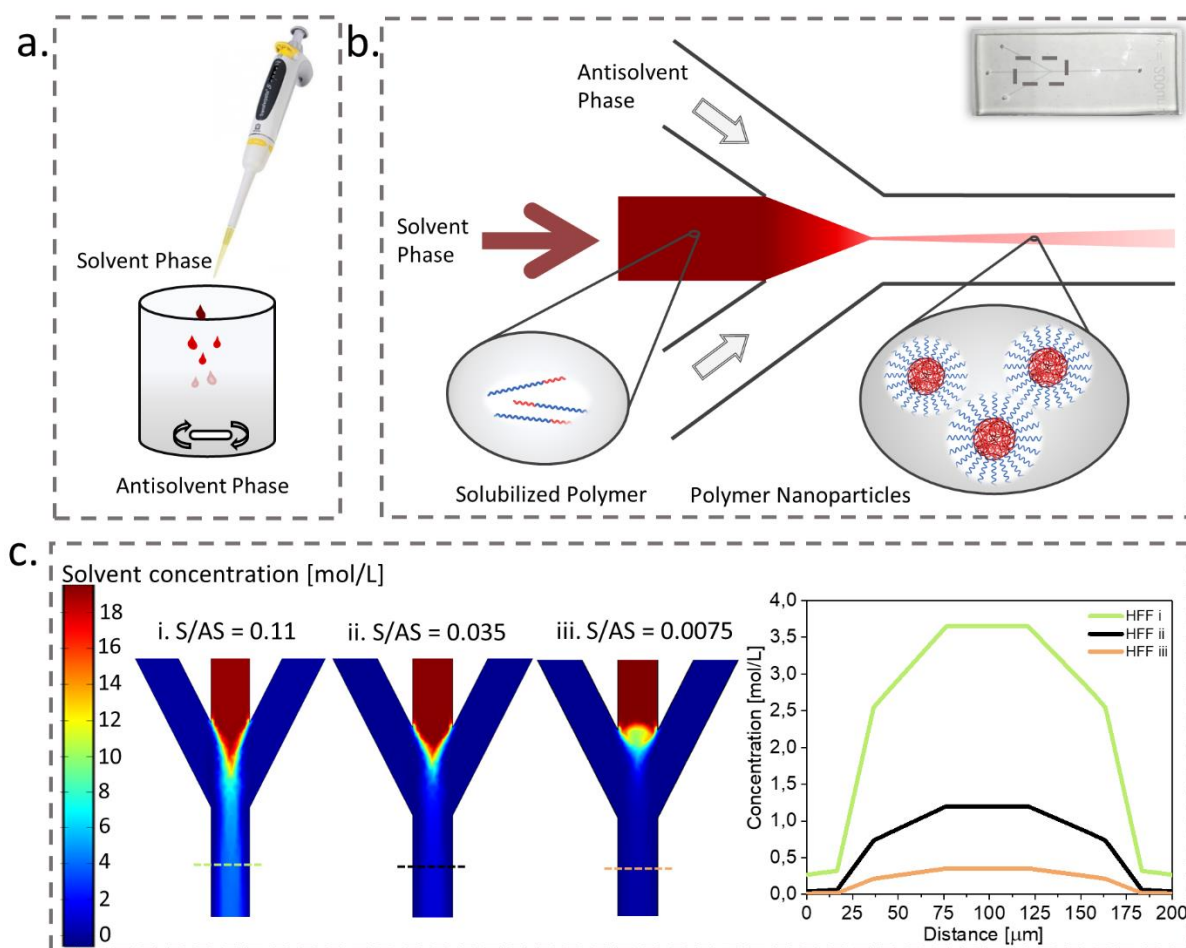


Figure 2.1 Formulation of nanoparticles via nanoprecipitation a. manual bulk mixing, b. hydrodynamic flow focusing, c. fluid dynamics simulation for three different S/AS and the solvent concentration (i-iii) at the outlet cross-section 0,3 mm below the junction (marked by the dashed line in the simulations on the left).

Figure 2.1b. The nanoparticle formation is divided into three phases: nucleation, growth, and aggregation. The pivotal role in the output of nanoprecipitation plays the mixing, responsible for homogenous supersaturation inducing polymer nucleation. Poorer mixing results in low nucleation rate and a growth of

larger particles because the polymer aggregation occurs in the presence of higher fractions of organic solvent ( $\tau_{\text{mix}} > \tau_{\text{agg}}$ ) and, if mixing occurs faster than the time scale for aggregation ( $\tau_{\text{mix}} < \tau_{\text{agg}}$ ), the aggregation phase takes place when mixing is almost complete and more nuclei are formed.<sup>68-70</sup>

Microfluidic chips are tools, that can aid spatial and temporal separation of the above-mentioned three phases of particle formation.<sup>68</sup> In our setup the main part is the chip with three inlets and one outlet (microchannels of 200  $\mu\text{m}$  width and 60  $\mu\text{m}$  height) connected to a syringe pump with a capillary tubing. We injected the solvent phase into the central inlet and controlled its stream width (at the outlet) by the flow rate of laterally injected antisolvent, as illustrated in the Figure 2.1b. Changes in the AS flow rate resulted in a range of solvent to antisolvent flow ratios, and the faster the lateral flow rate, the narrower the central stream and smaller the diffusion distance. To visually demonstrate it, we employed computational fluid dynamics (CFD) using parameters corresponding to water and ACN for the AS and S phase. The Figure 2.1c illustrates the impact of changing the AS flow rate in the microchip inlets on the solvent concentration gradient in the outlet channel. With the decrease of S/AS, we can observe significant decrease of the solvent concentration right after the junction of the inlet channels. As a result of narrowing the solvent stream, with the increase of AS flow rate, the solvent diffusion can occur more rapidly and promote faster mixing of the two miscible liquids.

### 2.3 Particle diameter tunability using microfluidic chip

The particle size resulting in the nanoprecipitation process is dictated by the mixing of S and AS phase. Faster mixing of the two phases leads to a locally lower fractions of organic solvent, what yields smaller NPs, as the forming clusters are kinetically locked in the non-solvent environment.<sup>69,70</sup> To probe the formulation of size-tailored NPs, resulting from the controlled diffusion of S into the AS phase, we used the above-described chip and manual droplet addition in a bulk mixing for the control. We formulated the NPs with the microfluidic device using the constant flow rate of 5  $\mu\text{L}/\text{min}$  for the polymer solution and an adjustable lateral inflow of the AS, ranging from 20 to 330  $\mu\text{L}/\text{min}$ , and resulting in the S/AS ratios between 0.0075 to 0.11. Within these parameters we calculated the mixing time  $\tau_{\text{mix}}$  in our system, which should be lesser than the aggregation time  $\tau_{\text{agg}}$  to control the particle size. We found values from 0.25 ms to 44 ms for the extremes of the tested S/AS from the following equation (for  $D = 10^{-9} \text{ m}^2/\text{s}$  and  $w = 200 \mu\text{m}$  and used R flow ratios (0.0075 – 0.11) which are lower than estimated unimer penetration time leading to aggregation.<sup>71</sup>

$$\tau_{\text{mix}} \sim \frac{w_f^2}{4D} \approx \frac{w^2}{9D} \frac{1}{\left(1 + \frac{1}{R}\right)^2}$$

To compare the HFF results with the bulk nanoprecipitation method, we formulated the NPs by manual addition of the solvent phase into the antisolvent, controlling the mixed volumes to achieve comparable S and AS final volumes in both approaches. Next, we measured the NPs diameter using dynamic light scattering (DLS) and imaged them with negative-staining transmission electron microscopy (TEM). The results of the DLS measurement shown in the Figure 2.2a demonstrated how the ratio of the S and AS phase flow dictates the particle hydrodynamic diameter. The lower the S/AS flow rate, the smaller the NPs size, ranging here from 44 to 97 nm. In the manual dropwise addition process we obtained particles in size of 71 to 89 nm, with only a slight diameter change in response to the S/AS volume modifications. The HFF formulation allowed to obtain even 50% smaller NPs comparing to the dropwise addition process and importantly, it permitted to tune the size of the NPs in the response to the S/AS flow ratio, what corresponds to the particle size tunability in response to the flow parameters reported in the literature.<sup>51,60,65</sup> We performed similar HFF experiment with higher absolute solvent flow rate ( $S_{\text{flow rate}} = 15 \mu\text{L}/\text{min}$ ) to check if the size tailoring trend is maintained at different flow rate values. However, the increase of corresponding AS flow rates (to maintain the same S/AS ratio as tested with the  $S_{\text{flow rate}} = 5 \mu\text{L}/\text{min}$ ) was not suitable for our chip, due to its integrity loss resulting from too high total flow rates. Nevertheless, the hydrodynamic diameter of NPs formulated with S flow rate of  $15 \mu\text{L}/\text{min}$  at a narrower range followed the same pattern as the NPs diameter formulated with S flow rate of  $5 \mu\text{L}/\text{min}$ , as it is shown in Figure 2.2a. All the performed formulations yielded monodisperse NPs with the polydispersity index (PDI) in the range of 0,06 – 0,15. Overall, we used two methods of nanoprecipitation-based particle formulation and we were able to achieve a broader range of NPs sizes using the microfluidic chip. This approach demonstrated how the particle size can be tuned (44 – 97 nm for HFF comparing to 71 – 89 nm for manual formulation) without modifying the copolymer molecular weight or other chemical or physical properties. It is especially important to control the particle size, as their biodistribution and cellular uptake depends on this feature.<sup>35,72</sup> DLS measurement rapidly provides the information about an average hydrodynamic diameter and dispersity of a batch, however it does not reveal details of a single NP. To look at the individual particle's size and its distribution we used transmission electron microscopy (TEM). The particles were deposited on carbon grids with uranyl acetate negative staining, dried and imaged. We measured the diameter of a minimum 200 particles for each batch and compared the results of formulations with different S/AS flow ratios, as well as between the two methods used for nanoprecipitation as demonstrated in Figure 2.2b and 2.2c. The analysis on the single particle level demonstrated the same trend as the hydrodynamic size measurement with the DLS, confirming the size tunability achieved with the microfluidic device, with the average particle diameter of 35 nm, 44 nm and 50 nm for the S/AS flow ratio of: 0,0075; 0,036; and 0,115, respectively. We found the NP average diameter values smaller for TEM image-based measurement than for the DLS method, which can be explained by the technique differences (DLS measures hydrodynamic

diameter in suspension, meanwhile in TEM images we measured the gyration radius of dried particles). Nevertheless, the TEM analysis was coherent with previously observed DLS measurement-based trend. The average diameter of NPs formulated using the microfluidic device was dependent on the S/AS flow ratio, yielding smaller size at lower S/AS. Additionally, the TEM images helped us to visualize the heterogeneity among the particles, in the Figure 2.2c (bottom row), we could identify particles in a range

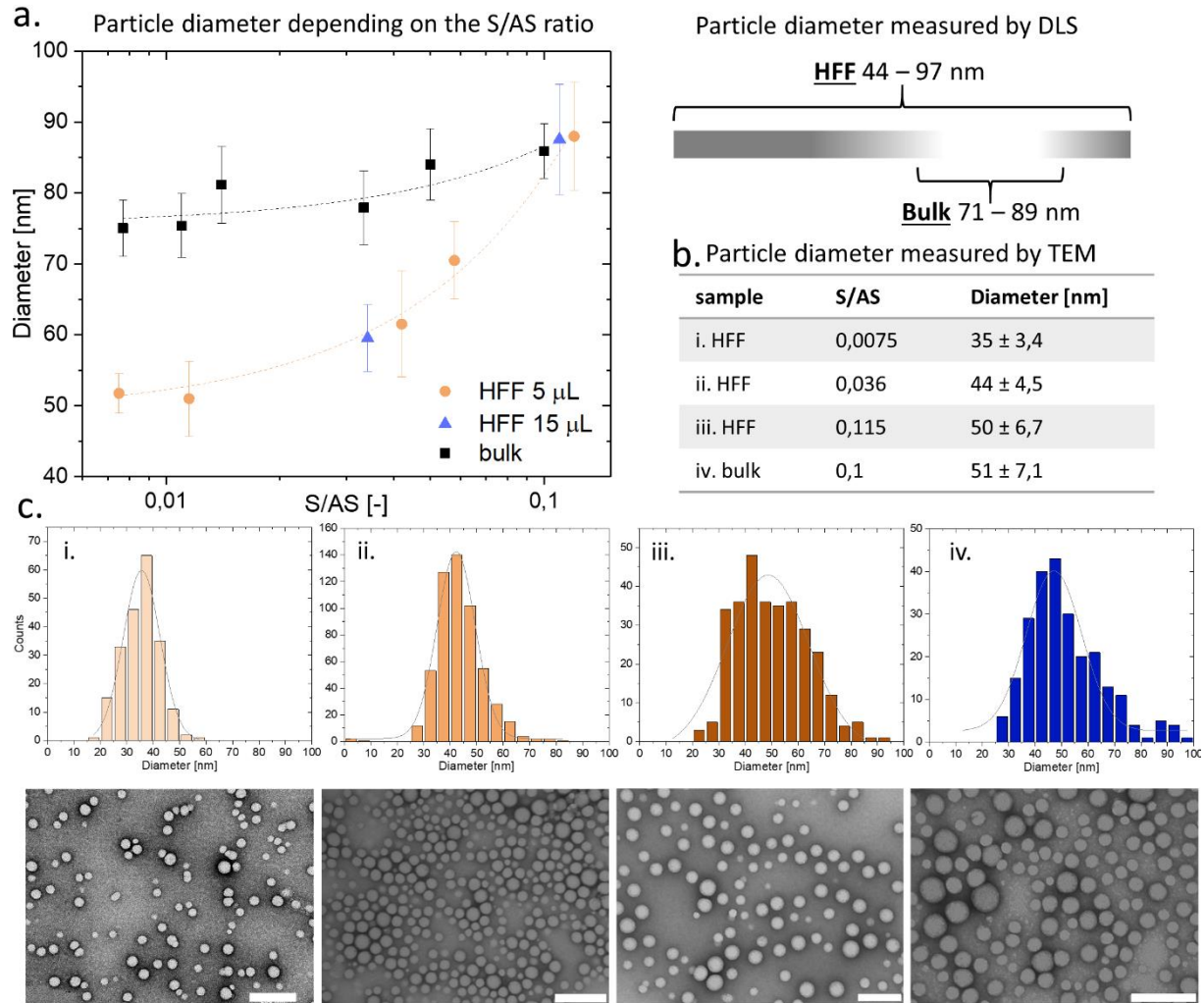


Figure 2.2 a. Particle diameter measured by DLS, (left) represented in the function of the S/AS flow ratio and (right) schematically illustrated dependency on the formulation method (bulk and HFF – hydrodynamic flow focusing); b. table with an average particle diameter obtained from analysis of TEM images; c. Particle size distribution obtained from TEM analysis (top row) and the corresponding TEM images (bottom row), scale bar 200 nm.

of 15 – 60 nm (in batch i), meanwhile the average size was 35 nm, however the dispersity of each batch was on the level of ~10%, similar to the values indicated by the DLS (PdI = 0,06 – 0,15). We also observed the particle morphology to be heterogenous, some of the NPs displayed distinctive core-corona structure, resulting from the separation of the PLGA and PEG blocks in the self-assembly process. The differences in these features, revealed only when analyzing single particles, contribute to the overall performance of

the nanocarriers in *in vitro* or *in vivo* tests. However, it is important to understand if the outcome often taken as the “average” information indeed is represented by most of the NPs in the bulk.<sup>57</sup>

## 2.4 Encapsulation of fluorescent compounds

Upon the self-assembly of the amphiphilic block co-polymers into the NPs, the PEG chains become exposed in the surface of the nanoparticle, meanwhile the PLGA blocks are folded in the core. A spontaneous encapsulation of hydrophobic molecules present in the solvent phase occurs during the particle formation.<sup>18</sup> This is a common strategy to encapsulate drugs into PLGA formulations.<sup>74,75</sup> We performed a series of formulations with different fluorescent compounds added to the solvent phase, aiming to investigate the encapsulation efficiency (EE) for both: manual and HFF formulation method. We loaded the nanocarriers with 1,1'-Dioctadecyl-3,3',3'-Tetramethylindocarbocyanine perchlorate (DiI), Nile Red (NR) and Doxorubicin (DOX), of which all have fluorescent properties, however different hydrophobicity from the most to the least hydrophobic listed, respectively. We formulated the particles by the manual bulk and the HFF nanoprecipitation using two S/AS to obtain different diameter NPs, then we collected them, washed and measured the EE. The absorbance measurement for each loaded compound revealed, that the highest EE of ~80% is associated with the most hydrophobic molecule (DiI), and lowest value of ~15% was measured for DOX. Similar values were found regardless the formulation method or the particle diameter (Figure 2.3a). The spontaneous entrapment depended here on the solubility of the compound in the antisolvent phase, therefore we measured the decreasing process yield for Nile Red and DOX. For therapeutic application it would be necessary to improve the DOX loading into the NPs, however in this study we investigated the trends regarding the encapsulation of different fluorescent molecules within the proposed nanoprecipitation protocol. In the literature there are strategies demonstrating improved DOX loading into PLGA-based NPs, including use of emulsification or modified nanoprecipitation formulation method, hydrophobization of DOX or its conjugation to the polymer chains.<sup>76–78</sup>

Parallel to the previous size measurements, the EE bulk measurement was followed by an analysis on a single particle level, using total internal reflection fluorescence (TIRF) microscopy. The DiI loaded NPs, formulated by HFF and bulk nanoprecipitation, were imaged using TIRF microscopy taking into account the dye's good EE. Thanks to the high signal to noise ratio we could visualize individual NPs and quantify their fluorescence proportional to the molecule encapsulation. The acquired images revealed heterogenous fluorescence intensity emitted by the particles in the same field of view as can be seen in Figure 2.3b (top image – HFF, bottom – bulk formulation). To understand the difference, we imaged at least 800 NPs per formulation method, and quantified the emitted fluorescence intensity per particle. We observed that between the two HFF formulations, the smaller NPs (HFF2 = 71 nm) exhibited narrower distribution of intensity profile comparing to the larger NPs of HFF1 as shown in the Figure 2.3c (top and middle graph). Interestingly, we measured lower total fluorescence intensity for the smaller NPs formulated with the HFF



method, however this difference was not observed in the bulk analysis, where the total amount of the encapsulated dye was similar irrespectively the particle size. This result of the TIRF image analysis can be possibly explained by the difference in particle size, thus its loading capacity per particle and emitted fluorescence. On the other hand, the bulk analysis, which did not indicate this difference among the two particle sizes, can be explained by higher the total number of smaller NPs over the larger ones (per batch). That in summary gave similar fluorophore EE values when looking at the bulk.

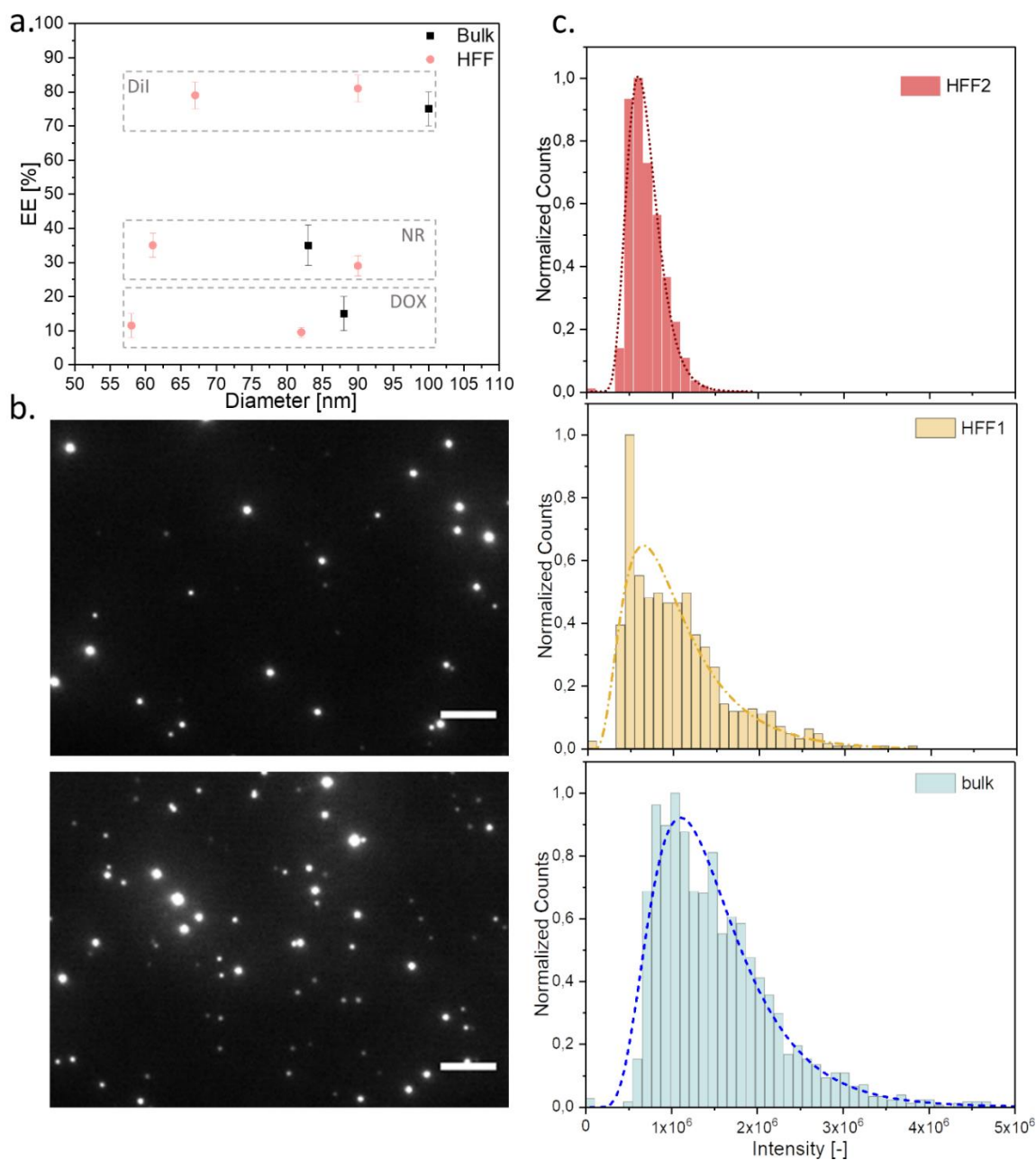


Figure 2.3 Encapsulation of fluorescent compounds; a. EE for Dil, NR and DOX loaded NPs, formulated with HFF and bulk nanoprecipitation, b. TIRF images of Dil loaded NPs formulated with HFF and bulk method (top: HFF1 = 95 nm, bottom: bulk = 89 nm), scale bar 5  $\mu\text{m}$ . c. Analysis of emitted fluorescence intensity per particle for Dil loaded NPs, formulated with HFF and bulk methods, size by DLS: HFF1 = 95 nm, HFF2 = 71 nm, Bulk = 89 nm.

The TIRF-based quantification of the similar diameter NPs formulated with the two different methods (microfluidic HFF1 and manual bulk) has shown alike distributions of collected fluorescence, with only slightly narrower profile for the HFF formulation. Similarly, to the previously observed heterogeneity in the size analysis, we observed uneven dye encapsulation among the particles. Again, in drug delivery, the homogenous drug distribution across all the particles imposes its controllability and better predictability *in vivo*, therefore the proposed characterization methods are crucial to assess these parameters.

## 2.5 NPs incubation with MCF-7 cells

We evaluated our NPs formulated using the microfluidic chip with human breast adenocarcinoma epithelial cell line MCF-7, to confirm they remained non-toxic and retained favorable properties. Here we measured cell viability after 72h of exposure to the following: free DOX, NPs without cargo (placebo), NPs with encapsulated DiI and NPs loaded with DOX. In the Figure 2.4a we can see that the placebo and DiI loaded NPs (60  $\mu\text{g}$  of polymer per well) did not affect the cell viability in comparison to the untreated cells (negative control). It indicates that the microfluidic formulation is a suitable method to obtain the NPs for drug delivery. On the other hand, unencapsulated Doxorubicin (80 ng of drug per well), which is known to intercalate into the genetic material, inducing cell apoptosis, had a major impact on the cell viability, with the result close to the positive control (cells exposed to Triton-X).<sup>79</sup> The NPs loaded with Doxorubicin (DOX in the NPs: 8 ng of drug per well) induced some cell toxicity, indicating successful delivery of the cargo, however not as significant as the free drug. One of the reasons can be the lower Doxorubicin concentration per well, originating from the low EE for this drug (in the range of 10-15%), what resulted in the cells to be exposed to 10-times less compound. Secondly, the entrapped molecules are slowly released from the nanocarrier matrix, therefore the cell exposure to the drug is gradual, as the PLGA degrades over time.<sup>80,81</sup> Overall, we observed that the NPs formulated with the microfluidic chip presented similar behavior in cell assay to the other PLGA-based NPs reported in the literature.<sup>25,28</sup>

Furthermore, we imaged the MCF-7 cells exposed to the microfluidic formulated NPs as can be seen in the confocal images (transmission Figure 2.4b and fluorescence Figure 2.4c). The cells were imaged after 24h of exposure to: free DiI, DiI-loaded NPs and placebo NPs, from left to right respectively. The free DiI stained whole cell membrane, meanwhile the dye loaded NPs were taken up by the cells and localized in distinctive spots, likely endosomes, as can be compared between the corresponding transmission and fluorescence images in Figures 2.4b and 2.4c. We did not collect any fluorescence from the placebo particles. We observed that the NPs formulated with the microfluidic chip presented similar behavior in cell assay to the other PLGA-based NPs reported in the literature.<sup>28,28</sup> Future work could include follow up

on the release studies of the encapsulated molecules, as well as incorporation of techniques enhancing DOX encapsulation, as mentioned above.

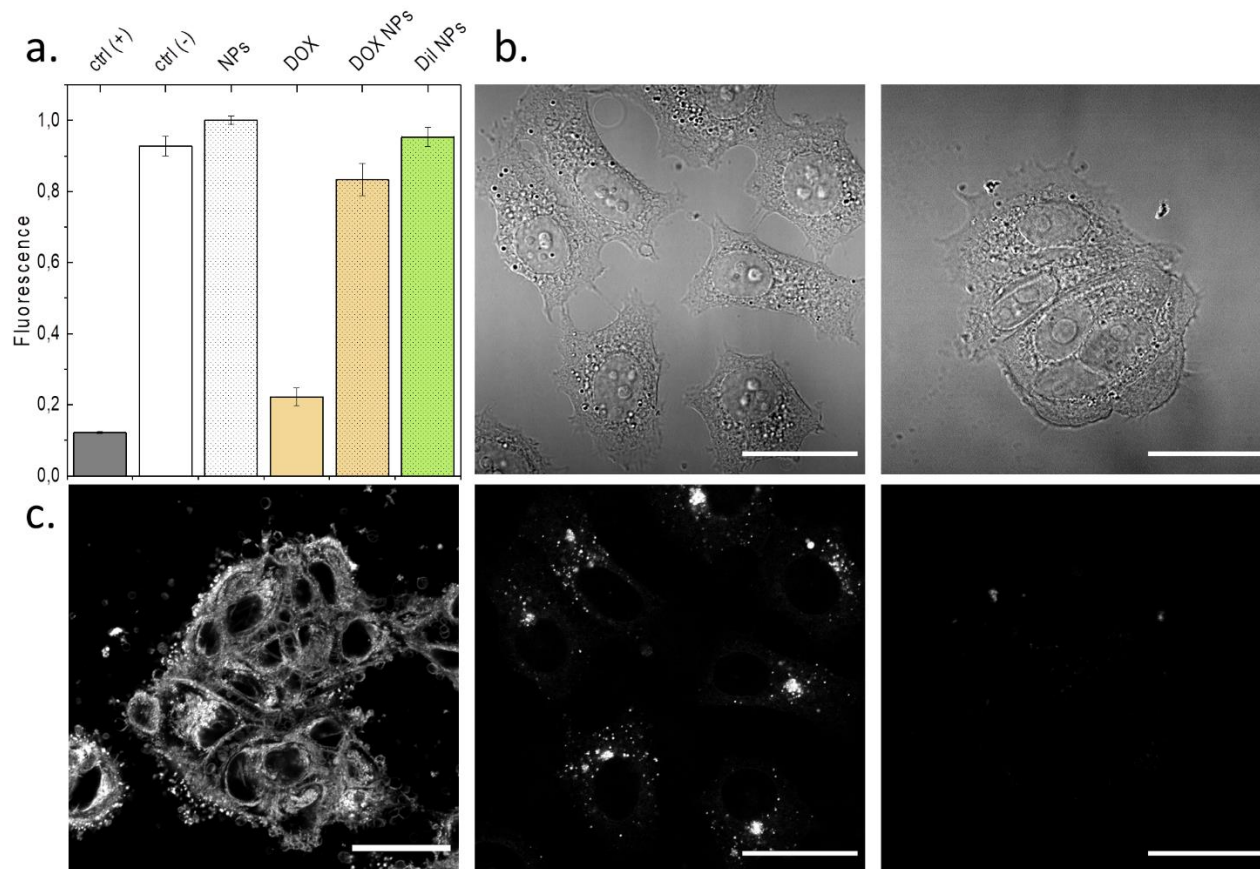


Figure 2.4 a. Presto Blue Cell viability assay graph demonstrating viability of MCF-7 cells exposed to different NPs for 72h b. Confocal microscopy transmission images of MCF-7 cells incubated with DiI loaded NPs (left), and MCF-7 cells exposed to NPs without loading (right). c. Fluorescent confocal microscope images of the MCF-7 cells exposed to (left to right): DiI, DiI loaded NPs (corresponding the transmission image above), NPs without cargo (corresponding to the transmission image above). All scale bars 30  $\mu$ m.

## 2.6 Conclusions

We formulated several PLGA-PEG nanoparticles batches by manual bulk mixing and hydrodynamic flow focusing self-assembly at a corresponding volumes of solvent and antisolvent, demonstrating that the adjustment of the solvent and antisolvent flow rates in confined mixing area allowed us to obtain broader range of diameters than with the bulk nanoprecipitation. The demonstrated NPs size tunability with the use of microfluidic chip highlights how a rational design could be executed in controlling certain properties of nanoparticles.

The studied encapsulation efficiency of three fluorescent compounds appeared to be dependent on the molecule type, and not the nanoprecipitation method, with DiI (most hydrophobic compound tested) having the highest EE.

We used the TEM and TIRF techniques, to analyze individual particles in terms of their size and encapsulation of fluorescent molecules. They revealed heterogeneities among the particles for both studied properties, which could not be visualized within the bulk analysis methods. The encapsulation of DiI, analyzed for single particles, appeared similar among both formulation methods yielding larger NPs and more homogenous for microfluidic formulated NPs with smaller diameter. Finally, we demonstrated performing *in vitro* tests on MCF-7 cell line, that the microfluidic formulation does not alter biocompatibility of PLGA-PEG NPs.

## 2.7 Experimental section

### *Solvent and antisolvent phase preparation*

PLGA (L:G 50:50, Mw. 25–35 kDa; PolySciTech, Akina) and PLGA-PEG (L:G 50:50, Mw. 30 kDa and 5 kDa; PolySciTech, Akina) were weighed in a ratio 15% to 85%, respectively and dissolved in a solvent compatible with the microfluidic chip body and miscible with water: Acetonitrile (Chem-Lab, HPLC grade, Sigma Aldrich) resulting in final PLGA concentration of 10 mg/mL. The dissolution took place in a capped glass vial, at RT during 2h with 10 second of vortex each 20 minutes. Next, the solvent phase was filtered with 0,22  $\mu\text{m}$  PTFE filter (Perkin Elmer, GC-Instruments) and used for the formulation.

For the antisolvent phase, freshly withdrawn milliQ water (MilliQ, Millipore) was filtered with a 0.22  $\mu\text{m}$  sterile filter (Merck Millipore, Millex GP) and used.

### *Fabrication of the PDMS chip*

The 200  $\mu\text{m}$  wide microchannel layout was designed in AutoCAD software and fabricated in an acetate photomask using CAD/Art Services (outputcity.com). The mask was used to prepare a master mold in the lithography process, briefly a glass substrate (microscope glass slide 25x75 mm, Corning) was washed with MilliQ water and soap, flushed with EtOH, dried, treated with oxygen plasma (Expanded Plasma Cleaner PDC-002, Harrick Scientific Corporation). A negative SU-8 2100 photoresist (MicroChem) was deposited on the glass slide surface using 2-step spin coating to obtain a 60  $\mu\text{m}$ -thick layer (following the instructions attached to the SU-8 photoresist). The deposition was followed by a 2-step soft bake (5 min. at 65°C, 20 min. at 95°C). To perform the photoresist polymerization the mask was placed on the top of the deposited layer, introduced into the UV-photolithography mask aligner (MJB4, SUSS Microtec) and exposed to 15.3 mW/cm<sup>2</sup> UV-light for 16 seconds. After UV irradiation the sample was post-baked for 5 minutes at 65°C and 10 minutes at 95°C. The unpolymerized photoresist was washed away with SU-8 developer (MicroChem) and the master mold dried and silanized with trichlorosilane (Sigma-Aldrich). The appearance of microstructures was examined using interferometer (Veeco Instruments, Wyko NT1100). Next, the PDMS replica was prepared by soft lithography molding: elastomer and curing agent (Sylgard 184, Dow Corning) were weighed in a plastic cup (in a ratio of 10:1, wt:wt) thoroughly mixed, degassed and poured over the master mold placed in a Petri dish. The dish with PDMS was left for 24h at RT and then placed into an oven at 60°C for 3h and then the cured PDMS replica was cut out, 0.8 mm holes punched out in the inlets/outlet, and bonded to a clean glass slide (25x75 mm, Corning).

### *Bulk formulation*

3 mL of the AS phase were added to a glass vial (5 mL) equipped with a magnetic stirring bar (VWR, size 8x3 mm) and placed on a magnetic stirring plate (IKA3050009 Big Squid White) at 100-200 rpm. Next the calculated volume of the S phase was added dropwise with a pipette (VWR 20-200  $\mu$ L) into a stirring AS to obtain the desired S/AS. The nanoparticles suspension was let stirring for the next 5h to enhance the solvent evaporation. Afterwards the capped vial was stored in the fridge at 4-8°C until further analysis.

### *Hydrodynamic Flow Focusing (HFF) formulation*

PDMS microfluidic chip was connected to 3 syringes (one filled with S phase and two filled with the AS phase) using PTFE tubing (OD: 1,6 mm; ID 0,8 mm; Sigma Aldrich). The AS syringes (BD Plastic, 10 mL) were placed in a double syringe pump (New Era, NE-300), the S syringe (BD Plastic 2mL) was placed in a separate syringe pump (Chemyx Fusion 200). The chip was equipped with an outlet capillary directed into a collecting vial with a stirring bar for solvent extraction (as in the bulk method). The solvent flow rate was set at 5  $\mu$ L/min or 15  $\mu$ L/min and the AS flow rate was adjusted between 20  $\mu$ L/min and 330  $\mu$ L/min to screen the S/AS ratios in the range of 0.0075 – 0.11.

### *Encapsulation of fluorescent compounds*

1,1'-Dioctadecyl-3,3,3',3'-Tetramethylindocarbocyanine Perchlorate (DiI, lipophilic cationic carbocyanine dye, Sigma Aldrich, 42364) was weighed and dissolved in ACN, resulting in stock solution of 1.1 mM. Calculated amount of the stock was added to the S phase to reach the concentration of 7.1  $\mu$ M.

Nile Red (Sigma Aldrich, 72485) was weighed and dissolved in ethanol, resulting in 0.46 mM stock solution, which was added to the solvent phase, reaching the final concentration of 7.1  $\mu$ M. Doxorubicin Hydrochloride (Xing Chem ChemPharm) was weighed and dissolved in DMSO, resulting in 1.04 mM stock solution, which was added to the solvent phase, reaching the final concentration of 7.1  $\mu$ M. The nanoprecipitation in bulk or with the HFF chip was performed as described before.

### *Nanoparticle concentration*

Nanoparticles were washed and concentrated using ultrafiltration centrifugal filters (Amicon Ultra–0.5 mL Ultracel, RC) with a nominal molecular weight limit 100 kDa. Briefly, the nanoparticles were filtered with 0.45  $\mu$ m sterile filter (Merck Millipore, Millex HV 0.45  $\mu$ m) and 400  $\mu$ L of the suspension was directed into the milliQ-rinsed Amicon filter. The filters were spun in a centrifuge (Eppendorf 5415 R) with the following parameters: 14kG, 5 min, 20°C. After the centrifugation, the supernatant collected in the tube was removed and another 400  $\mu$ L of NPs suspension added into the filter and the procedure repeated 3

times. Afterwards, the NPs were washed, resuspended in 80  $\mu$ L of milliQ water and collected by placing the tube upside down in the microcentrifuge and spinning at 1 kG during 2 min.

#### *Encapsulation Efficiency*

DiI, Nile Red and Doxorubicin absorbance spectrum in acetonitrile was acquired using spectrophotometer (Infinite PRO M200, TECAN) and the maximum absorbance was found at: 550 nm, 538 nm and 480 nm respectively.

Fluorophore solutions for the calibration curve were prepared by dissolving the PLGA-PEG copolymer in ACN (10 mg/mL) and adding the corresponding fluorophore. The loaded NPs were concentrated as described previously, dissolved in acetonitrile and the absorbance was measured at previously determined wavelengths in a quartz cuvette (High Precision Cell Quartz SUPRASIL, Hellma Analytics, 10 mm).

The encapsulation efficiency was calculated as:

$$[EE]\% = \frac{\text{Measured concentration}}{\text{Theoretical concentration}} * 100\%$$

#### *NPs characterization - Dynamic Light Scattering*

DLS (Malvern Zetasizer Nano – ZS) equipped with 633 nm laser and 173° detection optics, was used to measure the NPs size distribution in a colloidal suspension. The following SOP settings were used: Refractive index (RI): 1.460, Absorption: 0.0, Dispersant: water, viscosity: 0.887 cP, RI: 1.33, Temperature: 25°C, equilibration time: 30 seconds, Cell: Quartz cuvettes ZEN2112. 50  $\mu$ L of NPs suspension was added into the cuvette and the size measured in triplicate. Three independent batches were measured for each condition and the mean particle size value with standard deviation are reported. The cuvette was flushed 3x with milliQ water before each sample.

#### *NPs characterization - Transmission Electron Microscopy*

The stock NPs were 4-fold diluted in milliQ water and then 10  $\mu$ L of the NPs suspension was deposited on a carbon-coated copper grid (CF200-CU, 200 mesh, Electron Microscopy Sciences), washed 3x with 20  $\mu$ L of milliQ water and stained with 10  $\mu$ L of 2% uranyl acetate water solution (UB SCT). After the staining the excess liquid was blotted with a filter paper and the grid placed into a desiccator for not less than 10h prior the image acquisition. The samples were imaged with a JEOL 1010 (Gatan, Japan) microscope equipped with a tungsten cathode (Electron Cryomicroscopy Unit from CCiTUB). The images were acquired at various magnifications (x30k - x120k) at 80kV with a CCD Megaview 1kx1k. The NPs diameter (of minimum 200 NPs/batch) was measured using ImageJ software.

### *Comsol Multiphysics simulation*

Comsol Multiphysics 5.3 software was used for the CFD simulations. The chip mesh was generated from the AutoCAD design (the same as used for the acetate mask). The simulation was performed for fluid laminar flow in stationary conditions to observe the transport of diluted species upon different flow rates. Water and Acetonitrile properties at RT and 1 atm were introduced to perform the computation. The parameters used for the computation were as following: dynamic viscosity of ACN: 0.389 mPas, the density of ACN: 0.786 g/mL, the properties of water were selected automatically from the software library.

### *Total internal reflection (TIR) fluorescence imaging*

30  $\mu$ L of 10-fold diluted particles suspension was introduced into a flow chamber created with 24x24 mm glass cover slip (RS, France) attached with a two face Scotch tape to the edges of a glass slide (25x75 mm, Corning). The sample was incubated for 15 min. at RT and next 100  $\mu$ L of milliQ water were introduced into the flow chamber to flush away unattached NPs.

Images were acquired using a Nikon N-STORM 4.0 system configured for total internal reflection (TIR) fluorescence, using a Perfect Focus System imaging. Excitation under the TIR conditions allowed to avoid illumination of out of focus, improving signal to noise ratio. DiI fluorophore was excited by illuminating the sample with a 5% power of 561 nm (80 mW) laser built into the microscope. During acquisition the integration time was 300 ms. Fluorescence was collected by means of a Nikon x100, 1.4 NA oil immersion objective and passed through a quad-band-pass dichroic filter (97335 Nikon). Images were recorded onto a 256 x 256-pixel region (pixel size 160 nm) of a Hamamatsu ORCA Flash 4.0 CMOS camera. The images were analyzed using ImageJ software. Briefly, the intensity threshold was set to filter the NPs in each image, and next the fluorescence intensity per particle was measured (for minimum 800 NPs) and plotted in a histogram graph.

### *Cytotoxicity assay*

Cell viability test was performed in triplicate, using PrestoBlue Cell Viability Kit (Invitrogen A13262) on MCF-7 cell line (ATCC) exposed to microfluidic device formulated NPs. The cells (p. 9) were cultured in a t-25 NUNC cell culture flask with Dulbecco's Modified Eagle Medium (DMEM, as received with L-Glutamine, 4.5 g/L D-glucose and pyruvate, Gibco) supplemented with FBS 10% (Gibco) and penicillin/streptomycin 1% (Biowest) at 37°C and 5% CO<sub>2</sub>, until 70-80% confluency. Next, they were harvested using Trypsin-EDTA 0.25% (Gibco) and seeded in a 96-well plate (Nunc Delta Surface, Thermo Scientific) at a density of 6k cells/well and incubated at 37°C and 5% CO<sub>2</sub>. After 24 hours of incubation the cells were exposed for 72h to free Doxorubicin (~80 ng/well) and the following batches of the NPs (60  $\mu$ g /well): without a cargo (placebo), with encapsulated DiI (~ 3ng/well) and with encapsulated



Doxorubicin (~ 8 ng/well). All the NPs were formulated with the microfluidic chip at the same parameters. Untreated cells (in cell culture medium) were used as a negative control and cells with addition of 5% Triton-x were the positive control. In this work, cells viability was assessed by measuring the fluorescence value at the emission peak of resorufin. After the 72h the cells were washed with 1x PBS (Gibco) and the wells refilled with 100  $\mu$ L of the cell culture media and 10  $\mu$ L of PrestoBlue and further incubated for 1h 40 min. The fluorescence was measured at 590 nm using multimode plate reader (Infinite PRO M200, TECAN).

### *Confocal Microscopy*

MCF-7 cells were seeded in a Lab-Tek (Nunc, Fisher Scientific) at density of 20k cells/well and incubated for 24h at 37°C and 5% CO<sub>2</sub>. After the incubation to the wells were added: NPs without load (0,5 mg/well), NPs with DiI (polymer: 0,5 mg/well; dye: ~1.9  $\mu$ g/well) and free DiI (2.5  $\mu$ g/well) and further incubated for 20h. Next the cells were fixed with 4wt% solution of paraformaldehyde (PFA, Sigma Aldrich) in 1x PBS. After 10 minutes the fixative was washed away with 1x PBS. Cells were imaged using Confocal Microscope (Zeiss, LSM 800) with 63x oil immersion objective, pin hole 50  $\mu$ m and pixel size of 50 nm. The fluorophore was excited with 561 nm laser at 0,20% with the emission detection in the range of 410-617 nm.

## 2.8 References

- (1) Farokhzad, O. C.; Langer, R. Nanomedicine: Developing Smarter Therapeutic and Diagnostic Modalities. *Adv. Drug Deliv. Rev.* 2006, 58 (14), 1456–1459. <https://doi.org/10.1016/j.addr.2006.09.011>.
- (2) Steichen, S. D.; Caldorera-Moore, M.; Peppas, N. A. A Review of Current Nanoparticle and Targeting Moieties for the Delivery of Cancer Therapeutics. *Eur. J. Pharm. Sci.* 2013, 48 (3), 416–427. <https://doi.org/10.1016/j.ejps.2012.12.006>.
- (3) Salvioni, L.; Rizzuto, M. A.; Bertolini, J. A.; Pandolfi, L.; Colombo, M.; Prosperi, D. Thirty Years of Cancer Nanomedicine: Success, Frustration, and Hope. *Cancers* 2019, 11 (12). <https://doi.org/10.3390/cancers11121855>.
- (4) Blanco, E.; Shen, H.; Ferrari, M. Principles of Nanoparticle Design for Overcoming Biological Barriers to Drug Delivery. *Nat. Biotechnol.* 2015, 33 (9), 941–951. <https://doi.org/10.1038/nbt.3330>.
- (5) Bobo, D.; Robinson, K. J.; Islam, J.; Thurecht, K. J.; Corrie, S. R. Nanoparticle-Based Medicines: A Review of FDA-Approved Materials and Clinical Trials to Date. *Pharm. Res.* 2016, 33 (10), 2373–2387. <https://doi.org/10.1007/s11095-016-1958-5>.
- (6) Shi, J.; Kantoff, P. W.; Wooster, R.; Farokhzad, O. C. Cancer Nanomedicine: Progress, Challenges and Opportunities. *Nat. Rev. Cancer* 2017, 17 (1), 20–37. <https://doi.org/10.1038/nrc.2016.108>.
- (7) Salatin, S.; Dizaj, S. M.; Khosroushahi, A. Y. Effect of the Surface Modification, Size, and Shape on Cellular Uptake of Nanoparticles. *Cell Biol. Int.* 2015, 39 (8), 881–890. <https://doi.org/10.1002/cbin.10459>.
- (8) Jo, D. H.; Kim, J. H.; Lee, T. G.; Kim, J. H. Size, Surface Charge, and Shape Determine Therapeutic Effects of Nanoparticles on Brain and Retinal Diseases. *Nanomedicine Nanotechnol. Biol. Med.* 2015, 11 (7), 1603–1611. <https://doi.org/10.1016/j.nano.2015.04.015>.
- (9) Mout, R.; Moyano, D. F.; Rana, S.; Rotello, V. M. Surface Functionalization of Nanoparticles for Nanomedicine. *Chem. Soc. Rev.* 2012, 41 (7), 2539–2544. <https://doi.org/10.1039/C2CS15294K>.
- (10) Albanese, A.; Tang, P. S.; Chan, W. C. W. The Effect of Nanoparticle Size, Shape, and Surface Chemistry on Biological Systems. *Annu. Rev. Biomed. Eng.* 2012, 14 (1), 1–16. <https://doi.org/10.1146/annurev-bioeng-071811-150124>.
- (11) Upponi, J. R.; Torchilin, V. P. Passive vs. Active Targeting: An Update of the EPR Role in Drug Delivery to Tumors. In *Nano-Oncologicals: New Targeting and Delivery Approaches*; Alonso, M. J., Garcia-Fuentes, M., Eds.; Advances in Delivery Science and Technology; Springer International Publishing: Cham, 2014; pp 3–45. [https://doi.org/10.1007/978-3-319-08084-0\\_1](https://doi.org/10.1007/978-3-319-08084-0_1).
- (12) Golombek, S. K.; May, J.-N.; Theek, B.; Appold, L.; Drude, N.; Kiessling, F.; Lammers, T. Tumor Targeting via EPR: Strategies to Enhance Patient Responses. *Adv. Drug Deliv. Rev.* 2018, 130, 17–38. <https://doi.org/10.1016/j.addr.2018.07.007>.
- (13) Concepts of Nanoparticle Cellular Uptake, Intracellular Trafficking, and Kinetics in Nanomedicine. *Adv. Drug Deliv. Rev.* 2019, 143, 68–96. <https://doi.org/10.1016/j.addr.2019.04.008>.
- (14) Walkey, C. D.; Olsen, J. B.; Guo, H.; Emili, A.; Chan, W. C. W. Nanoparticle Size and Surface Chemistry Determine Serum Protein Adsorption and Macrophage Uptake. *J. Am. Chem. Soc.* 2012, 134 (4), 2139–2147. <https://doi.org/10.1021/ja2084338>.
- (15) McClements, D. J. Encapsulation, Protection, and Delivery of Bioactive Proteins and Peptides Using Nanoparticle and Microparticle Systems: A Review. *Adv. Colloid Interface Sci.* 2018, 253, 1–22. <https://doi.org/10.1016/j.cis.2018.02.002>.

- (16) Acharya, S.; Sahoo, S. K. PLGA Nanoparticles Containing Various Anticancer Agents and Tumour Delivery by EPR Effect. *Adv. Drug Deliv. Rev.* 2011, 63 (3), 170–183. <https://doi.org/10.1016/j.addr.2010.10.008>.
- (17) Narvekar, M.; Xue, H. Y.; Eoh, J. Y.; Wong, H. L. Nanocarrier for Poorly Water-Soluble Anticancer Drugs—Barriers of Translation and Solutions. *AAPS PharmSciTech* 2014, 15 (4), 822–833. <https://doi.org/10.1208/s12249-014-0107-x>.
- (18) Wais, U.; Jackson, A. W.; He, T.; Zhang, H. Nanoformulation and Encapsulation Approaches for Poorly Water-Soluble Drug Nanoparticles. *Nanoscale* 2016, 8 (4), 1746–1769. <https://doi.org/10.1039/C5NR07161E>.
- (19) Kamaly, N.; Yameen, B.; Wu, J.; Farokhzad, O. C. Degradable Controlled-Release Polymers and Polymeric Nanoparticles: Mechanisms of Controlling Drug Release. *Chem. Rev.* 2016, 116 (4), 2602–2663. <https://doi.org/10.1021/acs.chemrev.5b00346>.
- (20) Lee, J. H.; Yeo, Y. Controlled Drug Release from Pharmaceutical Nanocarriers. *Chem. Eng. Sci.* 2015, 125, 75–84. <https://doi.org/10.1016/j.ces.2014.08.046>.
- (21) Cieslewicz, M.; Tang, J.; Yu, J. L.; Cao, H.; Zavaljevski, M.; Motoyama, K.; Lieber, A.; Raines, E. W.; Pun, S. H. Targeted Delivery of Proapoptotic Peptides to Tumor-Associated Macrophages Improves Survival. *Proc. Natl. Acad. Sci.* 2013, 110 (40), 15919–15924. <https://doi.org/10.1073/pnas.1312197110>.
- (22) Schmid, D.; Park, C. G.; Hartl, C. A.; Subedi, N.; Cartwright, A. N.; Puerto, R. B.; Zheng, Y.; Maiarana, J.; Freeman, G. J.; Wucherpfennig, K. W.; Irvine, D. J.; Goldberg, M. S. T Cell-Targeting Nanoparticles Focus Delivery of Immunotherapy to Improve Antitumor Immunity. *Nat. Commun.* 2017, 8 (1), 1747. <https://doi.org/10.1038/s41467-017-01830-8>.
- (23) Zhang, B.; Shen, S.; Liao, Z.; Shi, W.; Wang, Y.; Zhao, J.; Hu, Y.; Yang, J.; Chen, J.; Mei, H.; Hu, Y.; Pang, Z.; Jiang, X. Targeting Fibronectins of Glioma Extracellular Matrix by CLT1 Peptide-Conjugated Nanoparticles. *Biomaterials* 2014, 35 (13), 4088–4098. <https://doi.org/10.1016/j.biomaterials.2014.01.046>.
- (24) Sindhvani, S.; Chan, W. C. W. Nanotechnology for Modern Medicine: Next Steps Towards Clinical Translation. *J. Intern. Med.* n/a (n/a). <https://doi.org/10.1111/joim.13254>.
- (25) Park, K.; Skidmore, S.; Hadar, J.; Garner, J.; Park, H.; Otte, A.; Soh, B. K.; Yoon, G.; Yu, D.; Yun, Y.; Lee, B. K.; Jiang, X.; Wang, Y. Injectable, Long-Acting PLGA Formulations: Analyzing PLGA and Understanding Microparticle Formation. *J. Controlled Release* 2019, 304, 125–134. <https://doi.org/10.1016/j.jconrel.2019.05.003>.
- (26) Langer, R. New Methods of Drug Delivery. *Science* 1990, 249 (4976), 1527–1533. <https://doi.org/10.1126/science.2218494>.
- (27) Makadia, H. K.; Siegel, S. J. Poly Lactic-Co-Glycolic Acid (PLGA) as Biodegradable Controlled Drug Delivery Carrier. *Polymers* 2011, 3 (3), 1377–1397. <https://doi.org/10.3390/polym3031377>.
- (28) Anderson, J. M.; Shive, M. S. Biodegradation and Biocompatibility of PLA and PLGA Microspheres. *Adv. Drug Deliv. Rev.* 2012, 64, 72–82. <https://doi.org/10.1016/j.addr.2012.09.004>.
- (29) Machatschek, R.; Lendlein, A. Fundamental Insights in PLGA Degradation from Thin Film Studies. *J. Controlled Release* 2020, 319, 276–284. <https://doi.org/10.1016/j.jconrel.2019.12.044>.
- (30) Zhong, H.; Chan, G.; Hu, Y.; Hu, H.; Ouyang, D. A Comprehensive Map of FDA-Approved Pharmaceutical Products. *Pharmaceutics* 2018, 10 (4), 263. <https://doi.org/10.3390/pharmaceutics10040263>.
- (31) Eliaz, R. E.; Kost, J. Characterization of a Polymeric PLGA-Injectable Implant Delivery System for the Controlled Release of Proteins. *J. Biomed. Mater. Res.* 2000, 50 (3), 388–396. [https://doi.org/10.1002/\(SICI\)1097-4636\(20000605\)50:3<388::AID-JBM13>3.0.CO;2-F](https://doi.org/10.1002/(SICI)1097-4636(20000605)50:3<388::AID-JBM13>3.0.CO;2-F).

- (32) D'Souza, S.; Faraj, J. A.; Giovagnoli, S.; DeLuca, P. P. Development of Risperidone PLGA Microspheres. *J. Drug Deliv.* 2014, 2014, 1–11. <https://doi.org/10.1155/2014/620464>.
- (33) Suk, J. S.; Xu, Q.; Kim, N.; Hanes, J.; Ensign, L. M. PEGylation as a Strategy for Improving Nanoparticle-Based Drug and Gene Delivery. *Adv. Drug Deliv. Rev.* 2016, 99, 28–51. <https://doi.org/10.1016/j.addr.2015.09.012>.
- (34) Sah, H.; Thoma, L. A.; Desu, H. R.; Sah, E.; Wood, G. C. Concepts and Practices Used to Develop Functional PLGA-Based Nanoparticulate Systems. *Int. J. Nanomedicine* 2013, 8, 747–765. <https://doi.org/10.2147/IJN.S40579>.
- (35) Owens, D. E.; Peppas, N. A. Opsonization, Biodistribution, and Pharmacokinetics of Polymeric Nanoparticles. *Int. J. Pharm.* 2006, 307 (1), 93–102. <https://doi.org/10.1016/j.ijpharm.2005.10.010>.
- (36) Panagi, Z.; Beletsi, A.; Evangelatos, G.; Livaniou, E.; Ithakissios, D. S.; Avgoustakis, K. Effect of Dose on the Biodistribution and Pharmacokinetics of PLGA and PLGA–MPEG Nanoparticles. *Int. J. Pharm.* 2001, 221 (1), 143–152. [https://doi.org/10.1016/S0378-5173\(01\)00676-7](https://doi.org/10.1016/S0378-5173(01)00676-7).
- (37) Figueroa, S. M.; Fleischmann, D.; Beck, S.; Goepferich, A. The Effect of Ligand Mobility on the Cellular Interaction of Multivalent Nanoparticles. *Macromol. Biosci.* 2020, 20 (4), 1900427. <https://doi.org/10.1002/mabi.201900427>.
- (38) Sharma, S.; Parmar, A.; Kori, S.; Sandhir, R. PLGA-Based Nanoparticles: A New Paradigm in Biomedical Applications. *TrAC Trends Anal. Chem.* 2016, 80, 30–40. <https://doi.org/10.1016/j.trac.2015.06.014>.
- (39) Chen, S.; Cheng, S.-X.; Zhuo, R.-X. Self-Assembly Strategy for the Preparation of Polymer-Based Nanoparticles for Drug and Gene Delivery. *Macromol. Biosci.* 2011, 11 (5), 576–589. <https://doi.org/10.1002/mabi.201000427>.
- (40) Gaucher, G.; Dufresne, M.-H.; Sant, V. P.; Kang, N.; Maysinger, D.; Leroux, J.-C. Block Copolymer Micelles: Preparation, Characterization and Application in Drug Delivery. *J. Controlled Release* 2005, 109 (1–3), 169–188. <https://doi.org/10.1016/j.jconrel.2005.09.034>.
- (41) Hornig, S.; Heinze, T.; Becer, C. R.; Schubert, U. S. Synthetic Polymeric Nanoparticles by Nanoprecipitation. *J. Mater. Chem.* 2009, 19 (23), 3838. <https://doi.org/10.1039/b906556n>.
- (42) Zhu, Z. Effects of Amphiphilic Diblock Copolymer on Drug Nanoparticle Formation and Stability. *Biomaterials* 2013, 34 (38), 10238–10248. <https://doi.org/10.1016/j.biomaterials.2013.09.015>.
- (43) Shen, H.; Hong, S.; Prud'homme, R. K.; Liu, Y. Self-Assembling Process of Flash Nanoprecipitation in a Multi-Inlet Vortex Mixer to Produce Drug-Loaded Polymeric Nanoparticles. *J. Nanoparticle Res.* 2011, 13 (9), 4109–4120. <https://doi.org/10.1007/s11051-011-0354-7>.
- (44) Valencia, P. M.; Pridgen, E. M.; Rhee, M.; Langer, R.; Farokhzad, O. C.; Karnik, R. Microfluidic Platform for Combinatorial Synthesis and Optimization of Targeted Nanoparticles for Cancer Therapy. *ACS Nano* 2013, 7 (12), 10671–10680. <https://doi.org/10.1021/nn403370e>.
- (45) Wang, L.; Sánchez, S. Self-Assembly via Microfluidics. *Lab. Chip* 2015, 15 (23), 4383–4386. <https://doi.org/10.1039/C5LC90116B>.
- (46) Tomeh, M. A.; Zhao, X. Recent Advances in Microfluidics for the Preparation of Drug and Gene Delivery Systems. *Mol. Pharm.* 2020, acs.molpharmaceut.0c00913. <https://doi.org/10.1021/acs.molpharmaceut.0c00913>.
- (47) Dongfei Liu, H. Current Developments and Applications of Microfluidic Technology toward Clinical Translation of Nanomedicines. *Adv. Drug Deliv. Rev.* 2018, 128, 54–83. <http://dx.doi.org/10.1016/j.addr.2017.08.003>.
- (48) Baby, T.; Liu, Y.; Middelberg, A. P. J.; Zhao, C.-X. Fundamental Studies on Throughput Capacities of Hydrodynamic Flow-Focusing Microfluidics for Producing Monodisperse Polymer Nanoparticles. *Chem. Eng. Sci.* 2017, 169, 128–139. <https://doi.org/10.1016/j.ces.2017.04.046>.

- (49) Jafarifar, E.; Hajialyani, M.; Akbari, M.; Rahimi, M.; Shokoohinia, Y.; Fattahi, A. Preparation of a Reproducible Long-Acting Formulation of Risperidone-Loaded PLGA Microspheres Using Microfluidic Method. *Pharm. Dev. Technol.* 2017, 22 (6), 836–843. <https://doi.org/10.1080/10837450.2016.1221426>.
- (50) Swider, E.; Koshkina, O.; Tel, J.; Cruz, L. J.; de Vries, I. J. M.; Srinivas, M. Customizing Poly(Lactic-Co-Glycolic Acid) Particles for Biomedical Applications. *Acta Biomater.* 2018, 73, 38–51. <https://doi.org/10.1016/j.actbio.2018.04.006>.
- (51) Amoyav, B., “Controlled and tunable polymer particles’ production using a single microfluidic device,” *Appl. Nanosci.*, p. 10, 2018.
- (52) M. Brzeziński, M. Socka, and B. Kost, “Microfluidics for producing polylactide nanoparticles and microparticles and their drug delivery application,” *Polym. Int.*, vol. 68, no. 6, pp. 997–1014, 2019, doi: <https://doi.org/10.1002/pi.5753>.
- (53) E. Lallana, R. Donno, D. Magri, K. Barker, Z. Nazir, K. Treacher et al., “Microfluidic-assisted nanoprecipitation of (PEGylated) poly (d,l-lactic acid-co-caprolactone): Effect of macromolecular and microfluidic parameters on particle size and paclitaxel encapsulation,” *Int. J. Pharm.*, vol. 548, no. 1, pp. 530–539, Sep. 2018, doi: 10.1016/j.ijpharm.2018.07.031.
- (54) M. Brzeziński, M. Socka, T. Makowski, B. Kost, M. Cieślak, and K. Królewska-Golińska, “Microfluidic-assisted nanoprecipitation of biodegradable nanoparticles composed of PTMC/PCL (co)polymers, tannic acid and doxorubicin for cancer treatment,” *Colloids Surf. B Biointerfaces*, vol. 201, p. 111598, May 2021, doi: 10.1016/j.colsurfb.2021.111598.
- (55) J. Ma, S. M.-Y. Lee, C. Yi, and C.-W. Li, “Controllable synthesis of functional nanoparticles by microfluidic platforms for biomedical applications – a review,” *Lab. Chip*, vol. 17, no. 2, pp. 209–226, Jan. 2017, doi: 10.1039/C6LC01049K.
- (56) Q. Feng, J. Sun, and X. Jiang, “Microfluidics-mediated assembly of functional nanoparticles for cancer-related pharmaceutical applications,” *Nanoscale*, vol. 8, no. 25, pp. 12430–12443, Jun. 2016, doi: 10.1039/C5NR07964K.
- (57) Y. Liu, G. Yang, D. Zou, Y. Hui, K. Nigam, A. P. J. Middleberg et al., “Formulation of Nanoparticles Using Mixing-Induced Nanoprecipitation for Drug Delivery,” *Ind. Eng. Chem. Res.*, vol. 59, no. 9, pp. 4134–4149, Mar. 2020, doi: 10.1021/acs.iecr.9b04747.
- (58) S. Ding, N. Anton, T. F. Vandamme, and C. A. Serra, “Microfluidic nanoprecipitation systems for preparing pure drug or polymeric drug loaded nanoparticles: an overview,” *Expert Opin. Drug Deliv.*, vol. 13, no. 10, pp. 1447–1460, Oct. 2016, doi: 10.1080/17425247.2016.1193151.
- (59) A. Bains, J. E. Wulff, and M. G. Moffitt, “Microfluidic synthesis of dye-loaded polycaprolactone-block-poly(ethylene oxide) nanoparticles: Insights into flow-directed loading and in vitro release for drug delivery,” *J. Colloid Interface Sci.*, vol. 475, pp. 136–148, Aug. 2016, doi: 10.1016/j.jcis.2016.04.010.
- (60) F. Bally, D. K. Garg, C. A. Serra, Y. Hoarau, N. Anton, C. Brochon et al., “Improved size-tunable preparation of polymeric nanoparticles by microfluidic nanoprecipitation,” *Polymer*, vol. 53, no. 22, pp. 5045–5051, Oct. 2012, doi: 10.1016/j.polymer.2012.08.039.
- (61) J. He, L. Wang, Z. Wei, Y. Yang, C. Wang, X. Han et al., “Vesicular Self-Assembly of Colloidal Amphiphiles in Microfluidics,” *ACS Appl. Mater. Interfaces*, vol. 5, no. 19, pp. 9746–9751, Oct. 2013, doi: 10.1021/am4028839.
- (62) M. Khosravi Parsa, F. Hormozi, and D. Jafari, “Mixing enhancement in a passive micromixer with convergent–divergent sinusoidal microchannels and different ratio of amplitude to wave length,” *Comput. Fluids*, vol. 105, pp. 82–90, Dec. 2014, doi: 10.1016/j.compfluid.2014.09.024.
- (63) J. He, Z. Wei, L. Wang, Z. Tomova, T. Babu, C. Wang, et al., “Hydrodynamically Driven Self-Assembly of Giant Vesicles of Metal Nanoparticles for Remote-Controlled Release,” *Angew.*

- Chem. Int. Ed., vol. 52, no. 9, pp. 2463–2468, 2013, doi: <https://doi.org/10.1002/anie.201208425>.
- (64) S. Rezvantab and M. K. Moraveji, “Microfluidic assisted synthesis of PLGA drug delivery systems,” *RSC Adv.*, vol. 9, no. 4, pp. 2055–2072, 2019, doi: 10.1039/C8RA08972H.
- (65) X. Li and X. Jiang, “Microfluidics for producing poly (lactic-co-glycolic acid)-based pharmaceutical nanoparticles,” *Adv. Drug Deliv. Rev.*, vol. 128, pp. 101–114, Mar. 2018, doi: 10.1016/j.addr.2017.12.015.
- (66) S. Streck, H. Neumann, H. M. Nielsen, T. Rades, and A. McDowell, “Comparison of bulk and microfluidics methods for the formulation of poly-lactic-co-glycolic acid (PLGA) nanoparticles modified with cell-penetrating peptides of different architectures,” *Int. J. Pharm. X*, vol. 1, p. 100030, Dec. 2019, doi: 10.1016/j.ijpx.2019.100030.
- (67) M. Pannuzzo, B. A. C. Horta, C. L. Rosa, and P. Decuzzi, “Predicting the Miscibility and Rigidity of Poly(lactic-co-glycolic acid)/Polyethylene Glycol Blends via Molecular Dynamics Simulations,” p. 12, 2020.
- (68) N. Lababidi, V. Sigal, A. Koenneke, K. Schwarzkopf, A. Manz, and M. Schneider, “Microfluidics as tool to prepare size-tunable PLGA nanoparticles with high curcumin encapsulation for efficient mucus penetration,” *Beilstein J. Nanotechnol.*, vol. 10, no. 1, pp. 2280–2293, Nov. 2019, doi: 10.3762/bjnano.10.220.
- (69) R. Karnik, F. Gu, P. Basto, C. Cannizzaro, L. Dean, W. K. Manu et al., “Microfluidic Platform for Controlled Synthesis of Polymeric Nanoparticles,” *Nano Lett.*, vol. 8, no. 9, pp. 2906–2912, Sep. 2008, doi: 10.1021/nl801736q.
- (70) B. K. Johnson and R. K. Prud’homme, “Flash NanoPrecipitation of Organic Actives and Block Copolymers using a Confined Impinging Jets Mixer,” *Aust. J. Chem.*, vol. 56, no. 10, p. 1021, 2003, doi: 10.1071/CH03115.
- (71) B. K. Johnson and R. K. Prud’homme, “Mechanism for Rapid Self-Assembly of Block Copolymer Nanoparticles,” *Phys. Rev. Lett.*, vol. 91, no. 11, p. 118302, Sep. 2003, doi: 10.1103/PhysRevLett.91.118302.
- (72) J. Fang, H. Nakamura, and H. Maeda, “The EPR effect: Unique features of tumor blood vessels for drug delivery, factors involved, and limitations and augmentation of the effect,” *Adv. Drug Deliv. Rev.*, vol. 63, no. 3, pp. 136–151, Mar. 2011, doi: 10.1016/j.addr.2010.04.009.
- (73) J.-M. Rabanel, V. Adibnia, S.F. Tehrani, S. Sanche, P. Hildgen, X. Banquy et al., “Nanoparticle heterogeneity: an emerging structural parameter influencing particle fate in biological media?,” *Nanoscale*, vol. 11, no. 2, pp. 383–406, Jan. 2019, doi: 10.1039/C8NR04916E.
- (74) C. Wischke and S. P. Schwendeman, “Principles of encapsulating hydrophobic drugs in PLA/PLGA microparticles,” *Int. J. Pharm.*, vol. 364, no. 2, pp. 298–327, Dec. 2008, doi: 10.1016/j.ijpharm.2008.04.042.
- (75) N. Wilkosz, G. Lazarski, L. Kovacik, P. Gargas, M. Nowakowska, D. Jamroz et al., “Molecular Insight into Drug-Loading Capacity of PEG–PLGA Nanoparticles for Itraconazole,” *J. Phys. Chem. B*, vol. 122, no. 28, pp. 7080–7090, Jul. 2018, doi: 10.1021/acs.jpcc.8b03742.
- (76) I. Orienti, G. Zuccari, A. Fini, A. M. Rabasco, P.G. Montaldo, L. Raffaghello, et al., “Modified Doxorubicin for Improved Encapsulation in PVA Polymeric Micelles,” *Drug Deliv.*, vol. 12, no. 1, pp. 15–20, Jan. 2004, doi: 10.1080/10717540590889574.
- (77) O. Maksimenko, J. Malinovskaya, E. Shipulo, N. Osipova, V. Razzhivina, D. Arantseva et al., “Doxorubicin-loaded PLGA nanoparticles for the chemotherapy of glioblastoma: Towards the pharmaceutical development,” *Int. J. Pharm.*, vol. 572, p. 118733, Dec. 2019, doi: 10.1016/j.ijpharm.2019.118733.

- (78) H. S. Yoo, K. H. Lee, J. E. Oh, and T. G. Park, "In vitro and in vivo anti-tumor activities of nanoparticles based on doxorubicin-PLGA conjugates," *J. Controlled Release*, vol. 68, no. 3, pp. 419-431, Sep. 2000, doi: 10.1016/S0168-3659(00)00280-7.
- (79) C. F. Thorn et al., "Doxorubicin pathways: pharmacodynamics and adverse effects," *Pharmacogenet. Genomics*, vol. 21, no. 7, pp. 440-446, Jul. 2011, doi: 10.1097/FPC.0b013e32833ffb56.
- (80) K. Avgoustakis, A. Beletsi, Z. Panagi, P. Klepetsanis, A. G. Karydas, and D. S. Ithakissios, "PLGA-mPEG nanoparticles of cisplatin: in vitro nanoparticle degradation, in vitro drug release and in vivo drug residence in blood properties," *J. Controlled Release*, vol. 79, no. 1, pp. 123-135, Feb. 2002, doi: 10.1016/S0168-3659(01)00530-2.
- (81) T. Musumeci, C. A. Ventura, I. Giannone, B. Ruozi, L. Montenegro, R. Pignatello, et al., "PLA/PLGA nanoparticles for sustained release of docetaxel," *Int. J. Pharm.*, vol. 325, no. 1, pp. 172-179, Nov. 2006, doi: 10.1016/j.ijpharm.2006.06.023.

## Chapter 3| Microfluidic mixer for combinatorial formulation of drug nanocarriers

*This chapter presents microfabrication and evaluation of a microfluidic passive mixer device, designed to facilitate combinatorial formulation of nanoparticles. Initially PDMS prototype is presented and finally it is superseded by a glass model, which helps to eliminate the weaknesses of associated to the polymer. The micromixer chip is incorporated into a platform, that consists of previously described chip, to accelerate formulation of NPs based on different precursors. Proof-of-concept formulations are executed.*

*The design of the microfluidic micromixer was supervised by Hans Wyss, TU/e.*



### 3.1 Introduction

The microfluidic technology is maturing in the field of self-assembly for nanoparticles formulation. It is clear now that the polymeric drug nanocarriers can be fine-tuned in microfluidic devices thanks to the controlled environment they provide. Considering the countless formulation options involving mixing of different polymer chain lengths, precursors with targeting ligands or with conjugated fluorophores, encapsulating drug or co-encapsulating more than one type of molecules,<sup>1,2</sup> the process feasibility becomes the question. Rapid prototyping of NPs with different size, ligand density, drug load and so on, appears very appealing in the search for best performing formulation and for the general understanding of NPs characteristics and correlated biological interactions. Indeed, it becomes urgent to reevaluate these drug nanocarriers, as it was reported that on average only staggering number of 0.7% of total introduced dose ends up in a disease site, with not much difference between targeting and passive delivery strategies.<sup>3</sup>

Furthermore, knowing the heterogeneity of tumors in cancer patients, it is challenging to encounter most effective treatment for each individual.<sup>4</sup> *In vitro* culturing of specific tumor cells derived from a sick person, for screening of the best option from the library of drug-loaded NPs envisions a solution that could accelerate anticancer therapy.<sup>5</sup> Additionally, a small fabrication scale offered by microfluidic chips seems to be a realistic solution for treatment of single or small groups of patients. Ideally such microfluidic combinatorial formulation device should be easy to operate by healthcare professionals i.e. as a “plug and play” system. Similar concept is under development by Tide Pharmaceuticals B.V. (Solstice Pharma), where stand-alone device with built-in microfluidic chip can be placed in hospitals and used for rapid formulation of microbubbles for diagnostic purposes.<sup>6</sup> This approach facilitates convenient and easy formulation of small quantities necessary for diagnostics right before the procedure is performed and envisions the future of microfluidic devices in healthcare.

As it was mentioned in the introductory Chapter 1, section 1.5, currently, the personalized nanomedicine is being extensively explored in research labs, aiming to generate large libraries of NPs that are characterized and bioevaluated.<sup>7,8</sup> The strategy to handle high number of NP formulations proposes their unique coding, that can be later recognize during *in vitro* or *in vivo* screening procedures. Some of the barcoding methods use synthetic DNA strands, linkage with QDs or encapsulation of fluorophores.<sup>8-10</sup> The authors aim to accelerate the development of drug nanocarriers, however, the presented NPs are formulated with manual bulk mixing methods, with only few formulations reported, what in the light of high throughput screening of DDS candidates, is the slowing down step of the process. To face this challenge a microfluidic mixer (micromixer) could be incorporated in the formulation step to advance this process and to provide better

control over the NPs properties as it was demonstrated in the previous chapter and reported in the literature.<sup>11–14</sup> In the literature, the use of micromixers is reported for microfluidic chips with the purpose of handling chemical reactions or biological samples.<sup>15</sup> Among them two families of micromixing devices can be distinguished: passive and active micromixers.

Passive micromixers in general do not require any external source of stimulation to fulfill the mixer function, as there are no mechanically moving parts. They rely on chaotic advection and the diffusion to provide the mixing. For that reason, they are usually easier to fabricate and implement as a stand-alone unit, comparing to the active mixers. Among the proposed solutions, are passive micromixers with special geometries that stretch, fold and break the fluid flow to amplify the chaotic advection, resulting in improved mixing of fluids.<sup>16,17</sup> Typically designs suitable for intermediate and low Reynold numbers include C-shape, L-shape and similar segments connecting perpendicular planes or designs with grooved channels. A simple example is a T-junction chip with periodic geometric features that enhance mixing as illustrated in Figure 3.1. The authors proposed addition of staggered bars in the channel and performed computational fluid dynamics (CFD) analysis as well as fabrication and fluid test of the chip with 28 repeating units to demonstrate its performance.<sup>18</sup> Other type (2-layer micromixer) was proposed in a crossing-channel design, demonstrating more efficient mixing than the C-shaped model (Figure 3.2).<sup>19</sup> It was further adapted into a platform for combinatorial formulation of NPs.<sup>12</sup> Other widely used passive mixer is so called herringbone design (as illustrated in Figure 3.3) that was well adapted into biological applications, such as the chip for separation of circulating tumor cells (CTC).<sup>20</sup>

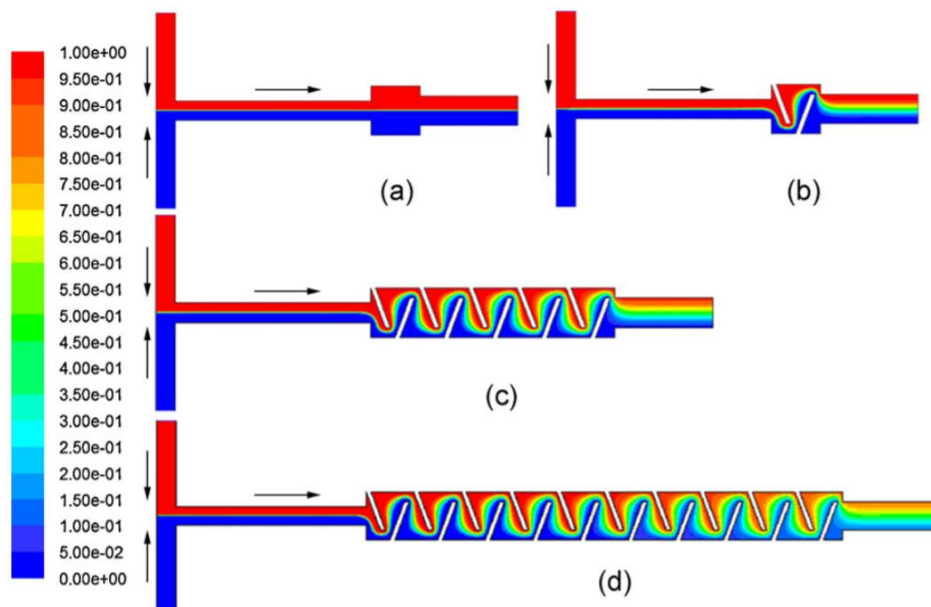


Figure 3.1 Computational Fluid Dynamics simulation of a concentration gradient in a passive micromixer with varying number of units with staggered bars in the mixing area. (a) no bars, (b) one pair of bars, (c) five pair units, (d) ten pair units.<sup>18</sup>

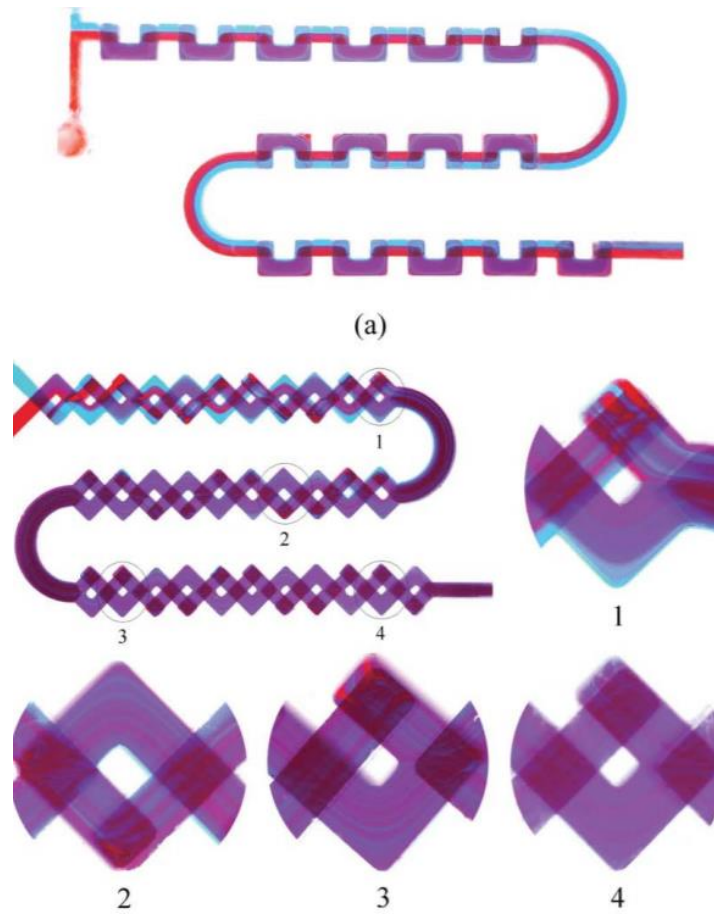


Figure 3.2 Images of 2-layer micromixer (top) and proposed crossing-channel design (bottom), demonstrating more efficient mixing than the C-shaped model.<sup>19</sup>

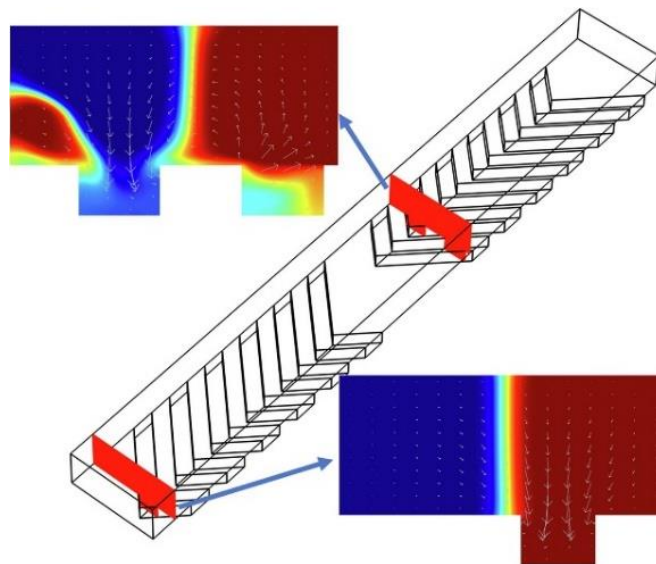


Figure 3.3 Demonstration of a mixing enhancement in a herringbone micromixer with the structures on the bottom of the microchannel.<sup>21</sup>

Active micromixers are an alternative to passive micromixers, they use external energy, such as pressure, magnetic field, acoustic field, etc. to generate flow disturbance, that results in liquid mixing. The active mixer design must include responsive parts, which will be mechanically operating upon the acting force. Often it is more expensive and technologically demanding to integrate the active mixers in the microfluidic device. Still relatively simple in construction are active micromixers employing pressure to generate pulse, which allows to improve the mixing through fluid stretching and folding as represented in the Figure 3.4.<sup>22,23</sup> Other option is a system actuated with acoustic field, where the mixing occurs directly from ultrasonic vibration causing movement of a membrane<sup>24</sup> or specific size microbubbles.<sup>25</sup> This approach demonstrated efficient mixing of small volume reservoirs containing biological sample. However the acoustic field can be problematic due to the generation of heat that may impact the reaction or biological samples.<sup>26</sup> Other approaches use magnetic field actuated micromixers, such as nature-inspired artificial cilia made of nanocomposites (e.g. polymer with superparamagnetic NPs). The rod- or fiber-like structures can oscillate in magnetic field, providing mixing and transport of liquids (Figure 3.5).<sup>27</sup> Other design works with ferrofluids located in a channel perpendicular to the main flow. The actuated ferrofluid causes perturbation in the main fluid flow and generates chaotic mixing of the streams (Figure 3.6).<sup>28</sup> Similar effects can be obtained with introduction of electrically conductive materials, that create flow vortices.<sup>29</sup>

Active micromixers can be further actuated with thermal energy or a combination of previously mentioned methods. Their common characteristic is the need for an external energy source, however thanks to that the mixing can be optimized, which is less feasible in passive micromixers.<sup>17,26</sup>

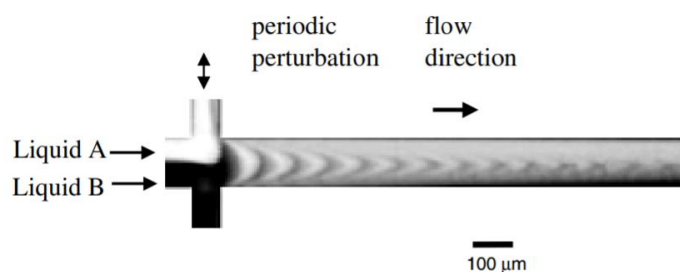


Figure 3.4 Illustration of an active micromixer employing pressure to generate pulse and consecutively mix the two streams.<sup>23</sup>

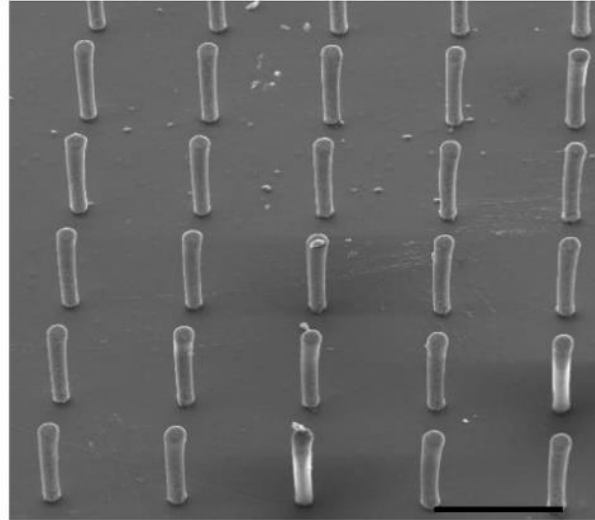


Figure 3.5 SEM image of magnetic field actuated micromixers with artificial cilia made of nanocomposites that can oscillate, providing mixing and transport of liquids, scale bar 350  $\mu\text{m}$ .<sup>30</sup>

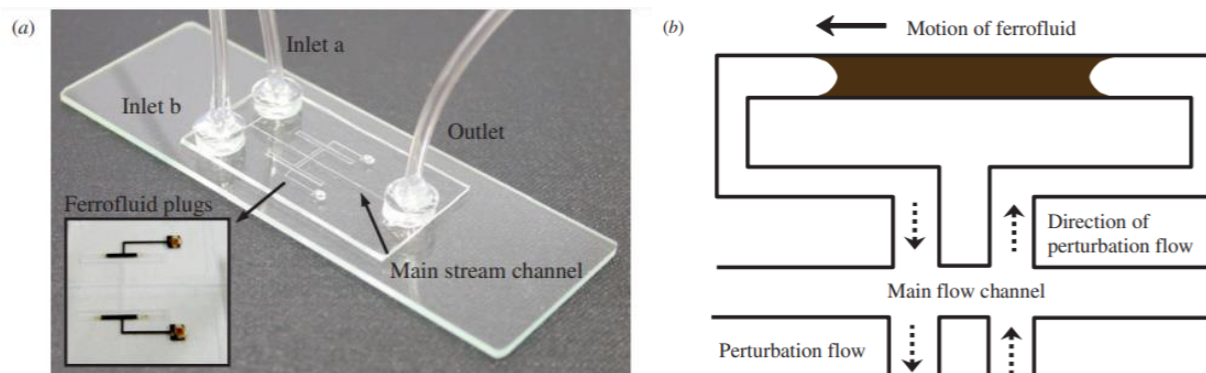


Figure 3.6 An active mixer using ferrofluid. (a) Mixer picture with a picture of a ferrofluid plug in the inset, (b) Schematic of a ferrofluid actuation mechanism.<sup>28</sup>

In this chapter fabrication of a microfluidic passive mixer is demonstrated as well as its incorporation into microfluidic platform for NPs fabrication. First, two-layer micromixer prototypes are made in PDMS and their performance assessed by perfusing fluorescent streams and monitoring with fluorescence microscopy. After the assessment, the selected design is coupled with hydrodynamic flow focusing chip (described in the previous Chapter 2) and the platform used to formulate first color-coded PLGA-PEG NPs via microfluidic nanoprecipitation. The NPs are prepared from micromixer-blended solvent streams carrying different precursors (cyanine dyes) precisely dispensed with a syringe pump. Furthermore, the chip is fabricated in glass to avoid some of the PDMS-related drawbacks and the new model reevaluated. This microfluidic approach in NPs formulation demonstrates applicability in the field of combinatorial and high throughput generation of nanomaterials library. It can support the development of personalized nanomedicine, providing advantage in a form of faster process and better control of the NPs characteristics.

### 3.2 Fabrication and characterization of prototype passive micromixer

The micromixer was designed as a passive model to enhance chaotic advection and diffusion without use of external stimuli. It embodies five inlet channels, facilitating perfusion of independent streams with different flow rate and composition as demonstrated in Figure 3.7 (left panel). The mixing part comprises two complementary layers with six repeating units and parallel line of rectangles for assembly guidance that can be seen in Figure 3.7 (right panel). The repeating geometries provide splitting and rejoining of the perfused stream in plane and out of plane, thanks to which the mixing is enhanced. The perfused and mixed streams are directed into one outlet, that can be further directed to a bulk formulation vessel or connected to another microfluidic chip.

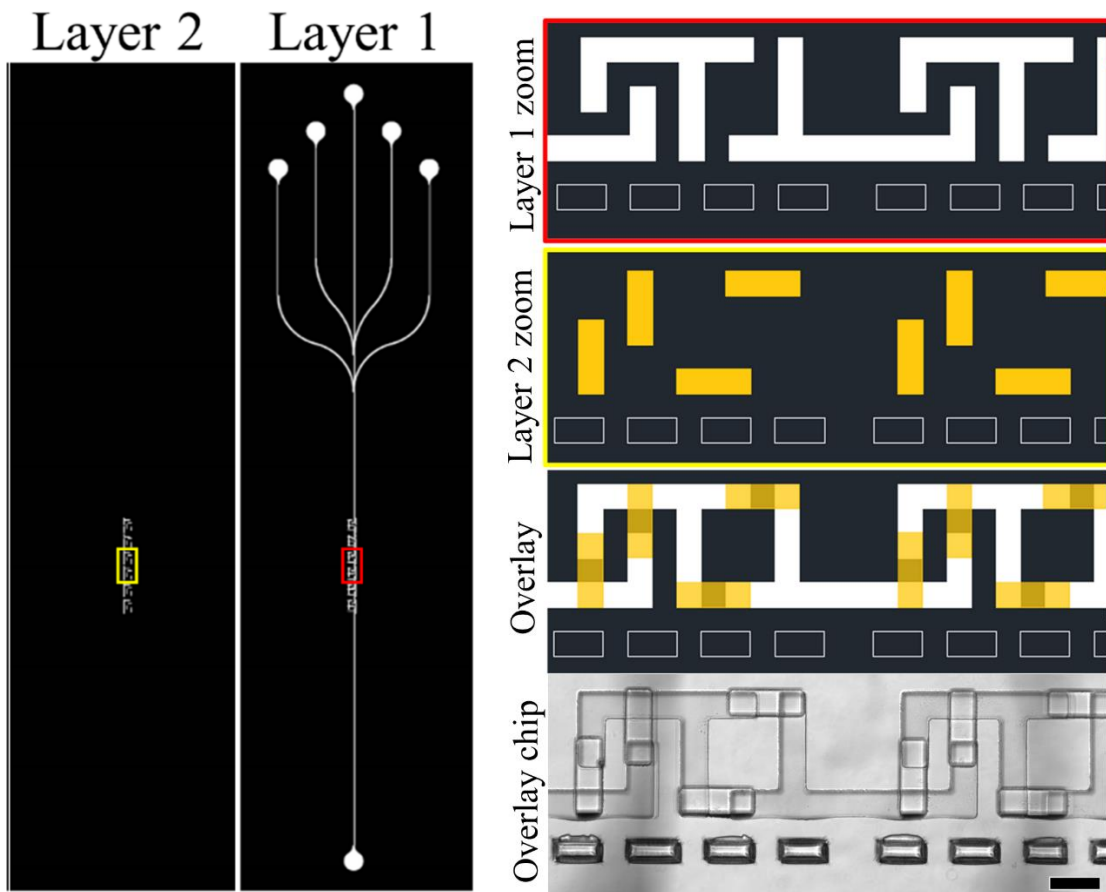


Figure 3.7 The five inlet, two-layer, passive micromixer design, (left panel) zoom out on the full chip, (right panel) zoom in to the mixing units layers, overlay and microscopy image of fabricated and assembled chip, scale bar 200  $\mu\text{m}$ .

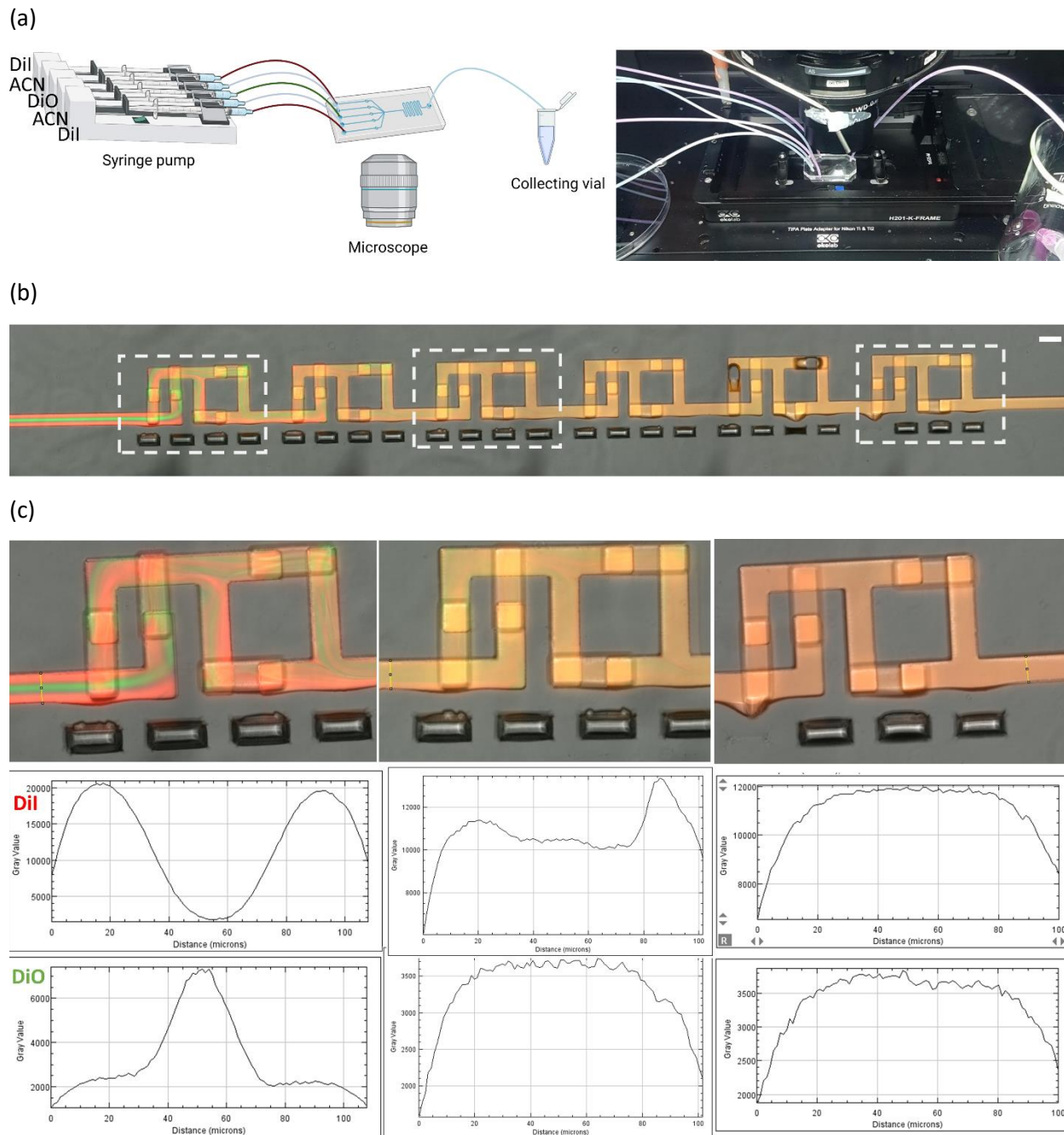
The chip was fabricated with standard photolithography and PDMS soft lithography procedures, similarly to the chip described in Chapter 2. However, an extra step of aligning and bonding the PDMS layers was added (further details in materials and methods): briefly, the surfaces with microstructures were cleaned,

activated with oxygen plasma, and aligned manually with microscope preview and the result can be seen in the bottom of the right panel of the Figure 3.7 that represents a microscope image of the prepared chip.

### 3.3 Fluorescence test of micromixer performance

Mixing efficiency of streams introduced through the five inlets was assessed with fluorescent cyanine dyes. Solution of DiI, DiO and pure ACN were injected using a syringe pump into the inlets in the following order: central channel - DiO, lateral channels – DiI and between central and lateral channels pure ACN, as demonstrated in scheme of the Figure 3.8a (left panel). The microfluidic chip was placed at the microscope holder to monitor the evolution of the mixing, as shown in the image 3.8a (right panel). The solutions were perfused at different flow rates and the mixing of the dyes assessed by measuring their intensity profiles at different parts around the repeating mixing units of the chip, as illustrated in figure 3.8b. First, the intensity profile measured at the straight channel reuniting streams of the five inlets and preceding the first mixing unit, demonstrates that the DiI (red) stream is localized laterally, meanwhile the DiO (green) stream has the intensity peak at the center of the channel as shown in the first panel of Figure 3.8c. The second intensity profile plots are based on a channel cross-section between the second and the third mixing unit (Figure 3.8c, middle panel).

From the graphs it can be seen that the previously clear “valley” and peak for DiI and DiO respectively have lost their geometry and more uniform profile appeared. However, the red stream still demonstrates higher lateral signal comparing to the middle of the channel, as well as the green signal is slightly higher in the channel center than close to the channel walls. After travelling through the six repeating geometries, the dye intensity is measured again, and it is found to be homogeneously distributed for both, the DiI and DiO across the channel width (Figure 3.8c, last panel). It indicates that the mixing of perfused streams was achieved, what can be also observed in the values of the intensity signal. Before reaching the mixing unit the DiI signal is measured with the highest intensity of 20k in the microfluidic channel, meanwhile the DiO signal with its peak halfway the channel cross-section reaches maximum of about 5k. In the outlet past the mixing units, the corresponding intensity signals are found homogenous across the channel with the maximum value about 30-40% lower than observed previously: 12k for the DiI and 3,75k for DiO, indicating dilution of the dyes. The microscope images presented in the Figure 3.8 correspond to a mixing evaluation at a flow rate of 50  $\mu\text{L}/\text{min}$  of each individual stream, however overall mixing performance was measured in the range of flow rates from 2  $\mu\text{L}/\text{min}$  to 50  $\mu\text{L}/\text{min}$  with good outcome across these values.



### PDMS absorption of dye molecules

After the positive mixing results the PDMS chip was flushed at low flow rate with the solvent (ACN) for 90 min. and the wash cycle assessed. As the PDMS is known to absorb small hydrophobic molecules, the



cleaning procedure was extended to face this challenge.<sup>31,32</sup> The intensity profile for DiI solution was measured in one of the inlet channels before the experiment, during the experiment and after the ACN wash (Figure 3.9a). Before dye injection an intensity value of  $\sim 175$  was found, corresponding to a background noise, meanwhile during the perfusion a value close to 100-fold higher ( $\sim 20k$ ) was detected in the same lateral inlet. Finally, the measurement was performed after the solvent wash cycle and the intensity measured in the same region gave values between 2.6k and 3.0k, which is at least an order of magnitude higher than the value found before the perfusion. The PDMS dye absorption was further explored in the area of the chip outlet channel and mixing units. Surprisingly it was found that the signal originating from the absorbed DiI could be detected not only in the microfluidic channel, but also far beyond it, at least 500  $\mu\text{m}$  into the depth of the polymer matrix. The Figure 3.9b demonstrates the dye penetration through the channel walls, with a relatively high intensity values reaching up to 5k in the outlet and on average double of that in the mixers area.

Despite the optimization of the wash cycle, the magnitude of the dye adsorbed and penetrated into the PDMS is too significant to be ignored. The potential desorption of the dye molecules upon future experiments could compromise quantitative and qualitative outcomes as well as interfere and mislead the characterization and evaluation of formulated nanocarriers.

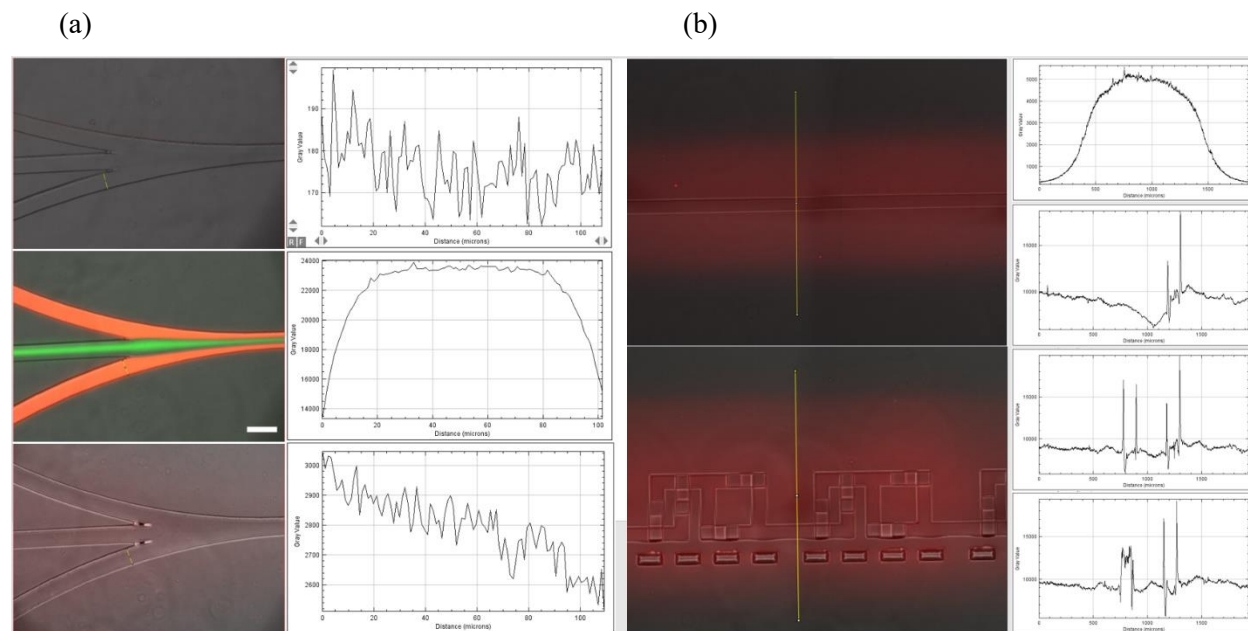


Figure 3.9 Evaluation of mixer cleaning procedure. (a) DiI intensity measured before the experiment, during and after experiment in the area of junction of the inlets, scale bar 500  $\mu\text{m}$ , (b) Fluorescence intensity of DiI measured in the area after the mixing units (top) and in the area of mixing units (bottom).

### 3.4 Combinatorial microfluidic formulation of color-coded nanocarriers

The micromixer chip introduced in the previous paragraphs was designed to facilitate formulation of library of NPs for drug delivery purpose. It was demonstrated that the mixing units yield homogenous stream into the outlet channel, what is crucial in control of the solvent phase composition to later formulate uniform NPs. The five inlets allow to introduce the same number of different precursors that can be further mixed at desired proportions, offering broad range of combinations.

For the proof of concept, the micromixer was connected to a nanoprecipitation chip (described in the Chapter 2) and the polymer mixture stream was directed into the central inlet of the HFF device, where nanoprecipitation occurred and finally the formulated NPs were collected in a vial, as schematically shown in figure 3.10a. The figure 3.10b demonstrates the footprint of assembled setup with the chips, two syringe pumps, collecting vessel, and side-located laptop to control the five-head pump.

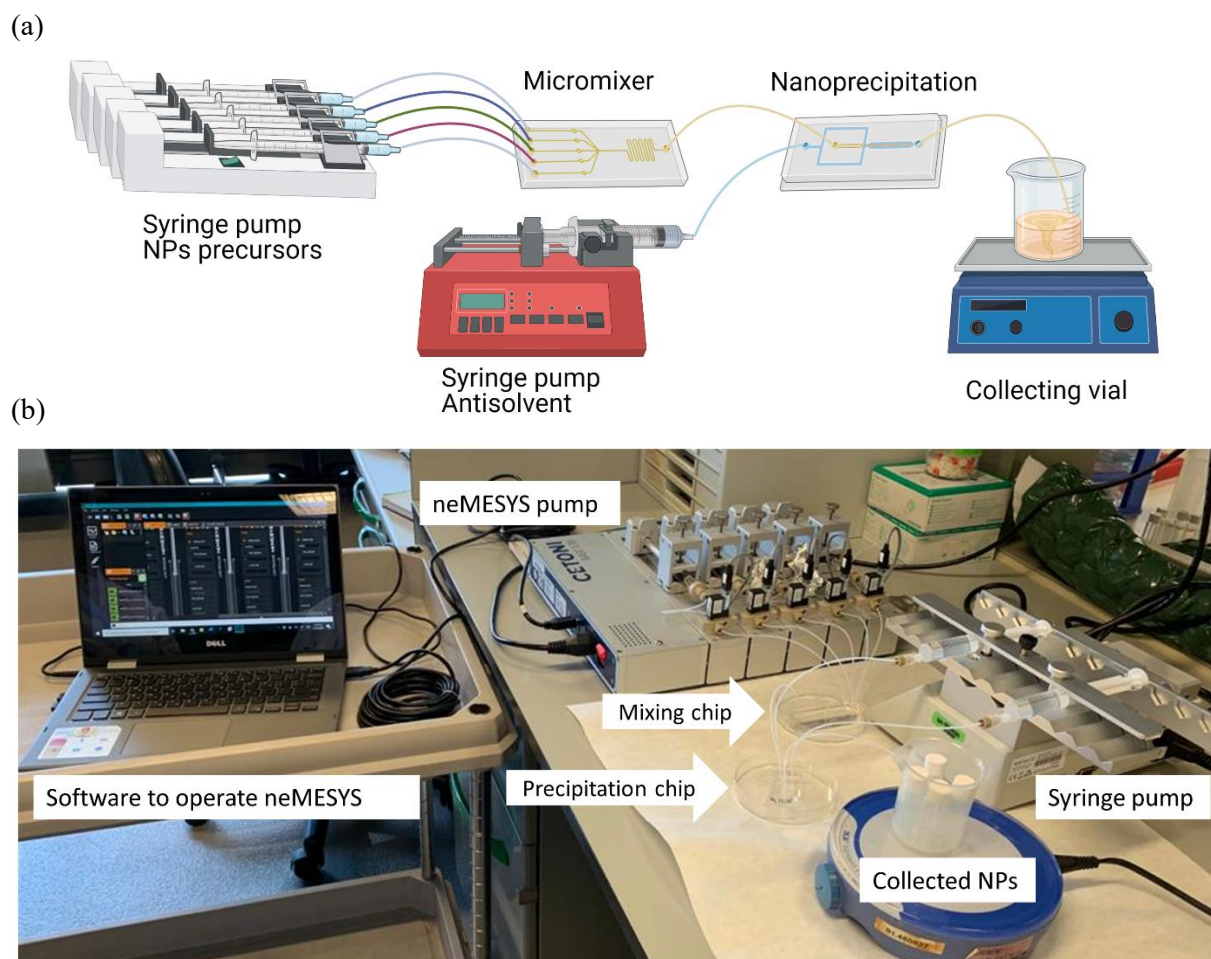


Figure 3.10 Microfluidic platform for combinatorial formulation of NPs consisting of two microfluidic chips (micromixer and HFF). (a) schematic illustration and (b) footprint of the full setup.

*Formulation of NPs in micromixer – nanoprecipitation setup*

The first experiments were designed to explore the micromixer-nanoprecipitation hybrid system. The micromixer chip inlets (Figure 3.11(a)) were connected to five independently-operating syringe pump heads equipped with syringes filled in with ACN and polymer with dye solutions as represented in the table of Figure 3.11(d). Two cyanine dyes DiI and DiD at the concentration of 20  $\mu\text{M}$  and with emission maxima at 565 and 665, respectively (Figure 3.11(b)) were used to formulate color-coded NPs, as this family of dyes is compatible with staining cellular membrane and has demonstrated good encapsulation efficiency (described in the previous chapter). The solvent streams, laterally connected to the micromixer inlets, were added to provide flushes between the batches, facilitating the switch from one to another formulation in possibly cleaned microchannels. Batches C, B and D were formulated first (in this order) with streams containing at least one dye, as demonstrated in Figure 3.11 (c) and (e). The antisolvent for batch B and D consisted of a 1:1 (v/v) mixture between polymer solution stream and respective polymer + dye solution, to provide constant (10  $\mu\text{M}$ ) concentration of each dye across all the formulations (i.e., 10  $\mu\text{M}$  of DiI in batch B, 10  $\mu\text{M}$  of DiI and 10  $\mu\text{M}$  of DiD in batch C and 10  $\mu\text{M}$  of DiD in batch D). The formulation was finalized with fabrication of dye-free (“placebo”) NPs (batch A) to assess the performance of the system by investigating the potential cross-contamination between the dyes and dye leaching from the chip matrix. For the reference manual bulk mixing formulations were performed for the same set of experiments, using manually mixed solvent phase, that was prepared identically for both approaches.

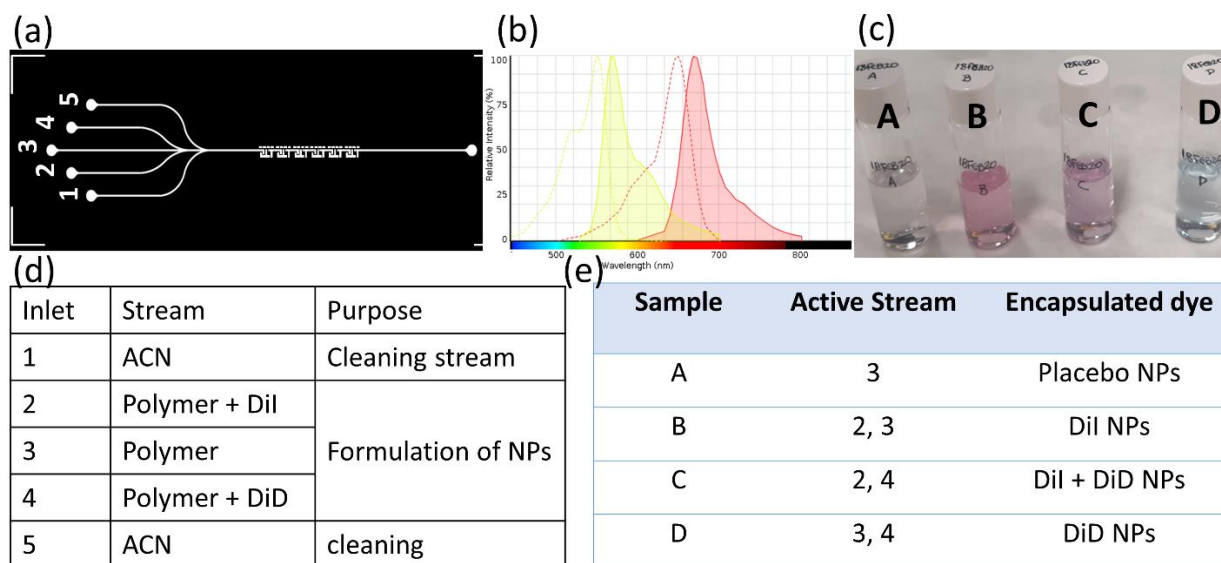


Figure 3.11 Representation of the experimental design: (a) represents numbered inlets of the micromixer chip, corresponding to the streams described in the table (d) below. (b) emission spectra of the selected dyes and (c) shows a picture of vials with formulated NPs and their formulation details described in the table (e) below.

The formulated NPs were characterized using DLS, TEM and TIRF to determine their size distribution and dye encapsulation based on fluorescence. According to DLS analysis, the hydrodynamic diameter of obtained particles is around 90-100 nm and the polydispersity index below 0.1, indicating monodisperse

size distribution as demonstrated in table below. In comparison, the manually formulated batches were slightly smaller in diameter ( $\sim 80$  nm) however a bit higher in size dispersity index ( $\sim 0.12$ ). The particle morphology and appearance were investigated using TEM and spherical shape as well as appearance of core-corona was confirmed for all the formulated batches (Figure 3.12). The TEM-based particle size was found to be a bit smaller than the hydrodynamic diameter, what was already reported before in Chapter 2, as a result of the differences between these two techniques.<sup>33</sup>

Sample	Dye	Diameter (vol.)	Diameter (int.)	Pdl
A	n/a	84.5 nm	92.6 nm	0.09
B	DiI	84.7 nm	94.7 nm	0.08
C	DiI, DiD	94.5 nm	102.1 nm	0.07
D	DiD	91.1 nm	100.6 nm	0.09

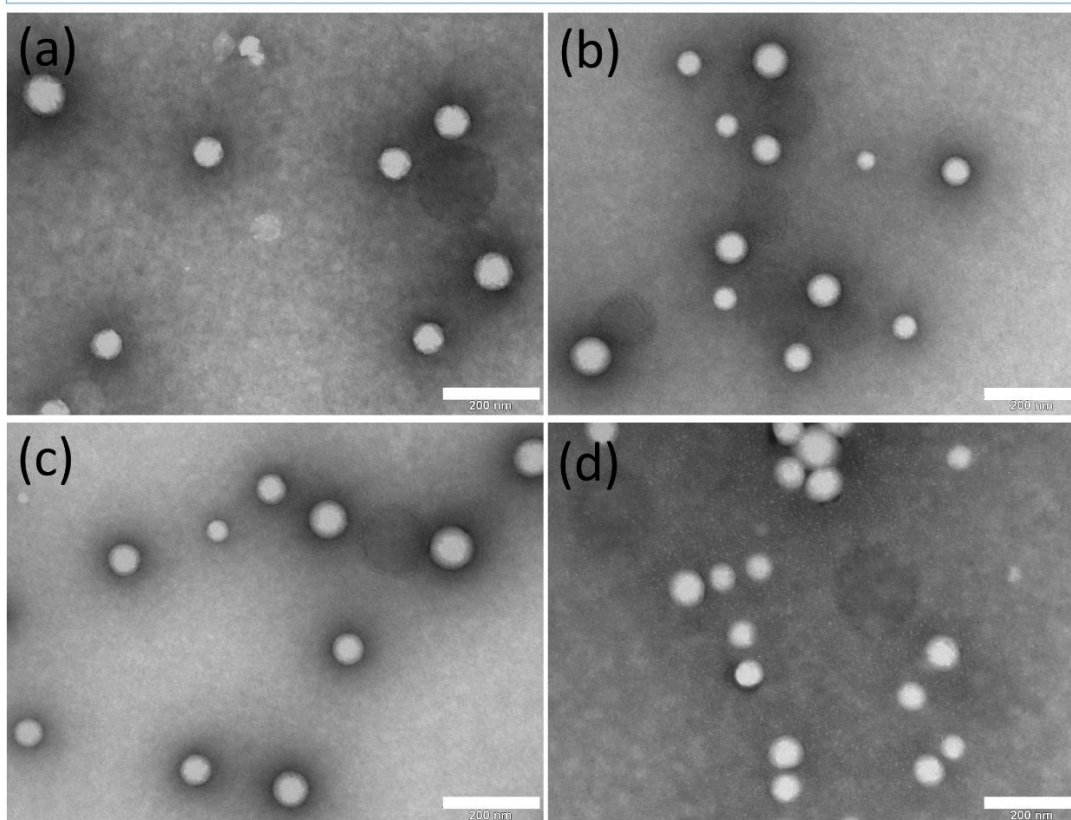


Figure 3.12 Particle size analysis by DLS (table) and TEM images of the corresponding batches a – d., scale bars 200 nm.

The color-coded NPs were analyzed using TIRF microscopy to investigate the dye encapsulation across the different batches. Each field of view was imaged using two laser excitation wavelengths: 561 nm and 647 nm corresponding to the excitation maxima of DiI and DiD, respectively and corresponding images presented in the Figure 3.13. The batch A, which was formulated last in the process, without any dye (placebo), showed some signal in the channel corresponding to the DiD spectrum. This can indicate that

the particles formulated in the preceding batch were carried over and contaminated the formulation A, however the number of detected NPs is not as large as for the preceding batch D. In the images of the batch B, which was formulated first to obtain NPs with DiI, a signal in 561 nm channel was detected, revealing very bright and dim NPs together in one field (Figure 3.13 B). It demonstrates rather heterogenous encapsulation of DiI. On the other hand, as expected, there was no signal detected in DiD excitation/emission spectrum. Next, the batch C was evaluated, which by design includes both dyes in 1:1 ratio. From the images in the Figure 3.13 C can be observed that NPs were detected in both channels, confirming presence of the two dyes. However, it is clear there is significantly more signal from the DiI channel, which was used in the formulation of preceding batch. Additionally, it can be observed that some of the DiI-loaded NPs do not correlate with any particle in DiD channel, meaning these particles are loaded only with one dye. Possibly, the non-matching DiI NPs detected in the batch C could be carried over from the previous formulation of batch B, for example in the outside walls of the tubing that was later immersed into the consecutive batch. Alternatively, they could be a result of the dye leaching from the previously absorbed amounts in the PDMS matrix. However, many of the particles detected in the DiD channel appear to have an analog in the DiI channel, what suggests that there are NPs co-encapsulating both dyes. Interestingly, in the batch D, particles correlating in both channels are visible, which is unexpected, as this formulation should only encapsulate DiD. This means the batch C formulation appears to be blended with D, which similarly to the previous observation, could be a result of carryover or dye leaching. The intensity signal characteristic for DiI is not homogenous, as brighter and dimmer NPs are visible, meaning that the presence of DiI loaded NPs could be twofold: related to carryover from the previous batch (brighter NPs) and associated with dye leaching from the PDMS (dimmer NPs).

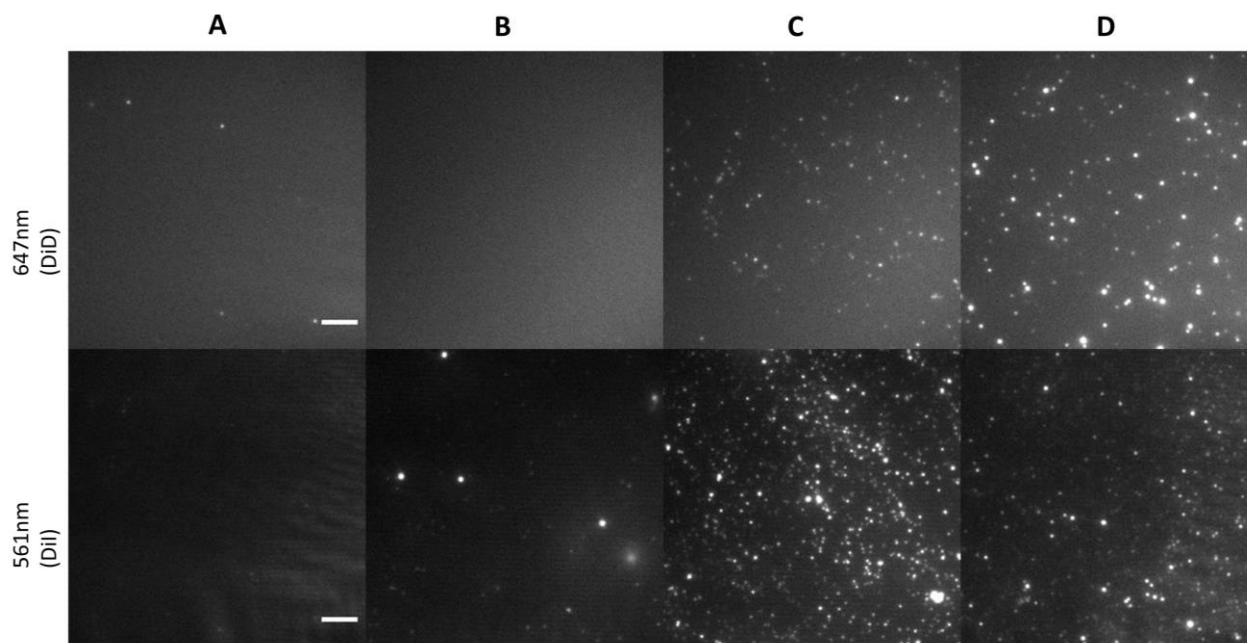


Figure 3.13 TIRF microscopy images evaluating the encapsulation of fluorescent dyes. In sample A (placebo, no dye) with few NPs detected in the wavelength corresponding to DiD, B (DiI loaded NPs) with a signal detected upon excitation with 561 nm laser, and for sample C (both dyes) and D (DiD) with the signal detected upon excitation with 561 nm and 647 nm laser, scale bar 5 $\mu$ m.

The microfluidic mixer demonstrated efficient mixing of five introduced streams, as well as compatibility with the nanoprecipitation setup, that altogether allowed to formulate monodisperse nanoparticles loaded with fluorescent dyes. However, the dye encapsulation was burdened with cross-contamination, that in the perspective of personalized nanomedicine would compromise any experimental design. For that reason the study was continued in a micromixer fabricated in glass.

### 3.5 Beyond PDMS: Micromixer in glass

For the reason of PDMS absorbing/desorbing dyes, the previously evaluated micromixer (as well as the nanoprecipitation chip, similar to the one presented in the Chapter 2), was fabricated in glass to eliminate this drawback. The fabrication was performed externally by Little Things Factory (LTF) GmbH, (Germany), employing their proprietary technology for microchannel fabrication and bonding of the layers. Due to their confidentiality, the details of laser etching and thermal bonding cannot be disclosed more specifically. The fabrication rules dictated by their technique were as follow: channel depth within 5-50  $\mu$ m and the channel width more than 50  $\mu$ m; which was compatible with the micromixer design already prototyped and tested in PDMS. The micromixer was fabricated in floated borosilicate glass (Borofloat33<sup>®</sup>, Plan Optik AG, Germany) characterized by chemical durability, thermal resistivity, and very good optical properties. Additionally, chip connectors were bonded to the inlets and outlet to be compatible with 1/4-28 threaded nut connectors and ferrules, typically used in microfluidic technology to provide robust and

standardized connection. Figure 3.14(a) represents top view on the glass micromixer chip with black o-rings inserts for leakproof connection, and before assembly. In the Figure 3.14(b) the chip is placed on a microscope stage and connected to the perfusion system, where the cleaning procedure of the microchannels (Figure 3.14(c) is further assessed by the same procedure in the case of PDMS prototype described above.

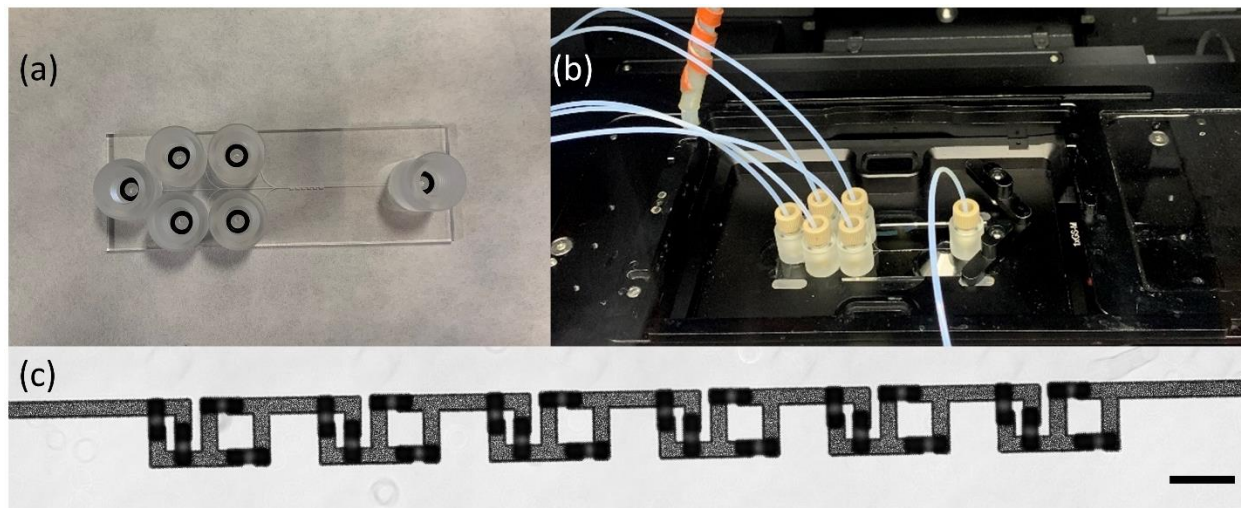


Figure 3.14 (a) Photo chip with orings before assembly, (b) Photo of the assembled chip in the microscope and (c) microscope image with zoom on the mixing microchannels, scale bar 500  $\mu\text{m}$ .

The micromixer installed on the microscope stage holder was connected to a five-head syringe pump and perfused with solution of DiI, DiD and pure solvent to perform the mixing of injected streams and further to evaluate the cleaning procedure. The process followed the steps described previously for the PDMS micromixer, with a special focus on the final acetonitrile wash. The microchannels were imaged during the perfusion of dyes as well as after solvent flush. The signal intensity for DiI was measured for both steps at two different parts of the chip: right after the second junction of the inlet channels and in the middle of repeating mixing units, as demonstrated in the top and bottom row of Figure 3.15. The signal intensity of DiI fluorescence reached 8k and 10k in two peaks originating from two lateral streams preceding the mixing units and a maximum of about 7k in the middle of the mixing part. The intensity measured after the solvent flush dropped to 0.11-0.12k, what corresponds to the values before flowing of the dye solution as well as to the intensity values found in PDMS micromixer before perfusion of the fluorescent solution. On base of that it can be confirmed that there is no dye absorption and ACN washing cycle efficiently cleans residual dye and prepares the chip for further use.

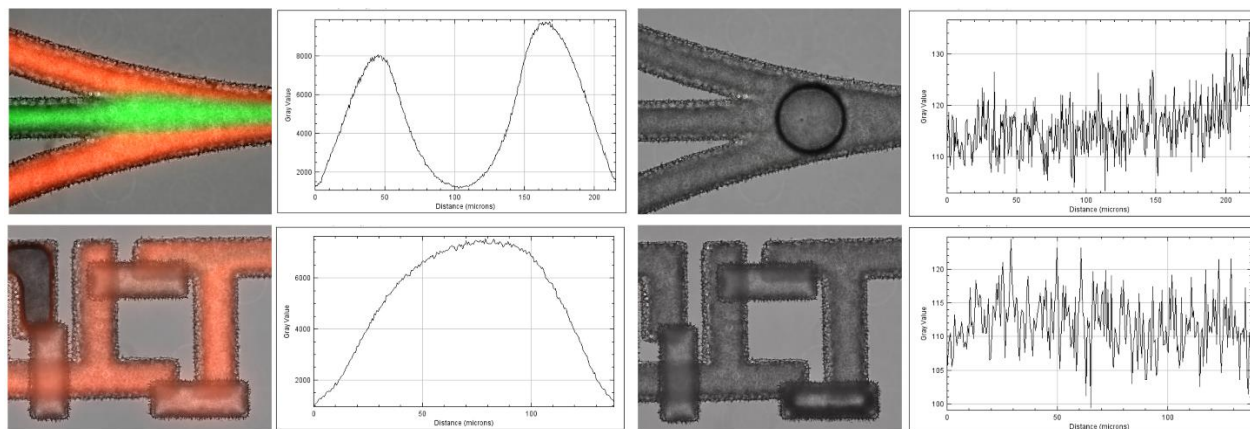


Figure 3.15 Evaluation of washing procedure in the glass microfluidic mixer. Top row demonstrates intensity profile of DiI (red) measured during dye perfusion and after the ACN cleaning in the inlet junction. Bottom row represents intensity profile of DiI in a mixing unit during the dye perfusion and after the ACN cleaning. Post-cleaning intensity values demonstrate lack of absorption of the dyes.

#### Formulation of NPs in glass micromixer – nanoprecipitation setup

The glass micromixer was coupled to a HFF microfluidic chip to formulate NPs as it was done for the PDMS micromixer. The design of experiment was the same as for the PDMS chip, that can be consulted in Figure 3.11, specifically: batch with DiI (B) was formulated first, and then batch with both dyes (C), with DiD (D) and a batch without activation of dye loaded streams (A). ACN flush was executed between the batches to wash away residual dye. The size of NPs was measure with DLS indicating monodisperse NPs with diameter between 80-100 nm and further the dye encapsulation was imaged with TIRF microscopy as described before. Briefly, the color-coded NPs were imaged using two laser excitation wavelengths: 561 nm and 647 nm corresponding to the excitation maxima of DiI and DiD, respectively and selected images presented in the Figure 3.16. In the formulation A (placebo) performed in the glass mixer setup, there was no signal detected neither for DiI channel, nor for DiD. This can indicate that the ACN flushes fulfilled the dye washing function and change of PDMS to glass helped to avoid undesired dye leaching. Further imaged and analyzed particles formulated in batches B – D reveal respectively the presence of DiI, both dyes and DiD, corresponding to the experimental design. Furthermore, the batch C, that contains NPs co-encapsulating the two dyes shows correlating localizations between the image acquired with excitation at 561 nm and 647 nm, what indicates successful and efficient process (Figure 3.16C). Looking closely at the Figure 3.16D it can be seen that there is some signal in the 561 nm excited field, suggesting that some DiI loaded NPs are present. This could be a small carry-over of DiI from the previous batch, that possibly could be avoided by prolonged ACN wash.



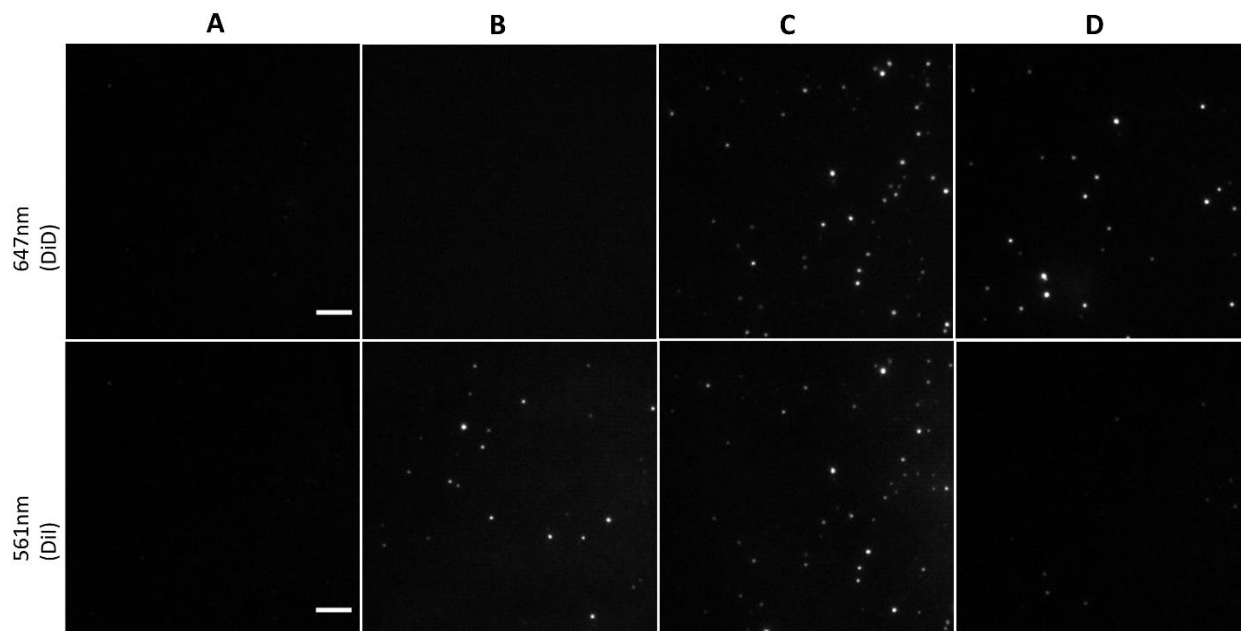


Figure 3.16 TIRF microscopy images evaluating the encapsulation of fluorescent dyes. In sample A (placebo, no dye) with few NPs detected in the wavelength corresponding to DiD, B (DiI loaded NPs) with a signal detected upon excitation with 561 nm laser, and for sample C (both dyes) and D (DiD) with the signal detected upon excitation with 561 nm and 647 nm laser, scale bar 5 $\mu$ m.

### 3.6 Conclusions

Microfluidic passive mixer design has been described in this Chapter with a special focus on a nanomedicine formulation. First the proposed design was prototyped in a cost-efficient manner, using photolithography and PDMS microfabrication to assess the mixing performance. The evaluation was performed using a solution of fluorescent dyes, which were later used as a model cargo of potential drug nanocarriers. The mixer design demonstrated good performance in a range of the tested flow rates. It was also connected with Nanoprecipitation chip (described in the Chapter 2) to demonstrate its applicability in the combinatorial formulation of color-coded monodisperse nanocarriers. Also, a cleaning procedure was probed, which unfortunately identified PDMS absorption issue that could not be eliminated in a simple manner. For this reason, the design and microfabrication were further outsourced to a company specialized in microfabrication of microfluidic chips in glass. The glass chips were created and equipped with standardized connectors. The mixing performance was maintained comparing to the PDMS prototype, furthermore the same cleaning procedure demonstrated that the glass, as a material, helped to eliminate the issue of dye adsorption occurring in PDMS. Glass turned out to be more suitable material of the microfluidic chip for NPs precursor mixing, especially that it opened the door to test other than acetonitrile solvents, which was previously selected as a compromise between polymer solubility and PDMS chemical compatibility. The glass micromixer incorporated into the NPs formulation platform demonstrated efficient mixing of five streams and improved control in dye encapsulation, comparing to the PDMS prototype.

### 3.7 Experimental section

*Solvent and antisolvent phase preparation for formulation of NPs*

*Fabrication of the PDMS chip*

*Hydrodynamic Flow Focusing (HFF) formulation*

*Encapsulation of fluorescent compounds*

*NPs characterization - Dynamic Light Scattering*

*NPs characterization - Transmission Electron Microscopy*

*Total internal reflection (TIR) fluorescence imaging*

See Chapter 2

#### *PDMS Layers Bonding*

The complementary layers were washed with soap, sonicated for 1 min. in EtOH and dried at 95degC on a hotplate for 10 min. In the next step they were plasma treated during 30 sec. at high RF level (Plasma Cleaner Harrick, PCD-002-CE) and moved under the microscope objective (Olympus, SZX2-ILLB). The layers were faced together with a droplet of 70% EtOH to facilitate the sliding and prevent immediate bonding. The alignment was manually performed with a pair of metal tweezers, following the matching of side channel guiding rectangles. The aligned layers were carefully placed onto a hot plate at 95degC for 30 min to accelerate the liquid evaporation and further baked at 65degC for 24h in the oven (Selecta).

### 3.8 References

- (1) Luque-Michel, E.; Sebastian, V.; Larrea, A.; Marquina, C.; Blanco-Prieto, M. J. Co-Encapsulation of Superparamagnetic Nanoparticles and Doxorubicin in PLGA Nanocarriers: Development, Characterization and in Vitro Antitumor Efficacy in Glioma Cells. *Eur. J. Pharm. Biopharm.* **2019**, *145*, 65–75. <https://doi.org/10.1016/j.ejpb.2019.10.004>.
- (2) Motevalli, S. M.; Eltahan, A. S.; Liu, L.; Magrini, A.; Rosato, N.; Guo, W.; Bottini, M.; Liang, X.-J. Co-Encapsulation of Curcumin and Doxorubicin in Albumin Nanoparticles Blocks the Adaptive Treatment Tolerance of Cancer Cells. *Biophys. Rep.* **2019**, *5* (1), 19–30. <https://doi.org/10.1007/s41048-018-0079-6>.
- (3) Wilhelm, S.; Tavares, A. J.; Dai, Q.; Ohta, S.; Audet, J.; Dvorak, H. F.; Chan, W. C. W. Analysis of Nanoparticle Delivery to Tumours. *Nat. Rev. Mater.* **2016**, *1* (5), 1–12. <https://doi.org/10.1038/natrevmats.2016.14>.
- (4) Guo, M.; Peng, Y.; Gao, A.; Du, C.; Herman, J. G. Epigenetic Heterogeneity in Cancer. *Biomark. Res.* **2019**, *7* (1), 1–19. <https://doi.org/10.1186/s40364-019-0174-y>.
- (5) van de Wetering, M.; Francies, H. E.; Francis, J. M.; Bounova, G.; Iorio, F.; Pronk, A.; van Houdt, W.; van Gorp, J.; Taylor-Weiner, A.; Kester, L.; McLaren-Douglas, A.; Blokker, J.; Jaksani, S.; Bartfeld, S.; Volckman, R.; van Sluis, P.; Li, V. S. W.; Seepo, S.; Sekhar Pedamallu, C.; Cibulskis, K.; Carter, S. L.; McKenna, A.; Lawrence, M. S.; Lichtenstein, L.; Stewart, C.; Koster, J.; Versteeg, R.; van Oudenaarden, A.; Saez-Rodriguez, J.; Vries, R. G. J.; Getz, G.; Wessels, L.; Stratton, M. R.; McDermott, U.; Meyerson, M.; Garnett, M. J.; Clevers, H. Prospective Derivation of a Living Organoid Biobank of Colorectal Cancer Patients. *Cell* **2015**, *161* (4), 933–945. <https://doi.org/10.1016/j.cell.2015.03.053>.
- (6) Activation Station | Solstice Pharma - Ultrasound Contrast Agents. *Solstice*.
- (7) Schork, N. J. Personalized Medicine: Time for One-Person Trials. *Nat. News* **2015**, *520* (7549), 609. <https://doi.org/10.1038/520609a>.
- (8) Yaari, Z.; da Silva, D.; Zinger, A.; Goldman, E.; Kajal, A.; Tshuva, R.; Barak, E.; Dahan, N.; HersHKovitz, D.; Goldfeder, M.; Roitman, J. S.; Schroeder, A. Theranostic Barcoded Nanoparticles for Personalized Cancer Medicine. *Nat. Commun.* **2016**, *7* (1), 13325. <https://doi.org/10.1038/ncomms13325>.
- (9) Medina, D. X.; Householder, K. T.; Ceton, R.; Kovalik, T.; Heffernan, J. M.; Shankar, R. V.; Bowser, R. P.; Wechsler-Reya, R. J.; Sirianni, R. W. Optical Barcoding of PLGA for Multispectral Analysis of Nanoparticle Fate in Vivo. *J. Controlled Release* **2017**, *253*, 172–182. <https://doi.org/10.1016/j.jconrel.2017.02.033>.
- (10) Andreiuk, B.; Reisch, A.; Lindecker, M.; Follain, G.; Peyri ras, N.; Goetz, J. G.; Klymchenko, A. S. Fluorescent Polymer Nanoparticles for Cell Barcoding In Vitro and In Vivo. *Small* **2017**, *13* (38), 1701582. <https://doi.org/10.1002/sml.201701582>.
- (11) Kim, Y.; Lee Chung, B.; Ma, M.; Mulder, W. J. M.; Fayad, Z. A.; Farokhzad, O. C.; Langer, R. Mass Production and Size Control of Lipid–Polymer Hybrid Nanoparticles through Controlled Microvortices. *Nano Lett.* **2012**, *12* (7), 3587–3591. <https://doi.org/10.1021/nl301253v>.
- (12) Valencia, P. M.; Pridgen, E. M.; Rhee, M.; Langer, R.; Farokhzad, O. C.; Karnik, R. Microfluidic Platform for Combinatorial Synthesis and Optimization of Targeted Nanoparticles for Cancer Therapy. *ACS Nano* **2013**, *7* (12), 10671–10680. <https://doi.org/10.1021/nn403370e>.
- (13) Lim, J.-M.; Swami, A.; Gilson, L. M.; Chopra, S.; Choi, S.; Wu, J.; Langer, R.; Karnik, R.; Farokhzad, O. C. Ultra-High Throughput Synthesis of Nanoparticles with Homogeneous Size Distribution Using a Coaxial Turbulent Jet Mixer. *ACS Nano* **2014**, *8* (6), 6056–6065. <https://doi.org/10.1021/nn501371n>.

- (14) Yang, C.-G.; Xu, Z.-R.; Lee, A. P.; Wang, J.-H. A Microfluidic Concentration-Gradient Droplet Array Generator for the Production of Multi-Color Nanoparticles. *Lab. Chip* **2013**, *13* (14), 2815–2820. <https://doi.org/10.1039/C3LC50254F>.
- (15) Beebe, D. J.; Mensing, G. A.; Walker, G. M. Physics and Applications of Microfluidics in Biology. *Annu. Rev. Biomed. Eng.* **2002**, *4* (1), 261–286. <https://doi.org/10.1146/annurev.bioeng.4.112601.125916>.
- (16) Nguyen, N.-T.; Wu, Z. Micromixers—a Review. *J. Micromechanics Microengineering* **2004**, *15* (2), R1–R16. <https://doi.org/10.1088/0960-1317/15/2/R01>.
- (17) Cai, G.; Xue, L.; Zhang, H.; Lin, J. A Review on Micromixers. *Micromachines* **2017**, *8* (9), 274. <https://doi.org/10.3390/mi8090274>.
- (18) Fang, Y.; Ye, Y.; Shen, R.; Zhu, P.; Guo, R.; Hu, Y.; Wu, L. Mixing Enhancement by Simple Periodic Geometric Features in Microchannels. *Chem. Eng. J.* **2012**, *187*, 306–310. <https://doi.org/10.1016/j.cej.2012.01.130>.
- (19) Xia, H. M.; Wan, S. Y. M.; Shu, C.; Chew, Y. T. Chaotic Micromixers Using Two-Layer Crossing Channels to Exhibit Fast Mixing at Low Reynolds Numbers. *Lab. Chip* **2005**, *5* (7), 748–755. <https://doi.org/10.1039/B502031J>.
- (20) Stott, S. L.; Hsu, C.-H.; Tsukrov, D. I.; Yu, M.; Miyamoto, D. T.; Waltman, B. A.; Rothenberg, S. M.; Shah, A. M.; Smas, M. E.; Korir, G. K.; Floyd, F. P.; Gilman, A. J.; Lord, J. B.; Winokur, D.; Springer, S.; Irimia, D.; Nagrath, S.; Sequist, L. V.; Lee, R. J.; Isselbacher, K. J.; Maheswaran, S.; Haber, D. A.; Toner, M. Isolation of Circulating Tumor Cells Using a Microvortex-Generating Herringbone-Chip. *Proc. Natl. Acad. Sci.* **2010**, *107* (43), 18392–18397. <https://doi.org/10.1073/pnas.1012539107>.
- (21) Hadjigeorgiou, A. G.; Boudouvis, A. G.; Kokkoris, G. Thorough Computational Analysis of the Staggered Herringbone Micromixer Reveals Transport Mechanisms and Enables Mixing Efficiency-Based Improved Design. *Chem. Eng. J.* **2021**, *414*, 128775. <https://doi.org/10.1016/j.cej.2021.128775>.
- (22) Glasgow, I.; Aubry, N. Enhancement of Microfluidic Mixing Using Time Pulsing. *Lab. Chip* **2003**, *3* (2), 114–120. <https://doi.org/10.1039/B302569A>.
- (23) Niu, X.; Lee, Y.-K. Efficient Spatial-Temporal Chaotic Mixing in Microchannels. *J. Micromechanics Microengineering* **2003**, *13* (3), 454–462. <https://doi.org/10.1088/0960-1317/13/3/316>.
- (24) Yang, Z.; Matsumoto, S.; Goto, H.; Matsumoto, M.; Maeda, R. Ultrasonic Micromixer for Microfluidic Systems. *Sens. Actuators Phys.* **2001**, *93* (3), 266–272. [https://doi.org/10.1016/S0924-4247\(01\)00654-9](https://doi.org/10.1016/S0924-4247(01)00654-9).
- (25) Liu, R. H.; Yang, J.; Pindera, M. Z.; Athavale, M.; Grodzinski, P. Bubble-Induced Acoustic Micromixing. *Lab. Chip* **2002**, *2* (3), 151–157. <https://doi.org/10.1039/B201952C>.
- (26) Bayareh, M.; Ashani, M. N.; Usefian, A. Active and Passive Micromixers: A Comprehensive Review. *Chem. Eng. Process. - Process Intensif.* **2020**, *147*, 107771. <https://doi.org/10.1016/j.cep.2019.107771>.
- (27) Toonder, J. M. J. den; Onck, P. R. Microfluidic Manipulation with Artificial/Bioinspired Cilia. *Trends Biotechnol.* **2013**, *31* (2), 85–91. <https://doi.org/10.1016/j.tibtech.2012.11.005>.
- (28) Oh, D.-W.; Jin, J. S.; Choi, J. H.; Kim, H.-Y.; Lee, J. S. A Microfluidic Chaotic Mixer Using Ferrofluid. *J. Micromechanics Microengineering* **2007**, *17* (10), 2077–2083. <https://doi.org/10.1088/0960-1317/17/10/020>.
- (29) Kazemi, Z.; Rashidi, S.; Esfahani, J. A. Effect of Flap Installation on Improving the Homogeneity of the Mixture in an Induced-Charge Electrokinetic Micro-Mixer. *Chem. Eng. Process. Process Intensif.* **2017**, *121*, 188–197. <https://doi.org/10.1016/j.cep.2017.08.015>.

- (30) Zhang, S.; Wang, Y.; Lavrijsen, R.; Onck, P. R.; den Toonder, J. M. J. Versatile Microfluidic Flow Generated by Moulded Magnetic Artificial Cilia. *Sens. Actuators B Chem.* **2018**, *263*, 614–624. <https://doi.org/10.1016/j.snb.2018.01.189>.
- (31) Li, N.; Schwartz, M.; Ionescu-Zanetti, C. PDMS Compound Adsorption in Context. *J. Biomol. Screen.* **2009**, *14* (2), 194–202. <https://doi.org/10.1177/1087057108327326>.
- (32) When PDMS Isn't the Best. *Anal. Chem.* **2007**, *79* (9), 3248–3253. <https://doi.org/10.1021/ac071903e>.
- (33) Sperling, R. A.; Liedl, T.; Duhr, S.; Kudera, S.; Zanella, M.; Lin, C.-A. J.; Chang, W. H.; Braun, D.; Parak, W. J. Size Determination of (Bio)Conjugated Water-Soluble Colloidal Nanoparticles: A Comparison of Different Techniques. *J. Phys. Chem. C* **2007**, *111* (31), 11552–11559. <https://doi.org/10.1021/jp070999d>.

## Chapter 4| Real-time imaging of micelle stability in a microfluidic cancer-on-a-chip

*This chapter reproduces almost literally the article: **Real-time Ratiometric Imaging of Micelles Assembly State in a Microfluidic Cancer-on-a-chip** ACS Appl. Bio Mater. 2021, 4, 1, 669-681, Glinkowska Mares, A., Feiner-Gracia, N., Buzhor, M., Rodriguez-Trujillo, R., Samitier Marti, J., Amir, R. J., Pujals, S., Albertazzi, L. My contribution to this manuscript was the execution of experimental part, design of experiments and writing the manuscript together with Feiner-Gracia N. Further, Pujals S. and Albertazzi L. supervised the work and contributed to experimental planning. Pujals S., Albertazzi L and Samitier Marti, J. provided periodic feedback on the results and reviewed the manuscript. Amir R. J. and Buzhor, M. synthesized and provided the micelles, as well as reviewed the manuscript.*

*This chapter presents multidisciplinary approach to in vitro screening of drug delivery systems. We created a model of a tumor blood vessel in a microfluidic chip to recapitulate parts of 3D tumor microenvironment. Further this microscopy-friendly platform served as a screening device for stability and extravasation of fluorescent micelles with special optical properties. We compared obtained results with previously reported findings in 2D cell culture, revealing important differences between the two models.*

## 4.1 Introduction

Supramolecular nanocarriers, such as liposomes or micelles, are broadly investigated as potential drug delivery systems (DDS) for cancer therapy <sup>2, 3</sup>. Since Doxil, a liposome-encapsulated Doxorubicin, was approved in 1995 <sup>4</sup>, the therapeutic efficacy of many nanosystems with different chemical features have been tested. However, low accumulation of the nanoparticles (NPs) in the solid tumor is still a major issue<sup>5</sup> and one of the key reasons for failures in clinical trials. One of the main challenges with the use of supramolecular nanocarriers is to control their assembly-disassembly equilibrium, which determines *in vivo* success. The exposure to physiological environment affects the properties and decreases the number of fully assembled NPs arriving to the target site <sup>6</sup>. Therefore, it is important to design nanosystems that are stable once injected into the body, and “smart” to free up the cargo when the target is reached.

Right at the injection site, the NPs are subjected to a high dilution, interactions with serum proteins and shear stress in a blood vessel, which favors their disassembly and leads to premature drug release into the blood stream, causing systemic cytotoxicity or uncontrolled drug distribution <sup>7, 8, 9</sup>. Internal walls of blood vessels are layered with endothelial cells (ECs), connected by characteristic tight junctions, which create a physical barrier, allowing the diffusion of small molecules only <sup>10</sup>. Interactions with ECs membrane, upon NPs extravasation, can further compromise their stability. Nowadays, most of nanoparticles-based drug delivery systems (DDS) rely on the enhanced permeability and retention (EPR) effect<sup>11</sup>. During EPR the endothelial junctions are impaired, creating gaps that allow larger molecules to leave the systemic circulation <sup>12</sup>, thus opening an escape route for the NPs <sup>13</sup>. Particles able to extravasate through the “leaky” endothelial barrier (EB), arrive to the extracellular matrix (ECM) and the cancer cells. The ECM can differ in pH and shear stress comparing to the blood vessel <sup>14</sup> and its components can affect the NPs assembly equilibrium <sup>6</sup>. The predictability and understanding of the stability of supramolecular assemblies within these changing conditions, can pave the way to an improved design of nanosystems to be translated into the clinics.

Due to the difficulties in real-time monitoring of NPs in physiologically relevant milieu many aspects are not addressed when screening DDS candidates. Recently, a Förster Resonance Energy Transfer (FRET) approach was used to follow the disassembly of supramolecular structures in blood serum <sup>15-18</sup>, and in animal models <sup>19</sup>, by encapsulation or covalent attachment of a FRET fluorophore pair into one micelle. In our recent work we employed PEG-Dendron amphiphiles that were functionalized with a spectral-shifting coumarin to track the stability of micelles in serum and cells <sup>20</sup>. These micelles can self-report their disassembly by the change of their fluorescent spectrum to the intrinsic emission of the labeling coumarin dyes. The change in assembly can be detected in complex media using spectral imaging, enabling the NPs

stability study in space and time. Nevertheless, the *in vitro* assays consist mainly of 2D systems, which despite of being high throughput and rapid, do not provide complete information reflecting the *in vivo* conditions <sup>21</sup>. In the last years microfluidic 3D models have been extensively used to study cancer cells migration <sup>23–26</sup>, vascularization and angiogenesis <sup>27–30</sup>, EB permeability <sup>31–33</sup>, impact of 3D cell architecture <sup>34–36</sup> and tumor penetration <sup>35,37–39</sup>. Recently, more complex blood vessel models have been designed in order to assess the differences in nanoparticles permeation in various conditions <sup>14,31,32,40,41</sup>, demonstrating an impact of cancer cells on the endothelial permeability. However, in majority of them only the intervals or end time point of nanoparticles incubation are reported, lacking the important time-resolved information. Herein, we address this challenge by combining a real-time spectral confocal imaging of polymeric, self-reporting micelles which are perfused through tumor blood vessel model in a cancer-on-a-chip platform, to map their stability when encountering biological barriers. By evolving conventional 2D studies into more adequate 3D models <sup>34,42,43</sup> we aim to expand our previous work <sup>20</sup> and provide additional screening before use of animal models <sup>22,44–46</sup>.



## 4.2 The system: amphiphilic PEG-dendron micelles and cancer-on-a-chip

Three amphiphilic PEG-dendron hybrids, differing by their lipophilic end-groups in the hydrophobic block, were synthesized and characterized following the previously reported methodology<sup>20,47</sup>, the structures are shown in Figure 4.1a. The amphiphiles were labeled with a responsive dye, 7-diethylamino-3-carboxy coumarin, which forms an excimer when the hybrids self-assemble into micelles, resulting in a red-shift of the dye emission spectra, allowing to discriminate the assembled state from the disassembled state, as shown in Figure 4.1a. The responsive properties of these micelles, studied in presence of serum proteins, HeLa cells and at physiologically relevant temperature (37°C), have been previously demonstrated<sup>20</sup>. Here we study the stability of these nanostructures in a cancer-on-a-chip platform and compare the results to the previously reported behavior in 2D cell culture.

In the cancer-on-a-chip model we recapitulate the four important barriers that the micelles will have to overpass when injected into the body: 1) the flow of the blood vessel model; 2) the endothelial barrier; 3) the ECM, and 4) the tumor spheroid (Figure 1b). To recreate this environment in a microfluidic platform we used the 3D cell culture chip developed in Kamm's Lab and currently available commercially<sup>48</sup>. It consists of 3 microfluidic channels: the central channel of 1.3 x 0.25 mm (w x h) and the two lateral media channels of 0.5 x 0.25 mm (w x h), as represented in Figure 4.1c. The middle channel is separated from the two lateral channels by rows of triangular microposts distant by 100  $\mu\text{m}$  from one another, as shown in Figure 4.1c and f. These posts are designed to contain the unpolymerized gel (spheroids + collagen) in the central channel, by ensuring adequate surface tension, preventing gel leaks. In our model, one of the lateral channels represents the blood vessel and the middle channel recreates the ECM with embedded tumor spheroids as in the Figure 4.1d. Human Umbilical Vein Endothelial Cells (HUVECs) seeded in the lateral channel, lined it and formed a lumen-like geometry, creating a vertical endothelial wall on the collagen gel scaffold (Figure 4.1e and f).

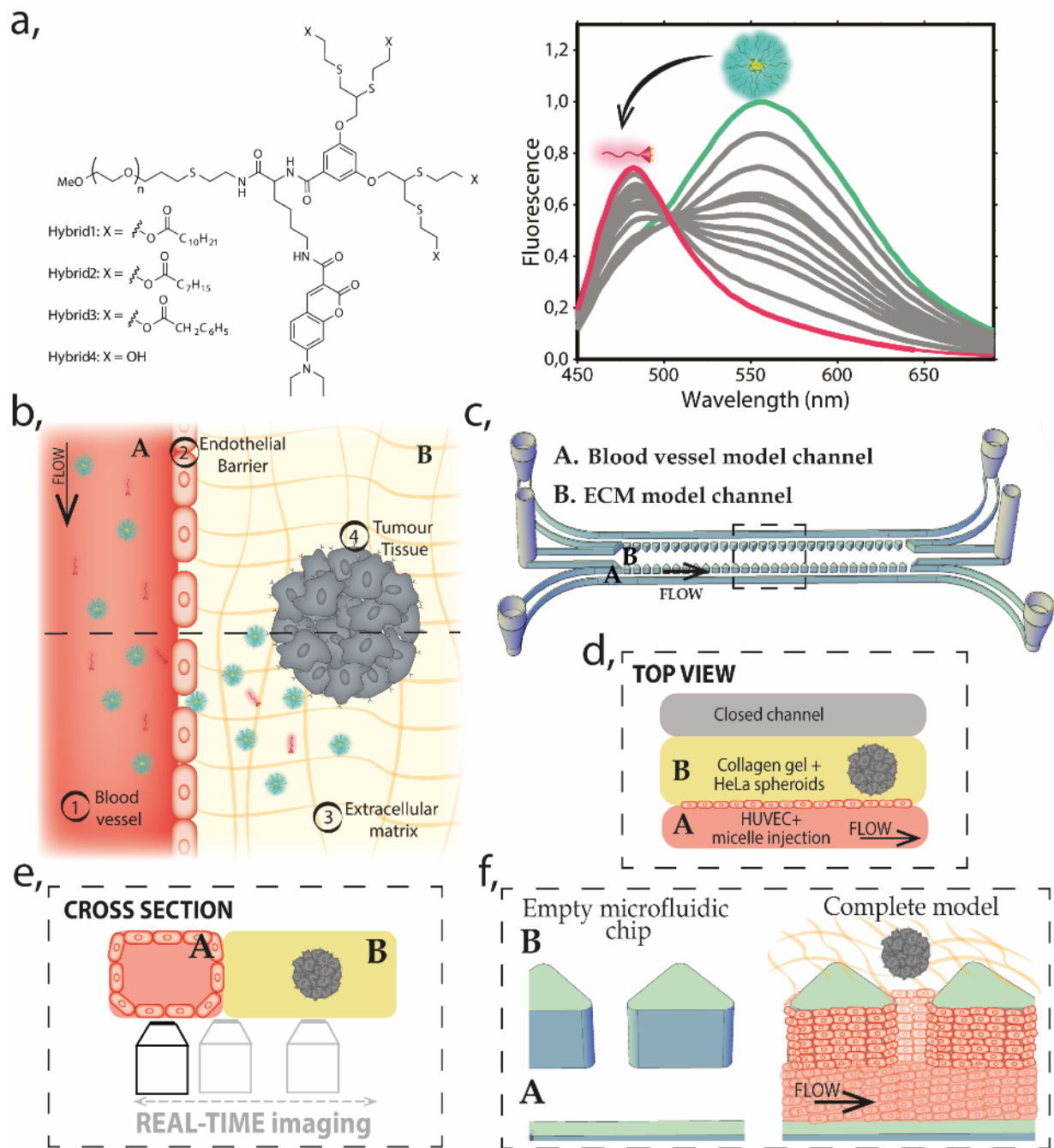


Figure 4.1 Schematic representation of the model. *a*, Molecular structure of the amphiphilic PEG–dendron hybrid polymers (left). Fluorescence emission graph for micelle–monomer equilibrium (right). In magenta monomer (fully disassembled structure) and in green (fully assembled) micelle. *b*, Schematic illustration of the Top View of the model, with the reconstructed barriers marked as (1–4), two main regions (A. blood vessel channel and B. ECM model), and a cross-section indicated by dashed line for the projection of figure 4.1e, *c*, 3D drawing of the microfluidic chip, including inlets and outlets of each channel. A and B indicate two main compartments of the model: the blood vessel and ECM and the dashed-line marks area for the projection of the view in figure 4.1d. *d*, Top view illustration of the microfluidic chip indicating the localization of the blood vessel model channel (A) and the ECM model (B). The channel A is under continuous perfusion as schematically represented *e*, Cross-section illustration of the model (A and B – blood vessel/ECM model channels, respectively) and the scheme of the real-time imaging setup. *f*, Zoom into the 3D representation (from fig. 4.1c) showing the perspective of the channels before and after the complete model reconstruction. It

illustrates how HUVECs line the blood vessel model channel covering the pillars and the collagen gel scaffold, forming a vertical endothelial barrier.

The created EB separates the inner lumen of the blood vessel model from the ECM channel, where we embedded preformed HeLa spheroids into the Type 1 Collagen Gel (Figure 4.1f). The co-culture of endothelial and cancer cells in the same systems adds complexity to the model, therefore, growth kinetics of HeLa cells and HUVECs were evaluated to determine the optimal medium for the healthy growth of both cell lines (Figure 4.2). Overall, we recreated elements of tumor microenvironment in cancer-on-a-chip, where micelles stability can be evaluated during unidirectional perfusion through the blood vessel model channel. The parallel channel geometry of our platform enables continuous imaging of the nanocarrier interactions with the indicated barriers, as represented in Figure 1e. Once the tumor blood vessel model was recreated (continuously perfused with cell culture medium at 37°C and 5%CO<sub>2</sub>), the chip was placed in an optical confocal microscope, at 37°C and reconnected to the perfusion system to track the assembly state of Hybrids 1-4 (see representation in Figure 4.1e)

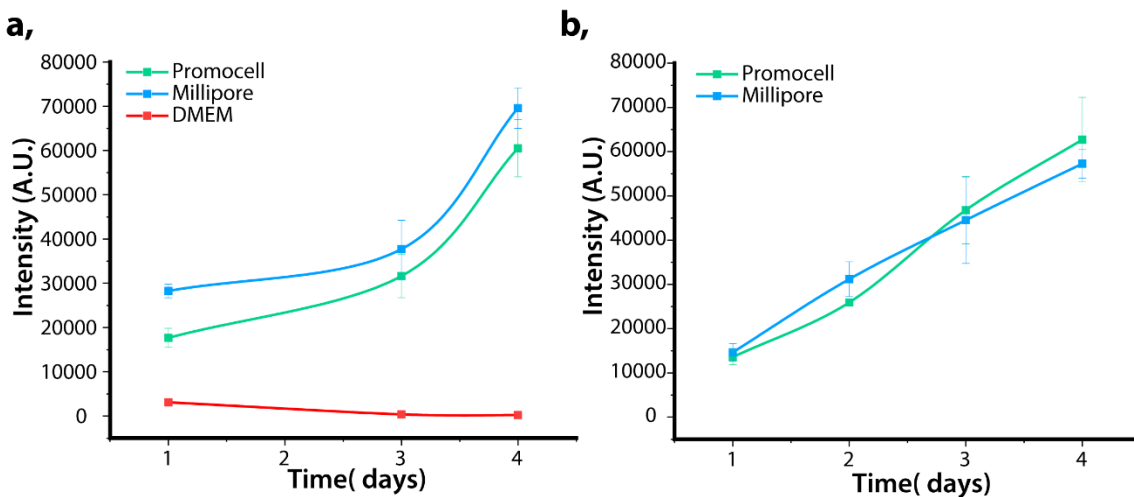


Figure 4.2 Growth kinetics of HUVECs and HeLa. **a**, HUVECs were seeded in a 96 well plate at a density of 2500 cells/well and incubated with three different media types: DMEM medium supplemented with 10% FBS (which is used for HeLa cell monoculture) and Promocell or Millipore media optimized for HUVECs. PrestoBlue cell viability test was performed after 1, 3 and 4 days of incubation. The absorbance at 570 nm is plotted as a function of time. HUVECs did not grow in DMEM medium but they grew similarly using both HUVEC optimized media. **b**, HeLa cells were seeded at a density of 2500 cells/well in a 96 well plate and incubated with the two HUVEC media to decide which was the optimal for HeLa grow. PrestoBlue cells viability test was performed after 1, 3 and 4 days. The graph shows the absorbance intensity as a function of time. HeLa cells growth kinetic was similar using both media. Every condition was performed in sextuplicate, error bar represents S.D. between wells

### 4.3 Characterization of reconstructed barriers in microfluidic cancer-on-a-chip model

To validate our model, first we characterized the formation of an endothelial barrier created in the lateral channel. The magnified transmission image of the blood vessel channel and adjacent ECM channel with embedded HeLa spheroid (Figure 4.3 and 4.4) demonstrates the complete, prepared chip after 3 days of unidirectional medium perfusion. HUVECs are present in both: the upper and lower plane of the blood vessel model, as shown in the transmission images of Figure 4.4b and the formation of confluent endothelial monolayer lining the lumen was further validated by fixing and staining the cells, as shown in confocal image in Figure 4.4c-d, where actin (red), nucleus (blue) and formation of tight junctions (green) can be observed. The endothelial cell to cell contact results in the expression of zonula occludens-1 (ZO-1) protein, which is essential to form these junctions in a healthy endothelial barrier<sup>49</sup>. Moreover, 3D reconstruction of confocal imaging demonstrates the presence of the EB between the microposts, on the gel scaffold (Figure 4.4d), physically separating the lumen of the vessel from the ECM channel, mimicking the *in vivo* barrier. Additionally, HUVECs exhibited the alignment parallel to the flow direction, as a result of the shear stress present in the lumen<sup>50,51</sup> (Figure 4.4e). In contrast, cells cultured in static conditions shown random filament organization, as observed previously<sup>52</sup>. Finally, we tested the structural integrity of the HUVECs barrier by measuring the retention of fluorescently labeled 10 kDa Dextran, continuously perfused through the endothelialized channel. The fluorescence signal was detected in the lumen of the EB channel but not in the collagen gel (Figure 4.4f) indicating proper functionality of the endothelial barrier. However, a low gradual penetration of the Dextran into the ECM was observed after 30 min. (Figure 4.5), similarly to other reported studies<sup>48,53-55</sup>. Altogether, these measurements indicate the formation of a functional EB with good structural integrity.



Figure 4.3 HUVECs monolayer formation. Cell growth in the microfluidic chip after 2 hours, 24 hours and 72 hours. Magnified image of the lateral channels (left hand side from the triangular posts) where HUVECs were seeded to form the blood vessel model and part of the gel channel (right hand side from the posts). Distance between triangular posts is 100  $\mu\text{m}$ .

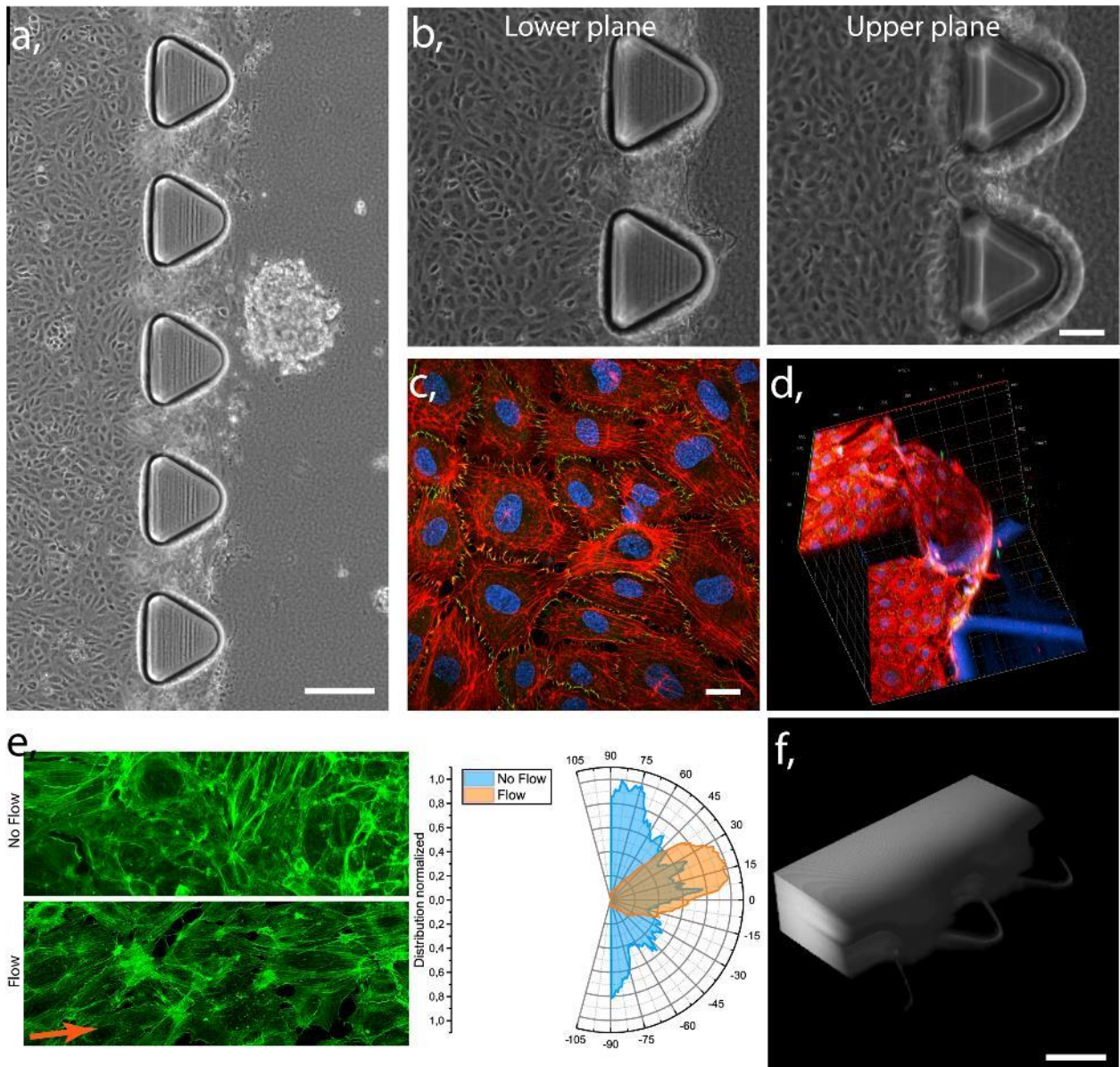


Figure 4.4 Functionality of the endothelial barrier model. *a*, Transmission image showing complete tumor blood vessel-on-a-chip model with HUVECs lined lateral channel (left part of the chip) and adhering ECM model channel (right) with gel embedded HeLa spheroid. Scale bar 200  $\mu\text{m}$ , *b*, Transmission image of the lower and upper plane of the blood vessel model covered with confluent HUVECs monolayer. Scale bar 100  $\mu\text{m}$ , *c*, Confocal image of HUVECs confluent monolayer (red: Phalloidin, blue: Hoechst, green: ZO-1). Scale bar 20  $\mu\text{m}$ , *d*, 3D reconstruction of confocal image of vertically grown HUVECs layer on the scaffold of collagen gel between the chip's microposts (red: Phalloidin, blue: Hoechst, green: ZO-1), scale: axis ticks separation 40  $\mu\text{m}$ , blue triangles represent base of the microposts, *e*, Confocal images of actin stained (green) HUVECs in static (upper image) and perfused (lower image) blood vessel model channel and graph of actin filaments organization, demonstrating alignment under the flow and random orientation in static culture. *f*, Epifluorescent microscopy 3D reconstructed image of continuously perfused 10 kDa Dextran through the endothelialized blood vessel model channel at a time point 10 min. Scale bar 150  $\mu\text{m}$ .

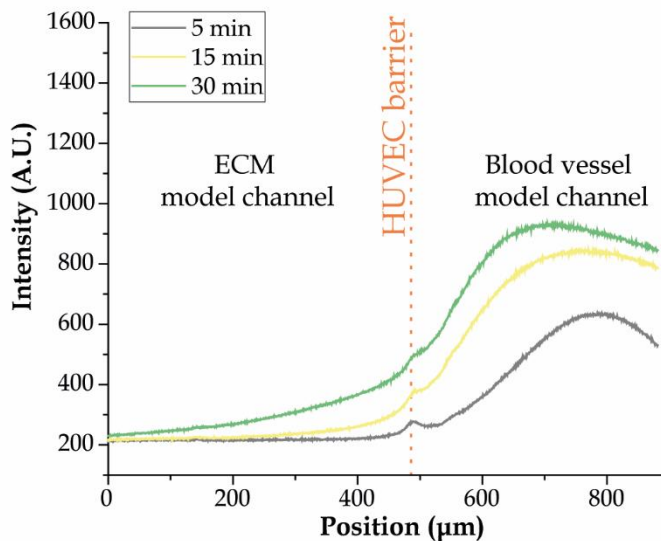
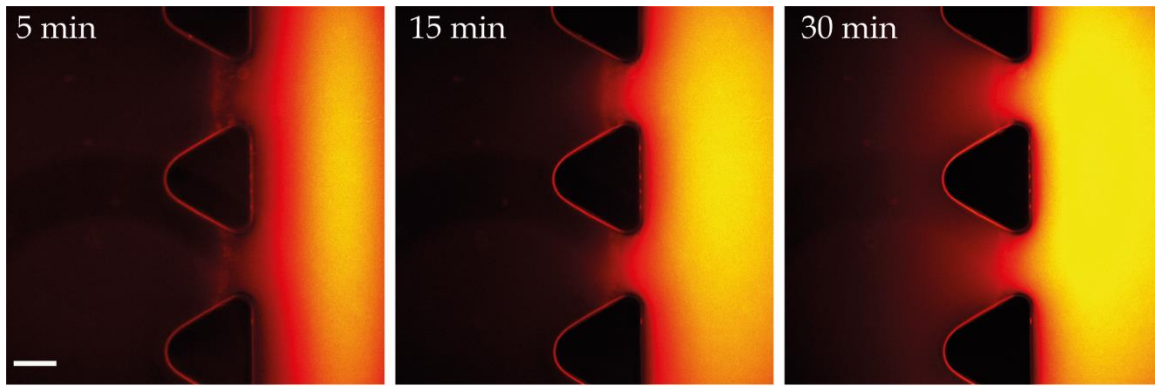


Figure 4.5 Snapshots of continuous perfusion of 10 kDa dextran through blood vessel model channel. 3 time points have been selected to show the HUVECs barrier functionality, from left to right: 5 minutes, 15 minutes and 30 minutes. Scale bar 100  $\mu\text{m}$ . The graph below quantifies the mean fluorescent intensity of the image in each position, we can see that at time 5 minutes the dextran did almost not cross through the HUVECs barrier, while in time some of the molecules cross, still the intensity in the ECM model channel is much lower than the one of the blood vessel model perfused channel.

Finally, we characterized the ECM central channel with gel embedded HeLa spheroids. The transmission microscopy allowed to observe the 3D spheroid conformation (Figure 4.6a) recapitulating aspects of geometry present in physiological conditions. This arrangement implies less available surface area per cell, than in 2D cell culture models, it also alters cell proliferation rate and its overall functionality<sup>21,35,56</sup>. The growth of prefomed spheroids, co-cultured in the perfused chip together with HUVECs is demonstrated in figure 4.6b. The spheroids with size of  $100 \pm 50 \mu\text{m}$  were introduced into the chip, and after 3 days of culturing they grew on average by 220% of their initial size, as shown in graph of Figure 4.6c. HeLa viability was confirmed with a live/dead staining assay, revealing that the cells were viable throughout the spheroid after 3 days of culture (Figure 4.6d), indicating good nutrients and oxygen diffusion. Given the

size of our spheroid after 3 days, we expected to observe high viability, as the phenomena of necrotic core development is reported in the spheroids beyond 500  $\mu\text{m}$  diameter<sup>57–60</sup>.

Overall, we adapted a microfluidic platform to a 3D dynamic tumor microenvironment, including a perfusable blood vessel model, and cancer cells conformed into spheroid.

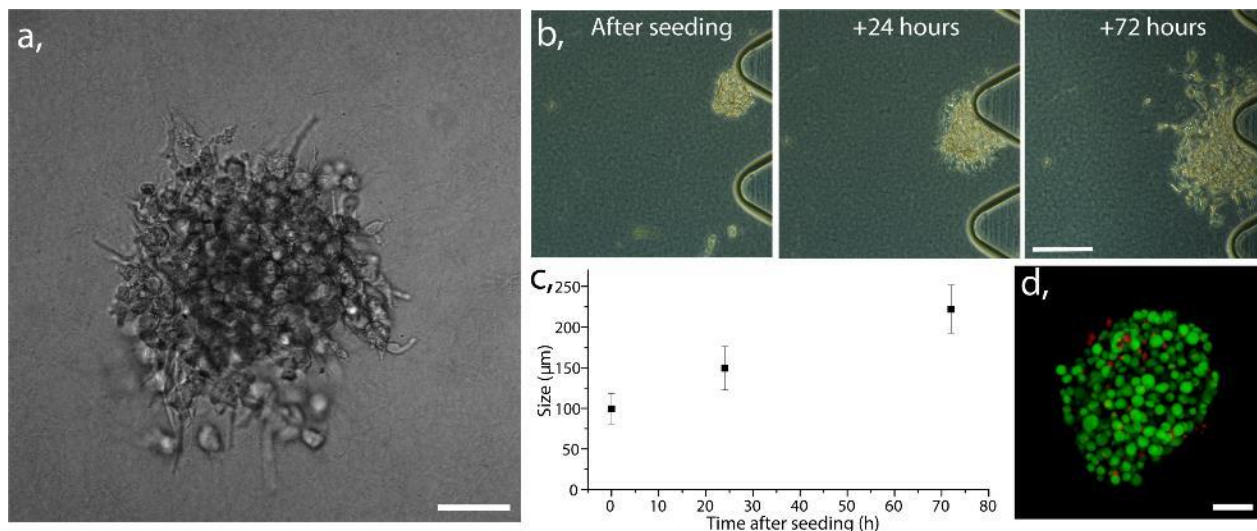


Figure 4.6 a, Transmission image of collagen gel-embedded HeLa cells conformed into 3D spheroid. Scale bar 50  $\mu\text{m}$ , b, Transmission images demonstrating proliferation of a gel-embedded spheroid from the preparation up to 3 days in perfused culture. Scale bar 100  $\mu\text{m}$ , c, Graph demonstrating size progression of gel embedded spheroids after 1 and 3 days of perfused culture, calculated on base of diameter measured in 10 different chips, average with standard error bars, d, Confocal image of stained HeLa spheroid with calcein (live cells: green) and Propidium iodide (dead cells: red). Scale bar 50  $\mu\text{m}$ .

#### 4.4 Increased extravasation of micelles is induced in tumor blood vessel chip

Having established our tumor blood vessel-on-a-chip model, we investigated the ability of the micelles to penetrate the EB into the ECM channel. Previous studies using microfluidic models reported enhanced permeability of endothelial cells when exposed to specific molecules, such as TNF- $\alpha$ <sup>40</sup> or when co-cultured with cancer cells<sup>32</sup>, leading to the formation of “leaky vessels”, representing one of the features of the EPR effect. However, most of these microfluidics models were used for studying only the selected or final time point of nanoparticles penetration. Herein, taking advantage of the characteristics of the chip, we could continuously monitor the perfusion of our micelles in three different experimental conditions: i) no HUVECs (non-endothelialized lateral channel) as negative control; ii) HUVECs barrier (healthy endothelialized blood vessel model), and iii) HUVECs barrier with HeLa spheroids embedded in the ECM (tumor blood vessel model).

First, we tested the micelle ability to cross the EB, perfusing the hybrid **1** into the three models (i-iii) and quantifying the fluorescence intensity, in the blood vessel model and ECM part, as plotted for the i-iii in

Figure 4.7a. A constant amount of the fluorescence was immediately detected in the collagen gel in case of lack of the EB (i), what demonstrates that our NPs freely diffuse through the ECM <sup>6</sup>. In contrary, the majority (>90%) of hybrid **1** was retained in the healthy blood vessel model channel (ii) for more than 30 min. of continuous perfusion. Meanwhile, a gradual diffusion of the hybrid into the ECM was observed in the tumor blood vessel model (iii). These results indicate that the HUVECs monolayer in the healthy model fulfills the barrier function and limits the hybrid penetration into the ECM. However, this function is affected by presence of HeLa spheroids in the gel. Our observations resemble experiments performed by Tang and co-workers where co-culture of cancer endothelial cells with breast cancer cells increased the permeation of nanoparticles through the EB <sup>32</sup>.

Interestingly, we hypothesized that the ~10% of the hybrid detected in the ECM of the healthy model (ii) could origin from the infiltration of the monomer (disassembled form ~6-7 kDa, assembled micelle ~20 nm), considering the healthy EB permeability <sup>48,61</sup>. To investigate this further we perfused hydrophilic hybrid **4**, which has four hydroxyl end-groups (does not self-assemble into micelles)<sup>20</sup>, into the same 3 models (i-iii) as hybrid **1**. As expected, the Figure 4.7b shows that the monomer penetrated instantly the ECM in the control (i) and the cancer (iii) models, but also some infiltration into the ECM was observed in the healthy (ii) one. Specifically, HUVECs barrier partially retained the monomer for 25 minutes of continuous perfusion, limiting its concentration in the gel to less than 40% of its intensity in the perfused channel. It is worth noting that after 5 minutes of perfusion, the hybrid **4** could already be detected in the gel of the healthy blood vessel model (Figure 4.8). However, the penetration into the ECM was far more significant and immediate in HeLa cells co-cultured model. Overall, we hypothesize that the monomer form can gradually cross into the ECM region of the healthy blood vessel model due to its small size, permitting the paracellular transport. We visually determined the morphological effect of co-culturing cancer cells on the structural integrity of the endothelial monolayer, to understand if a loss of EB integrity was the reason of the increased micelles permeation into the ECM in the cancer model. Tight and adherent junctions are the crucial structural elements formed between endothelial cells, regulating paracellular diffusion and restricting the permeation of molecules bigger than ~2 nm <sup>62</sup>.



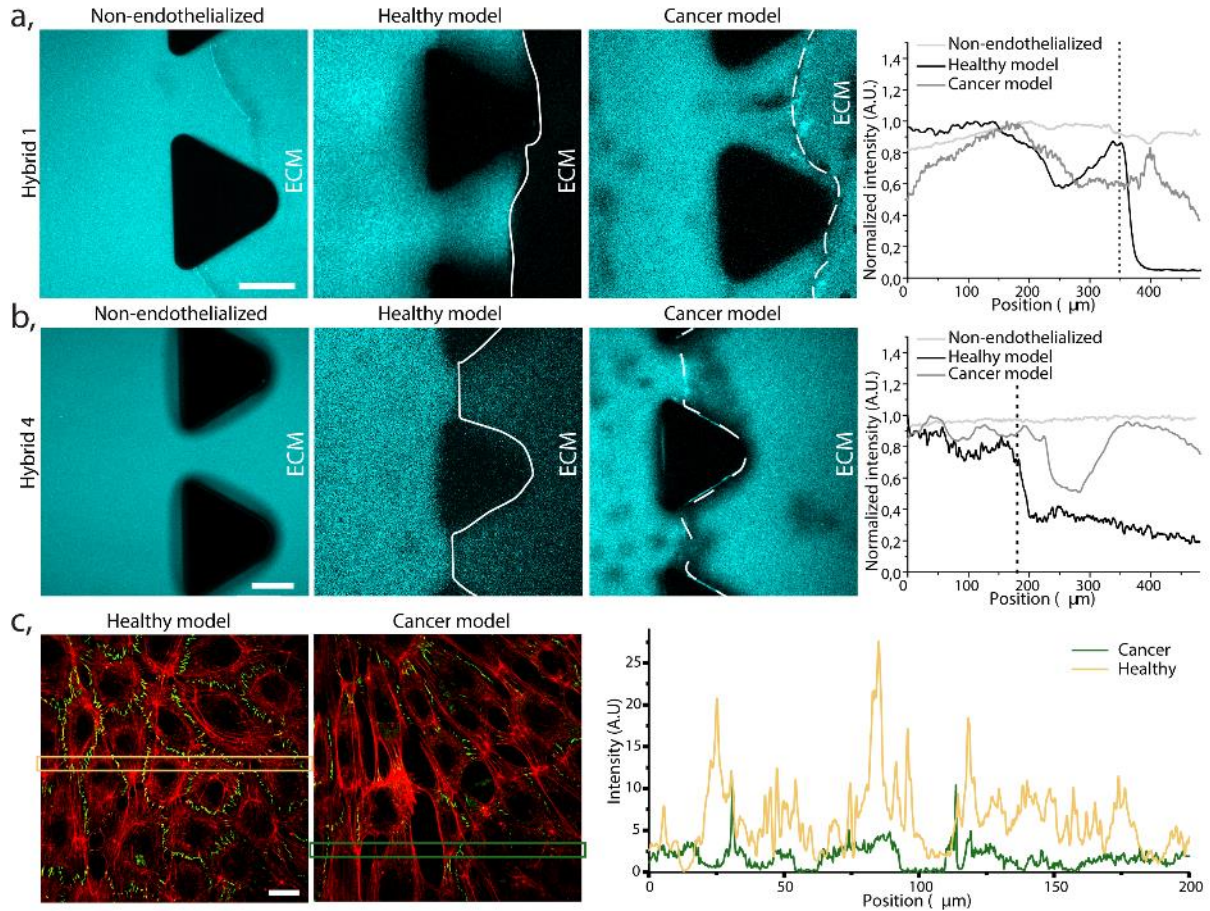


**Figure 4.7** Extravasation of PEG-dendron hybrids in non-endothelialized, healthy and cancer models. **a**, Confocal image of hybrid 1 extravasation in a (i) control chip (no EB), (ii) a healthy model and (iii) cancer model. The images show emitted intensity between 446-700 nm, which include both: the monomer and micelle signal. Scale bar 100  $\mu\text{m}$ . Quantification of the normalized micelle fluorescence intensity measured in a rectangular area between 2 neighboring posts, indicating the penetration from the blood vessel model channel into the ECM part, plotted for the i-iii) models. Vertical dotted line indicates the localization of the EB. **b**, Confocal image of hybrid 4 (monomer) extravasation in the 3 corresponding models. Scale bar 100  $\mu\text{m}$ . Quantification of the normalized monomer fluorescence intensity, measured in a rectangular area between 2 neighboring posts, indicating the hybrid 4 penetration from the blood vessel model channel into the ECM part, plotted for the i-iii) models. Vertical dotted line indicates the localization of the EB, **c**, Confocal image of HUVECs monolayer lining the healthy (left) and cancer (right) blood vessel channel model. Actin (red) and ZO-1 (green). Scale bar 20  $\mu\text{m}$ . Quantification of the fluorescence intensity over the 2 marked rectangular areas indicated in the images (on the left). The spikes in the healthy model (yellow) originated from higher expression of ZO-1 in contrast to lower expression in the cancer model (green).

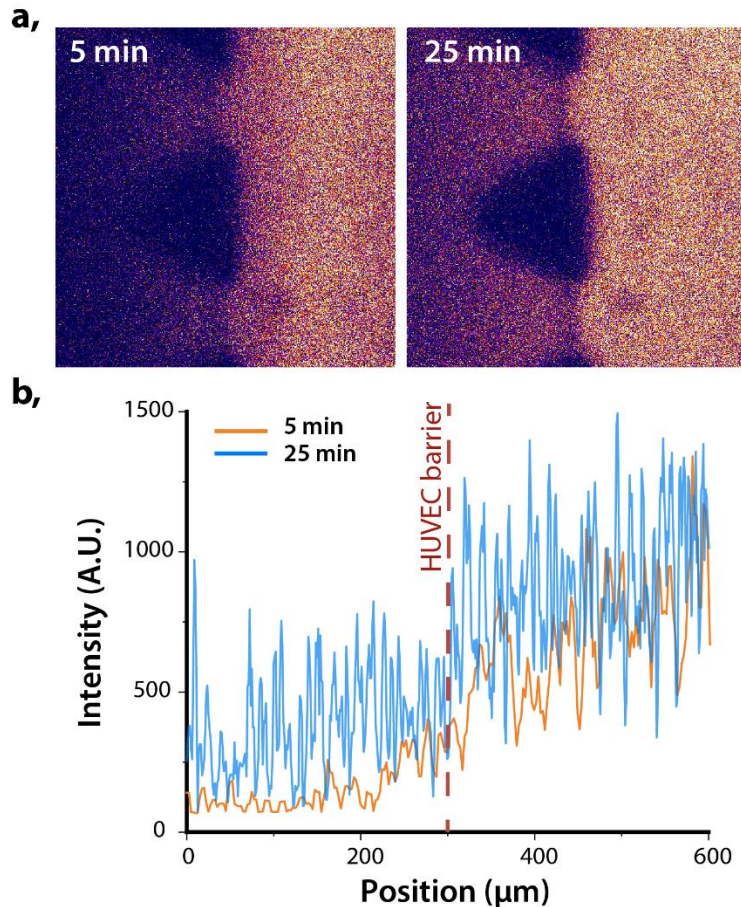


**Figure 4.8** Extravasation of hybrid 4 (6-7 kDa) in healthy model already occurs after 5 minutes of continuous perfusion. A healthy blood vessel model was prepared and hybrid 4 was flow for 25 minutes to study its extravasation a. Confocal images of the hybrid 4 being flow through the blood vessel model channel at 5 and 25 minutes. In the images the perfused channel (right) and part of the ECM model (left) can be observed. Look-up table “fire” is used for visualization purposes b. Plot profile of a horizontal line across each image showing the intensity detected in each position. After 5 minutes of perfusion the hybrid was detected in both: the gel and the lateral channel, however the intensity in the gel channel was only 15% comparing to the blood vessel model channel, while after 25 minutes it raised to 40%.

To confirm that the enhanced permeability of the EB in our model was induced by the presence of HeLa spheroids, we prepared the chips as mentioned previously and after 3 days of medium perfusion the cells were fixed, ZO-1 protein stained and quantified as shown in Figure 4.7c Figure 4.9. ZO-1 was clearly and uniformly expressed between HUVECs of the healthy model, however, the expression was reduced in the HeLa spheroids co-cultured model. It indicated that cancer cells impacted the HUVEC cell-cell interaction and the tight junction formation, therefore explaining the enhanced permeability in our cancer models. Similar findings were reported by Kaji *et al.*<sup>63</sup>, where HUVEC and HeLa co-culture affects the endothelial cells growth through the direct cell-cell contact as well as transmission of information via culture medium (paracrine communication). In that study the cytokines excreted by HeLa repulsed HUVECs and released reactive oxygen species, which lead to malfunction and death of HUVECs, resulting in leakiness of the EB.

However, it is worth noting that in our study there was a certain heterogeneity in the permeation of micelles out of the tumor blood vessel model. We observed that small variations in the number of spheroids (or their distribution) affects the EB retention capacity, potentially resulting in a variable concentration of signaling molecules (see Supporting Discussion). These observations may be reflecting one of the key features of the EPR effect, of which the heterogeneity has been extensively discussed recently, and attributed to the stage of the diseases <sup>64</sup>.

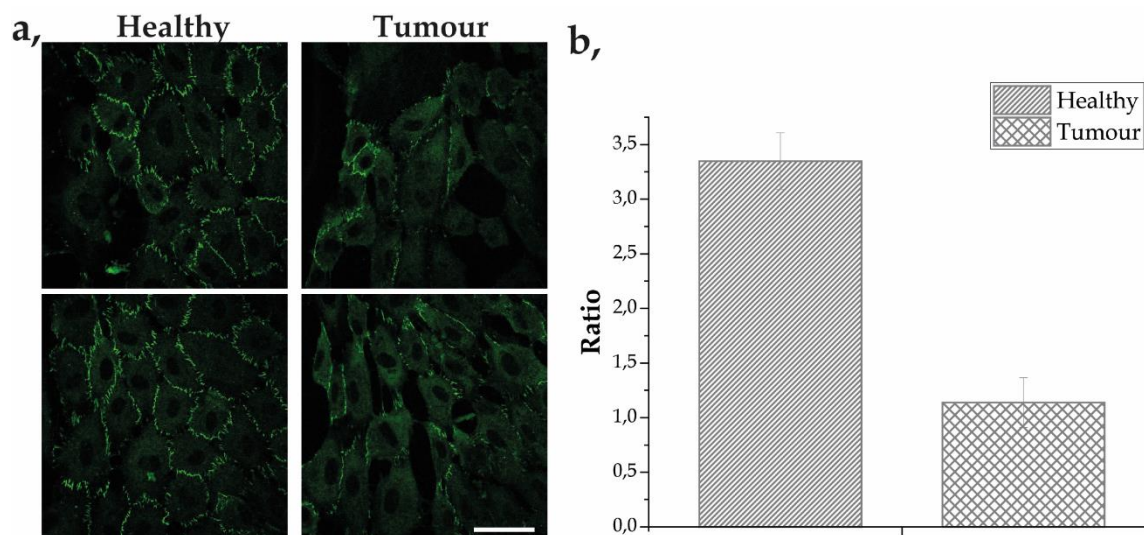


Figure 4.9 a, Confocal images of ZO-1 expression in the HUVECs monolayer lining the healthy and cancer blood vessel model channel. Scale bar 50  $\mu$ m. b, Ratio of ZO-1 expression in the membrane of the cells (tight junction formation) compared to the intracellular expression. 5 different images of 2 different chips were analyzed, where 6 membrane ROIs and 6 intracellular ROIs were defined. The mean intensity of the 6 ROIs of the membrane was divided to the mean intensity of the intracellular ROIs. The graph shows the mean ratio  $\pm$  s.d. of the 5 analyzed images.

#### 4.5 Time- and space-resolved micelle stability revealed in 3D tumor microenvironment model

The aim of our work was to study the stability of our micellar systems when introduced into the microfluidic 3D model. Previously the micelles and monomer were detected in the presence of serum proteins and their internalization pathway identified thanks to their self-reporting capabilities compatible with confocal fluorescence microscopy <sup>20</sup>. Herein, we hypothesized that the added complexity and dynamicity of the blood vessel model may induce premature disassembly due to multiple interactions. To evaluate these critical interactions, we continuously perfused micelles of hybrid **1** (the most stable system), in full culture medium at 15  $\mu$ L/min and 37°C into the blood vessel model channel. During perfusion, we continuously monitored the micelles' stability in key regions: the blood vessel model channel, the endothelial barrier, the ECM and the HeLa spheroids, providing real-time stability information as shown in Figure 4.10.

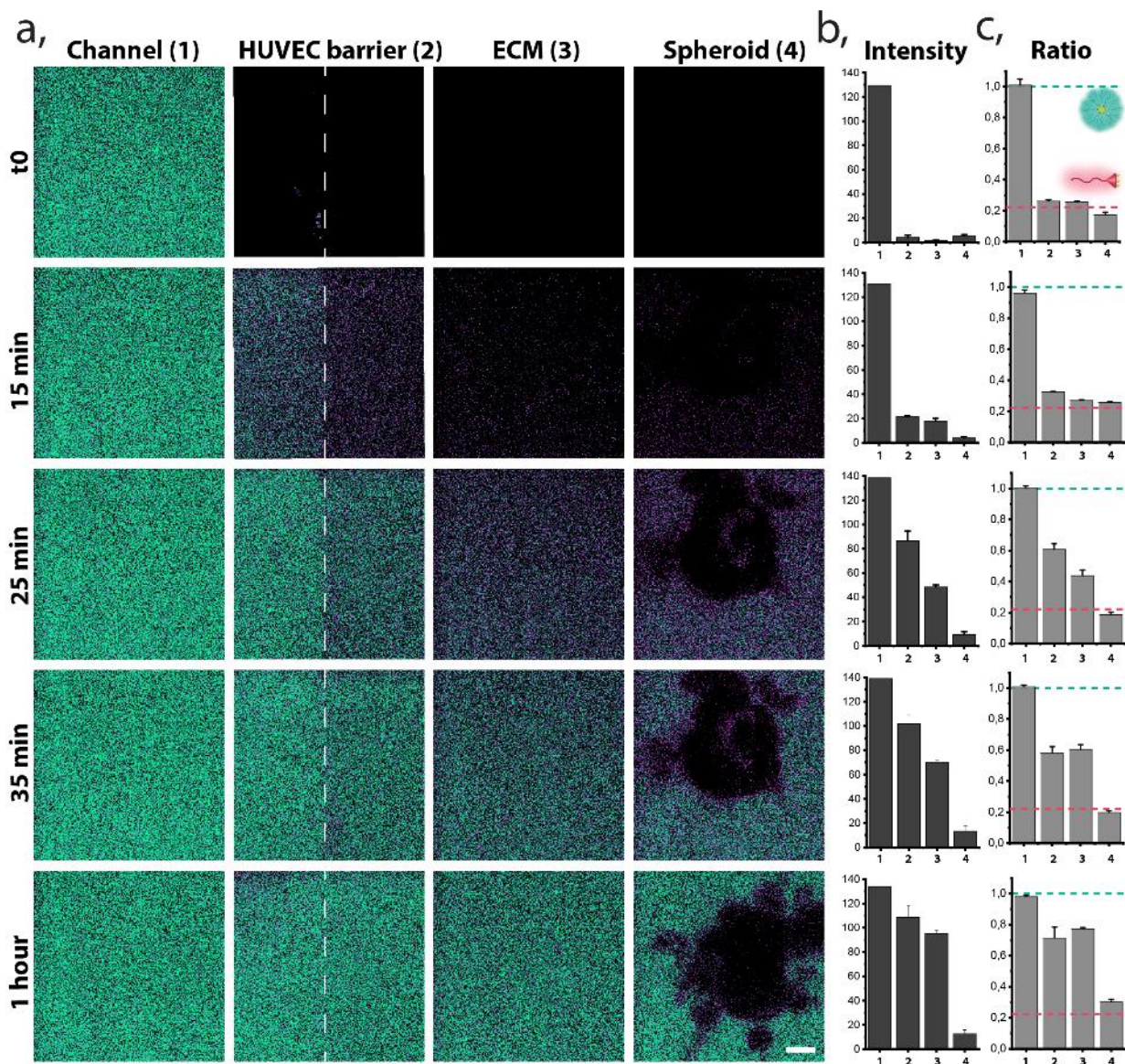


Figure 4.10. Space and time-resolved stability of hybrid 1. Representative images, selected from the 10 repetitions of experiments within hybrid 1 in the tumor blood vessel model. a. Ratiometric confocal images of real-time monitored micelle (green) and monomer (magenta) at reconstructed barriers (1 - blood vessel model channel, 2 - HUVECs barrier, 3 - ECM and 4 - HeLa Spheroid) during continuous perfusion of the hybrid 1, scale bar 15  $\mu\text{m}$ . Relevant time points were selected for representative purposes. b. Time-resolved intensity of fluorescence signal (A.U) originating from the sum up of both micelle and monomer channels at each barrier (1-4) of the presented images. c. Normalized ratio of fluorescence signal between micellar and monomer form monitored in time at different barriers. Green dashed line indicates the ratio of fully formed micelles in equilibrium and the magenta dashed line indicates the ratio of fully disassembled (monomer) form.

In the first minutes of perfusion fluorescence was detectable only in the blood vessel model channel (Figures 4.10a and b) and indicated the presence of assembled micelles (Figure 4.10c). Hybrid penetration into the depth of the ECM was observed over time. After 15 minutes of continuous flow the hybrid started to reach the EB, and we could observe that the disassembled form prevailed in passing through the wall and entering the ECM by detecting the monomer emission (magenta). After 25 minutes we observed the

assembled form traversing the EB, while the deep penetration into ECM was still achieved mostly by the disassembled polymers. This observation could be attributed to two factors: i) the micelles progressively overcame the endothelial barrier or ii) the monomer form, which entered the ECM through the EB previously, accumulated and reached the critical micelle concentration (CMC), re-assembling into micelles. Figure 4.10b demonstrates that both, micelle and monomer, coexist at the EB and in the ECM with the mean ratio 0.6 and 0.4 respectively. The assembled structures were detected in the surroundings of the spheroids after more than half an hour of the continuous perfusion. Surprisingly, after 1 hour we observed only weak penetration of the hybrid **1** into the depth of the HeLa spheroids, similarly to 2 hours of constant perfusion (Figures 4.11 and 4.12). In our previous 2D cell internalization studies the hybrids were detected inside the cell already after 10 minutes, meanwhile in the current work, only a small fraction of the disassembled form was detected in the outer layer of the spheroid. Interestingly, we observed a stabilization of monomer/micelle equilibrium in the monitored regions after 1h from the beginning of the perfusion, except for the spheroid area. Hybrid **1**, detected as a monomer in contact with HeLa cells, was a contrasting observation comparing to our previously reported internalization behavior in 2D cell cultures, where the assembled hybrid **1** was taken up by HeLa cell via endocytosis, and its disassembly progressed in time<sup>20</sup>. This discrepancy can be attributed to the spheroid form of the HeLa, promoting different endocytosis process, favored in the new 3D cells confluency and conformation. Other works, highlighting the importance of going beyond 2D cell culture models, investigated the penetration of nanosystems into tumor spheroids as a function of nanocarrier size, shape, charge and functionalization<sup>37,65,66</sup>. Likewise, the penetration of cross-linked and non-cross-linked micelles has been compared, showing an improved result for the cross-linked (more stable) ones<sup>67-69</sup>. Therefore, we hypothesized that the lower spheroid penetration in our model can be caused by a premature disassembly in the periphery of the spheroid leading to a different outcome than reported in the 2D static monoculture. It underlines the importance of model selection in rational evaluation and optimization of supramolecular for drug delivery.

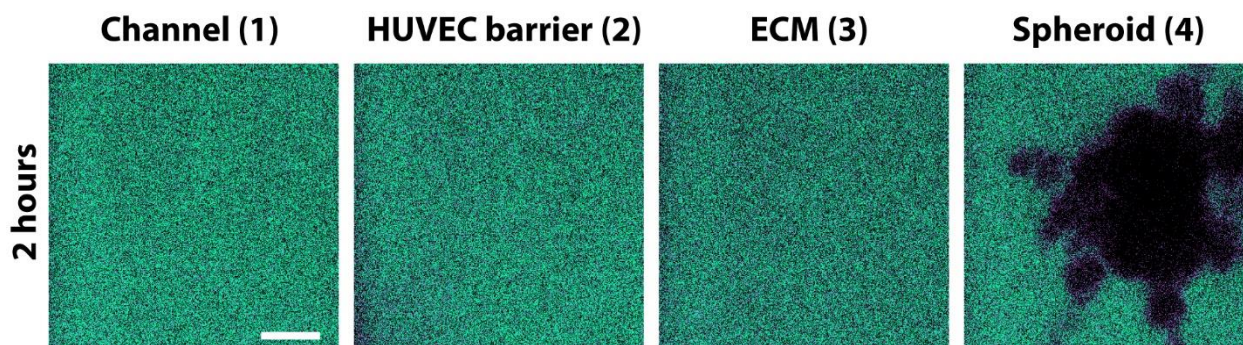


Figure 4.11 Space resolved stability of hybrid **1** after 2 hours of continuous perfusion through the blood vessel model channel. Ratiometric confocal images of real-time monitored presence of micelle (green) and monomer (magenta) at reconstructed barriers (1 - blood vessel model channel, 2 - HUVECs barrier, 3 - ECM and 4 - HeLa Spheroid). Scale bar 20  $\mu\text{m}$ .

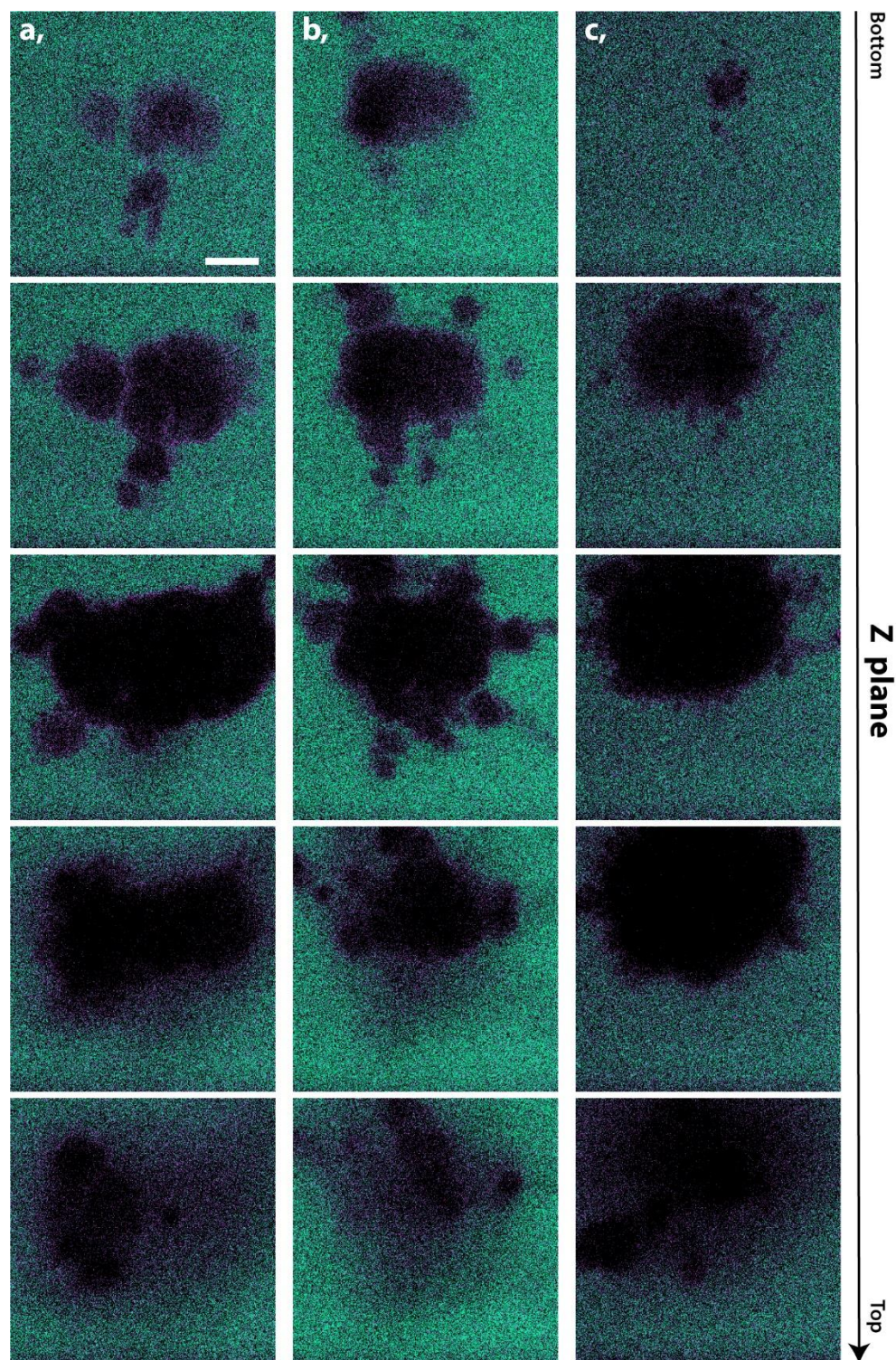


Figure 4.12 Penetration and stability of hybrid 1 in the HeLa spheroids after 2 hours of continuous perfusion through the blood vessel model channel. Ratiometric confocal images of real-time monitored presence of micelle (green) and monomer (magenta). **a.** Z-stack images of spheroid 1 **b.** Z-stack images of spheroid 2 **c.** Z-stack images of spheroid 3. Scale bar 20 $\mu$ m

## 4.6 Stability of hybrids dictates their infiltration/extravasation

Finally, we investigated the interplay between molecular structure, micellar stability and their ability to extravasate. Therefore, we compared the stability of three hybrids, with decreasing length of the hydrophobic end-groups, from hybrid **1** to hybrid **3**. In our previous 2D studies we demonstrated that the hybrid **1** was stable in the presence of serum proteins and upon dilution, meanwhile the stabilities of hybrid **2** and **3** were similar when diluted with serum, however, their disassembly kinetics were significantly different. While hybrid **3** disassembles rapidly upon dilution, hybrid **2** needed hours to reach the equilibrium.

To understand how these differences in thermodynamics and kinetic stability are reflected in a more complex model, we perfused each hybrid solution (in full culture media) through the blood vessel model channel during at least 30 min. In Figure 4.13 we show representative images, demonstrating observations for the sets of hybrid – cancer model experiments, where an individual chip was perfused only with one hybrid. We chose two different areas of each chip-hybrid set, taking as the selection criterium the distance of the HeLa spheroid to the HUVECs barrier, to illustrate the different behavior we observed. HeLa spheroids less than 400  $\mu\text{m}$  from the EB were considered as “close” to HeLa and EB regions at a radius of at least 1 mm were considered as regions “far” from HeLa, as reported in the Figure 4.13 and Figure 4.14. We observed extravasation of all hybrids **1-3** through the EB when HeLa spheroids were located close to HUVECs (Figure 4.13b). However, in the distant regions (far HeLa) only hybrid **3**, (which has the least hydrophobic dendron), was able to significantly extravasate to the ECM. Thus, we concluded that the endothelial barrier “leakiness” can be heterogenous, depending on the amount, distance and distribution of tumor spheroids in the ECM.

Monitoring stability of these three hybrids (Figure 4.13a and c), was based on the ratios between the emitted intensity of the coumarin dye at 480 nm and 550 nm (the disassembled and assembled state respectively). The hybrid **1** appeared as a micelle in the blood vessel model channel, with mean ratio of fluorescence signal between the both forms equal to 1 (indicative of the micelle), while slight disassembly of hybrid **2** and significant disassembly of hybrid **3** were observed, with mean ratios of 0.8 and 0.5 respectively. Our previous study showed that hybrid **2** and **3** were slightly unstable in presence of serum proteins, but their degree of disassembly based on the fluorescent ratio was equal. Therefore, we hypothesized the enhanced disassembly of hybrid **3** is not only due to interactions with serum proteins but also caused by the perfusion. This result indicates that the flow-induced shear stress can drastically affect the stability of supramolecular nanocarriers.

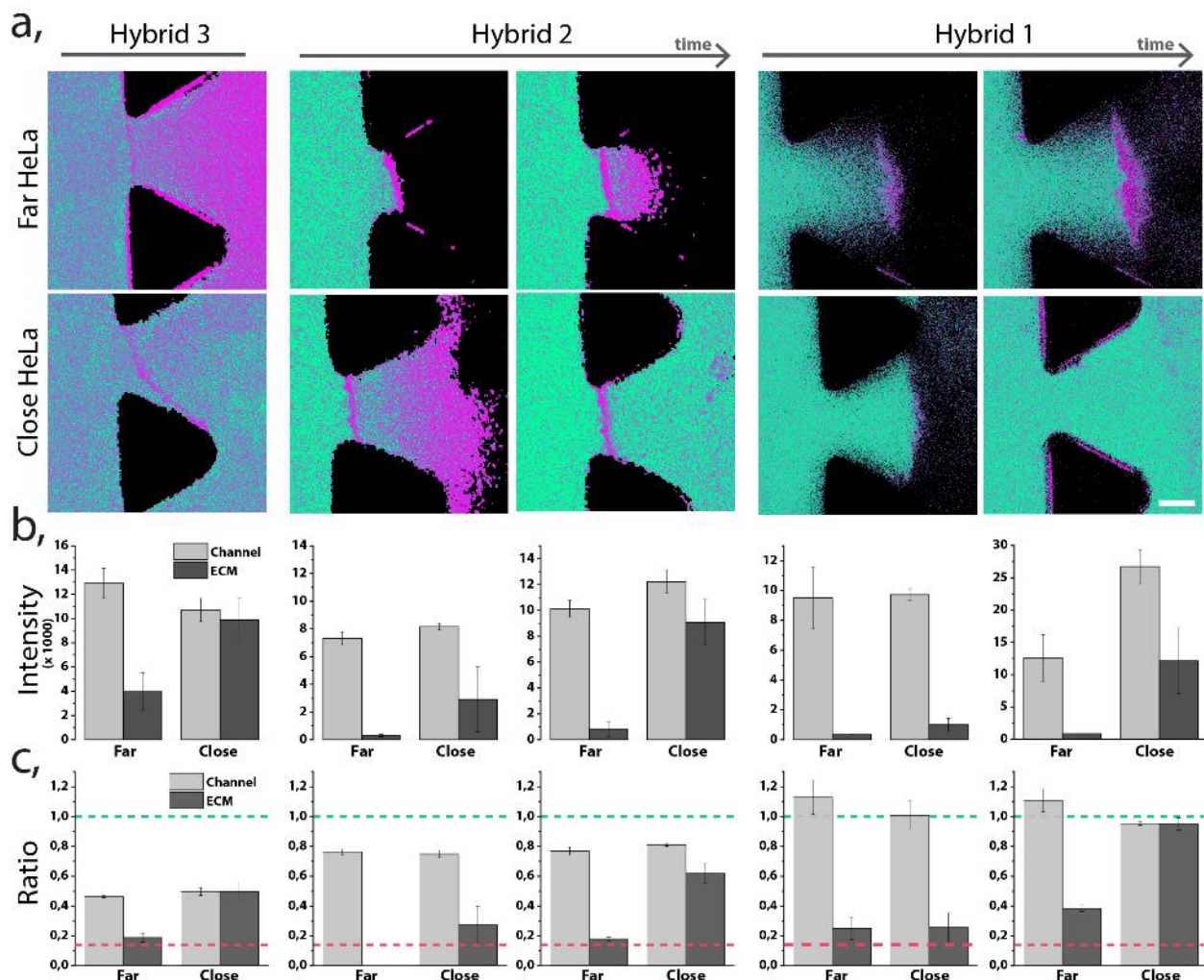
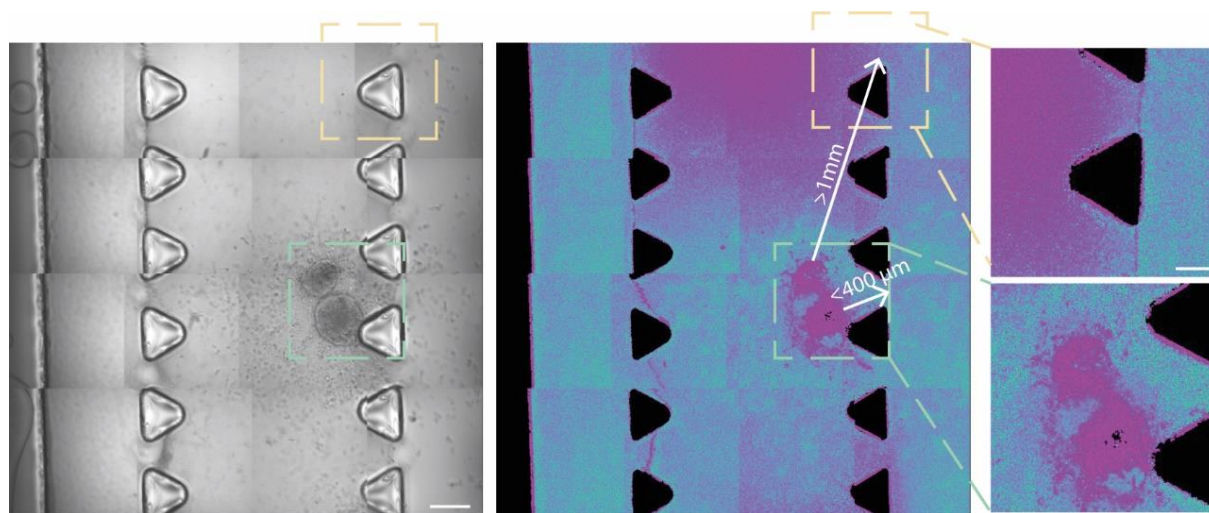


Figure 4.13 Stability of hybrids 1-3, perfused through a tumor blood vessel models with different EB distance to the HeLa spheroid (close: < 400  $\mu\text{m}$ , far: > 1 mm). **a**. Ratiometric confocal images of the different hybrids perfused through the chip in two regions. Hybrid 1 and 2 are shown at 2 different time points: less than 15 minutes and after 30 minutes of continuous perfusion, hybrid 3 demonstrated at one time point, due to its rapid penetration through the EB. Scale bar 75  $\mu\text{m}$ . **b**. Summed up fluorescence intensity originating from the monomer and the micelle channels. Intensity was measured in the blood vessel model channel and in the ECM region **c**. Normalized ratio of fluorescence signal between micellar and monomer form for each hybrid and in each region. Green dashed line indicates the ratio of fully formed micelles in equilibrium and the magenta dashed line indicates the ratio of fully disassembled (monomer) form.

Further, we monitored the stability of each hybrid at the previously defined barriers and observed significant differences among them. Interestingly, in regions far from spheroids only the monomeric form of hybrid **3** was able to efficiently extravasate. This phenomenon could occur due to the increased disassembly of the micelle in contact with the HUVEC barrier, which allowed the monomer to i) paracellularly extravasated due to its small size or ii) transcellularly cross the EB. In contrast to that, hybrid **3** crossed the EB in the semi-assembled state in the regions close to HeLa (as it appeared in the blood vessel channel), probably due to the disappearance of the tight junctions in the HUVEC barrier. On the other hand, the extravasation of hybrid **2** in regions close to HeLa had a time dependent response; first only monomer crossed the EB



and the micelles were detected in the ECM after more than 30 minutes. Finally, we observed that hybrid **1** behaves similarly to the hybrid **2**, where monomer molecules extravasated first, followed by the later penetration of the assembled micelles. Interestingly, while hybrid **2** and **3** accumulated in the endothelial barrier only as a monomer, hybrid **1** monomeric form accumulated at the EB only in areas far away from the HeLa cells. Previously, in 2D cell culture, hybrids **3** and **2** internalized as monomer and the hybrid **1** internalized as a micelle and disassembled over time<sup>20</sup>. Overall, we could correlate the interplay between stability of the micelles and their performance in a 3D model, as well as their ability to extravasate and reach the cancer cell regions.



*Figure 4.14 Transmission images of cancer model chip and corresponding ratiometric image, describing “far” and “close” selection criteria, referring to the distance of HUVECs barrier to the nearest gel embedded HeLa spheroid. Scale bar stitched image 200  $\mu\text{m}$ , scale bar zoomed in image: 100  $\mu\text{m}$ . If HeLa spheroids are closer than 400  $\mu\text{m}$  we considered the region as “close” to HeLa. In contrast, if HeLa spheroids were at a distance larger than 1 mm we considered the region as “far” from HeLa. Yellow (upper) dashed squared area demonstrates studied EB in “far” zone, and green (lower) dashed area represents studied EB in “close” zone.*

## 4.7 Conclusions

In the present work, we combined the spectral confocal imaging and a microfluidic cancer-on-a-chip model as a new approach to study the stability of supramolecular nanocarriers. The fluorescence properties of our micelles allowed tracking their assembly state across the changing conditions of the reconstructed elements of tumor microenvironment.

The results show the formation of functional endothelial barrier in a lumen of the blood vessel model and appearance of leaky vasculature in the co-culture with cancer cells. The permeable endothelial wall displays heterogeneity, dependent on the number and distance of HeLa spheroids, resembling to some extent the *in vivo* pathologies of many tumors.

We obtained a precise and direct information about the performance and stability of the micelles in each of the barriers, thanks to the time and space-resolved imaging. We reported the ability of the most stable hybrids **1** and **2** to extravasate from the blood vessel model as assembled micelles, while the shear stress and interactions with the EB induced disassembly of the hybrid **3**. Therefore, we believe these two micelles are the best candidates to be used as DDS *in vivo*. However, we observed the loss of stability of hybrid **1** in proximity of the spheroids, as well as, a poor penetration into its depth, which indicates a need for improvement to achieve good *in vivo* efficacy.

Our approach, combining spectrally responsive supramolecular structures with a cancer-on-a-chip platform has the capacity to provide new knowledge about nanoparticles performance, stability and accumulation in tumor, which is essential to bridge the gap between *in vitro* and *in vivo* testing of new drug delivery systems.

## 4.8 Experimental section

### *Microfluidic device and setup*

Microfluidic 3D culture chip DAX-1 (AIM Biotech) was used as a platform to reconstruct tumor microenvironment (blood vessel model channel and ECM with embedded spheroids). LUC-1 connectors (AIM Biotech) were used to connect the chip inlets with luer connector ended PTFE tubing to facilitate the continuous perfusion. The other end of the tubing was connected to a syringe placed in a double syringe pump (Nexus Fusion 200) and filled with HUVEC (EndoGRO, Millipore) basal medium, used to constantly perfuse the chip for 48 – 72h.

### *Cells and reagents*

Human Umbilical Vein Endothelial Cells (Promocell) were used to recreate blood vessel lining in the blood vessel model channel and HeLa cells were used in to create tumor spheroids. HUVECs were cultured in EndoGRO Basal Medium (Millipore) supplemented with SCME001 kit (EndoGRO-LS Supplement 0.2%, rh EGF 5 ng/mL, Ascorbic Acid 50 µg/mL, L-Glutamine 10 mM, Hydrocortisone Hemisuccinate 1 µg/mL, Heparin Sulfate 0.75 U/mL, FBS 2%) and penicillin/streptomycin 1% (Biowest). HeLa cells were cultured in Dulbecco's Modified Eagle Medium (DMEM, as received with L-Glutamine, 4.5 g/L D-glucose and pyruvate, Gibco) supplemented with FBS 5% (Gibco) and penicillin/streptomycin 1% (Biowest). HUVECs were cultured in 75 cm<sup>2</sup> flasks and HeLa in 25 cm<sup>2</sup> flasks at 37°C and 5% CO<sub>2</sub>. Cells were harvested using trypsin-EDTA (0.25%, Gibco) when reached 70-80% confluence.

### *Cell culture in the Microfluidic device*

Collagen gel at concentration of 2.5 mg/mL was prepared, introduced and polymerized according to the general protocol v5.3 (AIM Biotech). In brief, Rat tail collagen Type I (Corning Life Science) was mixed on ice with 10x PBS (Sigma Aldrich) and Phenol Red (Sigma Aldrich), and pH of the mixture was adjusted to 7.4 using 0.5 M NaOH (NaOH in pellets PanReac dissolved in MiliQ water), final volume was adjusted with MiliQ water (for healthy model) or with suspension of HeLa clusters (for cancer model).

For preparation of cancer model microfluidic chip HeLa cells were seeded into 96-well ultra-low attachment plate (Corning) at 0.5 – 1.5 k cells/well and cultured for 72 ± 24h. Formed cell spheroids were harvested, centrifuged and resuspended in previously prepared collagen gel, resulting in few clusters (of 100 ± 50 µm) per 10 µL of the gel at the concentration of 2.5 mg/mL. Prepared collagen was inserted into the central channel of 3D culture chip and allowed to polymerize during 30 min. at 37°C and 5% CO<sub>2</sub>. After

gel polymerization one of the lateral channels was prepared for HUVECs culture, by coating the channel with 50  $\mu\text{g}/\text{mL}$  fibronectin (FN) from bovine plasma (Sigma Aldrich) during 2h at 37°C and 5%  $\text{CO}_2$ . Remaining lateral channel was filled in with DMEM (HeLa culture medium) and closed using luer caps.

After the incubation time, the FN was washed away using 1x PBS (Gibco) and EndoGRO HUVEC medium. HUVECs were seeded in the prepared lateral channel at a density of 2.5-3.5M cells/mL. The 3D culture chip was flipped upside down to allow cell adhesion to the upper plane during 1.5-2.5h at 37°C and 5%  $\text{CO}_2$ . Second batch of HUVECs cultured in another flasks was harvested and introduced to the same lateral channel at the same concentration as previously. The cells were then incubated for minimum 2h at 37°C and 5%  $\text{CO}_2$  in the upright position to allow their attachment to the lower plane. Next, the chip was perfused with EndoGRO HUVEC medium at a flow rate 3-5  $\mu\text{L}/\text{min}$  during 48 - 72 hours (as described above), until HUVECs reached confluency.

#### *Hybrids perfusion setup*

Hybrids 1-4 were prepared at a concentration of 480  $\mu\text{M}$  in filtered PBS, sonicated for 5 minutes and let to equilibrate for at least 10 minutes. Prior to hybrid flowing into the chip they were mixed with full EndroGRO HUVEC medium resulting in final concentration of 160  $\mu\text{M}$ .

The microfluidic chip was placed into the on-stage incubator of a Zeiss LSM 800 Confocal microscope at a temperature of 37°C and 5%  $\text{CO}_2$ , and connected to peristaltic pump (Ismatec, Reglo Digital, ISM597) with a silicone tubing (Tygon, Kinesis) to perfuse hybrids during real-time imaging at 15  $\mu\text{L}/\text{min}$ . Hybrids were excited using 405 nm laser and emission spectra was collected using two different PMT detectors to detect both monomer and micelle separately and simultaneous. The windows of detection were set as following: i) monomer 446-500 nm and ii) micelle 500-700 nm. Ratiometric images were obtained from dividing the micelle image by the monomer image, after applying a mask to each image were noise was removed.

To calculate the amount of hybrid able to extravasate we first sum up the signal of both windows. Next, we calculated the mean intensity signal of the vessel channel and used this value as the maximum concentration. Next the mean intensity signal of the gel channel was calculated and divided by the maximum signal concentration.

#### *Dextran perfusion*

10kDa Dextran labelled with AlexaFluor568 (Thermo Fisher Scientific) was diluted in HUVEC (EndoGRO) medium at a final concentration of 1  $\mu\text{g}/\text{mL}$ . The solution was perfused into the blood vessel model channel at a flow rate of 5  $\mu\text{L}/\text{min}$  using the syringe pump. The perfusion of dextran was monitored

using Nikon Eclipse Ti2 epifluorescent microscope. The chip was placed in the on-stage incubator (OKOlab) at a temperature of 37°C and 5% CO<sub>2</sub>, the perfused fluorophore was excited at 525 nm and emission collected at 650 nm.

#### *HeLa spheroid viability assay*

The viability of HeLa cells within the spheroids were evaluated using Calcein (Fluka, Sigma Aldrich) and Propidium Iodide (Sigma Aldrich) to stain live and dead cells, respectively. First, cells were incubated with 10 µM Calcein solution for 20 min. at 37°C and 5% CO<sub>2</sub>. Next, the cells were incubated with 10 µg/mL Propidium Iodide solution for 5 min. at 37°C and 5% CO<sub>2</sub> and then washed with 1x PBS (Sigma Aldrich). The imaging was performed using Zeiss LSM 800 Confocal microscope. The Calcein and Propidium Iodide stained spheroids were excited at laser wavelength of 488 nm and 561 nm respectively and detection windows set at 400 – 600 nm for Calcein and 600 – 700 nm for Propidium Iodide. The 3D image was reconstructed (ZEN, Confocal microscope software) from slices acquired in a Z-stack mode with a plane interval of 1,5 µm.

#### *Immunostaining, labelling and Confocal Microscopy (Confocal Imaging Labelling)*

Cells in the microfluidic chip were washed with 1x PBS (Gibco) and fixed with 4wt% solution of paraformaldehyde (PFA, Sigma Aldrich) in 1x PBS. After 10 minutes the fixative was washed away with 1x PBS, cells were permeabilized during 10 minutes with 0.1% solution of Triton X-100 (Sigma Aldrich) in 1x PBS and exposed for 1h to a 3% Bovine Serum Albumin (BSA, Sigma Aldrich) blocking solution in 1x PBS.

Next, the HUVECs' tight junctions were stained using 5 µg/mL ZO-1 (Zonula Occludens-1) Monoclonal Antibody conjugated with Alexa Fluor 488 (Thermo Fisher Scientific) solution in previously prepared 3% BSA during O/N incubation at 4°C. In the next step the cells were washed with 3% BSA solution and incubated with 1x Phalloidin-iFluor594 (Abcam, stock 1000x) solution (in 1% BSA) for 30 min. at RT to stain actin filaments. The cell nuclei were stained after washing the cells with 1x PBS, using Hoechst 33258 stain at concentration 5 µg/mL. After 10 min. of incubation at RT the cells were washed with 1x PBS and imaged at RT using Zeiss LSM 800 Confocal microscope. Nuclei, tight junctions and actin were excited using 405 nm, 488 nm and 561 nm laser, respectively. The 3D images were acquired scanning the sample in a Z-stack mode, with an acquisition plane each 1 to 10 µm and later reconstructed into 3D image using the ZEN (Confocal microscope) software.

To calculate the orientation of actin filaments in static vs dynamic conditions; two independent chips were prepared as explained, however, one of the chips was incubated in static conditions, with medium change

every 24h, meanwhile the other was continuously perfused with cell medium. After 72 hours the cells were fixed and actin stained, confocal images of actin were acquired using Zeiss LSM 800. The images were analyzed using the OrientationJ plugin of ImageJ to obtain the distribution of the orientation's graphs.

## 4.9 References

- (1) Behan, B. L.; DeWitt, D. G.; Bogdanowicz, D. R.; Koppes, A. N.; Bale, S. S.; Thompson, D. M. Single-Walled Carbon Nanotubes Alter Schwann Cell Behavior Differentially within 2D and 3D Environments. *J. Biomed. Mater. Res. A* **2011**, *96A* (1), 46–57. <https://doi.org/10.1002/jbm.a.32939>.
- (2) Farokhzad, O. C.; Langer, R. Nanomedicine: Developing Smarter Therapeutic and Diagnostic Modalities. *Adv. Drug Deliv. Rev.* **2006**, *58* (14), 1456–1459. <https://doi.org/10.1016/j.addr.2006.09.011>.
- (3) Steichen, S. D.; Caldorera-Moore, M.; Peppas, N. A. A Review of Current Nanoparticle and Targeting Moieties for the Delivery of Cancer Therapeutics. *Eur. J. Pharm. Sci.* **2013**, *48* (3), 416–427. <https://doi.org/10.1016/j.ejps.2012.12.006>.
- (4) James, N. D.; Coker, R. J.; Tomlinson, D.; Harris, J. R. W.; Gompels, M.; Pinching, A. J.; Stewart, J. S. W. Liposomal Doxorubicin (Doxil): An Effective New Treatment for Kaposi's Sarcoma in AIDS. *Clin. Oncol.* **1994**, *6* (5), 294–296. [https://doi.org/10.1016/S0936-6555\(05\)80269-9](https://doi.org/10.1016/S0936-6555(05)80269-9).
- (5) Wilhelm, S.; Tavares, A. J.; Dai, Q.; Ohta, S.; Audet, J.; Dvorak, H. F.; Chan, W. C. W. Analysis of Nanoparticle Delivery to Tumours. *Nat. Rev. Mater.* **2016**, *1*, 16014. <https://doi.org/10.1038/natrevmats.2016.14>.
- (6) Jain, R. K.; Stylianopoulos, T. Delivering Nanomedicine to Solid Tumors. *Nat. Rev. Clin. Oncol.* **2010**, *7* (11), 653–664. <https://doi.org/10.1038/nrclinonc.2010.139>.
- (7) Owen, S. C.; Chan, D. P. Y.; Shoichet, M. S. Polymeric Micelle Stability. *Nano Today* **2012**, *7* (1), 53–65. <https://doi.org/10.1016/j.nantod.2012.01.002>.
- (8) Holme, M. N.; Fedotenko, I. A.; Abegg, D.; Althaus, J.; Babel, L.; Favarger, F.; Reiter, R.; Tanasescu, R.; Zaffalon, P.-L.; Ziegler, A.; Müller, B.; Saxer, T.; Zumbuehl, A. Shear-Stress Sensitive Lenticular Vesicles for Targeted Drug Delivery. *Nat. Nanotechnol.* **2012**, *7* (8), 536–543. <https://doi.org/10.1038/nnano.2012.84>.
- (9) Shi, Y.; Lammers, T.; Storm, G.; Hennink, W. E. Physico-Chemical Strategies to Enhance Stability and Drug Retention of Polymeric Micelles for Tumor-Targeted Drug Delivery. *Macromol. Biosci.* **2017**, *17* (1), 1600160. <https://doi.org/10.1002/mabi.201600160>.
- (10) Barua, S.; Mitragotri, S. Challenges Associated with Penetration of Nanoparticles across Cell and Tissue Barriers: A Review of Current Status and Future Prospects. *Nano Today* **2014**, *9* (2), 223–243. <https://doi.org/10.1016/j.nantod.2014.04.008>.
- (11) Maeda, H.; Wu, J.; Sawa, T.; Matsumura, Y.; Hori, K. Tumor Vascular Permeability and the EPR Effect in Macromolecular Therapeutics: A Review. *J. Controlled Release* **2000**, *65* (1), 271–284. [https://doi.org/10.1016/S0168-3659\(99\)00248-5](https://doi.org/10.1016/S0168-3659(99)00248-5).
- (12) Upponi, J. R.; Torchilin, V. P. Passive vs. Active Targeting: An Update of the EPR Role in Drug Delivery to Tumors. In *Nano-Oncologicals: New Targeting and Delivery Approaches*; Alonso, M. J., Garcia-Fuentes, M., Eds.; Advances in Delivery Science and Technology; Springer International Publishing: Cham, 2014; pp 3–45. [https://doi.org/10.1007/978-3-319-08084-0\\_1](https://doi.org/10.1007/978-3-319-08084-0_1).
- (13) Golombek, S. K.; May, J.-N.; Theek, B.; Appold, L.; Drude, N.; Kiessling, F.; Lammers, T. Tumor Targeting via EPR: Strategies to Enhance Patient Responses. *Adv. Drug Deliv. Rev.* **2018**, *130*, 17–38. <https://doi.org/10.1016/j.addr.2018.07.007>.
- (14) Heldin, C.-H.; Rubin, K.; Pietras, K.; Östman, A. High Interstitial Fluid Pressure — an Obstacle in Cancer Therapy. *Nat. Rev. Cancer* **2004**, *4* (10), 806–813. <https://doi.org/10.1038/nrc1456>.
- (15) Chen, H.; Kim, S.; He, W.; Wang, H.; Low, P. S.; Park, K.; Cheng, J.-X. Fast Release of Lipophilic Agents from Circulating PEG-PDLLA Micelles Revealed by in Vivo Förster Resonance Energy Transfer Imaging. *Langmuir* **2008**, *24* (10), 5213–5217. <https://doi.org/10.1021/la703570m>.

- (16) Lu, J.; Owen, S. C.; Shoichet, M. S. Stability of Self-Assembled Polymeric Micelles in Serum. *Macromolecules* **2011**, *44* (15), 6002–6008. <https://doi.org/10.1021/ma200675w>.
- (17) Gravier, J.; Sancey, L.; Hirsjärvi, S.; Rustique, E.; Passirani, C.; Benoît, J.-P.; Coll, J.-L.; Texier, I. FRET Imaging Approaches for in Vitro and in Vivo Characterization of Synthetic Lipid Nanoparticles. *Mol. Pharm.* **2014**, *11* (9), 3133–3144. <https://doi.org/10.1021/mp500329z>.
- (18) Aguilar-Castillo, B. A.; Santos, J. L.; Luo, H.; Aguirre-Chagala, Y. E.; Palacios-Hernández, T.; Herrera-Alonso, M. Nanoparticle Stability in Biologically Relevant Media: Influence of Polymer Architecture. *Soft Matter* **2015**, *11* (37), 7296–7307. <https://doi.org/10.1039/C5SM01455G>.
- (19) Sun, X.; Wang, G.; Zhang, H.; Hu, S.; Liu, X.; Tang, J.; Shen, Y. The Blood Clearance Kinetics and Pathway of Polymeric Micelles in Cancer Drug Delivery. *ACS Nano* **2018**, *12* (6), 6179–6192. <https://doi.org/10.1021/acsnano.8b02830>.
- (20) Feiner-Gracia, N.; Buzhor, M.; Fuentes, E.; Pujals, S.; Amir, R. J.; Albertazzi, L. Micellar Stability in Biological Media Dictates Internalization in Living Cells. *J. Am. Chem. Soc.* **2017**, *139* (46), 16677–16687. <https://doi.org/10.1021/jacs.7b08351>.
- (21) Breslin, S.; O’Driscoll, L. Three-Dimensional Cell Culture: The Missing Link in Drug Discovery. *Drug Discov. Today* **2013**, *18* (5), 240–249. <https://doi.org/10.1016/j.drudis.2012.10.003>.
- (22) Gupta, N.; Liu, J. R.; Patel, B.; Solomon, D. E.; Vaidya, B.; Gupta, V. Microfluidics-Based 3D Cell Culture Models: Utility in Novel Drug Discovery and Delivery Research. *Bioeng. Transl. Med.* **2016**, *1* (1), 63–81. <https://doi.org/10.1002/btm2.10013>.
- (23) Jeon, J. S.; Zervantonakis, I. K.; Chung, S.; Kamm, R. D.; Charest, J. L. In Vitro Model of Tumor Cell Extravasation. *PLOS ONE* **2013**, *8* (2), e56910. <https://doi.org/10.1371/journal.pone.0056910>.
- (24) Truong, D.; Puleo, J.; Llave, A.; Mouneimne, G.; Kamm, R. D.; Nikkhah, M. Breast Cancer Cell Invasion into a Three Dimensional Tumor-Stroma Microenvironment. *Sci. Rep.* **2016**, *6*, 34094. <https://doi.org/10.1038/srep34094>.
- (25) Kim, M.-C.; Whisler, J.; Silberberg, Y. R.; Kamm, R. D.; Asada, H. H. Cell Invasion Dynamics into a Three Dimensional Extracellular Matrix Fibre Network. *PLOS Comput. Biol.* **2015**, *11* (10), e1004535. <https://doi.org/10.1371/journal.pcbi.1004535>.
- (26) Kalchman, J.; Fujioka, S.; Chung, S.; Kikkawa, Y.; Mitaka, T.; Kamm, R. D.; Tanishita, K.; Sudo, R. A Three-Dimensional Microfluidic Tumor Cell Migration Assay to Screen the Effect of Anti-Migratory Drugs and Interstitial Flow. *Microfluid. Nanofluidics* **2013**, *14* (6), 969–981. <https://doi.org/10.1007/s10404-012-1104-6>.
- (27) Jeong, G. S.; Han, S.; Shin, Y.; Kwon, G. H.; Kamm, R. D.; Lee, S.-H.; Chung, S. Sprouting Angiogenesis under a Chemical Gradient Regulated by Interactions with an Endothelial Monolayer in a Microfluidic Platform. *Anal. Chem.* **2011**, *83* (22), 8454–8459. <https://doi.org/10.1021/ac202170e>.
- (28) Farahat, W. A.; Wood, L. B.; Zervantonakis, I. K.; Schor, A.; Ong, S.; Neal, D.; Kamm, R. D.; Asada, H. H. Ensemble Analysis of Angiogenic Growth in Three-Dimensional Microfluidic Cell Cultures. *PLOS ONE* **2012**, *7* (5), e37333. <https://doi.org/10.1371/journal.pone.0037333>.
- (29) Ko, J.; Ahn, J.; Kim, S.; Lee, Y.; Lee, J.; Park, D.; Jeon, N. L. Tumor Spheroid-on-a-Chip: A Standardized Microfluidic Culture Platform for Investigating Tumor Angiogenesis. *Lab. Chip* **2019**, *19* (17), 2822–2833. <https://doi.org/10.1039/C9LC00140A>.
- (30) Nashimoto, Y.; Okada, R.; Hanada, S.; Arima, Y.; Nishiyama, K.; Miura, T.; Yokokawa, R. Vascularized Cancer on a Chip: The Effect of Perfusion on Growth and Drug Delivery of Tumor Spheroid. *Biomaterials* **2020**, *229*, 119547. <https://doi.org/10.1016/j.biomaterials.2019.119547>.
- (31) Ho, Y. T.; Adriani, G.; Beyer, S.; Nhan, P.-T.; Kamm, R. D.; Kah, J. C. Y. A Facile Method to Probe the Vascular Permeability of Nanoparticles in Nanomedicine Applications. *Sci. Rep.* **2017**, *7* (1), 707. <https://doi.org/10.1038/s41598-017-00750-3>.



- (32) Tang, Y.; Soroush, F.; Sheffield, J. B.; Wang, B.; Prabhakarapandian, B.; Kiani, M. F. A Biomimetic Microfluidic Tumor Microenvironment Platform Mimicking the EPR Effect for Rapid Screening of Drug Delivery Systems. *Sci. Rep.* **2017**, *7* (1), 9359. <https://doi.org/10.1038/s41598-017-09815-9>.
- (33) Young, E. W. K.; Watson, M. W. L.; Srigunapalan, S.; Wheeler, A. R.; Simmons, C. A. Technique for Real-Time Measurements of Endothelial Permeability in a Microfluidic Membrane Chip Using Laser-Induced Fluorescence Detection. *Anal. Chem.* **2010**, *82* (3), 808–816. <https://doi.org/10.1021/ac901560w>.
- (34) Griffith, L. G.; Swartz, M. A. Capturing Complex 3D Tissue Physiology in Vitro. *Nat. Rev. Mol. Cell Biol.* **2006**, *7* (3), 211–224. <https://doi.org/10.1038/nrm1858>.
- (35) Xu, X.; Farach-Carson, M. C.; Jia, X. Three-Dimensional in Vitro Tumor Models for Cancer Research and Drug Evaluation. *Biotechnol. Adv.* **2014**, *32* (7), 1256–1268. <https://doi.org/10.1016/j.biotechadv.2014.07.009>.
- (36) Ng, C. P.; Pun, S. H. A Perfusable 3D Cell–Matrix Tissue Culture Chamber for in Situ Evaluation of Nanoparticle Vehicle Penetration and Transport. *Biotechnol. Bioeng.* **2008**, *99* (6), 1490–1501. <https://doi.org/10.1002/bit.21698>.
- (37) Albanese, A.; Lam, A. K.; Sykes, E. A.; Rocheleau, J. V.; Chan, W. C. W. Tumour-on-a-Chip Provides an Optical Window into Nanoparticle Tissue Transport. *Nat. Commun.* **2013**, *4*, 2718. <https://doi.org/10.1038/ncomms3718>.
- (38) Lazzari, G.; Couvreur, P.; Mura, S. Multicellular Tumor Spheroids: A Relevant 3D Model for the in Vitro Preclinical Investigation of Polymer Nanomedicines. *Polym. Chem.* **2017**, *8* (34), 4947–4969. <https://doi.org/10.1039/C7PY00559H>.
- (39) Sindhvani, S.; Syed, A. M.; Ngai, J.; Kingston, B. R.; Maiorino, L.; Rothschild, J.; MacMillan, P.; Zhang, Y.; Rajesh, N. U.; Hoang, T.; Wu, J. L. Y.; Wilhelm, S.; Zilman, A.; Gadde, S.; Sulaiman, A.; Ouyang, B.; Lin, Z.; Wang, L.; Egeblad, M.; Chan, W. C. W. The Entry of Nanoparticles into Solid Tumours. *Nat. Mater.* **2020**. <https://doi.org/10.1038/s41563-019-0566-2>.
- (40) Wang, H.-F.; Ran, R.; Liu, Y.; Hui, Y.; Zeng, B.; Chen, D.; Weitz, D. A.; Zhao, C.-X. Tumor-Vasculature-on-a-Chip for Investigating Nanoparticle Extravasation and Tumor Accumulation. *ACS Nano* **2018**, *12* (11), 11600–11609. <https://doi.org/10.1021/acsnano.8b06846>.
- (41) Chen, Y.; Gao, D.; Wang, Y.; Lin, S.; Jiang, Y. A Novel 3D Breast-Cancer-on-Chip Platform for Therapeutic Evaluation of Drug Delivery Systems. *Anal. Chim. Acta* **2018**, *1036*, 97–106. <https://doi.org/10.1016/j.aca.2018.06.038>.
- (42) Kwak, B.; Ozcelikkale, A.; Shin, C. S.; Park, K.; Han, B. Simulation of Complex Transport of Nanoparticles around a Tumor Using Tumor-Microenvironment-on-Chip. *J. Controlled Release* **2014**, *194*, 157–167. <https://doi.org/10.1016/j.jconrel.2014.08.027>.
- (43) Ravi, M.; Paramesh, V.; Kaviya, S. R.; Anuradha, E.; Solomon, F. D. P. 3D Cell Culture Systems: Advantages and Applications. *J. Cell. Physiol.* **2015**, *230* (1), 16–26. <https://doi.org/10.1002/jcp.24683>.
- (44) Doshi, N.; Prabhakarapandian, B.; Rea-Ramsey, A.; Pant, K.; Sundaram, S.; Mitragotri, S. Flow and Adhesion of Drug Carriers in Blood Vessels Depend on Their Shape: A Study Using Model Synthetic Microvascular Networks. *J. Controlled Release* **2010**, *146* (2), 196–200. <https://doi.org/10.1016/j.jconrel.2010.04.007>.
- (45) Pampaloni, F.; Reynaud, E. G.; Stelzer, E. H. K. The Third Dimension Bridges the Gap between Cell Culture and Live Tissue. *Nat. Rev. Mol. Cell Biol.* **2007**, *8* (10), 839–845. <https://doi.org/10.1038/nrm2236>.
- (46) Hutmacher, D. W. Biomaterials Offer Cancer Research the Third Dimension. *Nat. Mater.* **2010**, *9* (2), 90–93. <https://doi.org/10.1038/nmat2619>.

- (47) Buzhor, M.; Harnoy, A. J.; Tirosh, E.; Barak, A.; Schwartz, T.; Amir, R. J. Supramolecular Translation of Enzymatically Triggered Disassembly of Micelles into Tunable Fluorescent Responses. *Chem. – Eur. J.* **2015**, *21* (44), 15633–15638. <https://doi.org/10.1002/chem.201502988>.
- (48) Zervantonakis, I. K.; Hughes-Alford, S. K.; Charest, J. L.; Condeelis, J. S.; Gertler, F. B.; Kamm, R. D. Three-Dimensional Microfluidic Model for Tumor Cell Intravasation and Endothelial Barrier Function. *Proc. Natl. Acad. Sci.* **2012**, *109* (34), 13515–13520. <https://doi.org/10.1073/pnas.1210182109>.
- (49) Tornavaca, O.; Chia, M.; Dufton, N.; Almagro, L. O.; Conway, D. E.; Randi, A. M.; Schwartz, M. A.; Matter, K.; Balda, M. S. ZO-1 Controls Endothelial Adherens Junctions, Cell–Cell Tension, Angiogenesis, and Barrier Formation. *J. Cell Biol.* **2015**, *208* (6), 821–838. <https://doi.org/10.1083/jcb.201404140>.
- (50) Sinha, R.; Le Gac, S.; Verdonchot, N.; van den Berg, A.; Koopman, B.; Rouwkema, J. Endothelial Cell Alignment as a Result of Anisotropic Strain and Flow Induced Shear Stress Combinations. *Sci. Rep.* **2016**, *6*. <https://doi.org/10.1038/srep29510>.
- (51) Aird, W. C. Spatial and Temporal Dynamics of the Endothelium. *J. Thromb. Haemost.* **2005**, *3* (7), 1392–1406. <https://doi.org/10.1111/j.1538-7836.2005.01328.x>.
- (52) Tzima, E.; Irani-Tehrani, M.; Kiosses, W. B.; Dejana, E.; Schultz, D. A.; Engelhardt, B.; Cao, G.; DeLisser, H.; Schwartz, M. A. A Mechanosensory Complex That Mediates the Endothelial Cell Response to Fluid Shear Stress. *Nature* **2005**, *437* (7057), 426. <https://doi.org/10.1038/nature03952>.
- (53) Adriani, G.; Ma, D.; Pavesi, A.; Kamm, R. D.; Goh, E. L. K. A 3D Neurovascular Microfluidic Model Consisting of Neurons, Astrocytes and Cerebral Endothelial Cells as a Blood–Brain Barrier. *Lab. Chip* **2017**, *17* (3), 448–459. <https://doi.org/10.1039/C6LC00638H>.
- (54) Booth, R.; Kim, H. Characterization of a Microfluidic in Vitro Model of the Blood-Brain Barrier (MBBB). *Lab. Chip* **2012**, *12* (10), 1784. <https://doi.org/10.1039/c2lc40094d>.
- (55) Herland, A.; van der Meer, A. D.; FitzGerald, E. A.; Park, T.-E.; Sleeboom, J. J. F.; Ingber, D. E. Distinct Contributions of Astrocytes and Pericytes to Neuroinflammation Identified in a 3D Human Blood-Brain Barrier on a Chip. *PLoS ONE* **2016**, *11* (3). <https://doi.org/10.1371/journal.pone.0150360>.
- (56) Baker, B. M.; Chen, C. S. Deconstructing the Third Dimension: How 3D Culture Microenvironments Alter Cellular Cues. *J. Cell Sci.* **2012**, *125* (Pt 13), 3015–3024. <https://doi.org/10.1242/jcs.079509>.
- (57) LaBarbera, D. V.; Reid, B. G.; Yoo, B. H. The Multicellular Tumor Spheroid Model for High-Throughput Cancer Drug Discovery. *Expert Opin. Drug Discov.* **2012**, *7* (9), 819–830. <https://doi.org/10.1517/17460441.2012.708334>.
- (58) Wilson, W. R.; Hay, M. P. Targeting Hypoxia in Cancer Therapy. *Nat. Rev. Cancer* **2011**, *11* (6), 393–410. <https://doi.org/10.1038/nrc3064>.
- (59) Minamikawa-Tachino, R.; Ogura, K.; Ito, A.; Nagayama, K. Time-Lapse Imaging of HeLa Spheroids in Soft Agar Culture Provides Virtual Inner Proliferative Activity. *PLOS ONE* **2020**, *15* (4), e0231774. <https://doi.org/10.1371/journal.pone.0231774>.
- (60) Pereira, P. M. R.; Berisha, N.; Bhupathiraju, N. V. S. D. K.; Fernandes, R.; Tomé, J. P. C.; Drain, C. M. Cancer Cell Spheroids Are a Better Screen for the Photodynamic Efficiency of Glycosylated Photosensitizers. *PLOS ONE* **2017**, *12* (5), e0177737. <https://doi.org/10.1371/journal.pone.0177737>.
- (61) Tight Junctions <https://www.crcpress.com/Tight-Junctions/Cereijido-Anderson/p/book/9780849323836> (accessed Jul 10, 2019).

- (62) Tarbell, J. M. Shear Stress and the Endothelial Transport Barrier. *Cardiovasc. Res.* **2010**, *87* (2), 320–330. <https://doi.org/10.1093/cvr/cvq146>.
- (63) Kaji, H.; Yokoi, T.; Kawashima, T.; Nishizawa, M. Controlled Cocultures of HeLa Cells and Human Umbilical Vein Endothelial Cells on Detachable Substrates. *Lab Chip* **2009**, *9* (3), 427–432. <https://doi.org/10.1039/B812510D>.
- (64) Maeda, H. Toward a Full Understanding of the EPR Effect in Primary and Metastatic Tumors as Well as Issues Related to Its Heterogeneity. *Adv. Drug Deliv. Rev.* **2015**, *91*, 3–6. <https://doi.org/10.1016/j.addr.2015.01.002>.
- (65) Tchoryk, A.; Taresco, V.; Argent, R. H.; Ashford, M.; Gellert, P. R.; Stolnik, S.; Grabowska, A.; Garnett, M. C. Penetration and Uptake of Nanoparticles in 3D Tumor Spheroids. *Bioconjug. Chem.* **2019**, *30* (5), 1371–1384. <https://doi.org/10.1021/acs.bioconjchem.9b00136>.
- (66) Agarwal, R.; Journey, P.; Raythatha, M.; Singh, V.; Sreenivasan, S. V.; Shi, L.; Roy, K. Effect of Shape, Size, and Aspect Ratio on Nanoparticle Penetration and Distribution inside Solid Tissues Using 3D Spheroid Models. *Adv. Healthc. Mater.* **2015**, *4* (15), 2269–2280. <https://doi.org/10.1002/adhm.201500441>.
- (67) Lu, H.; Utama, R. H.; Kitiyotsawat, U.; Babiuch, K.; Jiang, Y.; Stenzel, M. H. Enhanced Transcellular Penetration and Drug Delivery by Crosslinked Polymeric Micelles into Pancreatic Multicellular Tumor Spheroids. *Biomater. Sci.* **2015**, *3* (7), 1085–1095. <https://doi.org/10.1039/C4BM00323C>.
- (68) Du, A. W.; Lu, H.; Stenzel, M. Stabilization of Paclitaxel-Conjugated Micelles by Cross-Linking with Cystamine Compromises the Antitumor Effects against Two- and Three-Dimensional Tumor Cellular Models. *Mol. Pharm.* **2016**, *13* (11), 3648–3656. <https://doi.org/10.1021/acs.molpharmaceut.6b00410>.
- (69) Arranja, A.; Denkova, A. G.; Morawska, K.; Waton, G.; van Vlierberghe, S.; Dubruel, P.; Schosseler, F.; Mendes, E. Interactions of Pluronic Nanocarriers with 2D and 3D Cell Cultures: Effects of PEO Block Length and Aggregation State. *J. Controlled Release* **2016**, *224*, 126–135. <https://doi.org/10.1016/j.jconrel.2016.01.014>.

## Chapter 5| Discussion

*This Chapter summarizes and discusses the work presented in the previous Chapters. It focuses on the impact of microfluidic technology in preclinical development of drug nanocarriers, highlighting its strengths and weaknesses from the perspective of research laboratories, as well as it looks at proposed solutions and obtained results through an eye of pharmaceutical industry.*

*Microfluidic technology in nanocarrier formulation and screening from the perspective of a research laboratory and pharmaceutical development*

The work presented in this thesis focused on development of microfluidic devices applied to drug delivery systems field. The main aim was to provide new solutions and improvements that could accelerate the nanomedicine discovery process. The work tackles the drug nanocarrier development at different phases: from formulation to *in vitro* screening, demonstrating the incorporation of microfluidic devices in each step.

In the Chapter 2 one can find a description of an uncomplicated design of a microfluidic chip, integrated into the process of drug nanocarrier formulation. The presented three-inlet/one-outlet microchannel architecture provides benefits in control of nanoparticles formulation in the nanoprecipitation process. The incorporation of microfluidic device allowed us to control mixing of the used liquid phases and modify process flow parameters, which are crucial in the nanoparticle formation stages. The results obtained with the microfluidic device have demonstrated tunability of particle size, a feature that is fundamental in the design of current cancer treatment drug nanocarriers. This tunability was directly correlated to the calculated mixing time of the solvent and antisolvent phase used for our microfluidic device geometry and setup, following the thesis of nanoparticle formation through nucleation and growth stages. In traditional manual bulk mixing methods such estimation cannot be easily modeled or predicted, what limits the possibility to control the process. Additionally, the proposed microfluidic strategy allowed us to process single batch of polymer material blend with uniform physical properties, to obtain wide range of nanoparticles average diameters. Typically, in bulk nanoprecipitation (where the particle size cannot be controlled via flow parameters) such diameter range would be obtained through prior modification of polymer(s) molecular weight, that eventually yields smaller or larger particle diameter. The possibility to study the nanocarrier formation using a single batch of polymeric materials is certainly an added value. It allows to eliminate the probable raw material heterogeneities occurring in polymer synthesis, which could cause incoherent trends in obtained nanoparticle size. As explained in Chapter 2, the size control may be one of few other features that could be potentially controlled engaging the microfluidic technology into nanocarrier formulation. Presented work also investigated encapsulation of fluorescent molecules (mimicking drugs) into the nanocarrier. It indicated a potential improvement in the homogeneity of encapsulated moieties using the microfluidic device, comparing to the standard manual technique. However, the results are still preliminary, and more research would be required to make such statement with confidence. Further understanding of what exactly can be achieved with control of flow parameters in hydrodynamic flow focusing nanocarrier formulation should go in hand with advanced analysis techniques. In case of this work, transmission electron microscopy helped to resolve the particle size and morphology,

meanwhile the total internal reflection fluorescence microscopy allowed to image the dye encapsulation in nanoparticles. These are examples of techniques that permit to “look” on a single particle level, which is an important approach for better understanding of their chemical and physical properties. These techniques have the potential to reveal certain flaws, which are easy to overlook in bulk analysis methods (such as the encapsulation heterogeneity). Thanks to them, the outcome of nanoparticle synthesis or formulation step could be better evaluated and understood already in early process stage.

The microfluidic device – assisted formulation provides above – mentioned advantages, however it comes at the price of difficult scale up. This is a serious obstacle from the perspective of the technology transfer to a pharmaceutical industry that requires tens to hundreds of kilograms of product yearly. The microfluidic formulation demonstrated to be robust and reproducible, which is in accordance with the industrial scale requirements, however the generally understood scale up would not be able to take place in a microfluidic device – based process. Typically increasing the batch size equals to increasing the vessel dimension, however the essence of microfluidic technology is irreversibly bound to the microscale size of structures and channels. Here, scaling out, rather than scaling up, would seem appropriate. This means a parallelization of multiple chips, stacked in the same controlled environment and coupled to precision equipment. It is imaginable, that this approach is not the perfect solution, as the setup would appear very complex, and the increased batch size would origin from blends of individual formulations, from each single one would require analysis. Having this in mind, currently the microfluidic technology in the formulation of drug nanocarriers appears to be vital in research laboratories, where the quality dominates the need of quantity. However, the growing interest in the area of personalized nanomedicine, where each individual patient requires custom made dose, makes the microfluidic technology become the medicine formulation approach of tomorrow.

Having in mind the research scale (and the personalized nanomedicine), to be able to formulate small quantities comes with an economic advantage. This is especially essential in the development of a formulation with desired characteristics, where the number of tested prototypes is likely to be high. Chapter 3 continues the exploration of nanocarrier formulation expanding the microfluidic device presented in the Chapter 2. It focuses on the development of a module, which has the potential to aid rapid combinatorial formulation of nanocarriers. As explained in the Chapter 3, the five-inlets microfluidic passive mixer chip was designed to permit formulation of nanoparticles from varying precursors, using a setup coupled with an independently operating syringe pump heads. This device aimed to accelerate the generation of possible combinations, in an economical and time-efficient fashion. In the proof-of-concept tests, the micromixer demonstrated efficient stream mixing at a range of different flow rates. Furthermore, the new module was connected with the previously described hydrodynamic flow focusing chip, to experimentally confirm its

applicability for the nanocarrier formulation. This type of device could be further used in any process from chemical reactions to biological applications, whenever thorough and rapid stream mixing at low operating volumes is required.

In the prototyping and testing stage it occurred how the use of PDMS can hinder experimental outcomes. The disadvantage of PDMS, related to its adsorption of small molecules, cannot remain unnoticed. As far as this material and techniques related with its processing are currently the best solution in designing and prototyping of microfluidic chips for many purposes, it should be considered (depending on the use) to exploit other materials. In the Chapter 3 the severity of a dye absorbed in depth of PDMS was demonstrated and to address this challenge, a borosilicate glass micromixer was fabricated and tested. With the new material the absorption problem was completely eliminated, and a set of run experiments confirmed it performed equally to the PDMS model in terms of the mixing efficiency. Furthermore, the glass body permitted for more robust solution of threaded, standardized connections with syringe tubing, and opened the gate for testing other than acetonitrile solvents, what can be appreciated in the potential translation of such designs to the industry. Overall glass or thermoplastic polymers are broadly used in common laboratory activities; therefore, these materials are more interesting than PDMS for translation of microfluidic technology to commercial scale. However, in the case of mass production, the end user reaching out for the commercial solutions, has little or no impact on the device design and microchannel geometry. The option proposed in the Chapter 3 resulted in the design freedom, however laser etching or similar glass-processing technologies are often out of research laboratories access, as it was in our case, the fabrication was outsourced to a specialized company. This implies also relatively long waiting times and high price per unit (comparing to commercialized options or PDMS prototypes). The use of chemically resistant borosilicate glass as the chip body opens the door for experimentation with other solvents, that could be interesting in the formulation of drug nanocarriers. This adds to chip's versatility as potential mixing device, that could be used in chemical synthesis or similar processes. However, glass brittleness must be commented here, what (considering the unit price) is an important disadvantage, that makes the device in between status of disposable and a long-lasting one.

Other compounds for fabrication of microfluidic devices, such as polystyrene or cyclic olefin polymers are very attractive for bioengineering purposes, where the optical transparency is still important, however the chemical resistivity gives way to biocompatibility, more affordable price, and robustness. With this being said, the cyclic olefin polymer – body AIM Biotech microfluidic chip used in the studies presented in the Chapter 4 may be one of the most widely sold and used bioengineering microfluidic platforms. It is a flagship example of how a design developed in a research lab became commercialized, and made the microfluidic technology applied in many facilities, that otherwise had limited

microfabrication capacity and access. Despite this chip design being publicly available and free of charge, also in our case we decided to proceed with the commercial solution. Our reason behind it was the scope of the study, which focused on reconstruction of tumor microenvironment elements (described with details in the Chapter 4). First of all, such microfluidic device should be single use, as having to clean and sterilize it after each experiment implies development and validation of cleaning and sterilization methods, which would not be reasonable in this case. Apart from that, the potential microfabrication in PDMS would require very precise process control, as the humidity and other clean room conditions can affect the outcome, comprising the model robustness.

Finally, the Chapter 4 represents how the microfluidic technology can make an impact in the area of disease modeling or screening of potential drug delivery systems. It is remarkable how this field of bioengineering has evolved in the last two decades. Perhaps drug screening and disease development are areas where microfluidics make the most of its impact and where this technology is the closest to regular incorporation into practices of preclinical trials, as we are witnessing it today. Our work focused on reconstruction of a tumorous blood vessel model, where the microfluidic chip was adapted into the experimental setup, allowing us to create perfusable lumen (blood vessel alike) and an adjacent compartment representing either healthy version or cancer – affected tissue. This work contributed to the knowledge about genesis of leaky vasculature, which (as already mentioned above) is the current fundamental principle of drug nanocarriers design for cancer treatment. The microfluidic channel facilitated studies of vascular model resembling physiological conditions thanks to the lumen – alike 3D geometry, where we perfused selected nanocarriers. The presence of adjacent parallel microchannel allowed us to monitor their stability at the modelled vessel – tissue interface, and further in the contact with cancer cells. The study demonstrated how such chip can serve as a drug delivery system screening platform revealing the micelle stability in real time. Although very similar study with the use of these particular nanocarriers was already performed in much simpler 2D setting, reporting corresponding micelle stability as was found in the 3D tumorous blood vessel-on-a-chip, the reconstruction of physiologically relevant barriers resulted in completely new information regarding the cellular uptake of the micelles. Although we did not quantify the amount of taken-up micelles, comparing the new results with the earlier presented reports it was staggering how little nanoparticles could reach and accumulate in the cancer cell spheroid. Despite the use of the same cell line in both studies, the newly recapitulated barriers, such as flow conditions, endothelial wall or extracellular matrix, created important obstacles in nanoparticle performance, that should not be neglected in preclinical evaluation.

Drawing conclusions based on organ-on-a-chip experiments may still encounter certain amount of hesitation. Bioengineered organs or tissues on microfluidic scaffolds have a clear advantage over 2D



systems by providing more accurate and complete information. Certainly, they successfully reflect essential *in vivo* features, however they are still away from exact replication of complexity level presented in many tissues. Nevertheless, certain simplifications in the bioengineering modelling allow them to be widely used with ever-growing applications. It is also important to highlight, that more the system is complex, the higher expertise and skills are required in its preparation and evaluation. Moreover, higher the number of uncontrollable parameters or elements that contribute to the whole, lower the model robustness, and chances of extraction of meaningful data that can be well analyzed and understood. The contribution of microfluidic technology into bioengineering should result with new, more accurate preclinical tools, which means there must be a compromise between these two fields to achieve benefits.

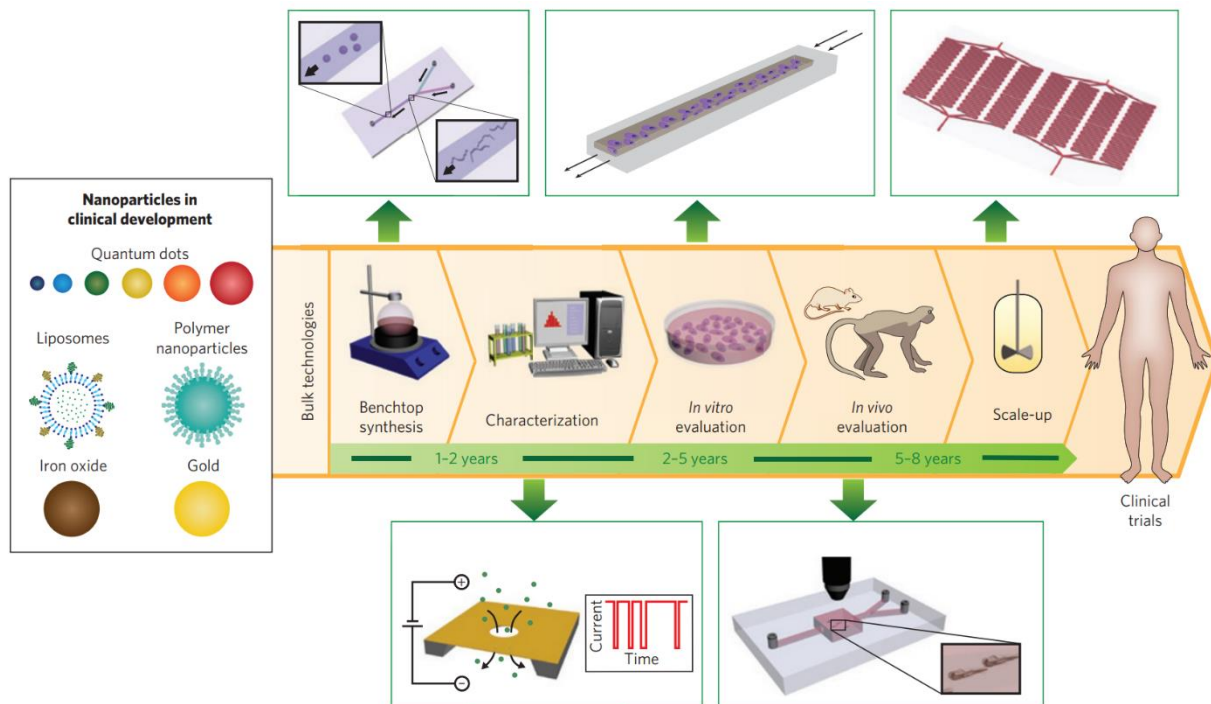
#### *Common requirements in the implementation of microfluidic solutions*

The adaptation of microfluidic technology into biotechnological or pharmaceutical research is a complex process for few reasons. First, there is no universal microfluidic device that “serves for all”, hence the scientific question should be addressed with an adequate chip design. This includes the material selection, geometry of the microstructures and compatibility with available analytical and monitoring techniques. Second, the dominating fields in drug development are biology and chemistry, therefore engineering of microfluidic devices is a foreign area in this environment. Therefore, new solutions based on microfluidics require multidisciplinary approach, that intertwines the knowledge and expertise from different fields and incorporates qualified staff from mentioned sectors. Results obtained through synergistic approach and presented in Chapters 2-5 are indeed an effect of contribution from scientists with various specializations. They reflect the dynamically expanding use of microfluidics in academic and industrial research, which we are witnessing in the last 10 – 20 years.

Behind the scenes of microfluidic chips integrated into formulation or screening of drug nanocarriers there is a whole battery of equipment supporting these activities and assays. This is especially relevant for experiments, where perfusion or dynamic manipulation of liquid is desired. In such case the miniaturization and use of “lab-on-a-chip” term is not exactly adequate or descriptive. As long as the reaction or formulation is indeed confined to microvolumes, the footprint of surrounding equipment is comparable to a regular one. Typically flow in microfluidic devices is generated by syringe, peristaltic or pressure pumps, with each of them having different advantages. As a rule of thumb, the more precise the perfusion equipment, the larger (and more costly) it is. Here it is important to mention, that these (flow) devices are not standard laboratory equipment and as an example, a pressure driven pump requires a gas outlet, reservoirs, monitoring and operation unit as well as pressure- or flowmeters. These advanced benchtop solutions come at a price of at least few thousands of euros. However, many microfluidic devices are used “only” as a static experimental platform or designed to take an advantage of flow induced by

hydrodynamic pressure. This, more economic approach, is especially employed in organ-on-a-chip solutions, where disease development or drug – cell interactions are followed in 3D reconstructed tissue models, where the key feature is microenvironment scale and organization and not necessarily the liquid perfusion.

The idea of “microfluidization” of preclinical development was planted more than a decade ago and well pictured in this illustration from Valencia, P. *et al.* (*Nature Nanotech* **7**, 623–629, 2012). It depicts all the stages of new drug nanocarrier development until the clinical trial phase, demonstrating current methods and their microfluidic alternatives. The whole clinical translation of new nanomedicines is a long and complex process, that could benefit from new solutions which can cut the process time, costs or improve product safety and efficacy. The work presented in this thesis aimed to create examples on microfluidic technology integration with bioengineering, to accelerate the research and development of drug nanocarriers, especially focusing on *in vitro* screening phase and formulation prototyping stage. In the reference to the illustration presented below, it is likely that microfluidic technology will not dominate the entire preclinical path, but considering the current achievements, it is becoming its integral part, giving us the solution of today and the vision of tomorrow.



## Conclusions

Cancer diseases are one of the most threatening health issues of current times. Opposite to the pathogens, which enter our body from external environment, the malignant cells develop from human organism native cells. This, together with the heterogeneity found among patients, makes it very difficult to treat effectively.

This work explored how the integration of microfluidic technology into formulation and screening of drug nanocarriers can improve the development of new anticancer therapies. It proposed solutions and provided tools that potentially could be translated out of the academic area and accelerate the research on drug delivery.

First, an FDA/EMA-approved polymer (PLGA-PEG) was chosen as a drug nanocarrier model and formulated into stable nanoparticles via self-assembly process. The nanoprecipitation method was adapted into the hydrodynamic flow focusing microfluidic chip to fine-tune the particle properties, with the focus on the size. The microchannels enabled control in the particle formation process comparing to the traditional manual bulk method. Specifically, in the microfluidic chip formulation particles with their size dependent upon the fluidic parameters of the injected solvent and antisolvent phases were obtained. The NPs were characterized using bulk methods and techniques providing single particle information, such as Transmission Electron Microscopy (TEM) and Total Internal Reflection Fluorescence (TIRF). The microfluidic approach demonstrated that the change of NPs size can be achieved by other means than the modification of the polymer molecular weight, as it is commonly done. Furthermore, *in vitro* bioevaluation performed on adenocarcinoma cell line (MCF-7) and full human blood demonstrated that the NPs biocompatibility was maintained. Here, the focus on NPs dimension was motivated by the phenomena of their passive transport upon administration into human body, however it was observed during the characterization that the microfluidic formulation could have an impact on other particle properties, such as homogeneity of drug/dye encapsulation.

Next, the development and characterization of a microfluidic passive mixer for NPs solvent phase precursors was demonstrated. The micromixer has a capacity of quick mixing of five independent streams, that can be precisely dispensed from a high-accuracy syringe pump. The main interest in such device originated from the need of a rapid and combinatorial nanoparticle formulation to create NP library. In the last few years, particle barcoding strategies have emerged as a method of their rapid detection and decoding of best performing formulation upon *in vitro* or *in vivo* screening. Despite the code combinations being from high to close to infinite, the proposed formulation methods are usually manual and rather slow. The micromixer has the potential to address this issue and provide higher throughput formulation. The micromixer proof of concept experiment was performed using fluorescent dyes for the microscopy-based

detection of mixing efficiency. Later the microfluidic mixer was integrated into a platform with NPs formulation device. Eventually the mixer was microfabricated in glass to address the issues arising from the use of PDMS prototype. Finally, the glass model was validated in the experiment integrating the mixer and nanoprecipitation chip, yielding monodisperse NPs.

Lastly, the microfluidic technology was engaged into creation of an *in vitro* screening platform for drug nanocarriers. Here, a perfusable tumor blood vessel model was engineered in a 3D cell culture chip. The lumen of the blood vessel model was exposed to flow-induced shear stress, which caused an alignment of endothelial cells. The endothelial barrier separated this dynamic environment from adherent extracellular matrix with embedded HeLa cells spheroids. The screened polymeric micelles were monitored at the recreated barriers: blood vessel lumen, endothelial barrier, extracellular matrix and the cancer cell spheroids. Their stability in space and time was revealed thanks to their spectral properties and the compatibility of the chip with confocal microscopy. Overall it was reported that the presence of cancer cells promoted leakiness of the endothelial barrier and higher intravasation of the tested NPs. However, in all the cases the permeation into the cancer spheroid was found to be low, as the micelles were detected only on the surface. Furthermore, the obtained results were confronted with previously reported findings in 2D cell culture, disclosing differences in micellar stability between the two models and demonstrating significantly different results in micelle uptake by cancer cells.

In summary, this chapters picture the microfluidic technology in the field of drug delivery and nanomedicine as a bridge between larger scale reactions and more biologically relevant microscale. It is an enabling tool, that requires adaptation into traditional methods and multidisciplinary attitude to assist this process. In this work it was supported by microscopy techniques, used to characterize the nanocarriers and evaluate their stability and performance in cancer-on-a-chip. In return the microfluidic technology offers an exploration of new areas, ranging from controlled and combinatorial drug nanocarrier formulation up to engineering of *in vitro* screening models that provide information not retrievable otherwise.

## Outlook

The year 2020 has been burdened with setbacks that affected the entire population. Research, which a continuous activity had to be paused in laboratories. It gave us time to think, rethink and replan. Below are listed few experiments that could be interesting addition to each chapter of the presented work.

The HFF formulation in Chapter 2 demonstrated its advantage over the control of particle size in response to the process parameters. It would be interesting to investigate if microfluidic formulation can provide other improvements, for example better homogeneity of dye/drug encapsulation in comparison to the manual bulk mixing method. Here, the TIRF microscopy analysis could be continued to characterize batches formulated with different fluidic parameters or co-encapsulating more than one dye. Furthermore, the diffusion-based process was here investigated for one solvent only (acetonitrile), due to its chemical compatibility with PDMS chips. Later in 2020, new, glass HFF chips were fabricated, where the chemical compatibility is not a concern anymore. It may be of interest to test other volatile organic solvents, such as tetrahydrofuran or acetone, that can potentially yield new NP diameters that can be obtained.

Chapter 3 presents the microfluidic passive mixer, which was chronologically the last piece of the work in the 3-years course of the PhD, hence it suffered most of the pandemics-related setbacks. Here, as mentioned above, the exploration of other solvents would be an integral part. However, more than that, the optimization and eventually formulation of NPs from different precursors, such as PLGA-PEG with different block lengths or targeting ligands would be of the highest importance. It would be interesting to determine the accuracy of the setup, along with fluid retention times and finally a creation of NPs library.

In the Chapter 4 the cancer on a chip platform was presented. The future work could take on different paths: one of them being the development of biological aspects, to improve the relevance of the model or enable more detailed studies on the disease development. Few examples may involve a replacement of HeLa spheroids with other cancer cell lines or even primary cells. Furthermore, addition of cancer associated fibroblasts could enrich the recapitulation of tumor microenvironment. The other path could focus on monitoring of other nanocarriers, such as the formulated in previous chapters PLGA-PEG NPs. It would be also interesting to test NPs with targeting functionalities against specific cell biomarkers and compare their performance versus the non-targeting formulation.

## Glossary

ACN – Acetonitrile,

AS – antisolvent,

CFD – Computational Fluid Dynamics,

DDS - drug delivery system,

DLS – Dynamic Light Scattering,

DMEM - Dulbecco's Modified Eagle Medium,

DOX – Doxorubicin,

EB – Endothelial barrier,

ECs - Endothelial Cells,

ECM - Extracellular Matrix

EE – Encapsulation Efficiency,

EMA – European Medicines Agency,

EPR - Endothelial Permeability and Retention,

FDA – Food and Drug Administration,

FRET - Förster Resonance Energy Transfer

HFF - Hydrodynamic Flow Focusing,

HUVEC - Human Umbilical Vein Endothelial Cells,

PdI – Polydispersity Index,

PDMS – Poly(dimethylsiloxane),

PEG – Polyethylene Glycol,

PLGA – Poly(lactic-co-glycolic) acid,

S – solvent, NPs – Nanoparticles,

NR – Nile Red,

TEM – Transmission Electron Microscopy,

TIRF – Total Internal Reflection Fluorescence,

TME - Tumor Microenvironment

## Acknowledgements

In the course of my 3-years fellowship I experienced all sorts of things, starting from moving between rainy and organized Netherlands to sunny and sometimes insane Barcelona. Also, stepping back to academia after few years of fantastic experience in pharmaceutical industry was a leap! I forgot how it is to be a “sort of” student, but luckily the people I have met, made this journey unforgettable, funny, interesting, or simply joyful.

First of all, I would like to thank to Natalia; we started to work together on an ambitious project from the first weeks of my incorporation. It has been everything: interesting, exciting, rewarding and sometimes difficult too. I am glad I could learn from you about microscopy and get some knowledge about biology. The journey that leads me to this moment has been pleasant thanks to you, scientifically as much as socially. Being in Nanoscopy Group was like having little family. Edgar, you are like a brother to me. It is impressive how calm you can stay in different situations, you dissipated your peace what was always soothing. You are a fantastic scientist and I wish you best of luck in your career and privately! Silvia, you are like a sister! I respect your ethics, attention to detail and care that you spread around us. You deserve everything and more. The cava is chilling. Maria, you have helped me to start (all the docs at UB...) and you have helped me to finish (all the docs at UB...), but actually it is more than that and you know it. The last year of pandemics and writing the thesis was hectic, thank you for your support and virtual meetings, they helped me to stay sane. Furthermore, I would like to thank to other N4N members who joined after me and shared bit of their life. Madhura, you brought the dance and music! Zumba on the beach! Teodora, I feel like we missed some coffees or beers together, thank you for all the support! Alis, I hope your talent grows and turns into not only passion but also profession. Gaia, such a beautiful soul you are, thank you for your contribution to this work and I hope we can finally meet soon! Pietro, your sense of humor is familiar, it have always made my day, from 8.00 in the morning! Sofia and Sheida, I am happy I could teach you something and learn from you in return.

N4N Eindhoven, you were the family who adopted me in 2019. Laura, your company in the lab and outside the lab was always a pleasure. Roger and Manos, thank you for helping me troubleshoot in ONI!

And of course, Lorenzo, I am glad I could join the group led by you. You have always inspired to think in a multidisciplinary way, and challenged us with scientific questions, yet gave a lot of freedom and faith for own ideas and growth.

In 2020, what was supposed to be the year of the thesis delivery, we all suffered setbacks, however, 2020 was still the year of delivery, just not of the thesis. I would like to extend my gratefulness to my supervisors, Silvia and Lorenzo, who have given me lots of understanding and trust, knowing how challenging it was for me to lose my final, neatly scheduled experimental plan, in the world of pandemics. And having to all



of a sudden, work from home with what is scientifically called “mummy’s brain”, being accompanied by all the body dimension changes that did not allow me to find a comfortable position for more than 5 minutes. I especially appreciate the extra time, that I was offered in 2021 to finalize this work. It has significantly contributed not only to this thesis, but also to my life-work balance and mental health.

Outside the Nanoscopy group I would like to thank to Josep, for staying truly involved and always having some kind and motivating words for me, that was so human, thank you! Many thanks to the Nanobioengineering Group, for letting me in and sharing your time, especially to Romen, for your guidance in the microfluidics.

Core Facilities, you are truly the Cor of IBEC, thank you for your support, help and trust. David, you are behind many achievements of individual PhD students, I owe you big thanks for your scientific input, but also encouraging and kind words. Agata, you are the example to follow, thank you for helping me with the “Pudgy” and taking care of it.

My fellow PhD students: Adrian I shared with you scientific discussions, equipment, incubators and many of my thoughts and opinions. You are a great company, thank you for sharing it all. Hari, literally you made this PhD sweeter, and as you said: “diabetes or go home”. Good luck to you, you deserve it!

Finally, I would like to thank to my family for their understanding and warm thoughts shared through the distance and to my parents in law, being best parents in law I could have, who made sure I am not hungry, so my body and brain are fueled.

Last but not least, special message to my life partner, always loving and supporting Gerard: I know that reading this thesis you are still going to ask me: “but what is this PhD? Are you a photographer?”

## Funding Acknowledgments

The project that gave rise to these results received the support of a fellowship from “la Caixa” Foundation (ID 1000010434). The fellowship code of Adrianna Glinkowska Mares is LCF/BQ/DI17/11620054. This project has received funding from the European Union’s Horizon 2020 research and innovation programme under the Marie Skłodowska-Curie grant agreement No. 713673.

Here, I would like to express my gratefulness to La Caixa Foundation, for launching the INPhINIT program, that apart from financial input, offered much more in form of personal and professional development. I truly enjoyed the annual meetings in all meanings, and I would love to have the last one, that was cancelled due to the pandemics.

All the La Caixa procedures and processes were performed with care and professionalism, that can be an example for other similar programs. This experience wouldn’t be the same without Gisela Coromines i Calders, who was always there to answer my questions and give support, together with wonderful la Caixa team, taking best care of us.

## Thesis Summary

Two decades ago, microfluidic technology begun to make its appearance in the fields of drug delivery and biomedical engineering to irrevocably revolutionize them. It was quickly realized how microchannels can aid formulation of microdroplets, microparticles and nanoparticles (NPs). They offer very small and controlled environment for reaction, that is unreproduced in bulk methods. As a result, the formulation is not limited only to the modification of compounds, but the flowing microvolumes open gates to the unexplored world of controllable mixing time and diffusion region impacting the formation of nanoparticles. Beyond the drug delivery systems formulation, the microfluidic technology is emerging as a gap-bridging element of the *in vitro* and *in vivo* tests in preclinical trials. Biocompatible and microscopy-friendly microfluidic chips are used to reconstruct physiological elements of human tissues (organ-on-a-chip). They recapitulate 3D, dynamic *in vivo* environment, that is lacking in 2D cell culture, revealing their relevance in understanding the development of a disease and screening of drug delivery candidates.

This work presents the use of microfluidic technology in the formulation of tunable size amphiphilic block co-polymer nanoparticles for drug delivery. The particle diameter is modified in the response to studied phase flow rates. The impact of fluidic parameters on drug/dyes encapsulation efficiency and NP size are analyzed using traditional bulk methods, as well as techniques with single particle resolution, such as Transmission Electron Microscopy (TEM) and Total Internal Reflection Fluorescence (TIRF). Furthermore, the NPs are bioevaluated with *in vitro* tests performed on MCF-7 cell line.

Following the NPs formulation, a chip for combinatorial mixing of NP precursors is presented. A passive micromixer is designed, prototyped and evaluated with fluorescent dyes, to visualize the mixing efficiency. Finally, the model is microfabricated in glass and re-assessed in terms of mixing and cleaning efficiency, which previously was poor due to the absorption of small molecules by PDMS. The micromixer is built into a platform for NPs formulation and first proof-of-concept experiments are performed, yielding monodisperse nanoparticles with encapsulated fluorescent dyes. The encapsulation of dyes is visualized in single particles with TIRF microscopy.

The last part of the thesis takes the microfluidic technology into organ-on-a-chip, where a reconstruction of tumor blood vessel model is presented. It recapitulates elements of tumor 3D microenvironment such as blood vessel, endothelial barrier, extracellular matrix and cancer cell spheroid. Observed *in vivo* leakiness of endothelial barrier is reproduced here in the presence of cancer cells. In this work the microscopy-friendly chip is used as a platform for time- and space-resolved monitoring of micelles stability followed during their interaction with the reconstructed barriers mentioned above. The special optical properties of perfused micelles allow to distinguish assembled from disassembled form. The results are consulted with

previously reported observations in 2D cell culture, revealing significant difference in cellular uptake between the two studies.

Overall, this work demonstrates how multidisciplinary approach of incorporation of microfluidic technology into formulation and screening of potential drug nanocarriers can accelerate development of nanomedicine. The proposed solutions deliver tunability of nanoparticle properties, combinatorial formulation to create library of NPs and a complementary method in *in vitro* screening.

## Resumen en castellano

Hace dos décadas, la tecnología microfluídica hizo su aparición en los campos de la industria farmacéutica y la ingeniería biomédica de manera revolucionaria. Rápidamente se descubrió cómo los microcanales pueden ayudar a la formulación de microgotas, micropartículas y nanopartículas. Ofrecen entornos de reacción muy pequeños y controlados comparados con la formulación de los métodos tradicionales. En consecuencia, la formulación no sólo se limita a la modificación de compuestos, sino que los flujos de microvolúmenes posibles con la tecnología abren puertas a un mundo inexplorado para la formulación de nanopartículas a través del control del tiempo de mezcla y el área de difusión. Más allá de la formulación de los sistemas de fármacos, la tecnología microfluídica está emergiendo como un elemento puente de las pruebas *in vitro* e *in vivo* en los ensayos preclínicos. Los chips de microfluidica biocompatibles y aptos para microscopía se utilizan para reconstruir elementos fisiológicos de tejidos humanos (órgano en un chip). Recapitulan el entorno dinámico *in vivo* en 3D, carente en el cultivo celular en 2D, desvelando su relevancia para comprender el desarrollo de una enfermedad y la detección de fármacos candidatos para la administración.

Este trabajo presenta el uso de la tecnología microfluídica en la formulación de nanopartículas de copolímeros de bloques anfifílicos de tamaño ajustable en respuesta a los caudales de las fases estudiadas. Se estudia el impacto de los parámetros de flujo sobre la eficiencia de encapsulación de fármacos/colorantes y el tamaño de NP. Además, se presenta un chip para la formulación combinatoria de nanopartículas fluorescentes, con potenciales aplicaciones en medicina personalizada. La última parte de la tesis traslada la tecnología de microfluidos a órgano en un chip, donde se presenta la reconstrucción del modelo de vaso sanguíneo tumoral. Recapitula las fugas observadas *in vivo* de la barrera endotelial en presencia de células tumorales. En este trabajo, se utiliza como una plataforma para el monitorización en el tiempo y en el espacio de la estabilidad de las micelas, mientras interactúan con las barreras reconstruidas que se encuentran en el cuerpo humano: vasos sanguíneos, barrera endotelial, matriz extracelular y esferoide multicelular de células cancerosas.